Bobines volumiques à base de métamatériaux pour l'imagerie par résonance magnétique à très haut champ

Anton Nikulin

PSL★
UNIVERSITÉ PARIS

THÈSE DE DOCTORAT
DE L'UNIVERSITÉ PSL

Préparée à ESPCI Paris, France

Bobines volumiques à base de métamatériaux pour l'imagerie par résonance magnétique à très haut champ

Volume RF coils based on metamaterials for ultra-high field magnetic resonance imaging

Soutenue par
Anton NIKULIN
Le 28 Septembre 2020

Ecole doctorale n° 564
Physique en Île-de-France

Spécialité
Physique

Composition du jury :

Eric, LHEURETTE		
Université de Lille, France	*Président*	
Christophe, CRAEYE		
Universit´e catholique de Louvain, Belgium	*Rapporteur*	
Jean-Yves, DAUVIGNAC		
Université de Nice-Sophia Antipolis, France	*Rapporteur*	
Charlotte, TRIPON-CANSELIET		
ESPCI Paris, France	*Examinateur*	
Nikolai, AVDIEVITCH		
MPI for Biological Cybernetics, Germany	*Invited*	
Redha, ABDEDDAIM		
Institut Fresnel, France	*Invited*	
Julien, de ROSNY		
ESPCI Paris, France	*Co-directeur de thèse*	
Abdelwaheb, OURIR		
ESPCI Paris, France	*Directeur de thèse*	

ESPCI 🎓 PARIS | PSL★   cnrs

Acknowledgements

First of all, I would like to express my genuine gratitude to my supervisors, Julien and Abdel. I could not imagine accomplishing of most of our goals without your wonderful scientific and life advising during my PhD. I had been so lucky to work with you!

At second, I would like to acknowledge the members of the defense committee for their work.

Further, I glad to write thank you to some colleagues who was willing to contribute to my work, and whom I was fortunate to work with.

Foremost, I would like to thank my colleagues from CEA NeuroSin (Gif-sur-Yvette, France). I am very thankful to Alexandre Vignaud, Benoit Larrat, and Luisa Ciobanu for their support during our joint experiments conducted in MRI. Benoit and Alexandre, I am also glad of your help with tremendous amount of administrative work we did together.

I cannot not mention all my colleagues from Marseille team (Institute Fresnel, CRMBM and Multiwave, France). Especially, I would like to mention Redha Abdeddaim who strongly involved me into the M-CUBE project and helped a lot during all the time I know this person. Marc, Tania and Marine thank you for your help over my project and for the nice time we spent during the conferences.

I also would like to express my regards to Nikolai Avdievitch with MPI (Tübingen, Germany) for his scrupulous advises over the engineering aspects of RF coils and its electronics!

Of course, I cannot forget my Russian colleagues Stas Glybovski, and Alexey Slobozhanyuk from ITMO University (St. Petersburg, Russia). Thank you for huge support before and during my PhD. I also would like to express best regards to my first supervisors from ITMO, Alexander Timofeev and Andrei Anisimov thank you for the effort you put in teaching me in the very beginning of my professional career.

Now, I would like to mention all my friends I had great time with. Pasha, Kolian, Kammel and Slava thank you for the entertaining moment we spent together in Paris! Dima, we had best fishing experience on the "Oyat" and "Izhora" rivers with you! Thank you also for being close at the difficult times. Nikita, I would say just one thing: "there was a guy, but now there is no a guy" (local joke).

Polina, I am very happy of being with you!

Contents

List of abbreviations

- **AFI**: Actual flip-angle

- **BP**: Band-pass

- **BS**: Band-stop

- **CP**: circular polarized

- **ESR**: Equivalent series resistance

- **FA**: Flip angle

- **FEM**: Finite element method

- **FOV**: Field of view

- **GRAPPA**: Generalized autocalibrating partial parallel acquisition

- **GRE**: Gradient echo sequence

- **HMA**: Hybridized meta-atom

- **HP**: High-pass

- **LHTL**: left-handed transmission line

- **LP**: Low-pass

- **MRI**: Magnetic Resonance Imaging-Magnetic Resonance Imaging

- **MRS**: Magnetic Resinance Spectroscopy

- **MTL**: Microstip transmission line

- **NRMSE**: Normalized root-mean-square error

- **PC**: Phase conjugation

- **pTx**: Prallel transmit

- **RHTL**: Right-handed transmission line

- **ROI**: Region of interest

- **SD**: Standard deviation

- **SE**: Spin echo sequence

- **SENSE**: Sensitivity encoding

- **SIV**: Signal invensity variation

- **SLR**: Split-loop resonator

- **SNR**: Signal-to-Noise Ratio

- **SRR**: split-ring resonator

- **TEM**: transverse electromagnetic

- **TR**: Time Reversal

- **UHF**: Ultra-high field

- **XFL**: Magnetization-prepared turbo-Fast Low Angle Shot sequence

Introduction

Magnetic Resonance Imaging (MRI) is a non-invasive apparatus using non-ionizing radiation developed for in-vivo imaging. MRI is based on nuclei magnetic resonance (NMR) that appears with some nuclei having angular momentum (spin) [1]. Thanks to the high concentration of nuclei (^{1}H), the main application of MRI scanners is to provide quantitative anatomical images of tissues based on proton resonance. However, MRI scanners are also useful for other purposes. For instance, being combined with magnetic resonance spectroscopy (MRS), it can be used for studying cellular metabolic processes [2], [3]. Taking benefit of the paramagnetic property of deoxygenated red cells, cerebral activity can be monitored (functional MRI - fMRI) [4]. However, for some applications the signal-to-noise (SNR) ratio provided by current clinical MRI scanners of field strength 1.5 Tesla and 3 Tesla is not sufficient [5], [6]. Because SNR is directly related to field strength, ultra-high field (UHF) MRI scanners such as at 7 T are promising and becoming more and more efficient tools [7]. They also open the door to new applications such as X-nuclei imaging (exploiting of other nuclei than ^{1}H) [3].

However, UHF MRI has certain unsolved issues [8], [9]. One of them is the decrease of wavelength due to the increase of Larmor frequency. For instance, the wavelength in tissues for proton at 7 T (298 MHz) is decimetric. Therefore, RF coils cannot be anymore considered as magnetostatic probes but more as radio frequency antennas. It makes the development of such antennas more tedious.

In this manuscript, we propose a method based on metamaterial analysis to develop volume coils for UHF MRI. More precisely, we develop a new family of metasurfaces to build volume coils with innovative features. The metasurface is made of a set of periodic resonators where the last resonators are connected to the first one. The metamaterial approach allows to precisely adjust the amplitude and the phase of the field that propagates along the ladder-like looped metamaterial and therefore can be used to shape the magnetic field almost as will. Actually, the birdcage coil that is one of the most efficient volume coils developed since the 80's for MRI belongs to this metasurface family.

The first application, to which we apply this approach, is for head imaging at 7 T. Typically, in that case, a phased array is used in reception and a birdcage in the transmission [10]. Despite having satisfactory performance, the combination of birdcage coil and phased array makes a bulky setup. Thereby, it reduces patients' comfort. In addition, this combination may not be used for some applications, such as motion correction [11].

To that aim, here, we propose to use this metasurface approach to develop a birdcage-like coil wherein the distance between the elements is not constant. We have called this optimized coil - opencage [12]. This opencage coil facilitates access to a patient or a sample to be scanned by the enlarged distance between certain elements of the coil. Two prototypes have been developed at 7 T. The first one is dedicated to preclinical imaging of small rodents and the second one to clinical imaging of human heads. Later, because X-nuclei becomes a common tool in UHF MRI, this concept of opencage coil is expanded for dual nuclei applications.

The second application is related to the lack of B_1 field homogeneity in UHF MRI. It implies SNR reduction in some regions wherein B_1 field is weak. This issue is especially associated with brain imaging or body imaging because the wavelength (λ) in tissues is smaller than the size of the volume under study. Parallel acquisition or transmission with phased coil arrays is one solution to mitigate this issue. Actually, parallel acquisition is already in use for clinical scanners working at 1.5 and 3 T [13], [14] as well as for 7 T [10]. As for transmission, the technique is called passive [9] or active B_1 shimming [15]. The combination of transmit array and receive array together provides outstanding performance, however, the cost and complexity of the coils increases, while its reliability decreases.

A simpler solution is passive shimming exploiting dielectric non-resonant pads [16] or hybridized resonator [17]. Here, we propose an intermediate alternative between full parallel transmission and passive B_1 shimming with pads or resonators. This alternative is called conjugated birdcage coil or metacage. It allows focusing the B_1 field on another location than the coil center. At first, we study this concept for 7 T brain imaging, then we show an experimental demonstration at 17.2 T for preclinical imaging of small animals.

This manuscript is divided into one review and four original chapters:

- Chapter 1 provides a historical overview of MRI emergence. The fundamental principles of MRI are also described. Then, the pros and cons of UHF MRI are discussed. Subsequently, we explain the main properties and requirements for RF coils. We start from the simplest example of a loop surface coil and then proceed with aspects of designing conventional volume coils, and finally explain the interest of phased array coils for UHF brain imaging. In the last section one provides short overview of metamaterials involved in RF coil design for UHF imaging.

- In Chapter 2 we describe the proposed principle of the metamaterial coils. Because it can be interpreted as a generalization of birdcage coils, in the first part we remind the theory of a conventional birdcage coil. In a second part, we provide an alternative to the conventional theory that is based on the transmission matrix approach. The unit cell is described in terms of phase shift and Bloch impedance. These 2 parameters, used commonly in metamaterial theory, play a key role to develop metamaterial coils with other geometries or functionalities than the birdcage ones.

- Chapter 3 presents the new type of coil - opencage coil. First, we show that due to the optimization, the conventional birdcage coil can be properly modified to have different spacings between the unit cells (rungs). In the first part, the design is done for ^{1}H preclinical imaging of small animals at 7 T. In this case the coil is used as a transceive

coil. The numerical simulations and experimental validations as well as in-vivo part are presented. The second part of the chapter shows the result of transceive head opencage coil for brain imaging at 7 T. Enlarged size of the coil and quadrature operation bring new challenges in the coil design. In the end, the coil is tested in MRI with a phantom.

- Chapter 4 shows two different dual-band coils. In the first part of this chapter, we develop a nested dual-band coil based on a birdcage coil combined with a coil made with split-loop resonators. This coil is optimized for ^{19}F/^{1}H imaging. The numerical analysis of the two structures and numerical investigation are provided. In the second chapter we show that the approach used previously for optimization of single frequency opencage coil can be expanded for the dual nuclei operations wherein two resonant frequencies are far enough, for example ^{13}C/^{1}H. In this chapter, we mainly focus on the theoretical and numerical parts of the dual band opencage coil.

- Chapter 5 raises some aspects of the design of a conjugated birdcage coil. This coil may be an effective replacement of passive B_1 shimming that can be done using dielectric pads or hybridized resonators. In this chapter, we provide a theoretical investigation of the setup for brain imaging at 7 T. Then the proposed approach is applied for 17.2 T preclinical imaging of small rodents. To that end, we perform the numerical and experimental investigations.

- Eventually, the conclusion of the manuscript is summarizing achievements of the manuscript and giving a glance of the future of RF coils in UHF MRI.

<div align="right">

CHAPTER 1

</div>

State-of-the-art and novel techniques in ultra-high field magnetic resonance imaging

---

Table of contents

In this chapter we describe the most important aspects of magnetic resonance imaging (MRI). A short history of the nuclear magnetic resonance (NMR) applications is reviewed in section 1.1. The physical principle of MRI is given in section 1.2. The next section reveals the pros and cons of the recent introduction of ultra-high field (UHF) magnetic resonance imaging. As this work is devoted to the development of new RF coils for UHF MRI, section 1.4 presents the basic principles and parameters of RF coils. Subsequently, in sections 1.4.1-1.4.3, we show currently existing solutions of surface, volume, and phased arrays coils. Eventually, in 1.4.4 we focus on metamaterial-based coils for MRI.

1.1   Historical overview and emergence of MRI

The story of NMR originated in 1938, when Isidor Rabi discovered and measured NMR effect in molecular beams [18]. The NMR implies resonant absorption and emission of electromagnetic waves at the so-called Larmor frequency of ω_0 by the matter containing nuclei with nonzero spins (angular momentum) and being placed inside a static magnetic field B_0. For this discovery, Isidor Rabi was honored by the Nobel Prize in 1944. Subsequently, his discovery was improved in 1946 by Felix Bloch and Edward Purcell, who observed NMR in liquids [19] and solids [20]. However, at that moment these discoveries did not turn the NMR into the imaging applications.

The application of NMR for imaging, initially called NMR zeugmatography, started with the work of Lauterbur in 1973 [1]. In his work, he showed that planar images based on NMR effect can be obtained when the object under interest is placed in a spatially varying static magnetic field. Indeed, in such a case, because the resonance frequency of a nucleus is dependent on the magnetic field strength, the position can be recovered from a spectral analysis of the RF signal generated by the nucleus spins. Later, in the late 1970s the fast post-processing method was developed by mathematician Peter Mansfield [21]. With his development, and NMR as a multidimensional medical imaging technique became possible. For these investigations, Paul Lauterbur and Peter Mansfield shared the Nobel Prize in medicine won in 2003.

In 1980s these methods as well as general improvements of semiconductors-based electronics made possible industrial production of NMR scanners, which was renamed MRI because the fear of nuclear danger, despite non-ionizing radiation used in NMR. At that time, most of the MRI scanners were low-field with field strength (B_0) below 0.5 T [22]. These scanners had a lot of restrictions and limitations, for instance the low SNR of acquired images.

To overcome these limitations, GE Research Center developed a full-body MRI scanner in 1980 [23]. This strength of static magnetic field of this scanner was 1.5T. Such increase in strength allowed to solve many issues attributed to low-field full-body MRI scanners such as low SNR and engineering difficulties of designing relatively small RF coils compared to wavelength [23]. During the 1980s, 1.5 T MRI scanners became essential and flexible clinical and preclinical non-invasive tools with shipment of over 20000 units at these days [22]. Nowadays, the vast majority (70%) of the MRI scanners is still working at 1.5 T [22]. More recently 3 T

scanners also became largely distributed in hospitals [24], [25]. Later, more complicated systems working at 4 T [26], 4.7 T, 7 T [8] and 8 T [27] have been introduced for research purposes. However, most of them are not considered as a common system for daily operations except 7 T systems. Eventually, one concludes that currently promising system for clinical routine is 7 T [25].

These 7 T systems provide ultimately high SNR compared to lower field systems such as 1.5 T and 3 T [5]. However, the technology becomes more expensive and difficult due to several reasons. For, instance the higher resonance frequency at 7 T leads to RF field inhomogeneities because of the smaller wavelength ($\lambda \approx 1$ m in free space and $\lambda \approx 12$ cm in tissues). Increase of magnetic field strength requires also more care about magnetic compatibility of the used components and the environment around the scanner. Phased array coils are preferred for UHF imaging [13], [10], because they allow to get rid of most flaws of the conventional coils, such as birdcage coil [9] or TEM coil [28]. The additional drawback is that the magnet employed in 7 T MRI is heavy, which requires especially adapted large rooms for carrying the system. Moreover, magnetic field penetrates thought walls, closets, and other environment, therefore, the room the scanner must be well shielded.

Eventually, even higher field strength full-body systems of 9.4 T [29] and 10.5 T [30] were invented and used purely for research purposes of imaging and spectroscopy. The cutting-edge full-body system, being deployed at CEA NeuroSpin (France) has recently reached 11.7 T [31].

In contrast to full-body scanners, there is another branch of scanners, called preclinical scanners for small animals or for humans. These scanners are mainly used for research purposes. The field strength in this scanner is typically equal to 4.7 T or 7 T. However, the cutting-edge MRI preclinical studies can be performed with magnets up to 21.1 T [32], 23.5 T [33], and even very recently 28 T working at 1.2 GHz [33]. To conclude, we have quickly reviewed the history of MRI, subsequently in thbee next chapter we reveal some fundamental aspects of that apparatus.

1.2 Principle of NMR

NMR is based on the Larmor precession of some nuclei in a strong static magnetic field B$_0$ [34]. Indeed, a magnetic field B$_0$ exerts on a particle showing a magnetic moment μ, a torque:

$$\Gamma = \mu \times \mathbf{B}_0. \tag{1.1}$$

The magnetic moment μ of the particle is proportional to its angular momentum $\mathbf{L}$, i.e., $\mu = \gamma \mathbf{L}$ where γ is gyromagnetic ratio. The angular momentum is solution of the fundamental relation of dynamic, i.e.,

$$\Gamma = \frac{dL}{dt}. \tag{1.2}$$

Consequently, the angular momentum is precessing with a frequency (Larmor frequency) given by:

$$f = \frac{\gamma B_0}{2\pi}. \tag{1.3}$$

However, if this classical view provides an intuitive interpretation of the Larmor frequency, only quantum mechanics can correctly describe the phenomenon. First, this theory is required to justify the intrinsic spin of protons and neutrons and therefore the spin of nucleus. Moreover, within this framework, the Larmor frequency is more related to the energy level difference between two consecutive nucleus spin states. For instance, for the hydrogen ^{1}H, the spin can be either in two spin states. Either the component of spin parallel to magnetic field is in the same direction as this last (state $1/2$ or up) or in opposite direction ($-1/2$ or down). Because of the interaction of the magnetic moment with the magnetic field, these 2 states show different energies:

$$E_{\pm 1/2} = \pm\frac{1}{2}\hbar\gamma B_0. \tag{1.4}$$

Thereby, when a material is being placed into a strong static magnetic field B_0, at thermal equilibrium, the lowest state of energy of the spin is more populated than the higher one(s) and the magnetization M becomes aligned to that B_0 field (Fig. 1.1).
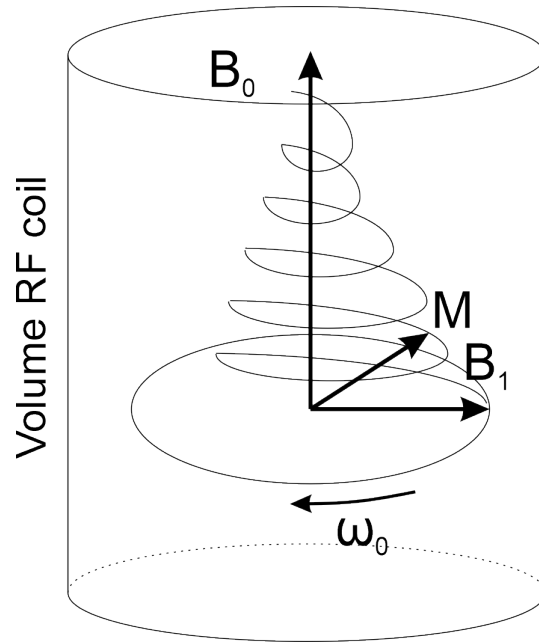
Figure 1.1 – Principle of NMR magnetization flip.

However, the population can be modified by applying an additional RF magnetic wave packet (B_1^+) oscillating at the Larmor frequency with a circular polarization that is transverse to the static B_0 field. The rotation direction should be in the same as the one of the Larmor precession [35]. Due to this stimulated excitation of the spin state, the magnetization M becomes progressively parallel to B_1 field. Hence, the maximum flip angle (FA) is 90°.

When the excitation of B_1^+ field is interrupted, the nuclear spins progressively stop being aligned, and as a result, the magnetization M goes back to its initial state. During this process, an echo, i.e., a RF field, B_1^- is generated by the spins at the Larmor frequency [35].

Two relaxation processes occur: the longitudinal relaxation (along axis parallel to B_0) and the transverse relaxation (in the plane perpendicular to B_0). Two characteristic times are associated with these processes, T_1 and T_2 respectively.

This echo can be collected by the same coil as the transmit one or another receive coil [36]. The resonant frequency of the particular nuclei and therefore, the working frequency of the transmit/receive coil as well is defined by the Larmor equation stated before. Because, the collected signal is very weak, the receive coil should be well tuned, and impedance matched at the working frequency in order to minimize the noise. The concrete properties of receive and transmit coils are presented in Chapter 1.4.

Spatial encoding of signal is based on an additional magnetic field G created by a gradient system that adds to the static field B_0. Note that the gradient can be changed during the acquisition. As a result, spatial encoding can be done by receiving the signal at different frequencies according to:

$$\omega_0 = \gamma[B_0 + G(x, y, z, t)]. \tag{1.5}$$

The raw data are the transversal components of the magnetization in the imaging object gathered from the receive coil and stored as a function of time during the acquisition process. One can show that in a transverse slice and with linear gradients, the raw data are directly linked to the k-space Fourier transformation of the magnetization. By changing the gradient over time, the complex k-space data can be sampled. Every point in the raw data matrix contains certain information related to the complete image, however this point does not correspond to a point in the image matrix. The "image" is then recovered by an inverse Fourier transform (see Fig. 1.2).
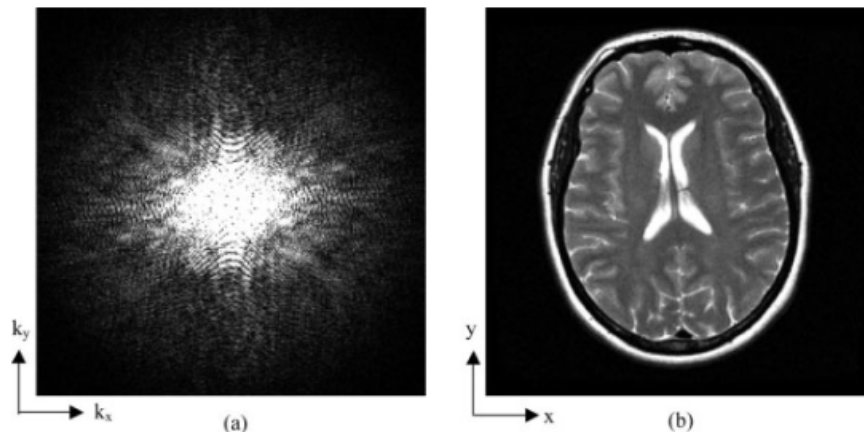
Figure 1.2 – On the left: raw k-space data and on the right the inverse Fourier transform corresponding to an image [37].

Because of the gradients, the RF excitation pulse should be provided not at the single frequency but in a narrow frequency band, which typically equals few a kHz [38].

The process of applying radiofrequency pulses, acquiring their echoes and tuning simultaneously the gradients is called a pulse sequence [39]. Generally, there are two basic types of sequences, spin echo (SE) applying 90° pulse called flip angle (FA) [40] and gradient echo sequence, with usually smaller FAs α from 10° to 80° [41]. Another type of sequence such as AFI [42] or XFL [43] can be used to map the RF field. In addition, depending on the applications of MRI, magnetic resonance spectroscopy (MRS) and functional MRI (fMRI) different specific sequences should be employed. However, developing pulse sequences is not a target

of the current PhD thesis, which focuses on designing of new RF coils using metamaterials approach.

As it was mentioned before, the frequency of NMR is defined by Larmor equation, wherein the gyromagnetic ratio depends on the nuclei. This ratio for some compatible nuclei is shown in Tab. 1.1 [35], [44].

Table 1.1 – The gyromagnetic ratio of some nuclei commonly used in MRI, MRS and fMRI.

Nucleus	$\gamma/2\pi$ (MHz/T)
Proton ^{1}H	42.6
Phosphorus ^{31}P	17.2
Fluorine ^{19}F	40.1
Sodium ^{23}Na	11.3
Lithium ^{7}Li	16.5
Oxygen ^{17}O	-5.7
Carbon ^{13}C	10.7

Amid this plurality of nuclei, the appropriate one for anatomical image is proton ^{1}H. Therefore, it is exploited in most clinical and preclinical imaging applications. The proton ^{1}H has almost the highest frequency in the NMR spectra. Moreover, there are also a bunch of nuclei, called X-nuclei (see Tab. 1.1), appropriate for imaging and spectroscopy used for the different medical or research purposes [45]. The application of MRI and MRS is very broad, it can be used for many different applications. For example, tracking of injected cells into a body or detection and quantification of immune cell therapy for cancer using fluorine ^{19}F [46], [47]; studying tissue metabolism using phosphorus ^{31}P associated with many disorders and diseases [48]. Sodium ^{23}Na imaging can be used for elucidating the effects of sodium disequilibrium in multiple sclerosis pathology using [7]; Study of Alzheimer's disease, Huntington's disease, epilepsy and other [3]. Carbon ^{13}C can be used imaging breast cancer using hyperpolarized carbon [49], Mapping of metabolism is possible with deuterium ^{2}H [50]. Some examples of MRI images are presented in Fig. 1.3.

1.3   Ultra-high field MRI

Since the clinical emergence of MRI in the early 80^s, the strength of magnetic field in MRI increased from bellow 0.5 T to 1.5 T and 3.0 T in clinical daily routine [6]. These values
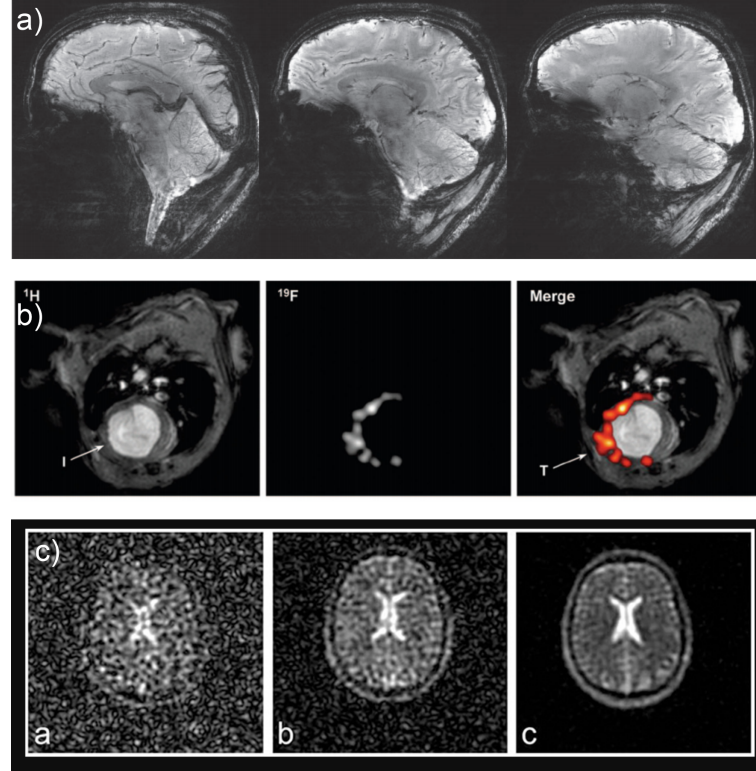
Figure 1.3 – (a) Anatomical (^{1}H) images of human brain [51]; (b) merged images (^{1}H and ^{19}F) of mouse thorax [52]; (c) [23]Na images of human brain at multiple field strength (1.5 T, 3 T and 7 T) [7].

correspond to moderate and high field strength, respectively. As explained before, the strength of the next generation of scanners is going to Ultra High Field (UHF). Even though MRI examinations can be conducted on scanners working between 9.4 T and 11.7 T, the most promising field strength for clinical routine is 7 T field [6].

The main advantage of UHF scanners, such as 7 T, is to provide a greater SNR compared to 1.5 T and 3 T systems [5], [7]. Higher SNR allows detecting earlier stage of diseases and in general allows improving quality of acquired images. Moreover, for the most spread MRI systems of 1.5 T the SNR for X-nuclei is dramatically small [see Fig. 1.3(c) for an example of [23]Na imaging] and its resonant frequency may be very low. Such a low SNR makes MRI at 1.5 T using X-nuclei less informative, whereas at 7 T the SNR and resonant frequency is acceptable [3].

Basically, the fundamental increase of SNR comes from spin magnetization M. Indeed this last is expressed by the formula [22]:

$$M = \rho_0 \frac{\gamma^2 \hbar^2}{4kT} B_0, \tag{1.6}$$

where ρ_0 is the proton spin density, γ is the gyromagnetic ratio, $\hbar$ is the reduced Planck constant, k is the Boltzmann constant, T is the absolute temperature (in Kelvin) and B_0 is the static magnetic field. We observe that the magnetization M scales linearly with field strength B_0. However, the SNR does not depend linearly on B_0 field. In practice, the SNR depends on many factors, for example, the spatial resolutions (voxel size), thermal noise of the sample, noise of the electronics, quality factor of the coil as well as the static B_0 field.

This non-linear improvement of SNR with field strength can be observed in Fig. 1.4(a). Increase of temporal SNR is especially important for functional MRI (fMRI) [see Fig. 1.4(b)] where the duration of a sequence and therefore SNR is limited by the characteristic evolution time of the function under study.
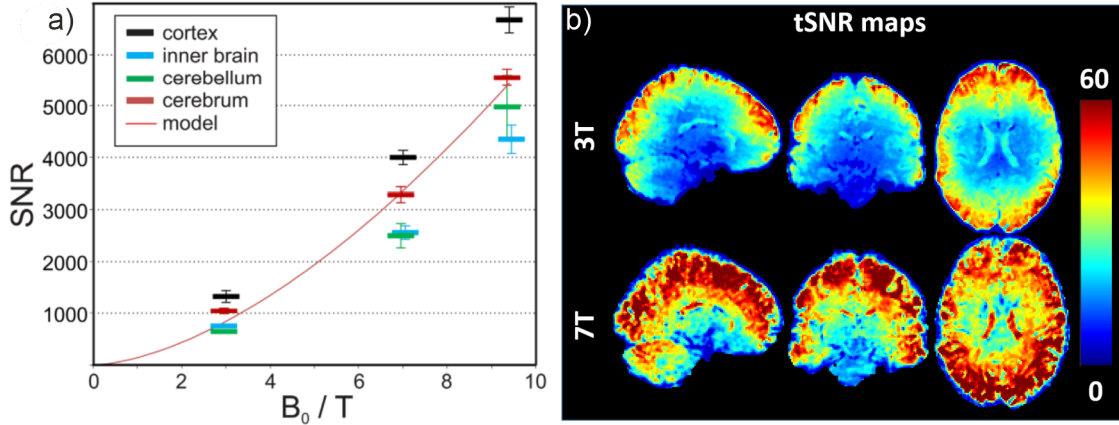
Figure 1.4 – (a) The SNR of images obtained in different parts of brain using 3 T, 7 T and 9.4 T MRI [5]. (b) The tSNR maps in the brain at 3 T and 7 T [31].

However, one of the major drawbacks of UHF MRI is the B1 field homogeneity because of the wavelength decrease (Fig. 1.5). For instance, at 7 T, the wavelength is as small as $\lambda \approx 12$ cm in tissues [8]. As a result, a conventional coil cannot generate a uniform field on some large organs such as head. Dark spot occurs where the RF field is not high enough to properly flip the magnetization (flip angle) leading to SNR drop. One solution to mitigate this issue is transmit phased arrays wherein the amplitudes and phases of each element can be passively tuned [9]. This technique to homogenize the field is called passive B_1 shimming. There is also active B_1 shimming or parallel transmission (pT_x) that allows to modify phases, amplitudes as well as pulse shape during running the sequence [15], [53], [54]. However, pT_x has certain flaws related to the fact that the B_1 field pattern from each independent element of the phased array should be analyzed independently for each subject. Consequently, pT_x is a time-consuming procedure, which requires measuring subject-specific field maps and does not fit into a routine clinical scanning. Furthermore, stated adjustment leads to fine adjustment of the transmit power allowing to finely tune the SAR [9]. In contrast to phased arrays, conventional coils are usually much closer to the SAR limits because of the higher power needed to converge the FA on dark spot [22].
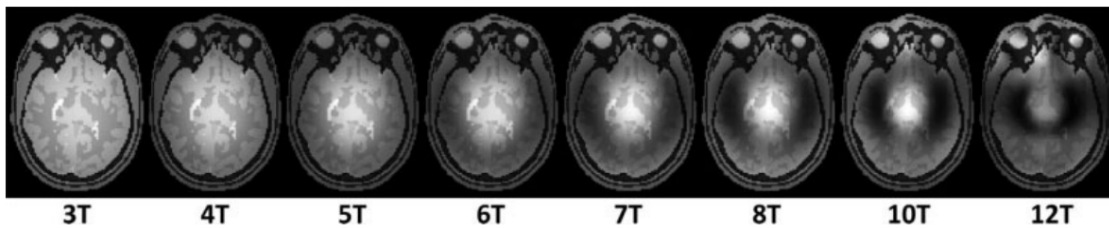
Figure 1.5 – The simulated images of the human brain at different magnetic field strength using a birdcage coil [9]. Inhomogeneity is clearly seen after 6T.

Of course, the same issue of homogeneity occurs in reception. Again it can be overcome using phased arrays (parallel imaging) as shown for example in references [10] and [51]. A significant

increase in SNR with 32 channels received phased array coil compared to birdcage coil can be seen in Fig. 1.6(a). This effect is less explicit when a 8 channel T_x array replaces a birdcage [Fig. 1.6(b)] where an overall increase in the mean SNR is about 10% [51]. However, use of T_x arrays allows to homogenize B_1 field map according to RF shimming.
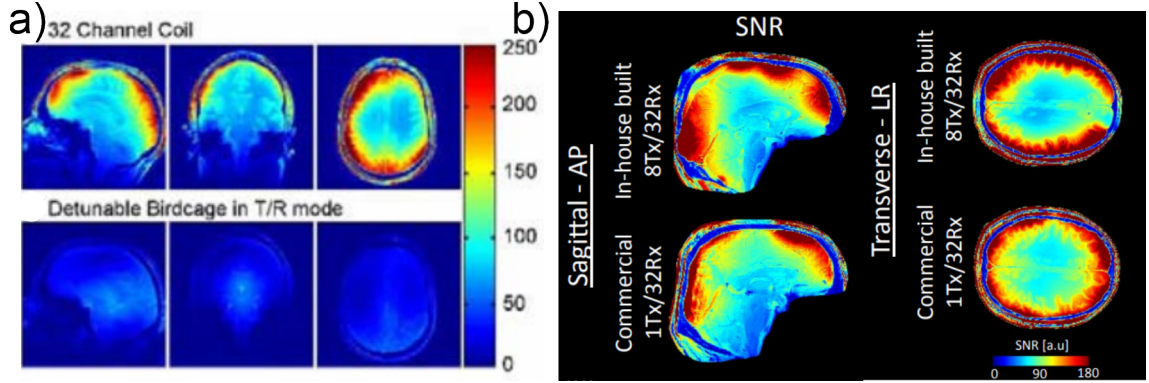

Figure 1.6 – The SNR maps in the brain: (a) maps obtained with 32 channels receive coil (T_x birdcage) and T_x/R_x birdcage coil [10]; (b) maps obtained with $8T_x/32R_x$ arrays and commercial $1T_x/32R_x$ arrays [51].

In addition, at UHF field, for instance 7 T, the examination takes more time than at 1.5 T and 3 T. The cause is the increase of T_1 relaxation time. Moreover, it is also known that a strong static magnetic field can introduce physiological effects such as dizziness, nausea, magnetophosphenes, or metallic taste [3], [55]. Therefore, it is important to decrease the scanning time for the sake of patients' comfort. One solution is to perform accelerations available in parallel imaging. These acceleration methods are SENSE [56] (Sensitivity Encoding for Fast MR) and GRAPPA [57] (Generalized Autocalibrating Partially Parallel Acquisition). Basically, they are based on under sampling in phase-encoding steps. In fact, both technologies are not especially done for UHF, and can be exploited with any scanner supporting multi-channel receive coils. However, acceleration techniques sacrifice the SNR of the images [56]. Indeed, in case of SENSE the SNR can be estimated by the following formula:

$$SNR_{SENSE} = \frac{SNR_{FULL}}{g\sqrt{R}}. \tag{1.7}$$

In this formula g is a spatially dependent term called geometrical factor, or g-factor, R is a parallel imaging acceleration factor.

At last, one would like to briefly note that the increase of magnetic field strength requires more care about magnetic compatibility of the electrical components and the environment around the scanner, such as extinguishers, stretchers, furniture, and others. For example, one situation appeared in 2001, when a boy was killed, when magnetized extinguisher started flying in the MRI room [58].

Eventually, all stated above challenges make UHF MRI, and RF coils quite expensive compared to 1.5 T and 3 T. To conclude, we have reviewed the advantages and challenges of UHF MRI, and now we would like to describe the framework devoted to resolve some fundamental issues of UHF MRI. The name of the project is M-CUBE.

M-CUBE (MetaMaterials for MRI) project. Our investigation has been done in the framework of European M-CUBE project [59]. This project gathers 8 universities and 2 commercial partners located all around the globe. The project is aimed to go beyond the limits of clinical UHF MRI. For example, UHF MRI scanners are constrained by the lack of homogeneity of the acquired images and by limitations related to the specific absorption rate (SAR) associated with the transmit RF coil. By gathering MRI experts and physicist working in the cutting-edge domain of electrodynamic-metamaterials, it is expected to solve some fundamental restrictions in UHF MRI due to RF coils. Before considering metamaterial inspired coils, we review conventional coils and phased array coils.

1.4 RF coil classification and parameters

Here we discuss the classification of RF coils employed for UHF MRI. Design and evaluation of properly selected RF coils are critical for a safe and successful MRI imaging. To remind, RF coils are required for exciting the nuclei' spins (flipping their magnetization) with B_1 field (transmit coil) and probing nuclei echo (receive coil). These two operations can be done by a single coil (transceive), or by two distinct coils (transmit only receive only - ToRo) [36].

Transmit coils Contrary to receive coils (see below) the dimensions of transmit coils are usually larger. The parameters that are important to assess performances of transmit coils are:

- Transmit efficiency ($\frac{B_1^+}{\sqrt{P}}$) related to the input power [60];

- Homogeneity of magnetic field B_1^+, which can be accessed with normalized root mean squared error (NRMSE) or normalized standard deviation;

- Specific absorption rate (SAR) measured in W/kg, or what is more relevant - SAR efficiency, defined as ($\frac{B_1^+}{\sqrt{SAR_{10g}}}$). Thus, the input power has certain limits related to a SAR limit [61]. Moreover, the inhomogeneity in electric field can produce some local hot spot, which is undesirable. This problem can also be overcome with T_x phased arrays by adjusting amplitudes and phases in each element [3].

Receive coils In contrast to transmit coils, the ideal receive coils should be as small as possible to tight fit and be the closest to the scanned sample. The Rx coil should be sufficiently sensitive to provide high SNR. The average SNR of the image can be defined as mean signal over the standard deviation of noise. Receive coils are mainly characterized by

- Homogeneity of magnetic field B_1^-, which can be assessed with normalized root mean squared error (NRMSE) or normalized standard deviation; Note that contrary to transmission, in reception, the generated signal is due to the counter-clockwise circularly polarized magnetic field.

- SNR map that is related to the received efficiency

Generally, the plurality of RF coils can be classified into two groups depending on the application: surface coils and volume coils

1.4.1 Surface coils

The loop coil is one of the basic coils for MRI imaging. This coil is useful for many applications, wherein it is less important to obtain a signal with high SNR from the whole sample than to acquire as much signal as possible from a small region of interest (ROI) [62]. The surface loop coil originates in 1970, when it was used to measure the blood velocity using a magnet of 0.36 T [63]. These days, loop coils are widely used for both transmit and receive regimes [64], albeit they can be used as receive probe only [65]. It is widely available commercially for any field strength [66], [67]. For example, preclinical imaging of small animals' organs; clinical imaging at 1.5 T and 3 T of wrist, joints of toes and fingers, skin, temporo mandibular joints imaging, knees. Several preclinical and clinical commercial examples related to surface loop coils are depicted in Fig. 1.7. In practice, the surface coil may have different shapes [68] or it may be flexible as well [69] in order to tightly fit the area under examination.
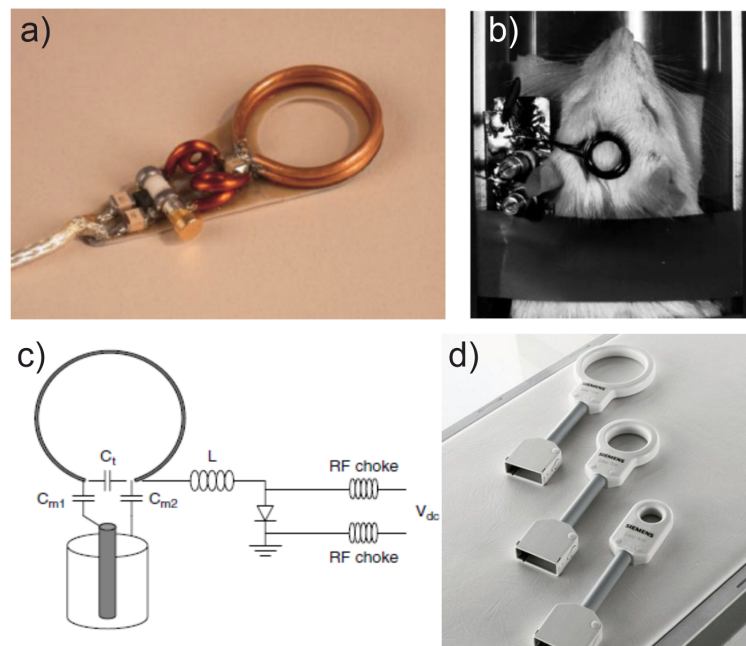
Figure 1.7 – (a) A 20 mm balanced receive only surface loop coil [64]; (b) earlier surface loop coil design performed for study of a rat brain [70]; (c) tuning, matching balancing and detuning circuit for receive only surface loop coil [70]; (d) commercially available clinical receive loop coils [66].

First of all, we would like to consider the physical principle of a surface loop coil. The sketch of a typical surface loop coil is shown in Fig. 1.8(a, b). In such a loop, the current I flowing around the loop produces a magnetic flux B that is coaxial to the ring axis.

The produced B field of this setup schematically depicted in Fig. 1.8(a) can be calculated using Biot-Savart law [70], [72]. According to this law the expression of the axial component (B_y) can be expressed as [71]:

$$B_y = \frac{\mu_0 I}{2} \frac{a^2}{(a^2 + y^2)^{(3/2)}}.$$

(1.8)
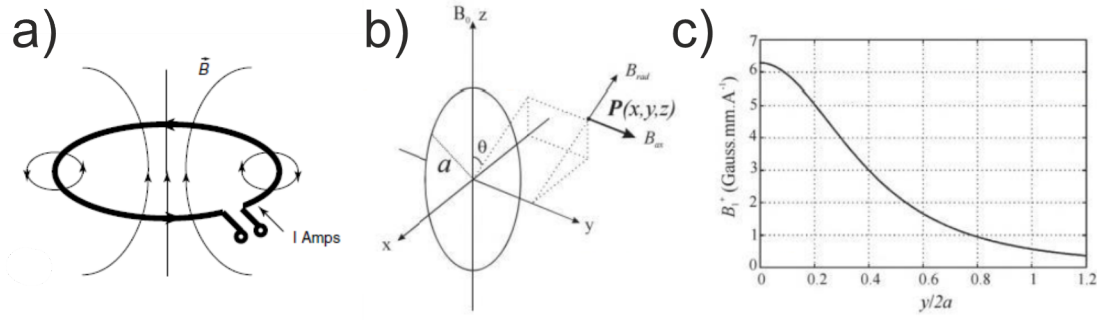
Figure 1.8 – (a) Schematic view of the surface loop coil [70], (b) B_1 field distribution of surface loop coil, (c) magnetic field strength of surface loop coil [71] over the loop axis.

Where μ_0 is the magnetic constant, I is the currents flowing around the loop, a is the loop's radius, y is the distance from the loop's surface. As it can be seen and according to the formula above, the field quickly decays along the axis of the loop [Fig. 1.8(c)], and therefore the efficiency of the coil also decreases toward the axis of the loop. Thus, to increase the penetration depth, the loop's diameter can be increased. However, this diameter increase sacrifices the SNR [70]. In Fig. 1.9, we show the spatial dependence of SNR for several loop sizes.
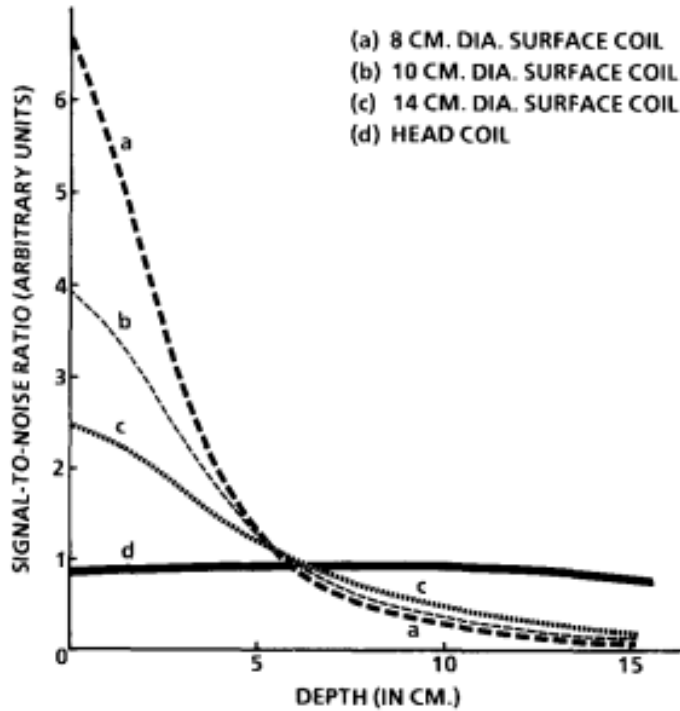
Figure 1.9 – Dependence of SNR as a function of distance for loops of different sizes and for the volume coil [73].

Usually, the perimeter of the surface loop is much smaller than wavelength. From an electrical point of view, this wire can be represented by an inductance L that can be easily calculated according to [71], [74]. To be resonant at the desired frequency of ω, capacitances of value C have to be inserted in the loop [Fig. 1.7(c)]. To resonate at ω, the capacitance value should be given by

$$C = \frac{n}{L\omega^2},$$

(1.9)

where n is the number of loop segments. In the loop design, it is important to meet the rule wherein the diameter of the coil should be smaller than $\lambda/20$ of wavelengths to stay much below its geometrical resonance that occurs when the perimeter is of the same order as the wavelength . In this case, the loop is considered as electrically small and it leads to homogeneous current distribution on it. As a result, the magnetic field distribution is symmetrical. At moderate field, for instance 1.5 T, λ in free space equals 4.7 m, while at 7 T it becomes only 1 m. Therefore, the maximal available diameter is 5 cm. In order to increase this geometrical size, the loop must be electrically shortened with capacitors distributed around the circumference. This segmentation also induces electrical field reduction, which is important to stay below the SAR limit in the transmit regime.

The surface coils are also appropriate for multi nuclei imaging and spectroscopy. After small modifications, the conventional loop may be suitable to resonate at two-frequency bands. It can be achieved, for example, by switching the the matching/tuning circuit as it is explained in [71]. Another method that can be used is multipole insertion method, wherein an additional resonant LC circuit inserted to the coil makes that last resonate at 2 frequencies [70].

1.4.2 Volume coils

There are two kinds of cylindrical volume coils that can either produce axial [Fig. 1.10(a)] or transverse [Fig. 1.10(b)] magnetic field with respect to their axis within their volume. In this work we do not consider axial resonators, such as a solenoid [75] that is a very common coil for example at 17.2 T imaging [76]. Transverse resonators are well adapted for head or body imaging because they generate magnetic field perpendicular to the bore axis. The basic principle of transverse volume coil shown on Fig. 1.10(b) is based on a cylinder with surface current $J(\varphi)$ flowing parallel to the cylinder axis(φ is the azimuthal angle). When the phase of current equals the angle φ, a homogeneous magnetic field B_1 is generated inside that cylinder [77] at least for scanners up to 4 T when considering brain imaging for example.

There are many different ways known in the literature to realize the principle shown in Fig. 10 (b) : cosine coil [78], saddle coil [79], birdcage coil [80], transmission line or TEM coils [81], [82], [83], [84], ... All these realizations are based on the same approximation: the continuous conductive cylinder is replaced by a set of conductive wires (legs) parallel to the cylinder axis. The greater the number of legs and the more homogeneous the magnetic field.

Birdcage coils A birdcage coil is a volume resonator invented in 1985 by C. Hayes [80]. The advantage of the birdcage coil is to generate a highly homogeneous magnetic field inside the resonator's volume. However, this general increase of homogeneity is at the cost of an increase of complexity. In the beginning, the birdcage coil was proposed for full-body imaging [80], while later it was used in many applications at various field strengths [85], [86], [87]. A birdcage coil is composed of N parallel conductors (legs or rungs). Each of them is at the edge of a regular polygon as it is shown in Fig. 1.11(a). Leg extremities are interconnected by way of end rings. Depending on the application; the number of legs N typically ranges between 4 and 32. The currents along the longitudinal legs generate the transverse magnetic field results from . These currents result from the electrical ladder network composed of N unit cells. Each element consists of one leg inductance and two end-ring inductances. In addition, each unit cell has
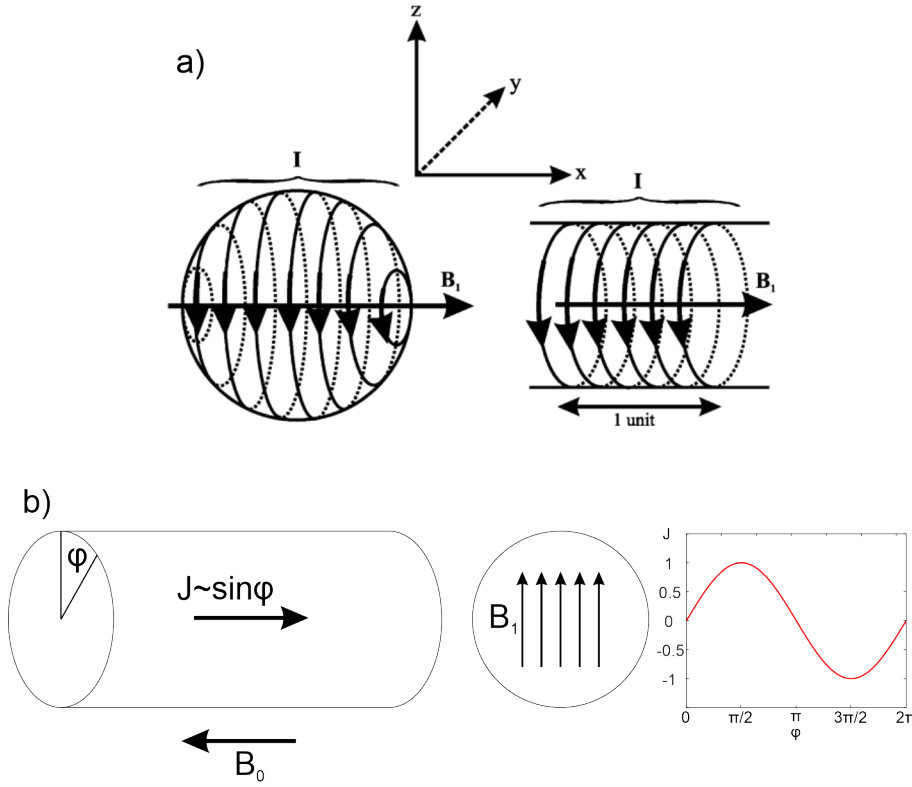
Figure 1.10 – **(a) Surface current [77] of axial resonators; (b) Surface current** J **showing cosine-like amplitude with azimuthal angles around the infinite cylinder produces homogeneous** B_1 **field inside that cylinder.**

capacitors placed in the legs in the end rings or in both segments [Fig. 1.11(b)]. These 3 kinds of unit cell correspond to a low-pass, a high-pass and a band-pass filter, respectively
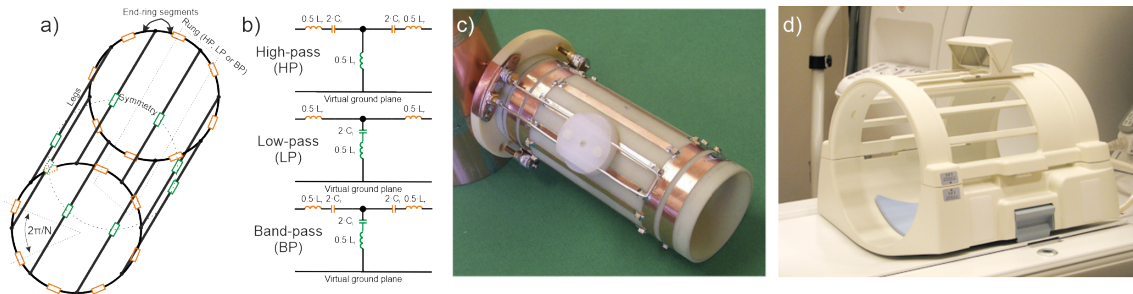
Figure 1.11 – **(a) Schematic view of the conventional birdcage coil composed of eight rungs; (b) unit cell of the conventional birdcage coil; (c) low-pass birdcage coil for preclinical imaging at 4.7 T [77]; (d) commercial head birdcage coil for clinical imaging from GE healthcare [88].**

By using an analysis based on the birdcage unit cell, it is possible to define the capacitance needed to tune the fundamental mode of the birdcage coil to a desired Larmor frequency. The detailed analytical analysis of the birdcage coil is provided in Chapter 2. Eventually, the different examples of preclinical and clinical birdcages are presented in Fig. 1.11(c, d).

A birdcage is a resonant system that exhibits resonant modes. For instance, the reflection parameter of a low-pass and a high-pass birdcage are shown in Fig. 1.12(a) and 1.12(b), respectively. The total number of modes k depends on the number of rungs N. Note that N

positively acts on homogeneity of B$_1$ field, whereas negligibly affects the field amplitude in the center [55]. The current distribution on the leg and the magnetic field of 6 modes of a low pass birdcage are shown in Fig. 1.12(c).

The fundamental mode ($k = 1$) is the mode that generates a homogenous field inside the birdcage. We observe in [Fig. 1.12(a)] (respect. [Fig. 1.12(b)]), that this mode occurs at the lowest (respect. highest) resonant frequency for low-pass (respect. high-pass) birdcage.
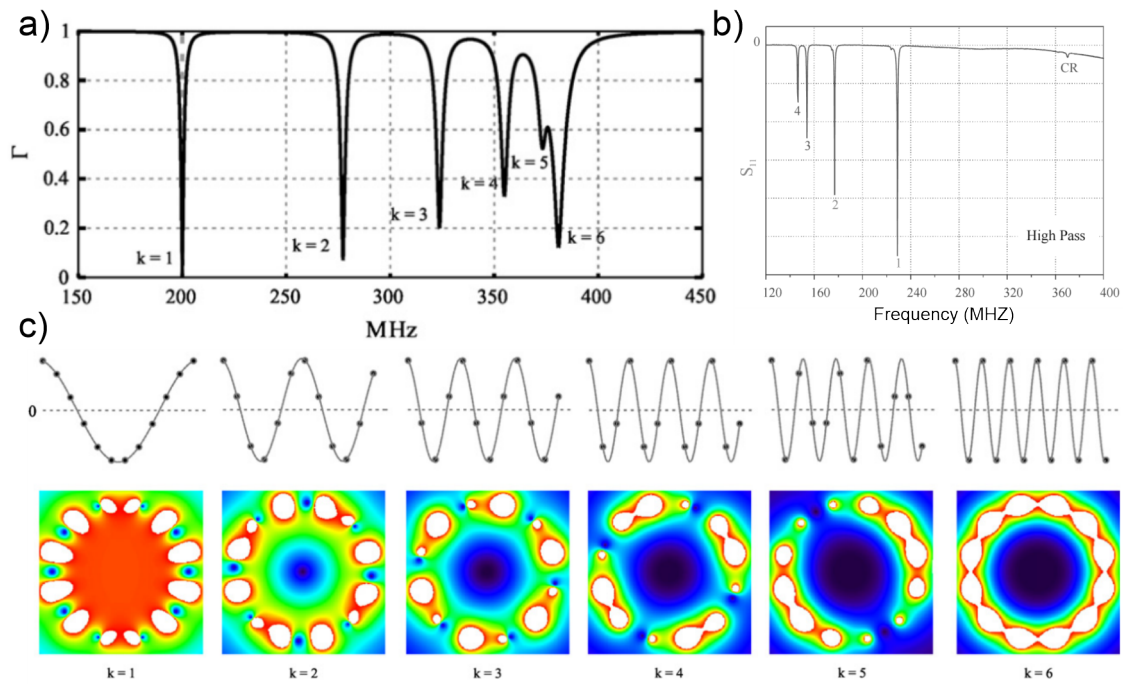
Figure 1.12 – S-parameter spectrum of the low-pass [77] (a) and high-pass (b) birdcages [71]; (c) Top: current distribution associated to mode k. Bottom: Magnetic field distribution associated to mode k.

These different topologies have different properties and features. For instance, high-pass is preferable for the coils at UHF MRI, whereas low-pass is better for lower field MRI because the fundamental (k=1) mode of the LP birdcage is lower in terms of frequency compared to the HP birdcage coil of the same size [88].

In addition, a birdcage coil supports quadrature operations (circular polarized mode), which can increase the SNR by $\sqrt{(}2)$ [89], [90]. Circular polarization results from two orthogonal linear modes that can be excited in a birdcage coil at the same frequency (degenerated modes). These modes are well decoupled due to their orthogonality. They are excited by 2 ports that are 90° distant. The isolation level ($|$S$_{12}|$) for the properly assembled coil is typically equal to -20dB. At the same time, because the modes are well decoupled it is possible to tune and match them independently. The frequency tuning is done by a capacitor that is 90° apart if the feeding ports are placed in ring (parallel to the capacitor) and 180° apart if the feeding ports are placed between ring and shield. The impedance matching can be done by placing a capacitor in serial or parallel to the feeding port. The development of a quadrature birdcage coil is slightly more complicated than a linear polarized birdcage coil because it also requires a power splitter providing 90° phase shift between two feeding ports and 2 T$_x$/R$_x$ switches for each receiving channel.

The head birdcage coils are convenient to handle at magnetic fields up to 7T for proton imaging and even higher field when exploiting X-nuclei because they usually have lower frequency.

Talking about UHF fields such as 7 T, the birdcage coil plays the role of a transmit head coil, while another phased array coil is typically employed for receive. In this case, the transmit birdcage coil should be detuned out of the resonance frequency in the receive regime to not perturb the receive array coils. One example of this detuned coil is provided in [36]. One of the best ways to provide detuning is inserting at each leg or end-ring segment an active controlled switch based on PIN-diodes creating open circuit, i.e., blocking currents flow. At the same time additional current path should be provided for controlling the PIN diodes by DC current. Moreover DC lines must be separated from RF signal using chokes [36].

A birdcage coil can also be designed for dual-nuclei operations. Many different designs are known in the literature. For instance, four ring birdcage [91], dual-band, band-pass or band-stop birdcage [92], nested birdcage for dual-nuclei operations [93], birdcage with even or odd capacitors [94]. Some of them are presented in Fig. 1.13. Depending on the chosen applications, the proper design must be selected. These approaches can be used when Larmor frequencies of both nuclei are far enough.
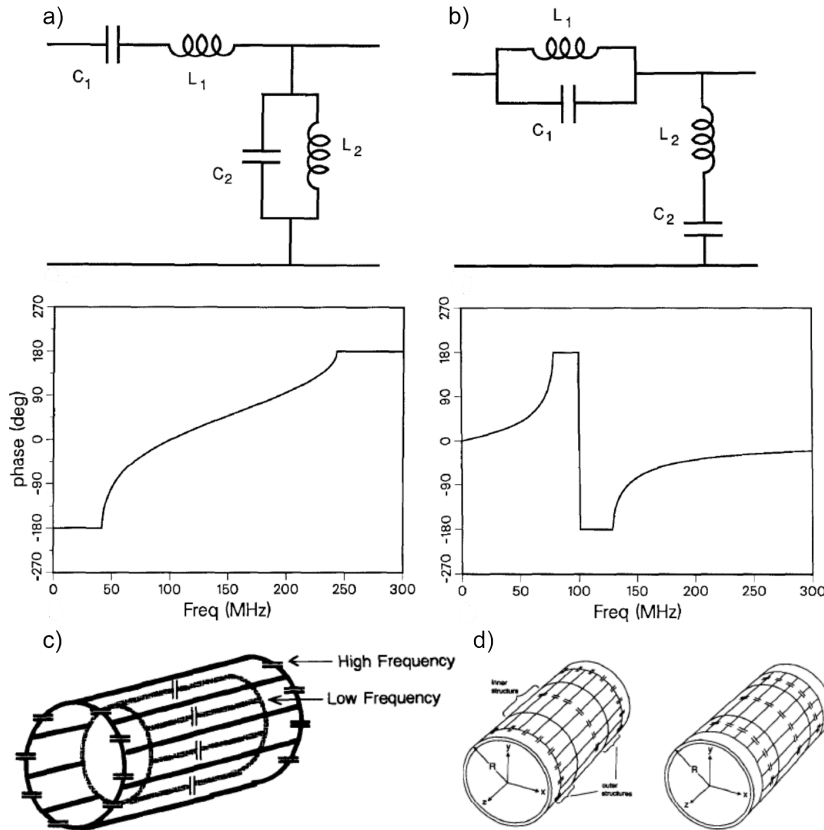
Figure 1.13 – Design of the several dual-tuned birdcages: (a) band-pass; (b) band-stop [92]; (c) nested birdcage coil [93]; (d) four ring birdcages [91].

TEM coils   TEM coils or, in other words, coupled microstrip line (MTL) coils [81], [82], [84] can advantageously replace birdcage coil for head from 4.7 T up to 9.4 T. The typical examples of TEM resonators are presented in Figure 1.14. Contrary to the birdcage coil wherein the

adjacent legs are capacitively coupled through electric field, in the TEM resonators the adjacent elements are mainly mutually coupled through the magnetic field (inductive coupling).
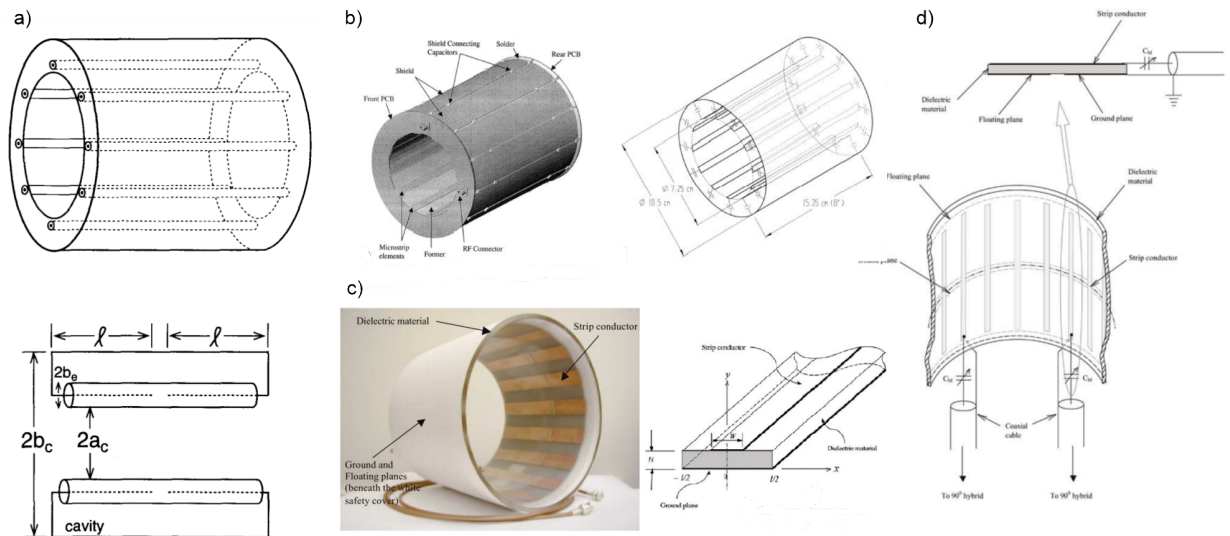
Figure 1.14 – Geometry of different TEM coils: (a) the first prototype of TEM coil based on tunable coaxial resonators [81]; (b, c) Coupled MTL [82], [84]; (d) feeding and matching of coupled TEM resonator [84].

As in the birdcage coil, in a TEM resonator, a total number of modes depends on the number of legs. However, among these modes, the mode "$k = 1$" has a homogeneous magnetic field distribution inside the resonator. Despite, this mode locates at the lowest frequency in the spectra, it can be tuned over a broad frequency range. The TEM coil supports this mode even at 9.4 T for full-body imaging at UHF field [95]. The S-parameters and the modes of the TEM coil are shown in Fig. 1.15.
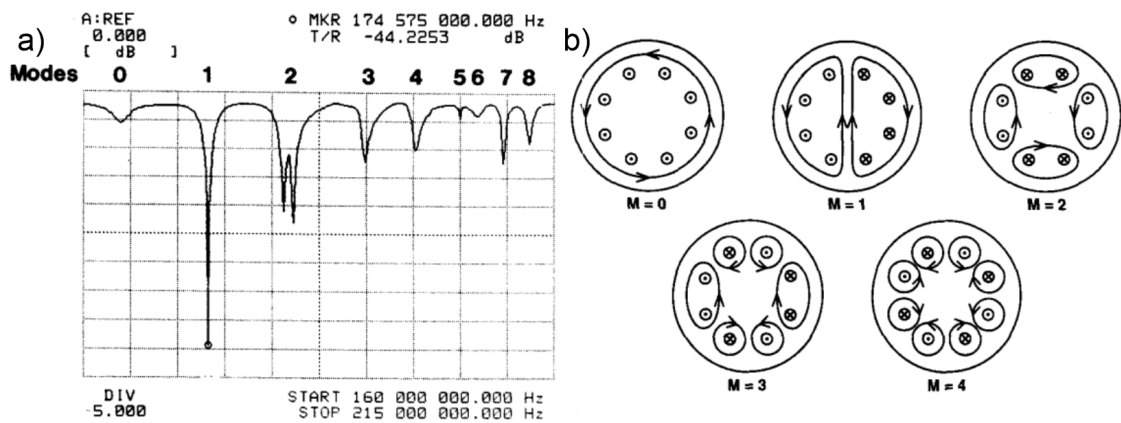
Figure 1.15 – (a) S-parameters of the coaxial tubes TEM resonator; (b) modal structure of the TEM resonator (magnetic field) [81].

As it can be seen the separation between the modes is only 12 MHz that may lead to some issues in experiments especially at UHF whereas for the HP birdcage coil this separation is about 50 MHz.

The TEM coils are compliant with quadrature regime [84] and dual nuclei operations [96]. Being compared to the birdcage, the TEM coil may show greater performance, especially at

higher frequency. This can be explained by the relatively high losses in the small capacitances needed to tune head birdcage coil [Fig. 1.16(a)]. For a TEM coil of the same size as a birdcage coil the self-resonance is higher in frequency compared to LP or HP birdcages [Fig. 1.16(a)]. Furthermore, the radiation losses are lower in a TEM coil compared to a shielded high-pass birdcage [95]. The graph of radiation resistance for several volume coils with respect to the frequency is shown in Fig. 1.16(a). Because TEM coils are less radiative and inductive than birdcages, full-body TEM coil can be used up to 8 T (350 MHz), whereas birdcages are limited to 3 T (128 MHz). In addition, here the authors observed that the extend of the magnetic field B_1 generated by a TEM body coil is slightly larger than the one obtained with a shielded HP body birdcage coils at 3 T [see Fig. 1.16(c)].

In the work [84] authors compared quadrature TEM head coil to the quadrature HP head birdcage coil optimized for 4 T (170 MHz) brain imaging. The in-vivo images of these coils are shown in Figure 1.16. The overall SNR increase with the TEM coil is about 53% in the human head over that of the RF shielded HP birdcage coil [Fig. 1.16(d)]. In addition, TEM coil shows a signal intensity variation (SIV) 43% lower than the shielded HP birdcage coil. In general, the reported coil does not need an additional RF shield whereas it is strongly required by the birdcage coil to avoid Q factor degradation.
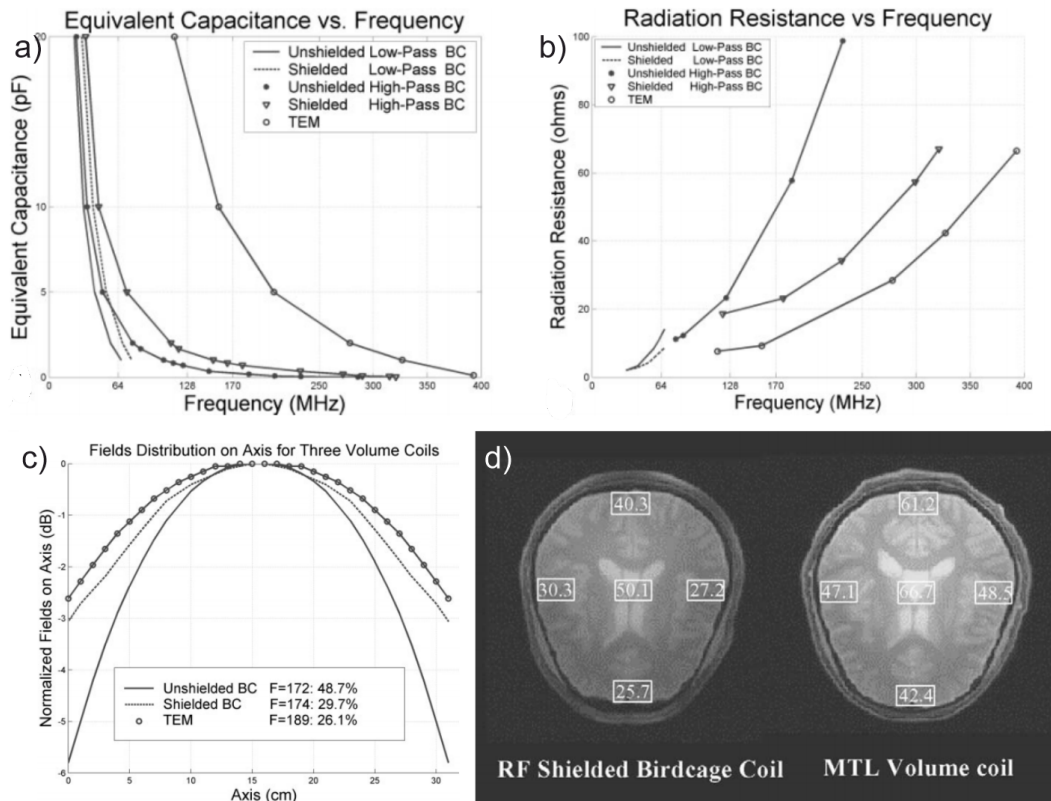
Figure 1.16 – **(a) Equivalent capacitors with respect to the frequency plotted for several volume coil [95]; (b) radiation resistance with respect to the frequency; (c) field distribution along the axis of the several resonators [95], (d) images of a brain acquired with two different coils [84].**

Half-volume coils Another sort of volume coils that we would like to mention is half-volume coils, which designs perfectly matches with one of our goal. The simplest way to design an open

resonator is to remove the top half of a birdcage coil [97], [98] or half-volume TEM coil [99].

One example of half-birdcage coil devoted to shoulder imaging at 1.5 T has been proposed in [97]. The sketch of that coil made of 9 rungs is shown in Fig. 1.17(a). The comparable quadrature TEM coil and its interfacing circuit are depicted in Fig. 1.17(b, c). However, in this work we are more focused on the birdcage-like coils rather than on TEM coils, therefore further explanation is mainly devoted to the half birdcages.
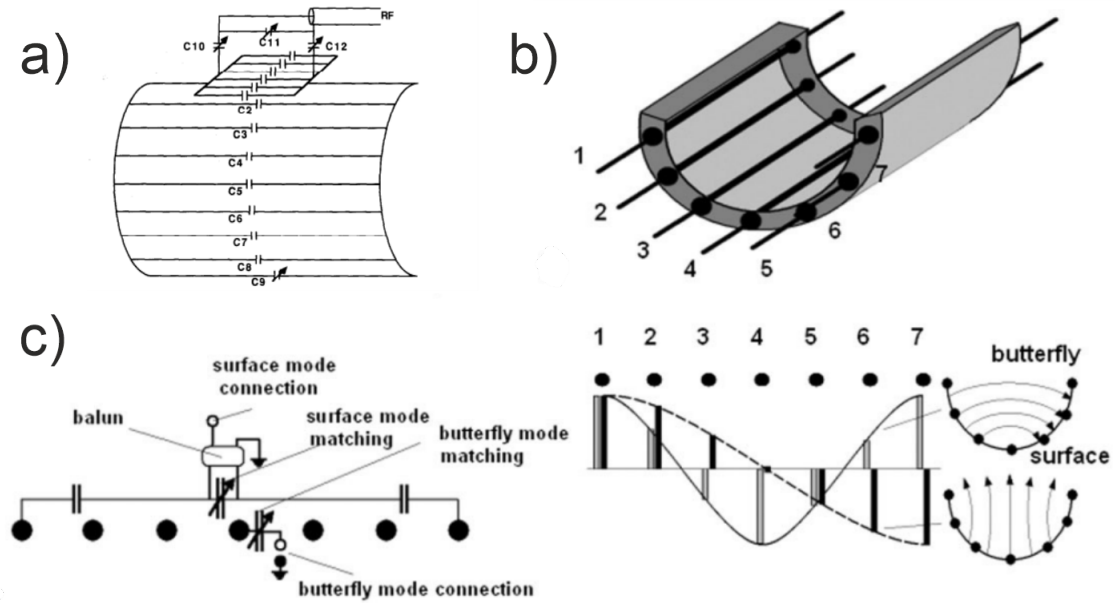
Figure 1.17 – **(a) Sketch of the half-birdcage coil of 20 cm diameter [97]; (b) Sketch of the half-TEM coil of 20 cm diameter [99]. (c) Interfacing of the coil and current distribution on the rungs for two orthogonal modes.**

Among the plurality of modes in such a resonator, there is the so-called volume mode, having proper magnetic field distribution polarized in the transverse plane. The SNR of a half-volume coil is greater over that one of a volume coil of comparable size [99]. However, this increase is only valid close to the coil. The SNR profiles of a 16-rung birdcage coil and 9 rungs half-birdcage coil are presented in Fig. 1.18(a), and the same kind of profiles for volume TEM coil versus half-volume TEM coil are shown Fig 1.18(b). As it can be seen, the half-volume coil cannot provide homogeneous signal as the one of fully closed volume coils [Fig. 1.18(b, d)]. In conclusion, half-volume coil can facilitate access to the patient under examination, and, they can improve the SNR in the vicinity of the coil. However, they cannot provide the homogeneous SNR distribution, compared to the full-volume coils.

Optimized birdcages The last branch of the RF coils that we would like to review is exotic birdcages with cross-sections that are not circular in order to better fit anatomical regions and therefore reduce the coil volume. Indeed, as it is known, the smaller the volume of a coil and the larger B_1 amplitude and consequently the larger the SNR. A few papers have been published on this topic: elliptical birdcage coil [100] and its theory [101], analytical approach to noncircular section birdcage coil design [102], asymmetric birdcage coil [103]. In this work we mainly describe the elliptical birdcage coil reported in [100]. This coil was proposed for head or body imaging at 3 T. The sketch of that coil is shown in Fig. 1.19(a).
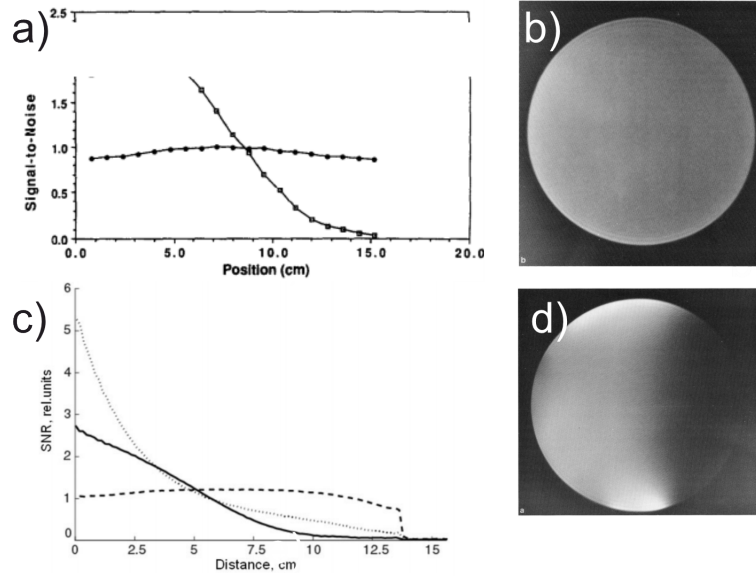
Figure 1.18 – (a) The SNR profiles of the half-birdcage coil compared to the full-volume coil [97]. (b) spin-echo images of the phantom obtained with (b) 16 rungs full-body quadrature birdcage coil; (a) The SNR profiles of the half-volume TEM coil (solid) compared to the volume TEM coil (dashed) and phased arrays (doted) [99]; (d) spin-echo image of the phantom obtained with 9 rungs half-birdcage coil [97].

According to their method, capacitances and inductances in each element of the coil should be calculated to satisfy current distribution on the coil's rungs. It is important to note that to calculate the mutual inductances between the elements, the same approach as in the conventional coil is used [104]. However, that approach is slightly different according to the elliptical cross-section of the coil.
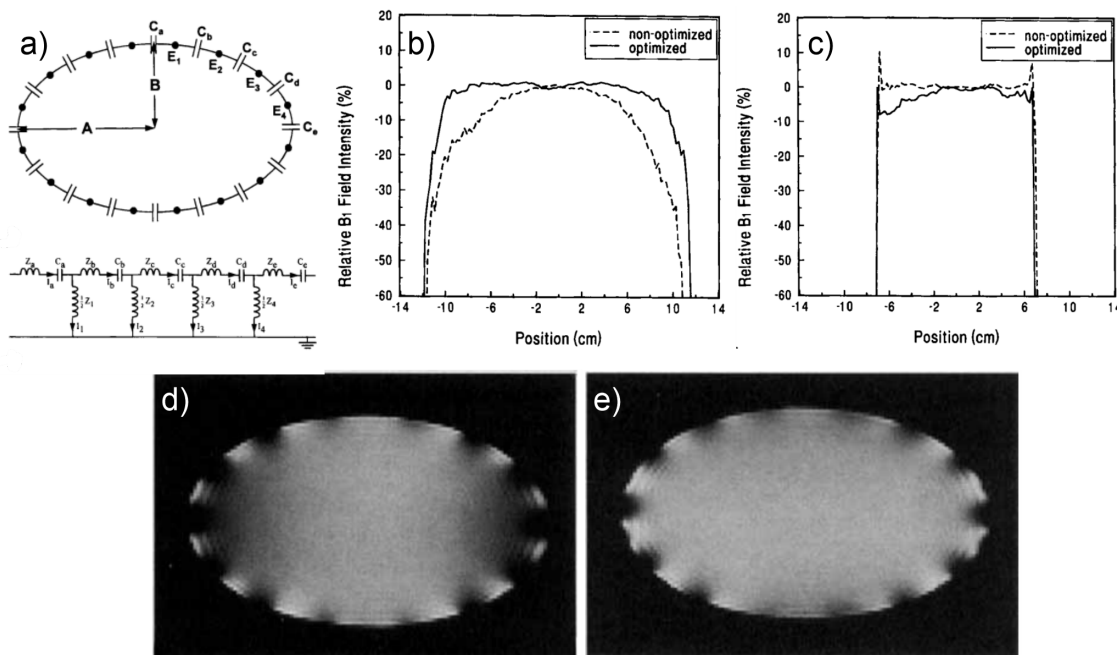
Figure 1.19 – Elliptical birdcage coil: (a) sketch of the coil; B_1 field profiles along: (b) long semi-axis; (c) short semi-axis of ellipse. Spin-echo phantom images obtained using: (d) non-optimized coil; (e) optimized coil [100].

When the elliptical birdcage coil is being compared to a conventional circular birdcage, it shows a 55% increase of SNR. In addition, the two types of coils are compared in that work: non-optimized (when all capacitors are identical) and optimized. The B_1 profiles are presented in Fig. 1.19(b, c). Image with much better homogeneity can be observed with the optimized coil [see Fig. 1.19(d, e)].

1.4.3 Phased array coils

In the 90^s, phased arrays already widely used for RADARS or in acoustics [13], [105] were introduced for MRI. They are now widely available commercially. It is important to note that any possible geometries of loops are available, circles and squares [13], triangle elements [106]. The basic principle of parallel MRI is based on the simultaneous or parallel acquisition the signal from multiple independent local elements [107]. The coil composed of these small independent elements provides higher SNR compared to the conventional coils sensitive to the same FOV. An addition, transmit phased arrays allows to use passive or active B_1 shimming due to pT_x that can homogenize B_1 field or FA over the transverse plane [15]. Passive 3d shimming is also possible by multi-row arrays reported for example in [108].

The first NMR phased array was composed of N surface loop coils [13]. At first, we remind that conventional single electrically small loop coil provides high SNR in the small FOV seen by a coil. Then there are two options for increasing that FOV. The first one implies increasing of the coils size. Unfortunately, in this scenario the SNR is degraded [13], [70]. In another scenario, the number of independent elements of the coil has to be increased.

The main issue with array is to mitigate the mutual coupling between the elements. Indeed, let consider a single loop coil resonating at frequency f_0. In order to understand the functioning of coupled loops in a phased array, we consider two associated loops placed at a subwavelength distance. Because of the coupling, two eigenmodes can be obtained (the two loops in phase or out of phase) at 2 frequencies different from of their initial frequency f_0 (Fig. 1.20).
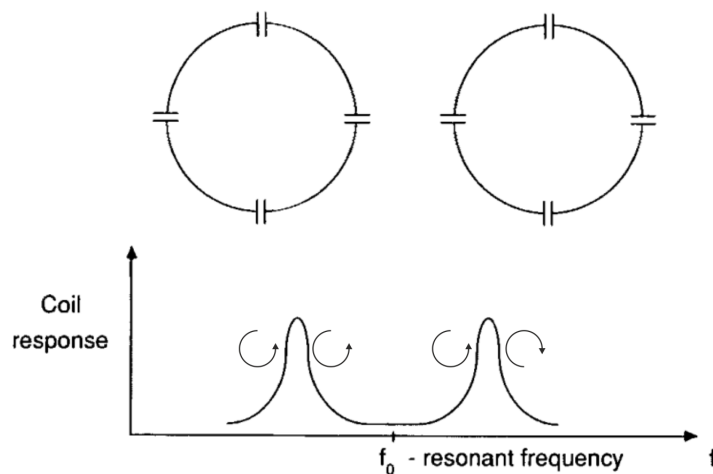
Figure 1.20 – Two coupled loop coils supporting two modes [13].

Consequently, the aim is to bring these two modes at the same frequency f_0. This can be done by several ways. However, the most intuitive way is to reduce the coupling between the

coils using different overlapping between the adjacent elements [13]. As it can be seen in Fig. 1.21(a), the ratio between distance and diameter of 0.9 leads to the zero of magnetic coupling (k_m) between two loops. However, electric coupling (k_e) equals 0.4 [Fig. 1.21(b)]. Practically this corresponds to -14 dB of $|S_{12}|$ coefficient between two adjacent elements [Fig. 1.21(b)]. We can also cite another techniques as resonant inductive decoupling (RID) [109], capacitive decoupling [110], [111].
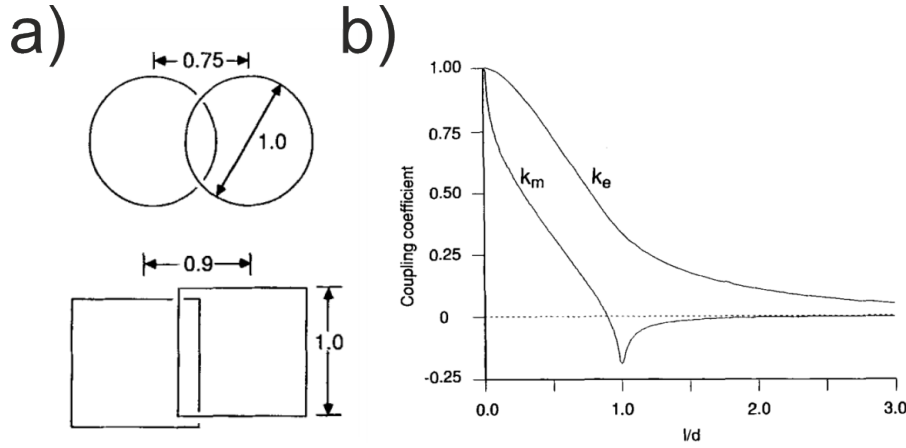
Figure 1.21 – (a) Decoupling of the elements can be simply done by the geometrical decoupling between the elements; (b) electric (k_e) and magnetic (k_m) coupling coefficients depending on mutual geometry of adjacent loops [13].
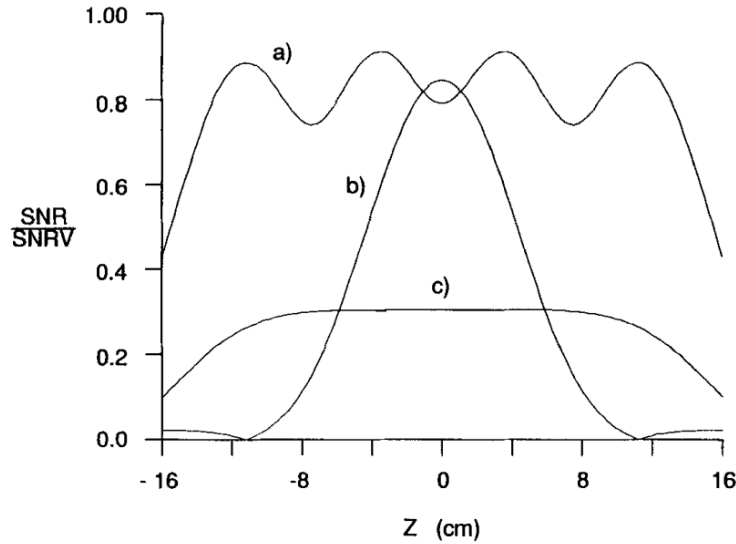
Figure 1.22 – The calculated SNR at the depth of 8 cm from the surface of three different coils: (a) four element phased arrays made of square loops of 8 cm; (b) single 8 cm loop coil; (c) a large 30 × 15 cm loop [13].

Thanks to these decoupled elements, a phased array can dramatically increase its FOV without degrading the SNR as it is shown in Fig. 1.22. The presented graph considers several coils: a phased array of four elements, one element of the array and a large loop having the same FOV as the entire phased array. It is obvious that with the phased array, the SNR of the entire image can be almost 4 times higher with the same FOV as for the large loop coil. As a drawback, the system is significantly more complicated because array element should have its

own matching and balancing circuits, its own a transmit/receive interface with a preamplifier and detuning circuit of the coil when it is a ToRo coil [36].

In addition, the phased arrays cannot improve the SNR in the center of the image [70]. For instance, we would like to consider a receive array composed of 12, 32, 96 channels for brain imaging at 3 T. The setup of 96 channels coil is shown in Fig. 1.23(a). In Fig. 1.23(b) it can be seen that increase in the number of channels does not increase the SNR in the center, while it does in the distal cortex (periphery).
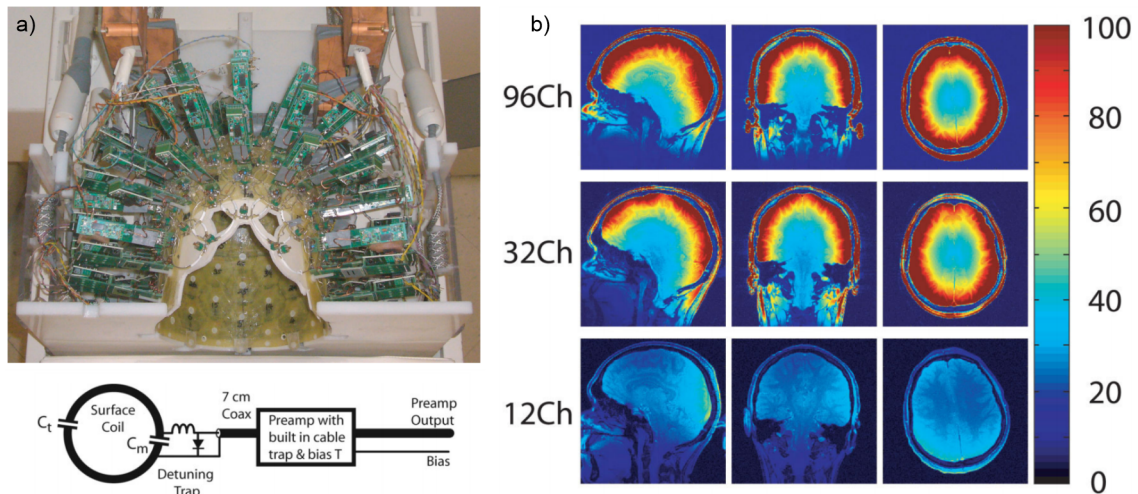
Figure 1.23 – (a) Photograph of 96ch coil and sketch of its elements; (b) SNR maps depending of number of channels [112].

As it was mentioned before, phased array channels have been initially used for reception, however it is also can be used as a transmit coil. Below 4 T, transmit phased array are not common, especially because the homogeneous magnetic field can be provided by conventional coils.

Another existing branch of coil is transceiver phased arrays. These arrays are more compact than ToRo phased arrays because the same elements are used for transmission and reception. They are also simpler to build than ToRo array because they are usually composed of a small number of channels (usually 8). However, because of this limitation, they do not provide as high SNR as R_x phased arrays exploiting for example 32 small elements do.

Phased arrays for UHF imaging As we considered the main pros and cons of phased arrays, now we would like to consider some features related to UHF brain imaging, which opens borders for new types of elements in phased arrays [113] such as $\lambda/2$ dipoles [114] or MTL lines (so-called TEM arrays) [115], [116]. These elements are shown in Fig. 1.24.

For example, at 7 T the length of $\lambda/2$ dipoles is ≈ 0.5 m. It is still relatively long compared to the anatomical size of a head. Therefore it can be geometrically shortened with lumped or meandered inductances [117] with folding [118], or it can be and bent [51] in order to better circumscribing a head.

Being compared to a T_x/R_x birdcage coil or a TEM coil, the phased arrays can also show superiority in their performance. For instance, in the work [10] a receive only phased array
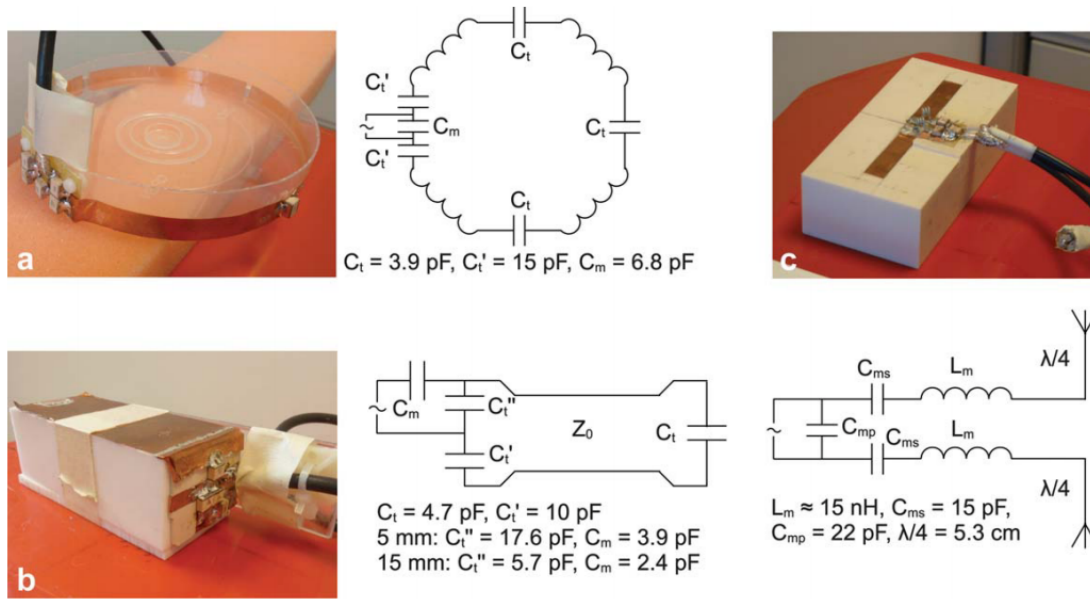
Figure 1.24 – Elements of the passed arrays: (a) loop; (b) radiating dipole; (c) microstrip transmission line [114].

is proposed for brain imaging at 7 T. The array has 32 loop-elements arranged on a close-fitting fiberglass helmet modeled [Fig. 1.25(a)]. This phased array can be embedded inside a detunable 16 rung head birdcage coil of diameter 28 cm and 20 cm of length. When the array is being compared to the same birdcage coil but used for both transmit and receive, it shows 5-fold greater SNR in the cortex and twice higher in the center [Fig. 1.25(b)]. The brain image obtained with this setup of a birdcage coil and receive only phased arrays is presented in Fig. 1.25(c). In such a case the quality of the image demonstrates enough spatial resolutions to distinguish small details inside the brain.
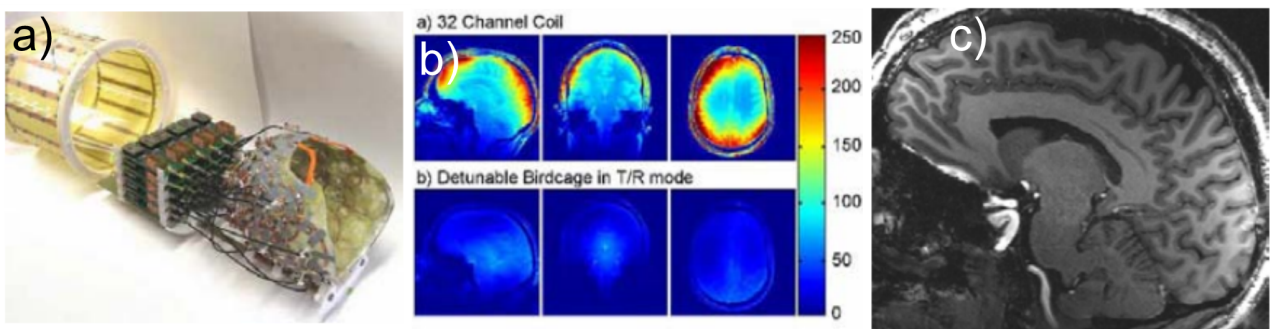
Figure 1.25 – (a) A Detunable transmit only birdcage coil combined with 32-channel receive only array; (b) the SNR maps of the T_x/R_x birdcage coil compared to transmit birdcage combined with 32ch receive only array; (c) brain images obtained with that configuration [10].

In the next work, the transceiver arrays composed of eight loops is reported [108] [see Fig. 1.26(a)]. This array is made elliptical to better fit a human head. We observe on Fig. 1.26(b), the phased array provides much greater performance in transmit regime compared to the conventional TEM coil of comparable size even though the input power is lower. Due to passive B_1 shimming when the amplitudes and phases are adjusted the field map can be homogenized.

Moreover, it is also reported in this work that by adding another row of elements it is possible to perform passive 3d shimming, naturally impossible in single row coil.
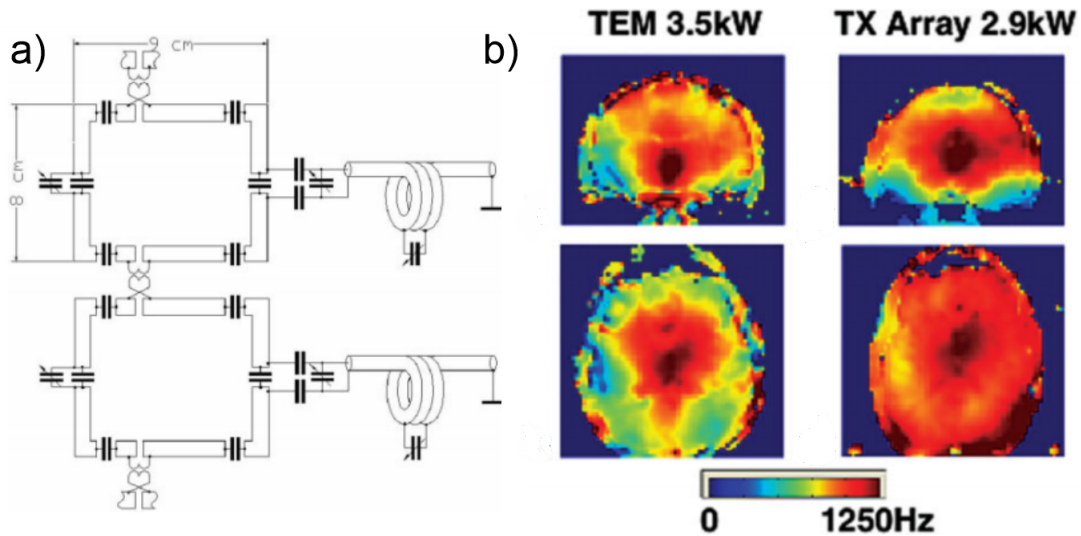
Figure 1.26 – (a) Eight channel transceiver array [108]; (b) B_1 field comparison between TEM coil and 8-channel phased array [108].

d, phased arrays are very flexible tool especially for UHF MRI. It allows creating almost any kind of geometries. For example, there is a coil proposed in [119] made of two open phased arrays: one for transmit with 4 channels loop layout and other one with two rows with 8 loops for receive. Although they are based on completely different principle, this coil is close in terms of applications to the opencage coil proposed later in Chapter 3.

However, these coils are complicated to manufacture because of numerous elements leading to a lot of electrical components. As a result, phased arrays are more expensive than conventional coils. are more complex to use. Some problems of the conventional coils can be solved using metamaterials.

1.4.4 Metamaterial-based coils

Another class of RF coil is the metamaterials-based coils. Metamaterials are artificial periodical materials that are not available in nature. The history of metamaterials originates in 1967 when Victor Veselago [120] introduced the concept of negative index material showing simultaneously negative permittivity and negative permeability. Subsequently, in 2000, John Pendry predicted that these negative index materials acts as superlens because they can focus a wave on a smaller spot than the one predicted by the classical diffraction limit, i.e., with a size smaller than half a wavelength [121]. Such an artificial material with effective parameters is made of a sub-wavelength (typically less than $\lambda/10$) periodic arrangement of meta-atoms, i.e., resonators. In 2001, the concept negative index material was confirmed experimentally in radiofrequency band (X-band) by David Smith et al. [122]. They created a lens based on split ring resonators (SRR) and dipoles having together both left-handed and right-handed behavior. After publishing of this work, many scientific groups in the world started studying metamaterials.

One of the first applications of metamaterial lens composed of SRR in MRI originates in 2008 [123], [124]. In this work authors showed that metamaterial structure with negative permeability can redistribute the magnetic field created by a surface loop coil at 1.5T [Fig. 1.27(a)].
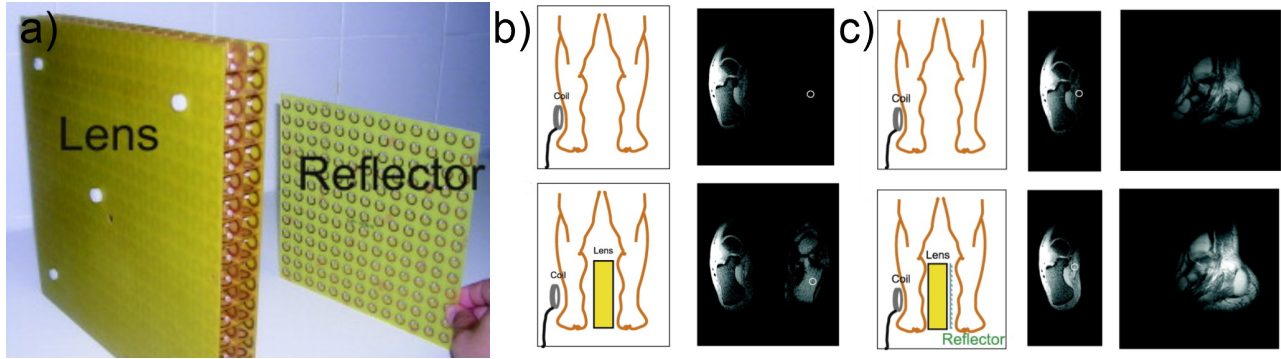
Figure 1.27 – **(a) Photograp of the metamaterials lens [124], (b) sketch of the setup on the left side and the MRI images on the right side, (c) sketch of the setup with reflectors in the left side and the MRI images in the right side.**

In this work authors show that their lens acts basically as a secondary source of RF magnetic field created by the loop coil. In this case, being installed between two legs, the metamaterial lens can expand magnetic field to the second ankle [Fig. 1.27(b, c)]. Here, the lens increases the penetration depth of RF magnetic field. Despite the fact it is a good example of metamaterials' applications, increasing penetration depth can also be done by using a vast loop coil [76] or by placing a secondary loop coil nearby the second ankle, or like it is done with wireless implants in [125].

Another example of application of metamaterial is wire medium [126]. This media also found use in MRI applications. First application of wire medium was pretty interesting but pretty far from real clinical or preclinical routine [127]. In this work the metamaterial wire medium was used in order take out the surface loop coil outside of the bore of 3T MRI scanner [Fig. 1.28(a)].
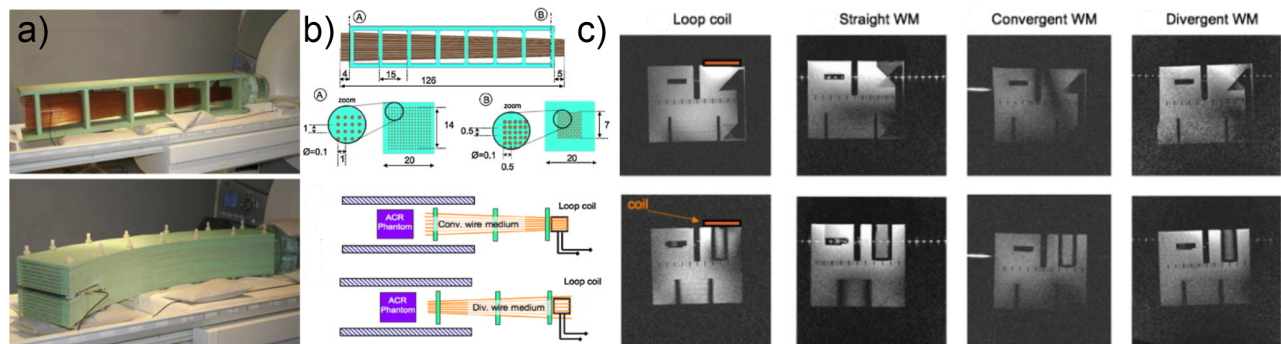
Figure 1.28 – **(a) Photograph of the metamaterials lens [127], (b) sketch of the setup, (c) several phantom images obtained with and without wire media.**

Different configurations of metalens (straight, convergent, divergent and bend) devoted to magnetic field transmission from a loop coil placed outside the MRI bore [Fig. 1.28(b)]. Meantime, the quality of the acquired images with the metalens are comparable to the one obtained

with a single loop placed around the scanned object [Fig. 1.28(c)]. The real application of this work can be found for using coils that are not MRI compatible. Indeed, some components, for instance capacitors and pin diodes become more expensive due to their magnetic compatibility.

Many interesting applications were achieved by using metasurfaces from microwaves to optical range [128]. For example, sub wavelength periodical wire structures that can be considered as metasurface supports hybridization of modes [129] [Fig. 1.29(a)]. Using the different modes of the wire medium, it is possible to provide better penetration depth into the sample. It is also possible to reduce scanning time by enhancing the sensitivity of the local coil in the presence of wire metasurface [130]. Meta solenoid can be designed and used as a wireless alternative to the local coil [131] [Fig. 1.29(b)]. Orthogonal eigenmodes can be excited in the wire metasurface for dual nuclei applications [132] (Fig. 1.29(c)).

Another type of metasurface is electrical band gap structures. These structures can also be used in MRI for decoupling of the arrays' elements [133]. In addition metamaterials and metasurfaces can be used for other applications: magnetic shielding [134], dual-nuclei operations [135], [136], locally homogenies magnetic RF field at 7 T for brain imaging using Kerker effect [137]. This hybridized meta-atom (HMA) [137] also matches with our goal of passive RF shimming. This HMA slows slightly improved transmit B_1 field, however, precise positioning inside a birdcage coil may be difficult. In addition, it may degrade comfort of patients under examination.

1.5 Conclusion

In this chapter we have first presented the emergence of MRI as a useful medical apparatus. The fundamental principles and abilities of MRI have been reviewed. Subsequently, the pros and cons of UHF MRI have been given. Then, we have defined the key parameters of RF coils for MRI, such as B_1 field, transmit efficiency, SAR and SNR and their role and importance. The several branches of coils, such as surface, volume and phased arrays have been reviewed. The last section provided the overview of metamaterials in MRI.

To make an overall conclusion, one would say that conventional volume coil such as birdcage or TEM remain one of the best transmit coil for moderate and high field MRI, respectively. However, the entire domain is going toward UHF, wherein conventional coils are inefficient in terms of field homogeneity. The issues of homogeneity may be mitigated with B_1 shimming provided by pT_x leading to more complexity in the coil design. Thereafter, this problem of inhomogeneity can also be partially solved by passive shimming provided by the dielectric pads or by hybridized meta atoms placed inside a transceiver conventional coil. Unfortunately, there are no mechanical stability and reliability of these structures. Therefore, they did not yet become routine medical tool. In addition, they cannot be combined with receive phased array.

In this manuscript, we propose a general framework inspired by the works on metasurface to develop volume coils for UHF scanners. The details of the framework and the link with birdcage are exposed in Chapter 2. The first application of this approach is the introduction of a new kind of volume coils with a large aperture operating at 7 T. This coil does not only improve the comfort of patients, but it can also facilitate access to the area under study to perform other tasks. Chapter 3 and 4 are dedicated to the development of a preclinical and a
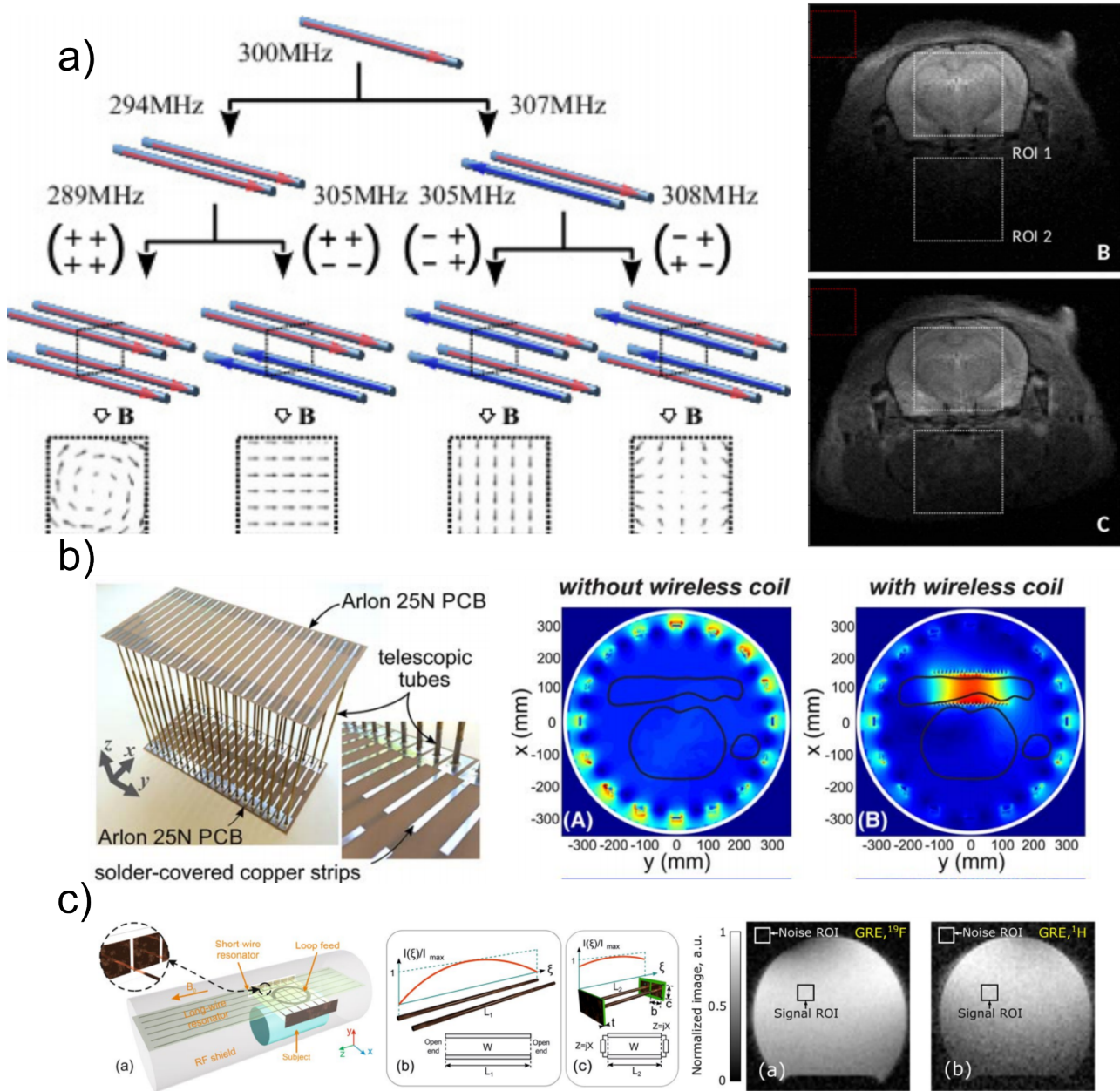
Figure 1.29 – **(a) Hybridized resonator improving the sensitivity of surface loop coil [129], (b) metasolenoid playing the role of local wireless coil [131], (c) hybridized resonator for dual-nuclei applications [132].**

clinical prototype of such coils, respectively. In chapter 5, we propose an elegant solution to build a dual-band birdcage-like coil. Finally, in the last chapter, a coil that performs passive B_1 shimming is introduced.

CHAPTER 2

Metamaterials theory for volume RF coils design

Table of contents

This chapter reveals the main theoretical aspects of novel volume RF coil design for preclinical and clinical ultra-high field (UHF) MRI. The coils, proposed in this work, are inspired by birdcage coils [80], [138]. Since their introduction in 1985, birdcage coils have been playing one of the key roles in clinical and preclinical MR imaging at various field strength [71], [70]. Several theoretical approaches to describe birdcage coils are already known in the literature, for example in [139], [140], [141]. In addition, there are a few approaches, which are very convenient from a practical point of view [104], [142]. All these approaches stated above can be used to design the birdcage geometry and the values of lumped capacitors needed to tune a birdcage coil at the desired frequency.

In this investigation we propose to apply transmission line theory to straightforwardly describe a birdcage coil [71]. Indeed, a birdcage coil can be considered as a periodical chain network composed of unit cells with LC elements where a single unit cell or a rung can be completely described by a transfer matrix or ABCD matrix [71]. This proposed approach is commonly used in metamaterials theory [12].

From this analysis, each unit cell of a birdcage coil can be completely described in terms of Bloch or characteristic impedance and phase shift. This approach allows to tune individually each unit cell. Eventually, this work is the corner stone of this manuscript to design metacages, i.e., birdcage-like coils showing other field distribution or other geometries.

2.1   Birdcage principle and design

As explained in Chapter 1, a birdcage coil is a resonator invented in 1985 by C. Hayes [80]. In the beginning, the birdcage coil was proposed for full-body imaging [80], while later it was adapted for many different applications at various field strength [85], [86], [87]. The advantage of the birdcage coil is to generate a highly homogeneous magnetic field inside the resonator's volume at its fundamental mode ($k = 1$). The birdcage coil is composed of N parallel conductors (legs or rungs) distributed around the circumference of radius r with a constant angle φ ($\varphi = 2\pi/N$) forming a cylinder as it is shown in Fig. 2.1(a). At both ends, the legs are connected to the end-rings. The field B_1 in an empty birdcage coil can be worked out in the quasi-static limit from the Biot-Savart law [70], [72]. The transverse magnetic field B_1 principally results from currents flowing inside the longitudinal legs. The currents are driven by the resonance of the ladder network consisting of N leg inductances, $2N$ end-ring inductances, and $2N$ capacitors placed in the legs (low-pass), in the end-rings (high-pass) or in both segments (band-pass) [Fig. 2.1(b)].

From analyzing a particular unit cell, it is possible to define the capacitance needed to tune the fundamental mode of the birdcage coil to a Larmor frequency. The detailed analytical analysis of the birdcage coil is provided in the next section
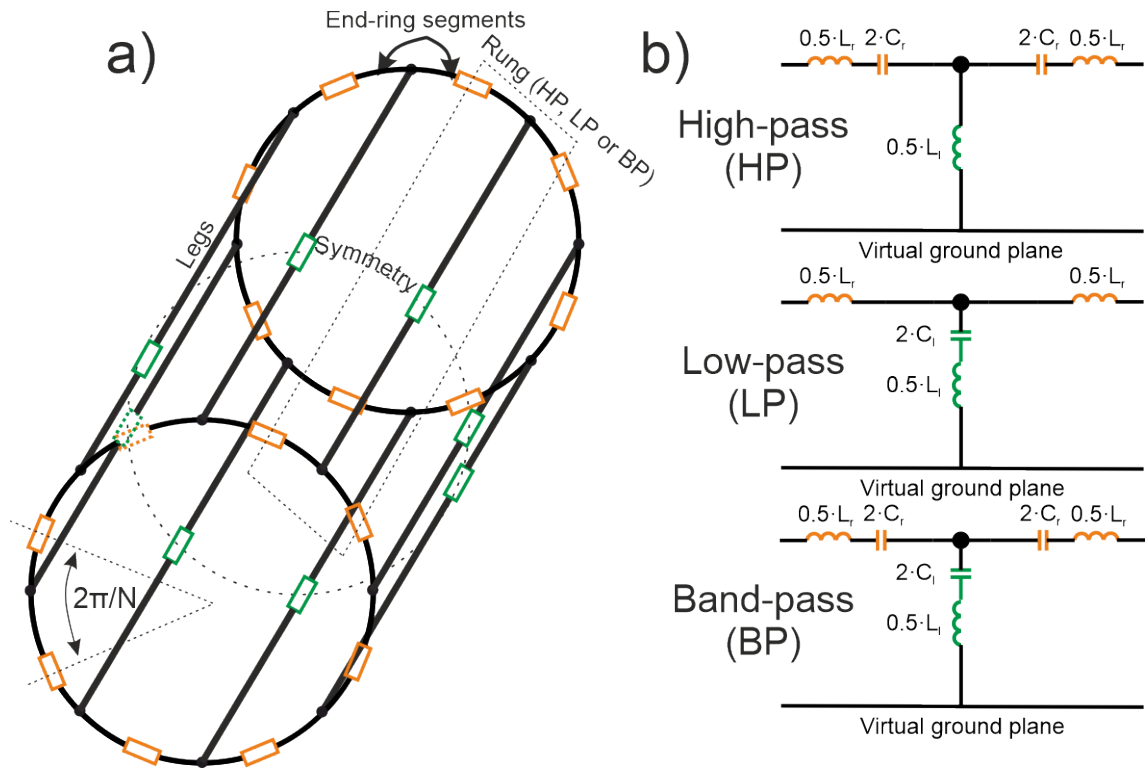
Figure 2.1 – (a) Sketch of the conventional birdcage coil composed of eight rungs; (b) different unit cells of the conventional birdcage coil.

2.2 Electrical representation of a birdcage

A birdcage of N legs can be modeled by an equivalent electric system made of a periodic arrangement of lumped LC elements. Such a system is shown in Fig. 2.2. In this system the Nth rung is connected to the first one because a birdcage is a close electrical system.
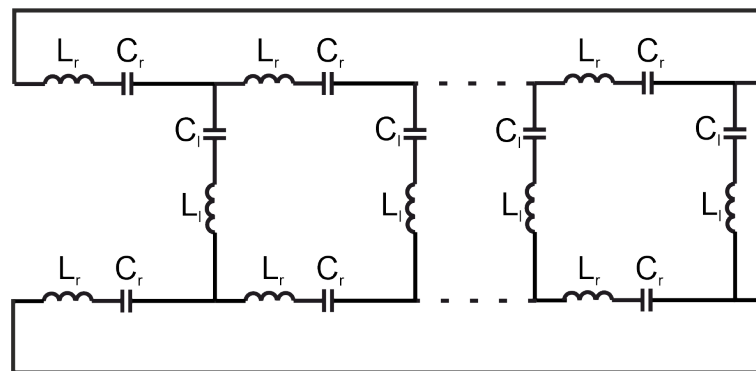
Figure 2.2 – Full electrical representation of a birdcage coil composed of N rungs.

On Fig. 2.2 the elements L_r and L_l represent the self-inductances of the ring and leg conductive wires. According to the references [74], [104], [143], the self-inductance of a flat conductor considered in this work can be expressed as:

$$L^s = 2l \cdot \ln\left(\frac{2 \cdot l}{w + t}\right),$$ (2.1)

where l is its length, w is its width, t is its thickness.

It also exists strong inductive coupling between the parallel legs (not represented on Fig. 2.2). The mutual inductance M_{ij} of two thin and parallel wires is given by:

$$M_{ij} = 2l \cdot \ln \left(\frac{l}{d} + \sqrt{1 + \frac{l^2}{d^2}} - \sqrt{1 + \frac{d^2}{l^2}} + \frac{d}{l} \right). \tag{2.2}$$

Where l is the length of the parallel wires and d the distance between them. When a shield is present, we use the image theorem to consider its effect. This mutual inductance also exists between end-ring segments. Because the elements are not parallel, the expression is more complex and can be found in [86]. Finally, the capacitances C_r and C_l are provided by lumped capacitors that should be inserted in the rung and leg conductive lines to get a resonance condition.

We only handle birdcages that are symmetric with respect to a plane that is normal to the birdcage axis and intersects this last in the middle. Moreover, we only consider modes wherein the current directions on the top and the bottom rungs are opposite. In such a case, the aforementioned mid-plane plays the role of a virtual ground plane and the schematic of a birdcage can be considerably simplified (see Fig. 2.3). Note that half of the mutual inductance between the legs has to be then taken into account.
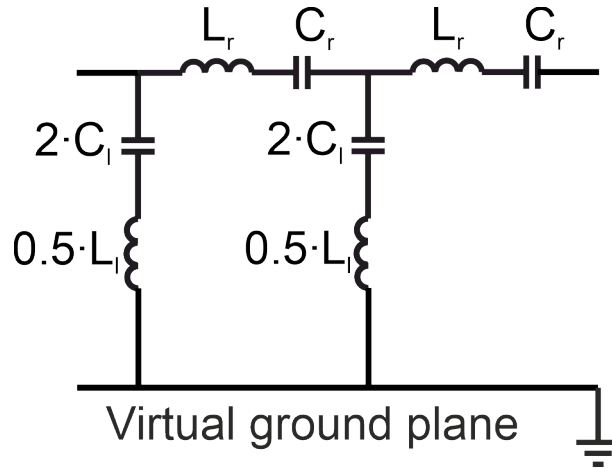
Figure 2.3 – Simplified electrical representation of a birdcage coil's unit cell

2.3   Simplified electrical representation of a birdcage

Before describing the metamaterial approach, we present the conventional way to calculate the capacitance of low-pass (LP) and high-pass (HP) birdcage coils in order to tune the fundamental mode ($k = 1$) at the operating frequency. The starting point is to apply the Kirchhoff's voltage law to one loop of a birdcage represented in Fig. 2.4. It comes:

$$U_n^r - U_n^l + U_{n+1}^l = 0. \tag{2.3}$$
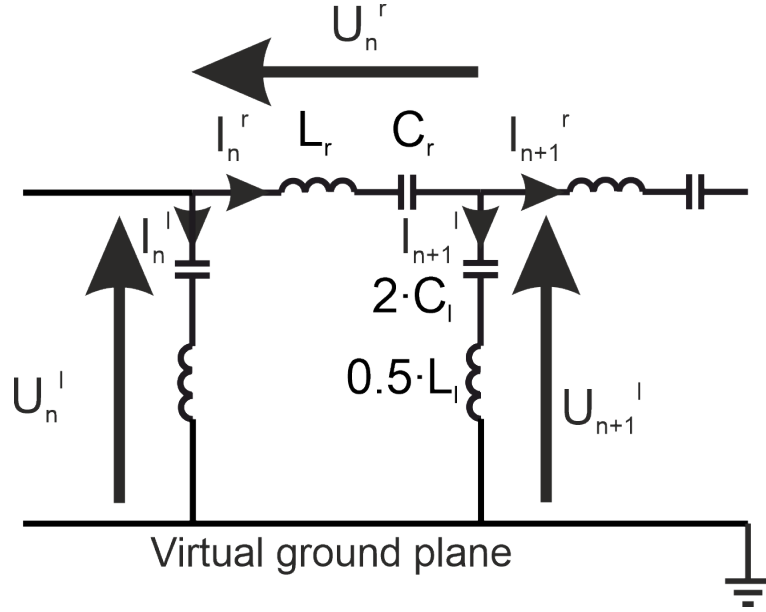
Figure 2.4 – To the calculation of the birdcage coil.

Where the rung and leg voltage drops are given by the following expressions:

$$U_n^r = i\omega \cdot \left(L_s^r I_n^r + \sum_{m=1}^{N-1} I_{n+m}^r M_{n,m}^r\right) + \frac{I_n^r}{i\omega C_r},$$
$$U_n^l = \frac{i\omega}{2} \cdot \left(L_s^l I_n^l + \sum_{m=1}^{N-1} I_{n+m}^l M_{n,m}^l\right) + \frac{I_n^l}{2i\omega C_r}. \tag{2.4}$$

Due to the Kirchhoff's current law, it comes:

$$I_n^l = I_{n+1}^r - I_n^r. \tag{2.5}$$

Note that because the last rung is connected to the first one $U_N^{r,l} = U_0^{r,l}$ and $I_N^{r,l} = I_0^{r,l}$.

We are looking for the system's resonant frequency, at which the current distribution on the rings is given by the k-th CP mode (2.5), i.e.:

$$I_n^r = I_0 e^{\frac{2i\pi kn}{N}}, \tag{2.6}$$

where I_0 is the maximum current intensity, k is the mode number and N is the total number of unit cell. The current flowing in the legs is then deduced from Eq. 2.5, i.e.,

$$I_n^r = I_0 e^{\frac{2i\pi kn}{N}} \left(e^{\frac{2i\pi k}{N}} - 1\right). \tag{2.7}$$

Moreover, the introduction of effective inductances L^r and L^l simplifies equations (2.4) to the following:

$$U_n^r = i\omega I_n^r L^r + \frac{I_n^r}{i\omega C_r},$$
$$U_n^l = \frac{1}{2} i\omega I_n^l L^l + \frac{I_n^l}{2i\omega C_l}. \tag{2.8}$$

The effective inductance of the ring or leg number m that takes into account the mutual coupling between conductors is given by:

$$L_m^{r,l} = \hat{L}_m^{r,l} + \sum_{n=0,n\neq m}^{N-1} M_{nm}^{r,l} e^{2i\pi k \frac{n-m}{N}}, \tag{2.9}$$

where $\hat{L}_m^{r,l}$ is the self-impedance of ring or leg m. Because all the legs and rungs are identical and equally spaced, $M_{nm}^{r,l} = M_{n-m}^{r,l}$. Therefore, the previous expression becomes:

$$L_m^{r,l} = \hat{L}_m^{r,l} + \sum_{n=0,n\neq m}^{N-1} M_{nm}^{r,l} \cos\left(2\pi k \frac{n-m}{N}\right). \tag{2.10}$$

Combining equations (2.5) and (2.8), it comes.

$$\left(L_r\omega - \frac{1}{C_r\omega}\right) \cdot I_n^r = \frac{1}{2}\left(L_l\omega - \frac{1}{C_l\omega}\right) \cdot \left(I_{n-1}^r + I_{n+1}^r - 2I_n^r\right). \tag{2.11}$$

Eventually, replacing the current by its expression from 2.6, we obtain the following relation between the capacitances, the frequency, and the order of the mode:

$$\frac{L_r\omega - \dfrac{1}{C_r\omega}}{L_l\omega - \dfrac{1}{C_l\omega}} = -2\sin^2\left(\frac{\pi k}{N}\right). \tag{2.12}$$

When two capacitors C_r and C_l are employed simultaneously, a band-pass (BP) or hybrid birdcage coil [71] is obtained. It is important to note that such a birdcage is different from a dual-band BP birdcage coil [92] as we are going to see in Chapter 4.

Now, we consider the case of low-pass (LP) and high-pass (HP) birdcages. In a LP birdcage, only the capacitances on the legs are present while in a HP birdcage, the capacitances are inserted only on the rings.

From Eq. 2.12, we can deduce the capacitance to obtain the $k = 1$ mode at the angular frequency ω. For the HP birdcage, C_{HP} is given by:

$$C_{HP} = \frac{1}{\omega^2\left(L_r + 2\sin^2\left(\dfrac{\pi}{N}\right)L_l\right)}. \tag{2.13}$$

While the capacitance C_{LP} for $k = 1$ of a conventional LP birdcage becomes:

$$C_{LP} = \frac{2\sin^2\left(\dfrac{\pi}{N}\right)}{\omega^2\left(L_r + 2\sin^2\left(\dfrac{\pi}{N}\right)L_l\right)}. \tag{2.14}$$

To prove the proposed theory and compare it to the conventional approach, we are going to consider three different types of LP and HP birdcages, composed of 4, 8 and 16 rungs, respectively. The schematically represented birdcage coil composed of 8 rungs is shown in Fig. 2.1. Despite, these considered birdcages are composed of a different number of rungs, their sizes, such as, radii, length, and widths, are chosen to be the same. The effective inductances are different due to different mutual coupling between the conductors. The following geometry

with length of 240 mm, width of rings and legs of 10 mm, radius of 130 mm and radius of shield of 155 mm is chosen for head imaging at 7 T. Thereby, the working frequency is approximately 300 MHz. Using these dimensions, one can calculate the self and mutual inductances for 4, 8 and 16 rungs birdcages. The results are presented in Table 2.1.

Table 2.1 – Effective inductances of 3 different birdcages at 300MHz.

Inductance type (nH)	4 rungs	8 rungs	16 rungs
Legs (L_l)	132.60	146.59	173.97
Rings (L_r)	149	86.05	42.09

In this table, L_r is the effective inductance of an end-ring segment, L_l is the effective inductance of a leg, ω is an angular frequency at 300 MHz and N is a legs number. Knowing the effective inductances, the capacitances can be deduced from Eqs (2.13) and (2.14). The values of capacitance to tune the $k = 1$ mode at the operating frequency of 300 MHz are shown on Tab. 2.2.

Table 2.2 – Ring and leg capacitances of the 3 different types of birdcages.

Capacitance type (pF)	4 rungs	8 rungs	16 rungs
C_{HP} or (C_r)	1	2.18	5.09
C_{LP} or (C_l)	1	0.64	0.39

As it can be seen in Table 2.2, LP birdcage calculation process leads to not feasible values of capacitance in order to tune the $k = 1$ mode at the frequency of 300 MHz. Indeed these values are below the self-parasitic capacitance [71]. Hence, at such a high frequency, the HP topology is preferable.

2.4 Transmission line-based approach

In this section we analyze the birdcage in terms of the transmission line. This formalism is the cornerstone of the metamaterial approach of this work. Indeed, a birdcage coil [Fig. 2.5(a)] can be seen as a transmission line (TL) composed of a periodic arrangement of unit cells.

Fig. 2.5(b) shows three-unit cells $(i - 1, i, i + 1)$, where Y represents leg admittance and Z represents end-ring segment impedance. Because of the symmetry, as explained in section 2.2, the analysis of one cell (rung in other words) can be reduced to an equivalent circuit composed only of three elements [caption in Fig. 2.5(b)]: a lumped parallel admittance $2Y_i$ on the leg section, and two equal lumped serial impedances $Z_i/2$ for the ring.
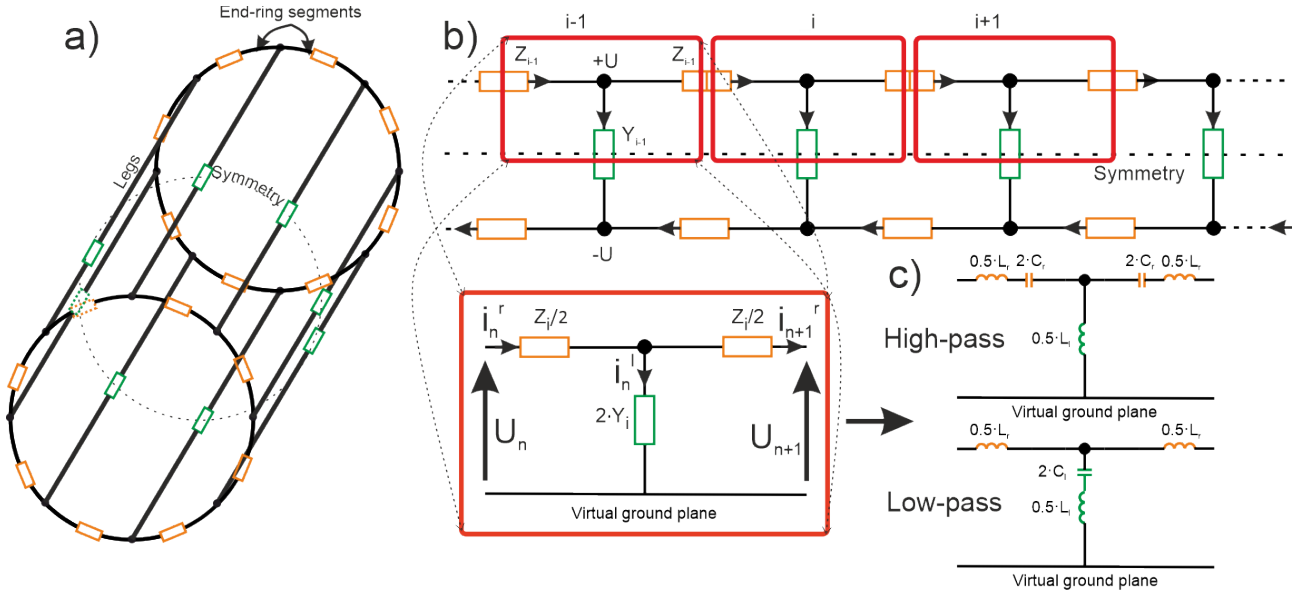
Figure 2.5 – (a) General view of a birdcage coil composed of eight rungs. (b) Simplified equivalent circuit of a birdcage coil segment. (c) The HP or LP unit cells in terms of inductances and capacitances.

To describe such a periodic network we have to refer to the transfer or ABCD matrix formalism [12], [71], which is very convenient to handle. This approach can be used even though the unit cells are not identical. This formalism allows to deduce the 2 main intrinsic parameters of a unit cell: the Bloch impedance and the phase shift [12]. The transfer matrix T_i of a single unit cell is a 2 by 2 complex matrix that links the input voltage (U_n) and current (I_n) to the output (U_{n+1} and I_{n+1}) ones:

$$\begin{pmatrix} U_{n+1} \\ I_{n+1} \end{pmatrix} = T_i \cdot \begin{pmatrix} U_n \\ I_n \end{pmatrix}. \tag{2.15}$$

From the schematic represented in the Fig. 2.5(b), it can be shown that the transfer matrix (2.15) of the ith cell is given by:

$$T_i = \begin{pmatrix} 1 + Z_i Y_i & -\dfrac{Z_i^2 Y_i + 2Z_i}{2} \\ -2Y_i & 1 + Z_i Y_i \end{pmatrix}. \tag{2.16}$$

In the case of a HP unit cell, Z_i and Y_i are given by:

$$\begin{aligned} Z_i &= \frac{1}{i\omega C_{r,i}} + i\omega L_{r,i}, \\ Y_i &= \frac{1}{i\omega L_{l,i}}. \end{aligned} \tag{2.17}$$

In case of LP unit cell, the expressions become:

$$\begin{aligned} Z_i &= i\omega L_{r,i}, \\ Y_i &= \frac{1}{i\omega L_{l,i} + \dfrac{1}{i\omega C_{l,i}}}. \end{aligned} \tag{2.18}$$

Here $C_{r,i}$, $C_{l,i}$, are the ring and leg capacitance for HP and LP respectively. $L_{l,i}$, and $L_{r,i}$ are the leg effective inductance, and the end-ring effective inductance of the ith unit cell (rung) respectively, ω is the angular frequency.

To evaluate the effective inductance, we use the same expression as the one presented in the previous section. The underlying approximation is that the current distribution on the ring and the legs are given by Eqs. (2.6) and (2.7) and may not exactly correspond to the ones provided by the transmission line model.

Finally, the phase shift $\delta\varphi_i$ induced by a unit cell can be determined by computing the eigenvalues of matrix T_i [12]. Eventually, from matrix (2.16) one can deduce the following formula for the phase shift:

$$\delta\varphi_i = \cos^{-1}(1 + Z_i Y_i). \tag{2.19}$$

The phase shift $\delta\varphi_i$ calculated in (2.19) provides the phase of the nodes of the unit cells. However, the magnetic field is mainly generated by the current flowing on the legs. Therefore, the important parameters are the amplitude and the phase on these lasts. According to Fig. 2.5(b), the current on the legs I_n^l can be derived from the current on rings I_n^r and I_{n+1}^r as follows:

$$I_n^l = I_{n+1}^r - I_n^r. \tag{2.20}$$

Assuming that only the phase varies from one rung to another one, the current becomes:

$$I_n^l = e^{i\varphi_{n+1}} - e^{i\varphi_n} = 2i e^{i\frac{\varphi_{n+1} + \varphi_n}{2}} \sin\left(\frac{\varphi_{n+1} + \varphi_n}{2}\right). \tag{2.21}$$

This expression shows that the current phase on a leg is the average of the current phases between the two adjacent ring nodes plus a phase shift of 90°. Note that in case of varying phase shifts between legs (see opencage or metacage chapters), an amplitude modulation factor is involved.

The second parameter characterizing the unit cell is the Bloch impedance, which is the ratio between voltage and current at the nodes of unit cells [Fig. 2.5(b)]. The Bloch impedance can be determined from eigenvector analysis [12] of the transfer matrix (2.16) as:

$$Z_b^i = \frac{1}{2}\sqrt{Z_i^2 + \frac{2Z_i}{Y_i}}. \tag{2.22}$$

For birdcages, because all the cells are identical, the Bloch impedance is set the same from one cell to another one by nature. This condition is important to avoid reflections of the progressive mode between the unit cells. For this reason, when the unit cells are not identical because the required phase shift between rings varying, one has to adjust the cell parameters to keep the same Bloch impedance.

For instance, in case of HP cell, based on equations (2.19) and (2.22), one can find explicit solutions of leg inductance and ring capacitance as the functions of Bloch impedance and the

phase shift for HP cells:

$$L_l = \frac{4{Z_b}^2 \left(1 - \cos\varphi\right) - 2\,L_r\,Z_b\,\left|\sin\varphi\right|\,\omega}{2Z_b\left|\sin\varphi\right|\left(1 - \cos\varphi\right)\omega - L_r\,\sin^2\varphi\,w^2} \tag{2.23}$$

$$C = \frac{L_r\left(\cos\varphi + 1\right)\omega - 2\,Z_b\,\left|\sin\varphi\right|}{{L_r}^2\left(\cos\varphi + 1\right)\omega^3 + {Z_b}^2\left(4\cos\varphi - 4\right)\omega} \tag{2.24}$$

Consequently, to keep the same impedance but varying the phase shift, one has not only to change the capacitance but also change the leg inductance, i.e., the width of the legs. We implement this approach in Chapters 3 and 5.

Finally, this section has explained the primary methods and aspect of transfer matrix formalism needed for optimizing of birdcage-inspired coils. Then, we have to compare our approach to a conventional way of capacitance evaluation in a birdcage coil on several examples explained in 2.4.

2.5 Comparison of the proposed theory to the reference approach

As it was concluded in the previous section, for our tasks, devoted to UHF, the HP is preferable. The typical view of a birdcage coil with eight rungs is presented in Fig. 2.1(a). Thus, to verify the robustness of the approach proposed in the previous section, the values in the tables 2.1 and 2.2 obtained for birdcages including 16, 8 and 4 rungs, are substituted to equations (2.19) and (2.22) in order to calculate the phase and the Bloch impedance respectively.

The phase shifts plotted in Fig. 2.6(a) demonstrate that at the frequency of interest, they corresponds to the geometrical angle between the legs, i.e., 22,5°, 45°, 90° for the 16, 8, 4 rungs birdcages, respectively. Moreover, as it can be clearly seen, HP birdcages behave as a LHTL, wherein phase velocity (phase shift) is decreasing with increase of frequency and vice versa for LP birdcages (RHTL).
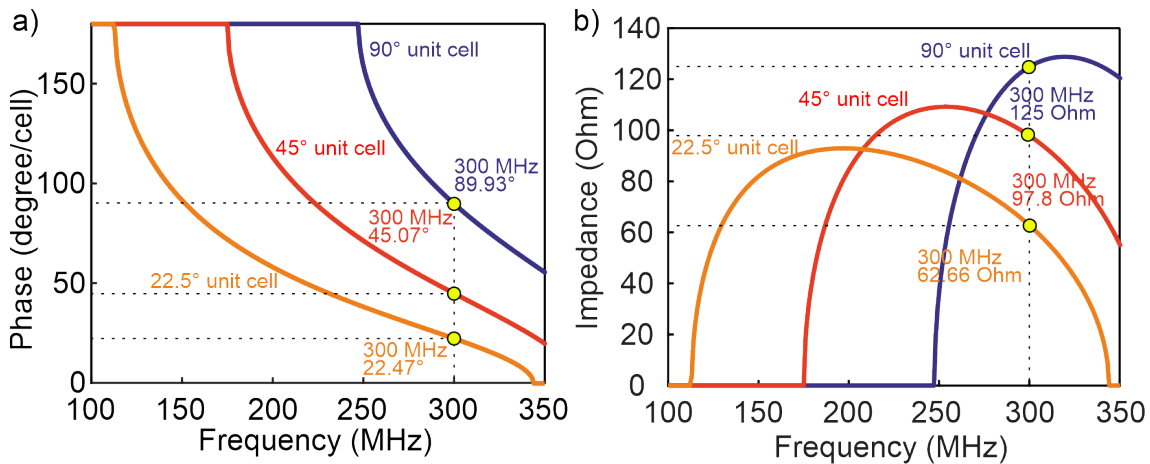
Figure 2.6 – **(a) Phase shift (dispersion) diagram plotted for three types of HP unit cells corresponding to 16, 8 and 4 rungs birdcages. (b) Impedance diagram plotted for three types of LH (HP) unit cells corresponding to 16, 8 and 4 rungs birdcages.**

Finally, Bloch impedance has been calculated according to formula (2.22) and plotted in Fig. 2.6(b). As for three different types of unit cells, the Bloch impedance is different at the operating frequency of 300 MHz. This effect of Bloch impedance mismatching is discussed in the next chapter.

To conclude, in this chapter, we have described the basics of first order filters for designing of LP and HP birdcages. It has been shown that a unit cell of a birdcage coil can be characterized by two parameters, namely phase shift and Bloch impedance adjusted by equations (2.19) and (2.22) respectively. In addition, values of inductance and capacitance for HP cells can explicitly be calculated analytically using equations (2.23) and (2.24), respectively.

The examples related to the particular RF coils, developed using the proposed transfer matrix approach are presented further in Chapters 3 to 5. In chapter 3, we take the benefit of the metamaterial formalism to build a birdcage with wide access to its inner volume. In Chapter 4, we generalize the proposed approach for dual-band coils. Finally, in Chapter 5, we describe an optimization method to build a "conjugated" birdcage that focuses a magnetic field spot at UHF operations [144].

Opencage RF coil

Table of contents

Having access to the region of interest (ROI) may be desirable in many clinical and preclinical applications. For instance, in brain imaging, it improves comfort of patients that may suffer from claustrophobia. It can also ease the optical pathway to send visual stimuli to patients during imaging process [145]. For multimodal and interventional imaging, it can facilitate access to the imaged organ with another modality such as a laser [146], an ultrasound probe [55], a RF or cryoablation device [147] or a biopsy needle [148]. Moreover, it may be helpful in some specific tasks such as a motion correction, where a camera is being placed inside MRI bore [11].

Numerous types of RF coils have been employed for applications stated above. However conventional coils have drawbacks and therefore, they are not perfectly suitable for these applications. For instance, surface loop coils [64] are very compact and efficient in terms of SNR but their field of view (FOV) is limited to a small volume around the loop. To overcome this limitation, surface coils with complex geometries such as half-birdcage coils [97], U-shaped birdcage coils [98] or quadrature half-volume TEM coils [99] can be used. Although the FOV of these coils is broader, it is still narrower than the FOV of full volume coils like a birdcage coil [80], [138], which is one of the golden standards in preclinical and clinical imaging at various field strength. In most applications, a birdcage coil provides suitable SNR. However, birdcages restrict access to a sample due to the dense arrangement of conductive rungs. Thus, another option would be to decrease the number of rungs to get wider access between them, but that option leads to a dramatic loss of homogeneity in the ROI [71]. Hence, designing of RF coils without these flaws is an interesting task to be resolved.

For that purpose, here we propose a birdcage-like coil wherein a few legs are removed in order to facilitate access to the ROI. We have called this RF coil "opencage". Such an opencage necessitates the realization of an aperiodic structure with a given current distribution on the rungs. An approach to set the current distribution could have been based on a brute-force electrical engineering approach. This solution was early used to develop elliptical or oval birdcage coils [100], [101], [102]. However, here we employ an approach wherein the opencage coil is considered as a metasurface or a Transmission Line (TL) metamaterial-based coil.

The current chapter is split in two sections. The section 3.1 is devoted to a linear polarized preclinical transmit/receive opencage coil for imaging of small rodents at 7T. While, the section 3.2 presents a quadrature transmit/receive opencage coil for head imaging, still at 7T.

3.1   Opencage coil for preclinical imaging at 7 Tesla

This subchapter describes the opencage coil developed for preclinical imaging of small animals at 7T. The operating frequency of the RF coil is the Larmor frequency of ^{1}H, which equals 300.1MHz. The principle of opencage is discussed in section 3.1.1. Subsequently, the numerical and experimental aspects of the opencage design are described in sections 3.1.2 and 3.1.3, respectively. The details of the prototype and its experimental examination are provided in

section 3.1.3. Finally, section 3.1.4 presents the results of phantom and in-vivo imaging. To assess, the image quality, the results are compared to the ones obtained with a birdcage coil.

3.1.1 Theoretical aspects of the preclinical opencage coil

As it was mentioned in Chapter 2, a unit cell can behave either as a left-handed transmission line (LHTL) or a right-handed transmission line (RHTL) [12]. Eventually, a LHTL topology has been chosen, because that topology is well adapted for an UHF MRI operation such as 7 T.

The general schematic view of the HP opencage coil is shown in Fig. 3.1(a). Whereas a conventional birdcage coil for UHF preclinical imaging at 7 T typically contains eight rungs (eight 45° cells), the proposed opencage coil is composed of two different types of rungs (cells), as it is shown in Fig. 3.1(b).
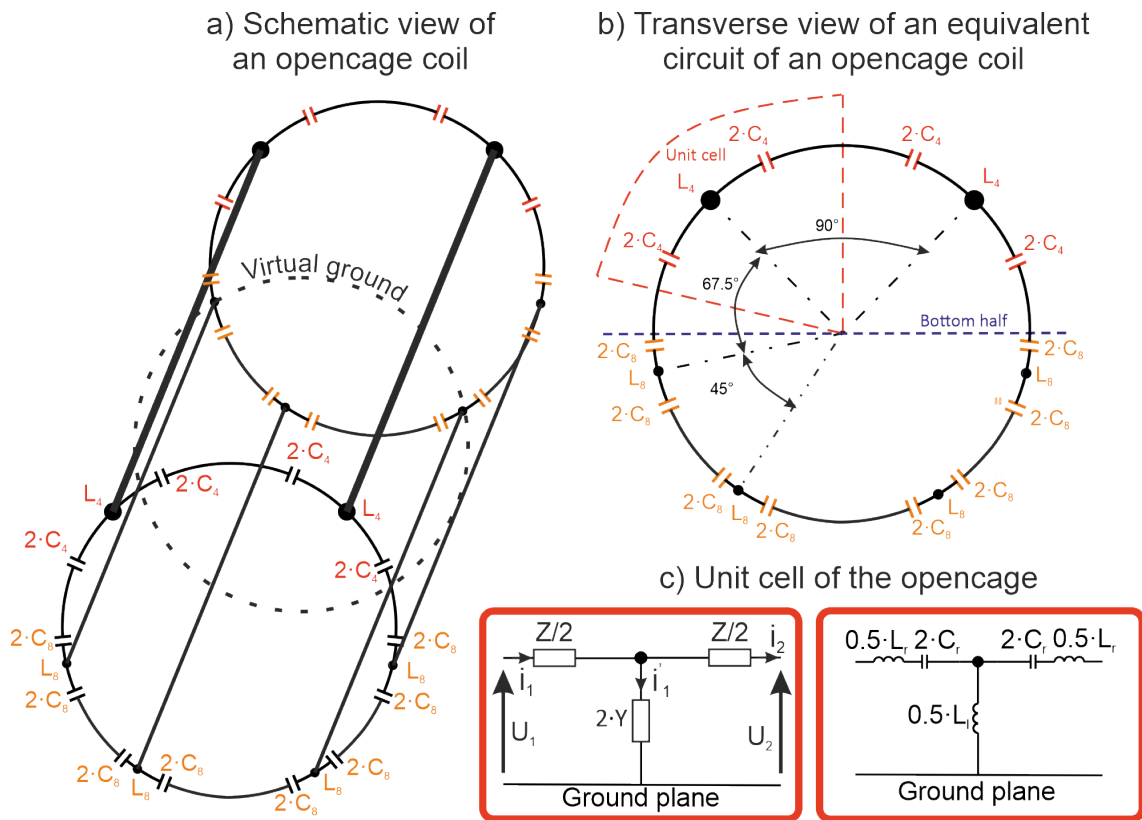
Figure 3.1 – (a) Sketch of the opencage coil composed of six rungs; (b) transverse view of the opencage coil; (c) unit cell used for the calculations.

Contrary to a birdcage coil, the angle between two rungs (cells) is no longer a constant due to the aperture at the top of a coil: the angle equals 90° (as for a birdcage coil composed of four rungs) for the top rungs and 45° (as for a birdcage coil of eight rungs) for the bottom rungs. The unit cell with the equivalent circuit shown in Fig. 3.1(c) contains different values of inductance (L and L_r) and capacitance (C_r) in order to obtain the proper phase shift between the cells.

By analogy with a birdcage coil, to generate a uniform magnetic field B_1^+, the phase of the current in the rungs should be equal to their azimuth angle [71]. Because the total phase shift

equals 2π, this current distribution corresponds to a resonant mode of the opencage coil. This mode is equivalent to the fundamental mode $k = 1$ of the birdcage coil.

As it was written in Chapter 2, there are two key parameters characterizing a unit cell. One of these parameters is the phase shift, while the other one is the Bloch impedance. Both parameters can be determined by formulas (2.19) and (2.22) from the prior chapter. To that end, the mutual inductances have been evaluated for the following selected geometrical parameters: coil length of 40 mm, coil radius of 17.5 mm, shield radius of 22.5 mm, leg width of 2.5 mm. At first, the 45° cell (as for eight rungs birdcage) and 90° cell (as for four rungs birdcage) are computed using the same rule as the one classically used for designing a birdcage coil as explained in Chapter 2 (without taking care of the impedance).

As it can be seen on Table 3.1, these unit cells are identical in terms of their self-inductance. However, due to different relative position of the legs, the effective inductances became different [74], [143]. Finally, to adjust the unit-cell based coils to the desired frequency of 300 MHz, the capacitances were computed using equation (2.13).

Table 3.1 – Used values of capacitances (C_r) and effective leg inductances (L_l), effective ring inductances (L_r).

Element	45° cells (as for 8 rungs)	90° cells (as for 4 rungs)	Modified 90° cells
C_r (pF)	16.94	7.63	8.3
L_l (nH)	22.96	19	16
L_r (nH)	9.88	17.9	17.9

The values of the capacitances and inductances were substituted into equations (2.19) and (2.22) in order to obtain the phase shift and the Bloch impedance for the considered unit-cells. In Figs. 3.2(a) and 3.2(b), the phase shift and the Bloch impedance are plotted with respect to the frequency. Thereby, for 45° cells, the determined phase shift and Bloch impedance equal 45.03° and 15.31 Ohm, respectively (Fig 3.2). For the 90° cells with the same self-inductances (sizes) as the 45° cells, the phase shift and the Bloch impedance equal 89.96° and 17.91 Ohm (Fig. 3.2), respectively.

This difference of impedance may involve some reflections of the traveling wave along the TL. In general, these reflections may induce non-uniform current distribution and therefore heterogeneous magnetic field. However, in this case, due to small difference of impedances, reflection between the cells is insignificant and can be neglected. An example where this effect cannot be neglected can be seen further in section 3.2 devoted to the head opencage coil.

Nevertheless, the capacitance and inductance values of 90° cells have been modified (Tab. 3.1) in order to obtain identical Bloch impedances as the one of the 45° cells and to retain the right phases. To that end, we have applied equations (2.23) and (2.24). As stated above, the width of a leg corresponds to an effective inductance of a leg. Therefore, its width was
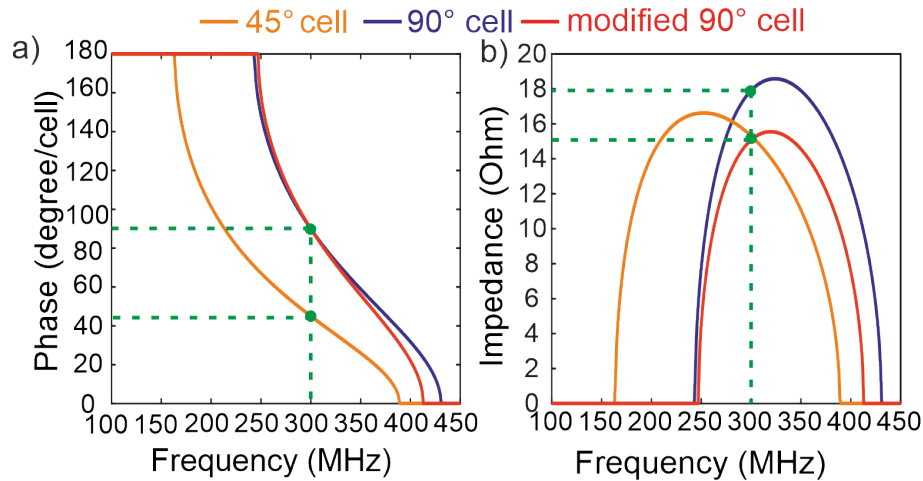
Figure 3.2 – **Calculated curves for the 45°, 90°, and modified 90° LHTL cells: (a) the dispersion diagram; (b) the Bloch impedance.**

increased from 2.5 mm to 5 mm. As expected, with the inductance corresponding to this width and the changed capacitance (Table 3.1), the evaluated phase shift equals 90.03° [Fig. 3.2(a)] and the Bloch impedance is lowered to 15.08 Ohm [Fig. 3.2(b)].

3.1.2   Numerical investigations of the opencage coil

After the analytical optimization, the opencage coil, has been simulated using commercial software CST Microwave suite 2018 using FEM-based Frequency Domain Solver. The coil illustrated in Fig. 3.3 has the following geometrical parameters: shield radius and length of 22.5 and 50 mm respectively, radius and length of 17.5 mm and 40 mm respectively, width of the bottom legs (w) of 2.5 mm and width of the top leg (w_1) equal 4 mm.

Contrary to the Fig. 3.3, in the first full-wave simulations, the shield is not open in front of two 90° rungs. In addition, the opencage coil is placed inside a copper cylinder corresponding to a 1m-long and 90-mm diameter MRI bore.

Moreover, unlike Fig. 3.3, wherein a mouse is depicted, in all conducted simulations the opencage coil is loaded by a homogeneous cylindrical phantom with a relative permittivity (ε_r) and a conductivity (σ) of 45.3 and 0.87 S/m, respectively. The length of the phantom is 105 mm and its radius equals 13 mm. The capacitances are slightly adjusted in order to tune the coil exactly at 300.1 MHz. The values became 17.23 pF for the 45° cells and 8.4 pF for the 90° cells. Furthermore, the capacitor distribution is slightly changed compared to the one of the analytical model. Contrary to the theoretical model, wherein all the capacitances are twofold, in the numerical investigation two capacitors in series are replaced by a single capacitor in order to reduce the number of elements. If the two capacitances are identical, they are replaced by a capacitance of half the value.

Capacitors that are in a ring that separates 90° and 45° cells are replaced by a capacitors of value $2 \cdot C_4 C_8/(C_4 + C_8)$, namely 11.3 pF. The ohmic losses of the capacitors are considered as the equivalent serial resistance (ESR) estimated from the quality factor of 1000. Two different cases of quadrature and linear driven opencage are studied independently.
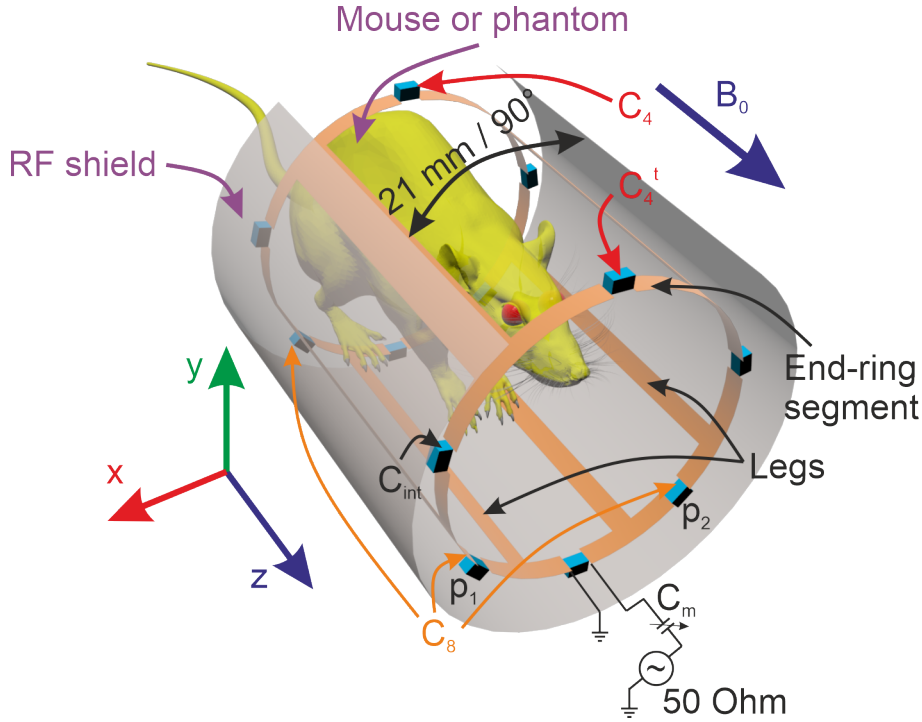
Figure 3.3 – **Final design of the opencage coil. The coil is placed inside the MRI bore (hidden). The shield of the coil is partially removed to fit the gap between the 90° cells. This setup is excited with one port at the bottom (i.e. linear driving). In case of quadrature driving (circular polarization) the ports would be placed at points p_1 and p_2**

Quadrature opencage coil. As for a conventional quadrature birdcage coil, the proposed quadrature opencage coil generates two modes, in which the magnetic field is polarized in the XY plane. These modes are the two orthogonal fundamental linear $k = 1$ modes excited by each port independently. The superposition of these two modes with a relative phase shift of 90° or -90° leads to 2 circularly polarized magnetic fields: B_1^+ or B_1^- [35]. These fields are counter rotating and perpendicular to the coil axis. Here it is proposed to investigate this case primarily using full-wave simulations.

As a result, the S-parameter spectra have been computed. Here, the coil is matched to the 50-Ohm feeding network by adjusting two trim capacitors (Fig. 3.3). Therefore, the reflection coefficients $|S_{11}|$ and $|S_{22}|$ are below -20 dB, as plotted in Fig. 3.4(a). The isolation between the ports is approximately -20 dB around the theoretically predicted frequency (300.1 MHz). Such a high level of isolation allows assessing the orthogonality of modes excited by port 1 and port 2. Eventually, this high level of isolation confirms that the proper values of the Bloch impedance and the phase shift of the rungs (unit cells) have been reached at the desired frequency of 300.1 MHz.

As it was stated in Chapter 1 devoted to state-of-the-art, the field B_1^+ (respect. B_1^-) is rotating in the same (respect. opposite) direction in transmission regime as the one of spin precession. The field B_1^+ is maximal in the ROI, while the opposite rotating field B_1^- should be as small as possible. In order to verify this property of B_1 field, the opencage coil is driven in quadrature regime by two 50-ohm ports in order to excite a circularly polarized mode. The two circularly polarized magnetic fields B_1 have been computed at the desired frequency. These field patterns are plotted inside the opencage coil, namely in the central (Z = 0) transverse
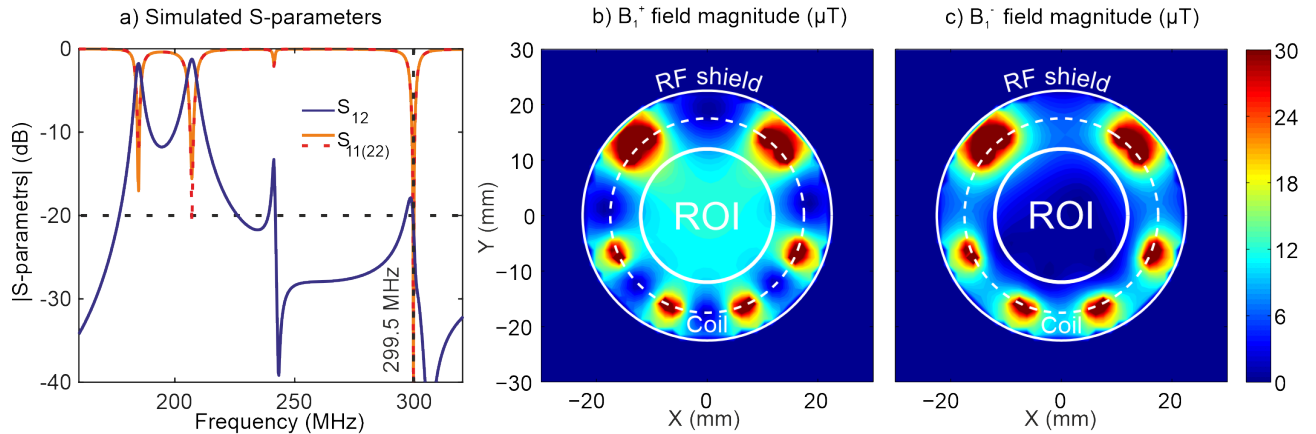
Figure 3.4 – **Simulated quadrature opencage coil. (a) Reflection and transmission coefficients (S_{11}, S_{22} and S_{12} in dB). Simulated field at 299.5 MHz: (b) B_1^+ field in the central (Z=0) transverse plane (XY); (c) B_1^- field. Here, the shield of the coil is not partially removed in order to simulate the ideal condition and confirm the correctness of the chosen optimization strategy. In addition, in order to homogenize the magnetic field, the width of the top legs (w_1) is slightly increased from 4 mm to 5 mm compared to the analytic value. The modified width is used in further simulations and experiments.**

plane [Figs. 3.4(b) and 3.4(c)]. Here, B_1^+ is maximal, while B_1^- is minimal due to destructive interferences. Thus, only the right clockwise or left clockwise modes are obtained depending on the sign of the 90° phase shift between the 2 ports. This confirms that the opencage coil behaves as a conventional birdcage coil.

Linear polarized opencage coil. For practical reasons, namely simplicity of connection to the MRI scanner, the opencage coil in the experiment is driven only by a single 50-ohm port (linear driving). Consequently, before the experimental part, an additional full-wave simulation has been performed in order to study this configuration.

The S_{11} parameter spectrum of that coil is illustrated in Fig. 3.5(a). As it can be seen, three modes ($k = 1, 2, 3$) can be excited in such a coil composed of six rungs (unit cells). The magnetic field |H| in A/m of these modes is presented in Fig. 3.5(b-d). As, it is expected the last mode $k = 1$ is homogeneous and linearly polarized in the y-direction. The other modes, like in a conventional birdcage coil, are not useful for MRI applications.

At last, the proposed opencage coil is compared to a conventional birdcage coil made of eight rungs of the same size. The normalized profiles of field B_1^+ are presented in Fig. 3.6. In these simulations, a 90° aperture is present at the top of the shield for the opencage coil.

Relative standard deviation (SD) of the B_1^+ is estimated in the region where the brain of a mouse would likely be placed. This region corresponds to the bottom half of the cage in the vicinity of the four 45° cells (rungs). The relative SD estimated for the opencage coil equals 8.8%, while for the birdcage coil this value equals 8.3%. These values indicate that the homogeneity of the B_1^+ field for both coils are comparable in half of the cage's inner volume. When the ROI is enlarged to the whole phantom, the value of relative SD increases to 20.4% for the opencage coil while retains almost constant (8.5%) for the birdcage coil. This increase in SD for the opencage coil is explained by lower density of the legs at the top. However, this drawback is expected and is the sacrificed for the sake of opening.
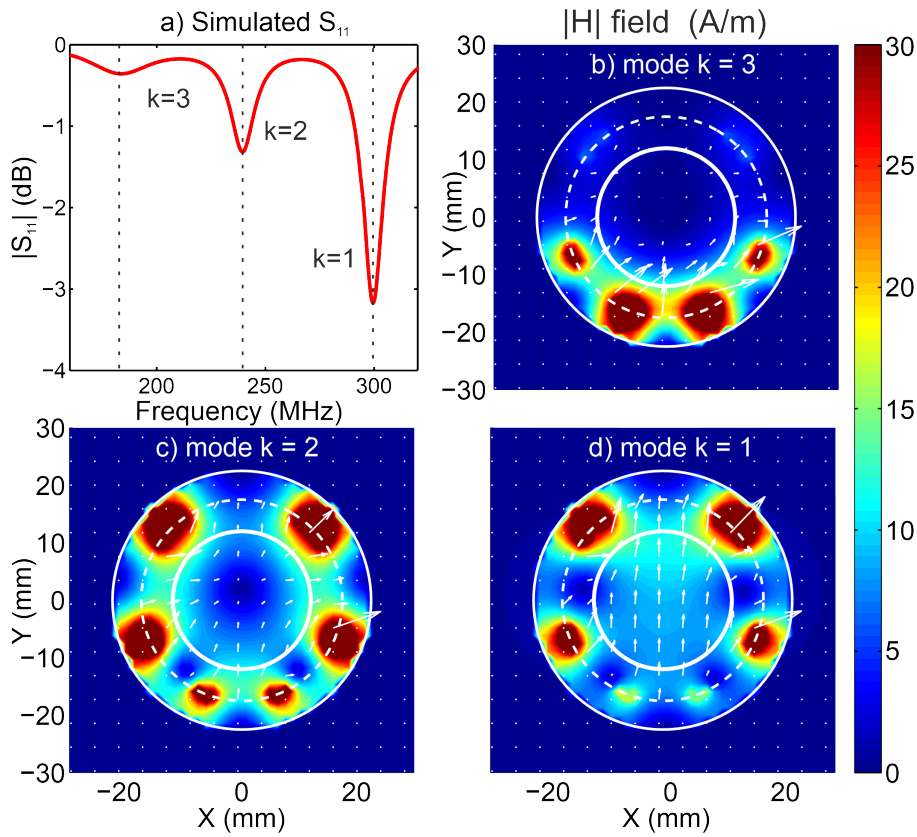
Figure 3.5 – **Results of full-wave simulations. (a) reflection coefficient (S_{11}) of the single port opencage coil. Simulated magnetic $|H|$ field of three different modes of the opencage coil: (b) magnetic field inside the volume of the opencage coil in the central ($Z=0$) transverse plane (XY) for mode $k = 3$; (c) mode $k = 2$; (d) mode $k = 1$ (mode of interest).**
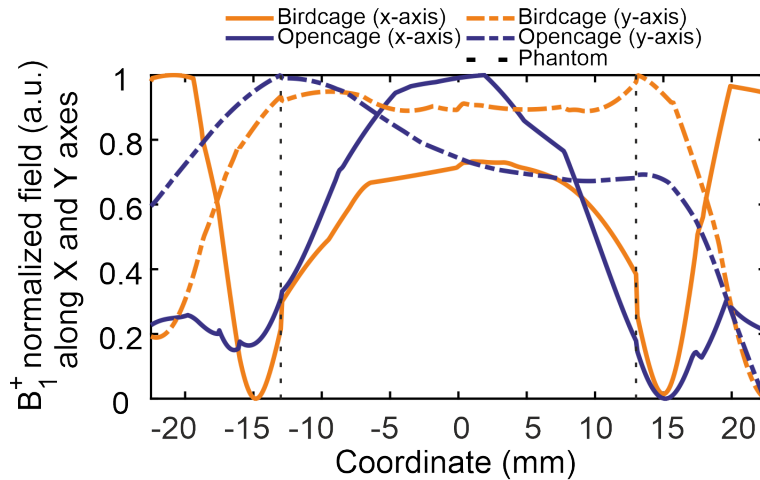
Figure 3.6 – **Simulated profiles of the normalized B_1^+ magnetic field for the eight rungs birdcage coil and for the opencage coil.**

3.1.3   Experimental prototype

After performing numerical tests, the linear polarized opencage coil has been assembled. As it was mentioned in the previous section, the opencage coil in the experiment is driven only by a single 50 ohm port. Moreover, due to a paradigm of an opencage, namely its openness, the RF

shield is partially removed in order to fit the gap between 90° cells [Fig. 3.3, Fig. 3.7(a)]. The plastic holder of the opencage coil has been 3d printed and coppered by a foil tape of 0.035-mm thickness [Fig. 3.7(a)]. The following ceramic capacitors were in stock: 21.3 pF (20 pF and 1.3 pF in parallel) for the 45° cells, 10.5 pF (7.5 pF and 3 pF in parallel) for the 90° cells and 13.7 pF (7.5 pF and 6.2 pF in parallel) as Cint. These capacitors are placed as shown in Fig. 3.3 and Fig. 3.7(a).
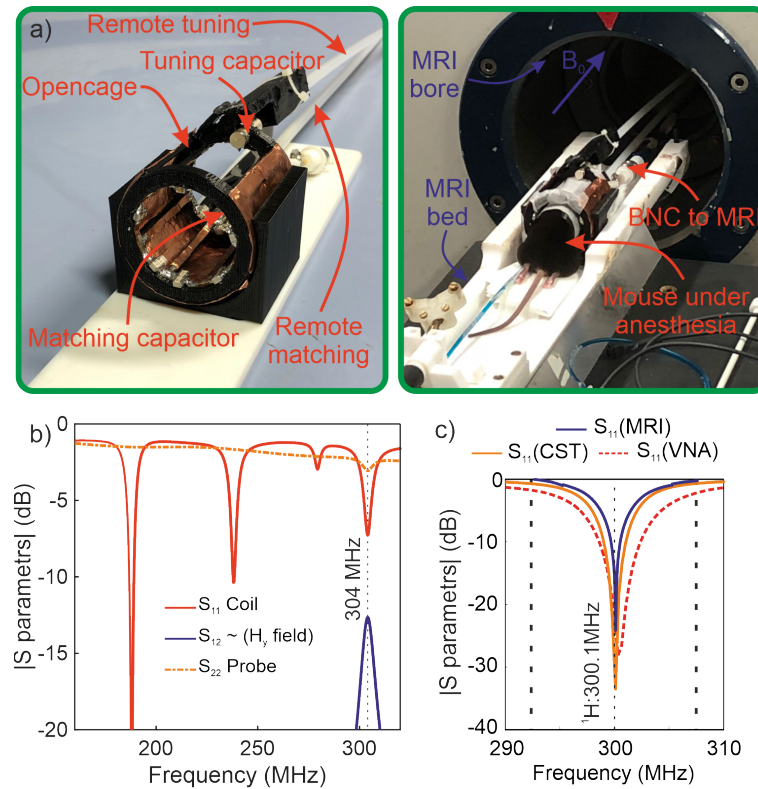
Figure 3.7 – **(a) The assembled opencage coil placed in the MRI bed. The setup includes the cable trap and the matching circuit adapted for remote tuning and matching implemented by rotation of the long polyamide rods. (b) Measured reflection coefficient ($|S_{11}|$) of the unloaded opencage coil and the measured transmission coefficient ($|S_{12}|$) to the magnetic probe. (c) The simulated, measured on bench and inside the MRI bore reflection coefficient $|S_{11}|$ in dB. In all three cases the loaded coil tuned and matched at the Larmor frequency of proton ^{1}H (300.1 MHz).**

A matching circuit composed of two tunable non-magnetic capacitors has been implemented in order to achieve the exact desired frequency and a suitable level of the reflection. In the details, a tunable capacitor C_t is mounted in place of the capacitor C_4 [Fig. 3.3 and Fig. 3.7(a)] to adjust the frequency and a tunable capacitor C_m is connected in series to the core of the feeding of the coaxial cable [Fig. 3.3 and Fig. 3.7(a)] to match the impedance to 50 ohms.

Because the tuning/matching depends on the coil load, a cylindrical phantom has been built with a plastic tube having the following geometrical parameters: 13 mm of radius and 105 mm of length filled by liquid with relative permittivity $\varepsilon_r = 45.3$ and conductivity $\sigma = 0.87$ S/m. With the load, the parameter S_{11} after matching and tuning is shown on [Fig. 3.7(c)]. A good matching coefficient $|S_{11}| < 20$ dB is obtained at the desired frequency of 300.1 MHz. When the coil is inside MRI scanner, revolving long polyamide roods connected to the trim element of the capacitors allows remote tuning and matching.

The coil was connected to the vector network analyzer (VNA). At the same time, a pick-up coil was connected to the second port of the VNA. This pick-up coil is a non-resonant magnetic probe (loop). The probe loop is oriented toward Y-axis that corresponds to the polarization of the magnetic field as it has been observed on the simulation results [Fig. 3.5(b-d)]. A S_{12} coefficient increase is observed at 304 MHz [Fig. 3.7(b)]. Because the coil is not loaded when the probe is inside the coil, a 3.9 MHz frequency shift is observed with respect to the 300.1 MHz resonant frequency seen in Fig. 3.7(c). The measurements in the scanner are considered in the next section.

3.1.4 MRI assessment and comparison to the birdcage coil

After several tests on the bench, the opencage coil loaded by the phantom was connected through a cable trap to the MRI scanner (Bruker PharmaScan 7T). In addition, it is important to note that in all the experiments the proposed coil was used for both transmit and receive regimes.

The B_1^+ fields in the phantom have been experimentally acquired using the Actual Flip Angle (AFI) MRI sequence, implemented on our Bruker PharmaScan 7T preclinical MRI scanner [42]. The measured patterns presented on Fig. 3.8(b) are acquired with the following MRI acquisition parameters: echo time (TE)/repetition time (TR)1/TR2 = 4/20/100 ms; flip angles (FA) $\alpha^1 = \alpha^1 = 50°$; an RF pulse duration of 1 ms; an excitation bandwidth of 14 kHz; a FOV of 32 mm by 32 mm; an in-plane resolution of 0.5 mm; spoiling gradients with a diffusion coefficient of $2.2 \cdot 10^{-9}$ $m^2 \cdot s^{-1}$, and a damping factor of 0.7. For comparison, the simulated B_1^+ magnetic field at 300.1 MHz inside the cylindrical phantom is presented in Fig. 3.8(a). Both simulated and experimental patterns are normalized to fit the maximum and minimum of the field in the ROI (phantom). Here, the mismatches between the simulated and measured fields can be explained by inaccuracy during the construction of our prototype and the tolerance of the capacitors (2%). Both these factors lead to the asymmetry of the coil and, as a result, to deviations from the ideal magnetic field as in simulations. The stronger magnetic field in the top of the coil can be explained by the higher currents' amplitude in the corresponding legs.
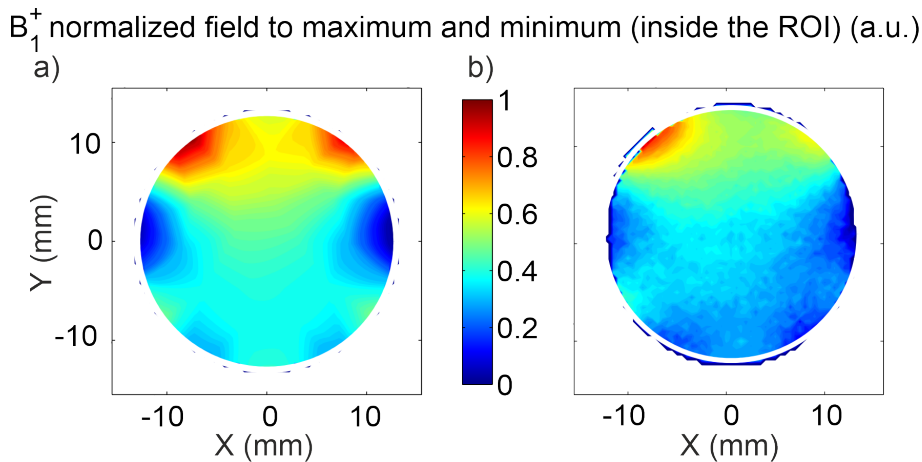

Figure 3.8 – **The simulated and measured opencage coil tuned at 300.1 MHz: (a) normalized B_1^+ magnetic field obtained in the simulation; (b) normalized B_1^+ Magnetic field acquired with AFI sequence.**

Then, the phantom images [Figs. 3.9(a) and 3.9(b)] have been acquired using the gradient echo sequence (GRE) with the following parameters: TR/TE = 200/3 ms, an isotropic voxel of 0.5 mm, an FOV of 32 mm by 32 mm by 64 mm, and a FA of 30°. We have built a prototype of conventional birdcage coil of the same size in order to make an experimental comparison to the opencage coil. The phantom images [Figs. 3.9(c) and 3.9(d)] have been acquired using the same sequence. In both cases, the reference power is adjusted by the Bruker ParaVision software. This adjustment is performed in the center of the phantom. The SNR of the images are evaluated as the mean signal at the center of the image in a square of 10 by 10 voxels divided by the standard deviation of noise. The noise is evaluated on a square of 10 by 10 voxels outside the phantom. The two squares are shown in the Figs. 3.9(a, c). For the central transverse image at the center of the coil along the longitudinal axis of the magnet [Fig. 3.9(a)], the average SNR is evaluated to 1865, meanwhile for the same plane with the birdcage coil [Fig. 3.9(c)], the average SNR equals 1752. Hence, one can conclude that the average SNR of both images are comparable. Moreover, both coils demonstrate sufficient homogeneity of the signal in the broad FOV.

Eventually, the proposed opencage coil was tested *in vivo* on an anesthetized mouse. The acquired images at several transverse slices are presented in Figs. 3.9(e-g) for the opencage coil and Figs. 3.9(h-i) for the conventional eight-leg birdcage coil. For the in vivo imaging, the spin echo sequence was used (TR/TE = 6200/30 ms, an anisotropic voxel of 0.125 mm^2 by 0.5 mm, an FOV of 20 mm by 20 mm by 32 mm, the number of averages of 14, and the FA of 90°). In conclusion, the signal level in the ROI is suitable, while the opencage coil provides sufficient FOV to scan a brain or a half body of small rodents.

As the coil has been successfully tested for preclinical imaging, our aim now is to test quadrature opencage coil for human brain imaging at 7 T. This new goal arises new challenges in coil designs. For instance, fabrication of quadrature coil with two feeding ports requires more care about isolation between the two ports that should be properly matched. Moreover, in head imaging safety rules are stricter than in preclinical imaging, therefore, the developed coil should also be safe for the patient. Thus, in the next section we rise all these aspects of head coil design for UHF MRI.

3.2 Quadrature opencage coil for clinical brain imaging at 7 Tesla

In contrast to the previous section wherein the opencage coil for preclinical imaging (i.e. for small animals) at 7 T has been described [149], this part focuses on a quadrature opencage coil for clinical brain imaging at 7 Tesla. Before we start reporting an opencage coil, the role of birdcage coils [80] in clinical MRI imaging should be explained.

At ultra-high field (UHF) MRI such as 7 T, birdcage coils usually play the role of transmit radiofrequency head coil [150]. It can also be used as a receive coil, however, SNR of acquired images is weak in this case [10]. At the Larmor frequency of proton ^{1}H, which is around 298 MHz, the wavelength in free space equals 1 m. Human brain acts like a dielectric with high effective permittivity ($\varepsilon_r \approx 75$), wherein the wavelength is as small as $\lambda \approx 12$ cm [151], [152]. Because the wavelength is smaller than the typical size of a brain, B_1^+ is inhomogeneous. As a
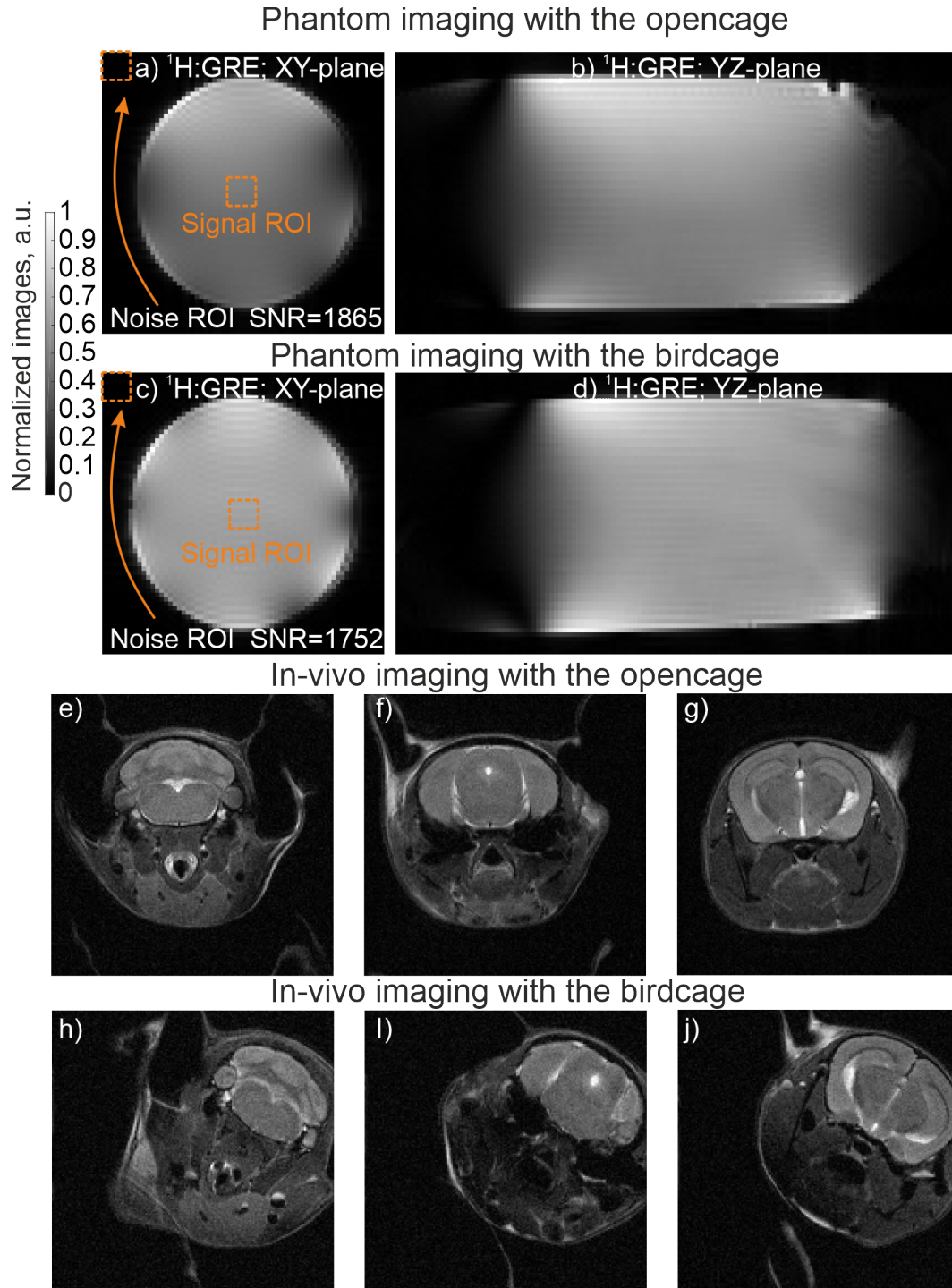
Figure 3.9 – **The normalized images acquired with the opencage coil: (a) phantom image in central transverse plane; (b) in central sagittal plane; normalized images acquired with the birdcage coil: (c) phantom image in central transverse plane; (d) in central sagittal plane; (e) - (g) *in vivo* images of the mouse brain acquired with the opencage coil in several transverse slices showing sufficient SNR and substantially suitable spatial homogeneity; (h) - (j) acquired with the eight rungs birdcage coil.**

result, B_1^+ spot appears in the center of a sample, while it is strongly decaying toward the periphery with a typical scale of a quarter wavelength, i.e., 3 cm [8], [153]. As a result, in transmit regime, a birdcage coil provides mediocre homogeneity for 7T head imaging. Simultaneously, in receive regime, the SNR of acquired images is moderate [10]. To overcome this issue, one

can use transceiver [109] or transmit only/receive only (ToRo) phased arrays [13], [36], [105].

Initially, phased arrays can be used for parallel imaging (receive) reducing data acquisition time and improving the SNR compared to conventional receivers [9], [154]. They can be composed of independent decoupled loops [118] or dipoles [155]. Furthermore phased arrays used in transmit regime can lead to passive or active B_1 (RF) shimming [53], [156], [157], [158] improving the homogeneity of the transmitted B_1 [159]. In addition, phased arrays lead to SAR reduction and RF input power reduction [53]. Eventually, multichannel arrays are very flexible because the array elements can be distributed over almost any surface that closely fits the imaged object. Thereby, phased receive arrays provide suitable SNR in receive regime and B_1^+ coverage in transmit regime as well.

Nowadays, one of the common solutions for UHF head imaging at 7T is a hybrid system based on a helmet coil composed of 32 channels with 32 electrically small loops for probing the RF echo in receive regime and a birdcage coil for RF emission [10]. The receive coil is made to tightly fit the head and is placed inside a T_x birdcage coil. This setup provides significant SNR enhancement compared to the conventional T_x/R_x birdcage coil.

In the newest devices for 7T, the transmit birdcage coil is replaced by an eight dipole transmit array [51]. Basically, this coil provides better homogeneity in some regions of the brain when compared to the birdcage coil. Another device made of 2 phased arrays has been proposed: one for transmit with 4 channels and the other one with 16 channels for receive has been designed in [119]. This coil has the same aim as opencage because it is dedicated to offer wide access.

However, the realization of all these varieties of phased array coils requires care about: decoupling (isolation) between the adjacent elements of an array [108], [160], decoupling between transmit and receive coils [106], detuning of the transmit coil in receive regime [36]. In addition, each element in the array needs a proper impedance matching circuit, cable trap or balun, which, in the end, require numerous MRI compatible electronic components. Moreover, despite the phased arrays provide outstanding performance, they are usually completely shielded and very bulky by themselves. Therefore, phased arrays may not be convenient and comfortable as an improved birdcage coil in some situations. All these factors bring a lot of engineering difficulties which, in the end, increase the cost of the coils. Although, UHF brain imaging moves toward parallel transmit or receive technologies, birdcage coils remain one of the reference coils.

For that purpose, we propose to develop an opencage coil that can be used for human brain imaging for those, who suffers from claustrophobia or for several specific applications in fMRI, in which extra space around a coil is needed [11], [145], [146]. Our solution provides a good trade-off between quality of acquired images and accessibility to the area under study. At first, the proposed coil can be used for both transmit and receive regimes. However, in the future, this coil may be improved to be transmit only, while another coil such as phased array for receive can be employed. Because of the larger size, we cannot use all the results of the previous section devoted to preclinical opencage coil. Moreover, here we focus on the experimental development of an opencage involving dual ports feeding leading to circular polarized mode.

Eventually, in section 3.2.1 we present the slightly modified approach that is used to optimize the currents in the quadrature opencage coil. Then, the results of theoretical modeling are validated with a full-wave numerical simulation in sections 3.2.2 and 3.2.3. These results are confirmed by an experimental demonstration in 3.2.4-3.2.6.

3.2.1   Theory of a quadrature opencage coil

Development of the opencage coil requires optimization of the current distribution of each radiating element of a coil (rungs or unit cell). In other words, the rungs distributions may be changed, but current distribution may retain the same as in the birdcage coil. The opencage coil is described using the formalism of transmission lines with lumped elements. This method has already been used to design the linear polarized opencage coil for preclinical imaging of small animals at 7 Tesla [149]. Here, we address the more complicated challenge of generating the circular polarization (CP) mode.

At lower B_0 field, such as 1.5T, 3T, 4T, a head birdcage coil provides homogeneous B_1^+ field distribution in its inner volume [8], [9]. However, at UHF the wavelength become shorter (about 12 cm in human tissue), and B_1^+ field become inhomogeneous [9]. Therefore, it decreases performance of a transceiver coil, namely, transmit efficiency and sensitivity (SNR of acquired images) in some regions of acquired images. Nevertheless, using a birdcage coil in CP regime helps the situation. Indeed, the SNR of images obtained with CP mode is $\sqrt{2}$ higher than using linear polarized mode [89].

As for the birdcage, the opencage coil must maintain 90° phase shift between the two feeding ports to generate this CP mode. That phase shift can be obtained with a 90° hybrid coupler or a combination of Wilkinson power divider and a phase shifter connected to the coil ports [71]. But, because of the lack of periodicity for opencage cells, it is more complicated to obtain that 90° between the two rungs.

Here, the aim is to design an opencage coil for UHF head anatomical imaging at 7T. The operating frequency of proton ^{1}H equal to 298 MHz. The geometrical parameters of the coil are the following: inner radius of 130 mm, length 240 mm, radius of RF shield is 155 mm.

These dimensions are used for calculating of mutual and self-inductances, as it is described in chapter 2. The coil is composed of eight rungs that are separated by 22.5° in the bottom and only two rungs in the top separated by 90°, where an aperture is provided. The general schematic view of the coil retains the same as in the previous section devoted to preclinical opencage coil. However, the number of rungs is different as it is shown in the transverse view of the coil [Fig. 3.10(a)].

As it has been observed in the previous section, the equivalent circuit of an unit cell is composed of two capacitances (C_i), one inductance (L_i) and two end-ring inductances ($L_{r,i}$). For such unit cell, 2 by 2 transmission matrix or ABCD can be composed. From this matrix the Bloch impedance ($Z_{i,b}$) and the relative phase shift ($\delta\varphi_i$) is deduced from formulas (2.19) and (2.22). Moreover, the leg inductances and ring capacitance can be evaluated directly using formulas (2.23) and (2.24).

First of all, one considered the unit cell with the relative phase shift of 22.5° per rung (as for sixteen rungs birdcage coil). For that geometry, the effective leg and ring inductances are evaluated. The result is shown in Tab. 3.2).

The same procedure has been performed for 90° cells (as for four leg birdcage coil). As in the previous chapter, here we compute the inductances and capacitances of the 90° cell by:

- considering only the 90° phase shift and retaining the same width for the legs and rings as the one of the 22.5° cells;
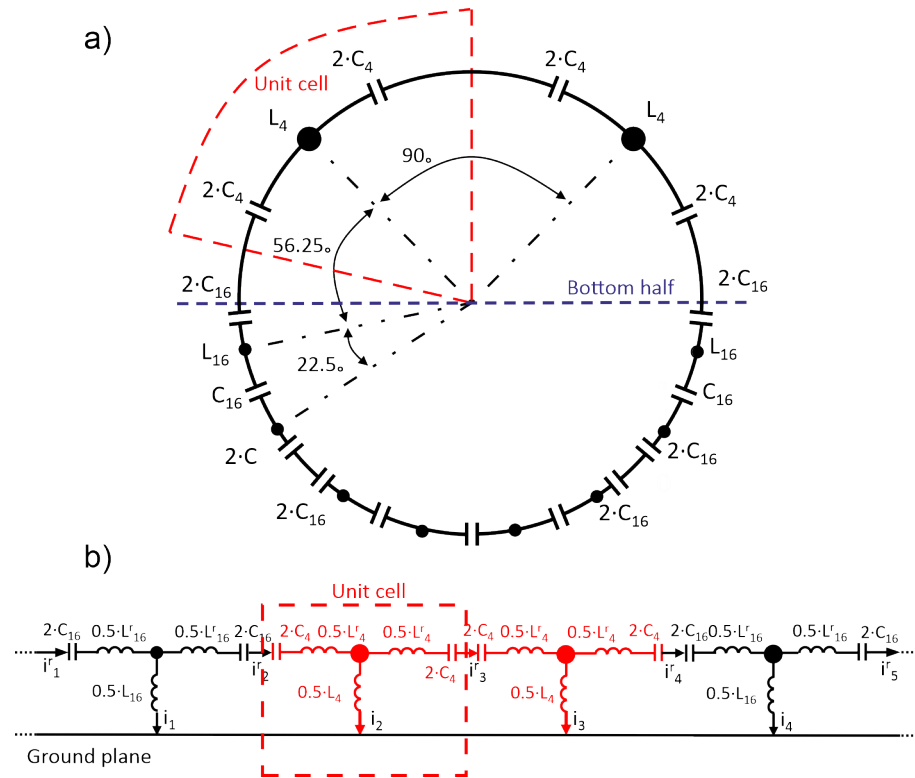
Figure 3.10 – **(a) Simplified representation of an opencage composed of ten rungs. Namely, eight rungs in the bottom and two rungs in the top. (b) Equivalent electrical circuit. A rung (or unit cell) is represented inside the dashed-line rectangle. The 2 top unit cells are shown in red and the bottom ones in black (only 2 of them are shown).**

- taking into account both the 90° phase shift and the Block impedance to be the same as the ones of the 22.5° cells. In that case, the width of legs and rings are different for the 22.5° and 90° cells. For that purpose, constrain optimization based on gradient descent method has been used to evaluate effective leg inductance (L_i) and capacitance C_i. In that optimization, the Bloch impedance and relative phase shift are set to 62.45 Ohm and 90° respectively. Here, the effective ring inductance $L_{r,i}$ was set constant to 165.4 nH.

The corresponding dispersion curves are shown in Fig. 3.11(a). As expected for the three kinds of unit cells (22.5° and the 90° optimized and non-optimized), the phase shifts at 298 MHz reach the expected values. The Bloch impedances have been calculated over the same frequency range for the three-unit cells [Fig. 3.11(d)].

As it can be seen from Fig. 3.11(d), the impedance of the unmodified 90° unit cell is approximately twice higher than the impedance of the 22.5° unit cell. Therefore, this result fully justifies the metamaterial approach to retain simultaneously the proper phase shift and the same Bloch impedance as the one of the 22.5° cell.

The dispersion and impedance diagram of this optimized unit cell are presented in [Fig. 3.11(a, d)]. Thus, to achieve the desired value of leg inductance, the width of a leg should be increased from 10 mm to 39.5 mm.

Thereafter, an additional electrical simulation using the circuit simulator of CST Microwave Suite has been performed in order to validate these theoretical values of impedances and phases.

Table 3.2 – Used values of capacitances (C_r) and effective leg inductances (L_l), effective ring inductances (L_r).

Element	22.5° cells (as for 16 rungs)	90° cells (as for 4 rungs)	Modified 90° cells
C_r (pF)	5.15	0.95	1.23
L_l (nH)	173.97	132.6	66.7
L_r (nH)	42.09	165.4	165.4
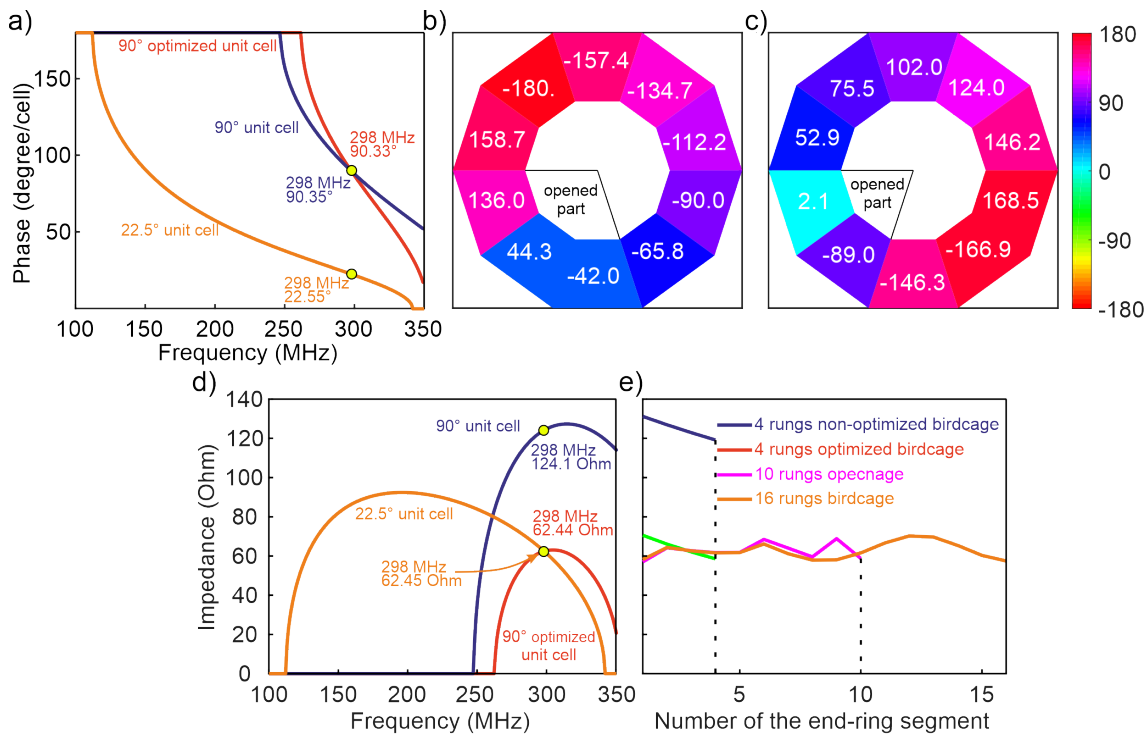
Figure 3.11 – (a) Band diagram of three different unit cells. Current distribution: (b) in end-ring segment, (c) in the legs. (d) Bloch impedance for the three different unit cells, (e) Impedance in end-ring nods for several birdcage composed of different unit cells.

Here, the coil is modeled as a ten-unit cells (rungs) circuit. The results of that simulation are presented in [Fig. 3.11(b, c, e)].

First, it can be seen from Fig. 3.11(b) that the computed phases along the whole transmission line composed of opencage unit cells are consistent with the expected ones. As it was stated before, the used approach is well adapted for controlling the relative phases in the nods (I_r^i) [Fig. 3.11(b)]. Therefore, current in the legs (I_l^i) is not explicitly defined in this case. However, as it has been stated in chapter 2, the currents in the legs is given by calculating the difference of the current between two neighbor cells (rungs) according to Eq. (2.19). As it can be seen in Fig. 3.11(c), two adjacent legs at the bottom, marked as the opened part, show a difference in relative phases of 90° as it is expected.

In addition, the Bloch impedance has been assessed by plotting the ratio between voltage

and current at the nods. Here, three different birdcages and one opencage are studied:

- birdcage with 22.5° distant cells (16 rungs);

- birdcage with 90° distant cells (4 rungs) - before the optimization;

- birdcage with 90° distant cells (4 rungs) - after the optimization;

- optimized opencage.

Eventually, it can be seen in Fig. 3.11(e) that the impedances are comparable to the expected ones [Fig. 3.11(b)]. As a result, the coil can be now designed more precisely and investigated in full-wave simulations.

3.2.2   The design of the opencage coil and full-wave simulations

The design of the opencage prototype is illustrated in Fig. 3.12. As it was mentioned in the previous subsection, the opencage coil has the following geometrical parameters: radius of 130 mm, length of 240 mm, and radius of the RF shield of 155 mm. The coil is shielded by copper with a gap of 139 mm width in front of the opening (90° rungs). The width of end-rings and bottom legs are equal to 10 mm, while the width of the modified legs in the top is 39.5 mm.
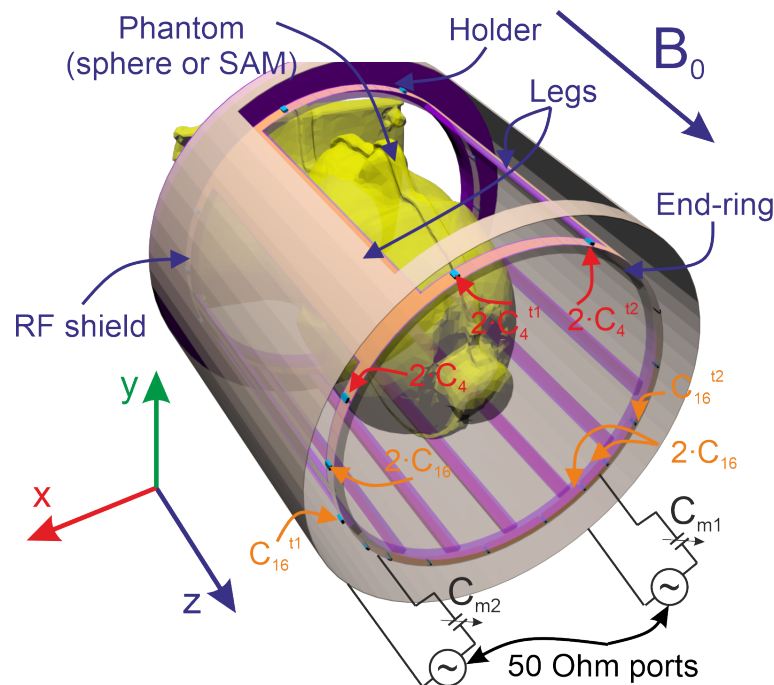

Figure 3.12 – Geometry of the loaded opencage coil driven in quadrature.

The coil is driven in quadrature by two 50 Ohm ports that are 90° distant at the bottom part (see Fig. 3.12). The ports are connected between the doubled capacitances in the end-ring segments and the shield, as it is shown in Fig. 3.12. In this case, the opencage coil is excited thought capacitive coupling.

The design has been tested using a full-wave simulation software (CST Studio Suite 2018). In the conducted simulations, the coil is loaded with a homogeneous dielectric sphere phantom of diameter 155 mm (not shown in Fig. 3.12). Its relative permittivity (ε_r) and conductivity (σ) equal to 75 and 1 S/m respectively.

However, it appears that with the values of the capacitors differ from the analytical model, the resonance frequency of the simulated opencage is 20% higher than the expected one. As a result, in order to tune the coil to the frequency of 298 MHz, the capacitors are slightly scaled compared to the analytical values. Thus, $2C_4$ becomes 2 pF instead of 2.64 pF and $2C_{16}$ became 8.3 pF instead of 10.3 pF. Moreover, the ESR of the capacitors are considered with a quality factor of 1000.

This 20% of difference between analytically predicted and simulated results may be explained by several factors. First, the geometry of the shield is complex because of the gap at the top. Second, the high index dielectric phantom modifies the mutual inductances. Finally, there is the influence of the two feeding 50 Ohm ports.

Moreover, from a practical point of view, the values of the capacitors are restricted by the ones available in stocks. Moreover, in order to reduce the number of capacitors, when it is possible, two capacitors in series have been replaced by a single capacitor. According to Fig. 3.12, twofold capacities are only retained on the rungs where: the feeding ports are connected, the two types of cells are connected, cells are on top part. For this last, this is because the total capacitance of the two $\approx$ 2pF-capacities would have been $\approx$ 1 pF which is below self-parasitic capacity of the coil [71].

To assess the relevance of matching both the phase shift and the Bloch impedance of the cells, we simulate the non-optimized coil [Fig. 3.13(a)]. Due to impedance mismatching between the different unit cells, an appropriate isolation level of S_{12} cannot be achieved at the desired frequency of 298 MHz. To excite the $k = 1$ mode at the proper frequency while achieving desirable S-parameter spectrum, the optimized opencage has been simulated [Fig. 3.13(b)]. The resonance occurs at frequency of 296.3 MHz. At this frequency we observe that the impedance matching level of the 2 ports is high enough (S_{11} and S_{22} are below 20 dB), with an appropriate isolation level (S_{12}) of approximately -15 dB.

The B_1^+ and B_1^- field maps at the resonance frequency (296.3 MHz) of the optimized opencage are plotted in Fig. 3.14 showing the fields in the central (Z=0) transverse plane (XY) at the top and the central sagittal (YZ) plane in the bottom. Due to the 90° phase shift between the 2 ports, when they are fed by a 90° hybrid coupler, B_1^+ field is maximal and B_1^- minimal.

These results that are similar to the birdcage ones indicate the rightness of optimization strategy. However, before going toward the experimental realization, SAR assessment should be provided.

3.2.3 SAR assessment

RF safety assessment has been numerically conducted for the opencage coil. The opencage coil has been compared to a simulated conventional birdcage coil made of sixteen rungs and comparable to the opencage coil size. Both coils are loaded by the head voxel model and then simulated in CST Microwave suite using Time Domain Solver. The open source voxel
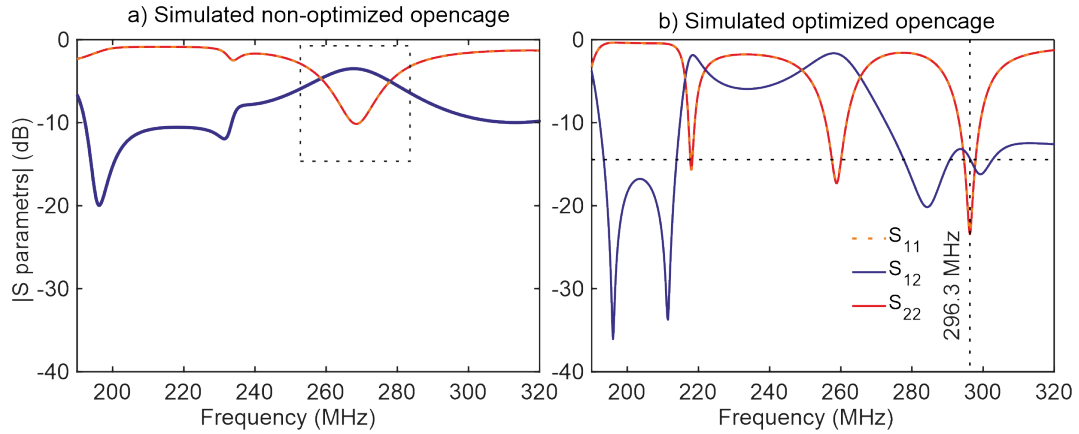
Figure 3.13 – **Simulated S-parameters on: (a) non-optimized and (b) optimized opencage coils. In optimized case, the width of the top legs is increased from 39.5 mm to 55 mm in order to adjust isolation level ($|S_{12}|$). This width is used in further simulations and experiments.**
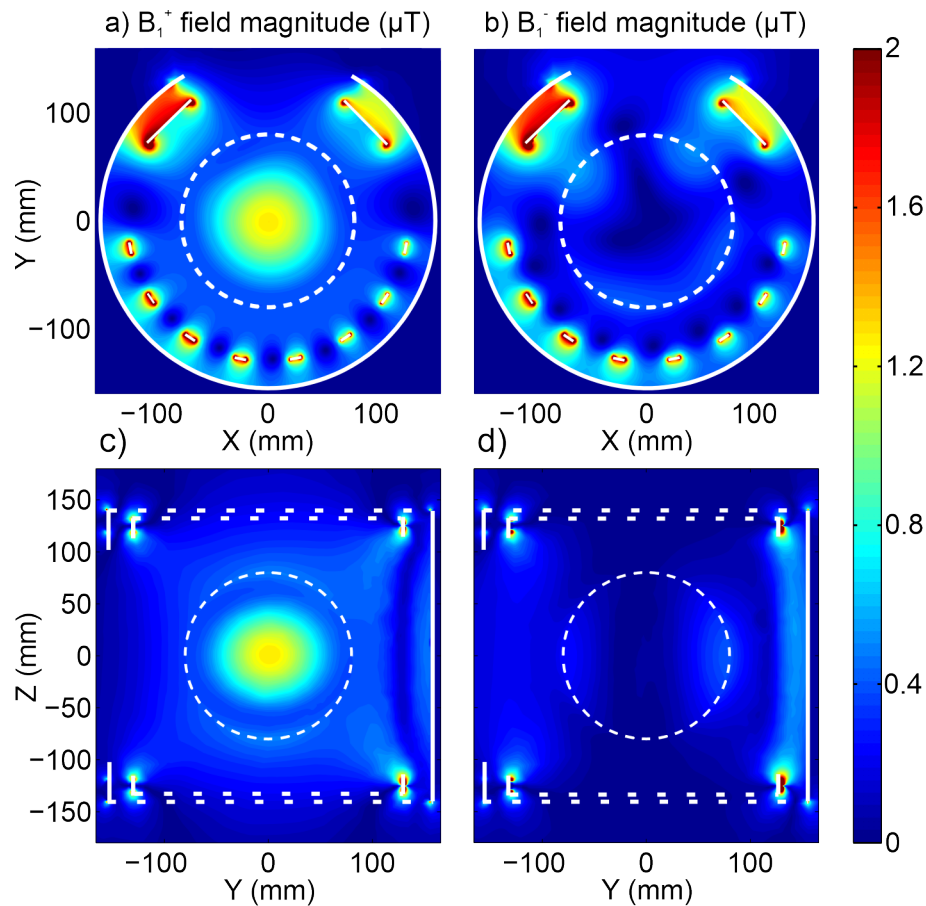
Figure 3.14 – **Simulated B_1^+ and (b, d) B_1^- at central transverse plane and central sagittal plane, respectively. Here the coil is loaded by the sphere phantom and part of the RF shield is removed.**

model Ella UWM adapted for 297 MHz has been used [161], [162], [163]. The voxel size of that phantom is 2 mm^3. In the conducted simulations, both coils are matched at the Larmor frequency. Finally, local SAR for 10 g of tissues is estimated and depicted in Fig. 3.15. In both cases local SAR$_{10g}$ maps are normalized for the same accepted power of 1W.
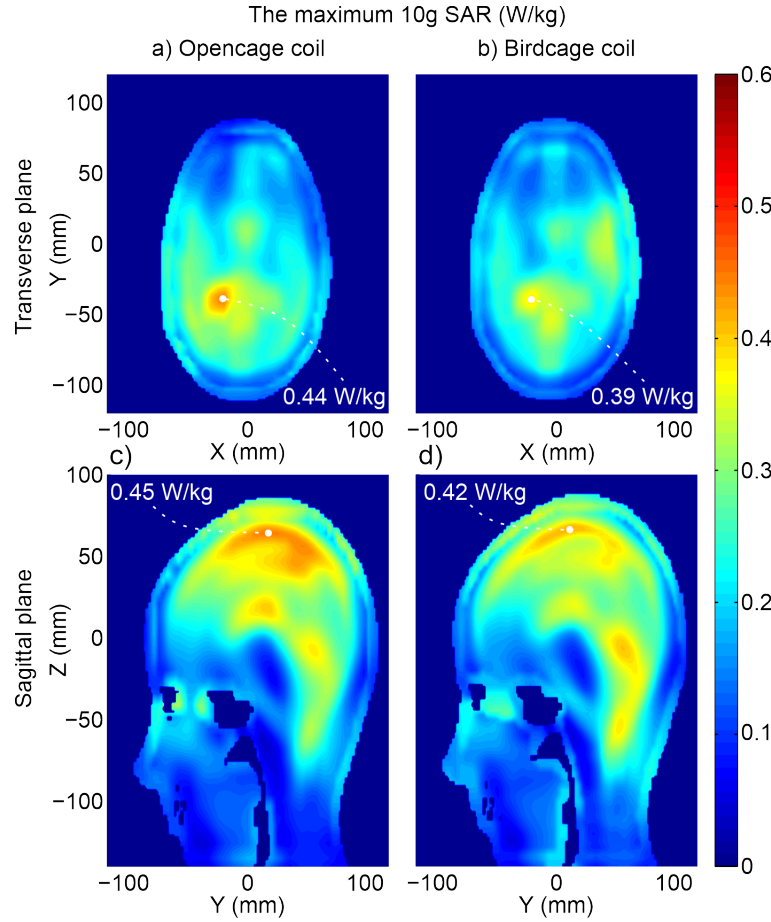
Figure 3.15 – **Numerically estimated local SAR for 10 g of tissues. All maps are normalized for 1 W of accepted power. Map of local SAR$_{10g}$ of the opencage coil (a, c) and the birdcage coil (b, d) in the central transverse plane and in central sagittal plane, respectively.**

As it can be seen in Fig. 3.15, the local SAR is comparable for both coils in transverse and sagittal planes. Assessing the local SAR in the whole head, shows slightly different values, namely 0.52 W/kg for the birdcage coil and 0.5 W/kg for the opencage coil. Eventually, one can conclude that the proposed opencage head coil provides identical safety as birdcage coil.

3.2.4   The prototype and $\mathbf{T}_x/\mathbf{R}_x$ interface

The optimized opencage coil has been assembled [Fig. 3.16(a)]. The frame of the coil was 3d printed using polylactic acid (PLA). The electrical tracks were made of 35 mm thick copper foil tape. Then, all the components were soldered. The RF shield is chemically etched on FR4 substrate with 5 narrow gaps along Z axis in the metal layer in order to prevent eddy currents. For that purpose, four nonmagnetic capacitors of 1 nF have been soldered between these gaps as proposed in [83].

In the prototype, the values of the capacitors are the same as the ones of the simulation. The tuning and matching circuit is implemented as shown in Fig. 3.16(b). Two trim capacitors connected in series to the feeding lines are employed for impedance matching. In order to tune the resonance frequency, two tunable capacitors were placed instead of the fixed ones as shown in Fig. 3.16(b). The S-parameters of the coil loaded by the phantom have been measured with

VNA (Fig. 3.17). The opencage coil has been tuned and matched ($|S_{11}| \approx |$ and $|S_{22}| \approx$ -20 dB) slightly below the exact Larmor frequency of 297.3 MHz, namely at 296.7 MHz because of the effect of the MRI bore that slightly detunes the coil to higher frequency. As a result, both simulated and measured S-parameter spectrums demonstrated good agreement [Fig. 3.17(a, b)].

To connect the coil to MRI scanner (Siemens 7T MAGNETOM Terra), two interfacing devices have been used [Fig. 3.16(c)]. The first one is composed of a T_x/R_x switch connected to one port of the coil via BNC connectors while the second port of the coil was connected to a 50-Ohm load BNC plug. In this case the coil works in a similar way as the preclinical opencage coil, i.e., in a linear polarization regime.

In order to excite the CP mode, a new T_x/R_x interface has been employed. In this interface, each single port of the coil is connected to 90° hybrid coupler in order to have circular polarization in transmit regime. In transmit regime, all pin diodes of the interface are non-active, and the signal emitted by the scanner is injected into the hybrid coupler. The input signal are split in into 2 signals that are 90° out of phase with each other. In receive regime, all pin diodes are set on by a DC current bias of 100 mA. As a result, the 2 signals coming from the 2 ports flow now directly to 2 low noise preamplifiers. The outputs of the low noise amplifier are connected to the receive channels 1 and 3 of the scanner. They are then combined by the scanner software.

3.2.5 Experimental assessment

At first, we tested the coil in the single port regime in order to compare independently the contribution of each port with the simulated results. The coil is loaded by a phantom made of a sphere of agar gelatin (agar 3%m, NaCl 0.5%m, $NiCl_2$%m). The XFL sequence has been used for flip angle (FA) mapping [43]. The parameters of the used sequence are the following: TR/TE = 20000/1.44 ms, in plane pixel spacing of 4 mm and slice thickness of 8 mm, FOV of 256 mm by 256 mm by 176 mm, flip angle (FA) of 8°.

At first, two independent B_1^+ maps for the ports 1 and 2 have been measured [Fig. 3.18(d, e)] and compared to the simulated B_1^+ maps [Fig. 3.18(a, b)]. The measured FA maps (in degree) were converted to B_1^+ map (in Tesla) by dividing the FA map by several constants: 2π, proton frequency (42.576 MHz), saturation pulse duration (5010 μs), conversion factor for saturation SLR pulse (0.1049).

Subsequently, the CP mode has been retrieved in post-processing as: $|\sqrt{0.5}B_{11}^+ + i\sqrt{0.5}B_{12}^+|$, where B_{11}^+ is B_1^+ induced by port 1 and B_{12}^+ is B_1^+ induced by port 2 and $\sqrt{0.5}$ is a splitting coefficient. The simulated CP mode B_1^+ field is presented in Fig. 3.18(c), while the measured one is shown in Fig. 3.18(f). The B_1^+ field in the simulated maps [Fig. 3.18(a-c)] are nullified outside the phantom. While, the measured maps [Fig. 3.18(d-f)] are filtered by applying a mask based on FA amplitude maps with a threshold level of 25 and by a median filter (smoothing filter) with a 4 by 4 pixel window. A good agreement is observed between the simulated and experimental magnetic maps.

After analyzing each port independently, the T_x/R_x interface for circular polarization has been used in order to drive the developed coil in quadrature regime. To assess the efficiency
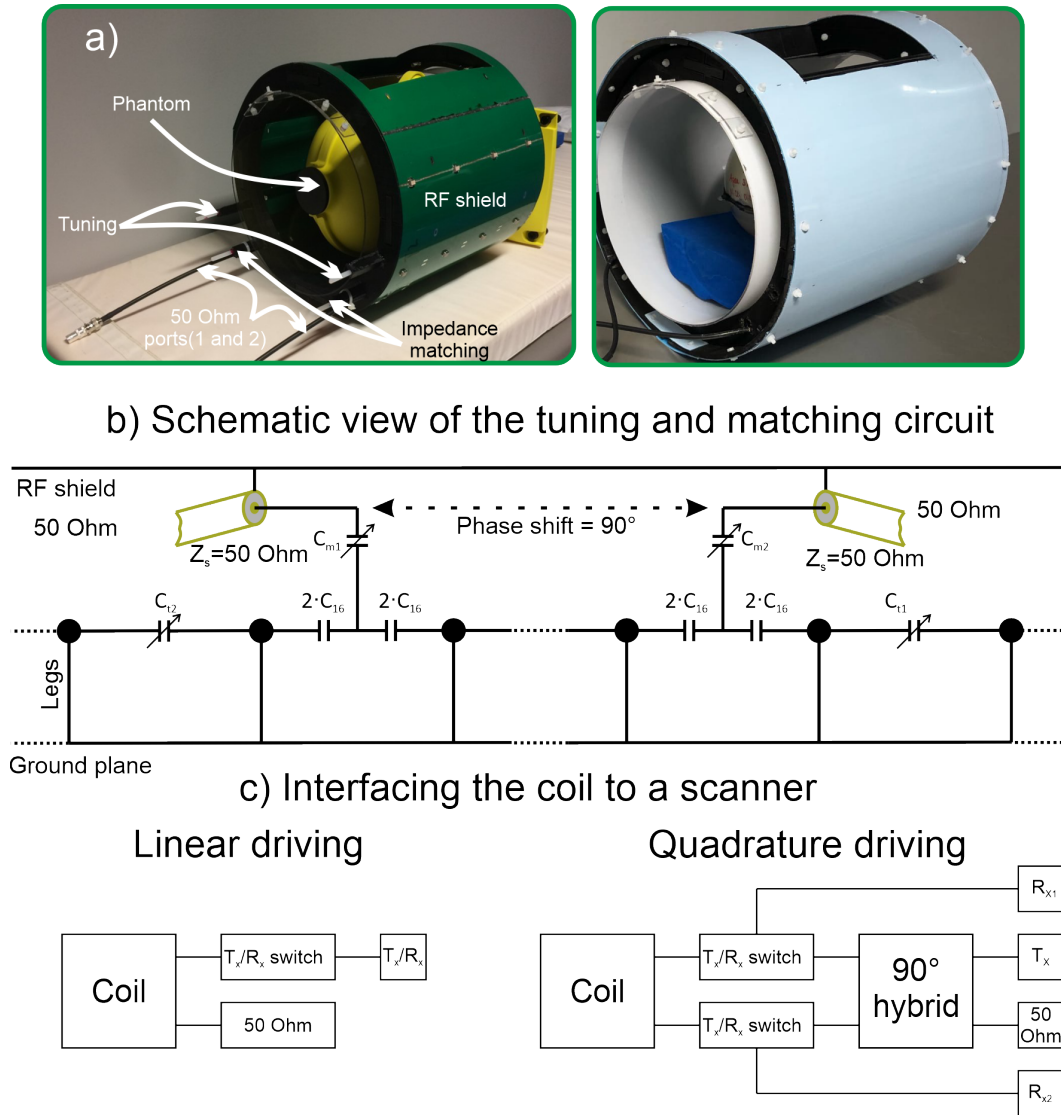
Figure 3.16 – **Photograph of the opencage coil (a). Sketch of the tuning and matching circuit (b). The two ways of interfacing the opencage to the scanner (c).**
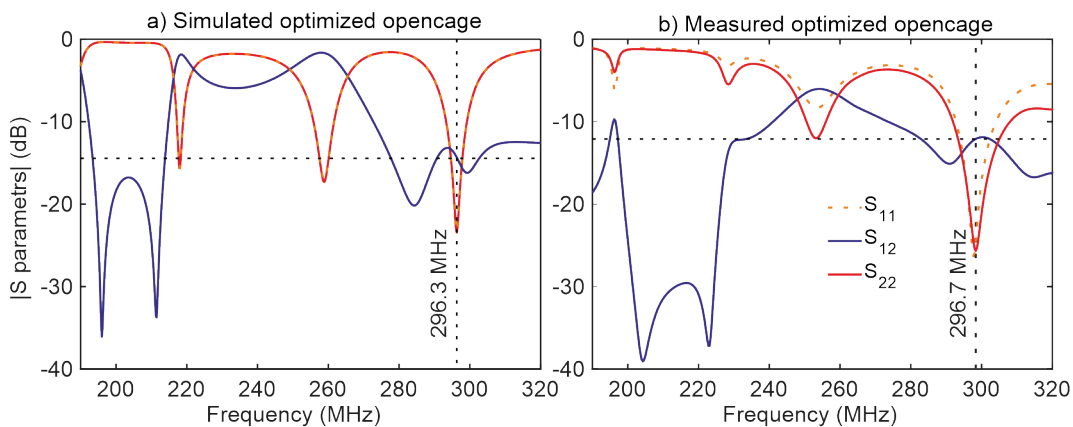
Figure 3.17 – **(a) Simulated and (b) measured S-parameters of the opencage coil.**

of the opencage coil, the same measurements have also been performed with a commercial birdcage coil (Invivo manufacturer) made of 16 rungs. The dimensions of the used birdcgae coil are comparable (radius of 140 mm and length of 200 mm) to the built opencage coil.
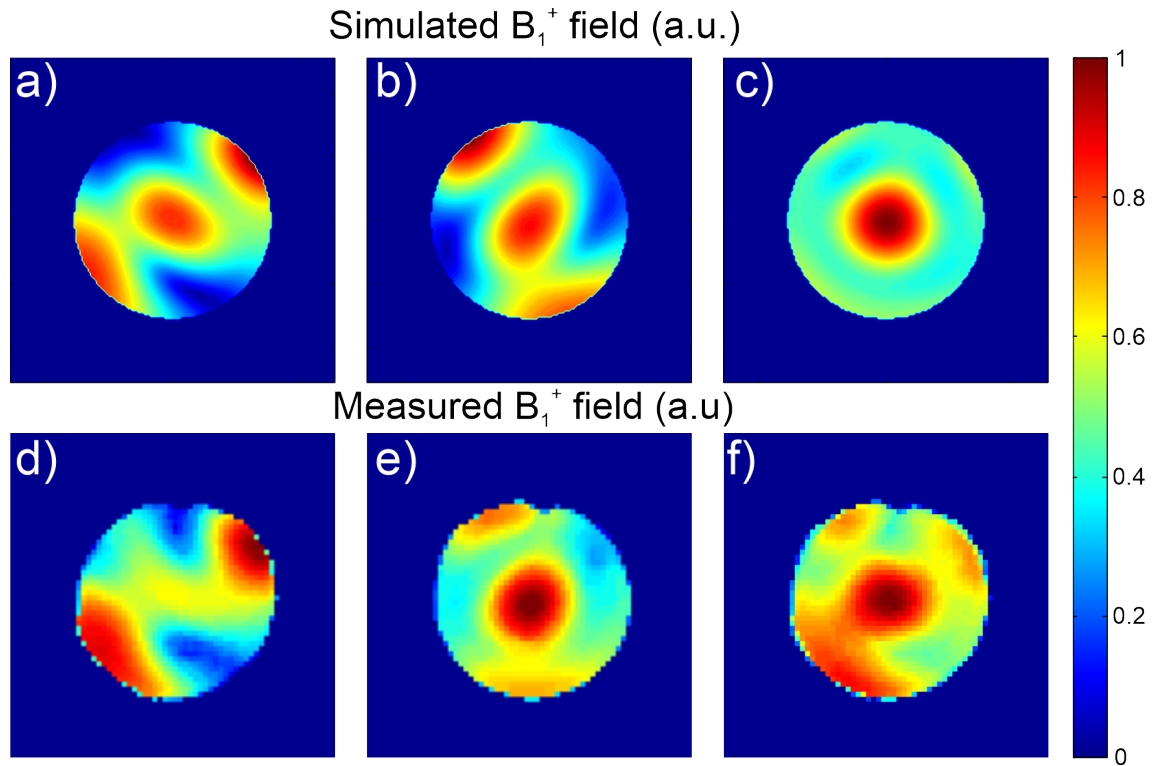
Figure 3.18 – **The B_1^+ maps in the central axial plane in a spherical phantom of 165 mm diameter. Simulated maps when port 1 is excited (a), port 2 is excited (b), combined CP mode (c). Experimental maps when port 1 was excited (d), port 2 was excited (e), combined CP mode (f).**

The resulting B_1^+ maps and reference voltage maps are presented in Fig. 3.19(a, b) and Fig. 3.19(c, d), respectively. The reference voltage maps show the voltage needed to obtain 500 μs rectangular 90° pulse (FA). As in the previous case, the XFL sequence has been employed for FA mapping [43]. The parameters of the used sequence are the following: TR/TE = 20000/3.06 ms, pixel in plane spacing of 4 mm and slice thickness of 8 mm, FOV of 256 mm by 256 mm by 168 mm, and FA of 7°.

The measured B_1^+ maps have been acquired with 212 V as reference voltage for the commercial coil and 174 V as reference voltage for the opencage coil. As it can be seen in Fig. 3.19(a, b), the birdcage coil demonstrated slightly higher transmit efficiency. Being normalized to reference voltage, the transmit efficiency of the birdcage equals 0.034 μT/V in the center of the maps, while for the opencage it equals 0.050 μT/V.

Moreover, the B_1^+ field homogeneity has been assessed for the opencage coil and compared to the reference birdcage coil. As a quantitative parameter, normalized root means square error (NRMSE) has been calculated for two coils. The NRMSE equals 0.63 for the birdcage coil and 0.71 for the opencage coil in the central sagittal slice. The estimated NRMSE for the entire phantom is 0.5665 for the birdcage coil and 0.6589 for the opencage coil. Such relatively high numbers for NRMSE could be explained by the choice of the reference image for homogeneity estimation. For that image, the absolutely homogeneous pattern of B_1^+ field has been chosen. Nevertheless, one can conclude that opencage shows a slightly worse (14%) homogeneity of B_1^+ in the entire phantom whereas higher transmit efficiency (32%) is observed compared to the conventional birdcage coil.
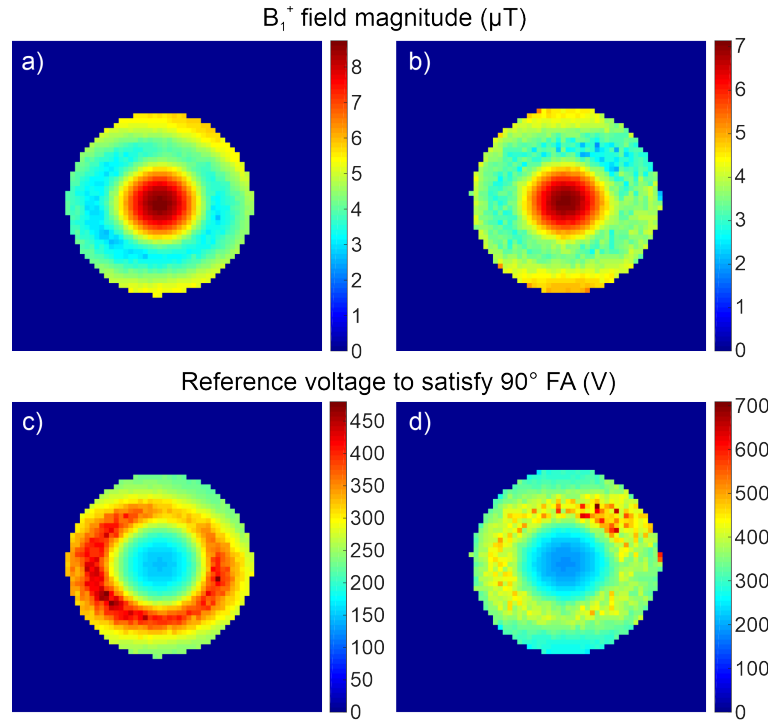
Figure 3.19 – (a, b) Measured B_1^+ field in the central sagittal slice for the opencage head coil and birdcage coil; (c, d) Measured reference voltage maps in the central sagittal slice required to satisfy 90° FA.

3.2.6   Phantom imaging

At first, two gradient echo images of spherical phantom have been obtained for the ports 1 and 2 independently. The following sequence parameters have been sets: TR/TE = 8.6/4 ms, pixel in plane spacing of 0.4883 mm, a FOV of 250 mm by 250 mm, a FA of 20° and 2 averages. Both images are shown in Fig. 3.20. As it can be seen, two images show comparable spatial distribution. Obviously, they are 90° flipped according to the feeding port position.
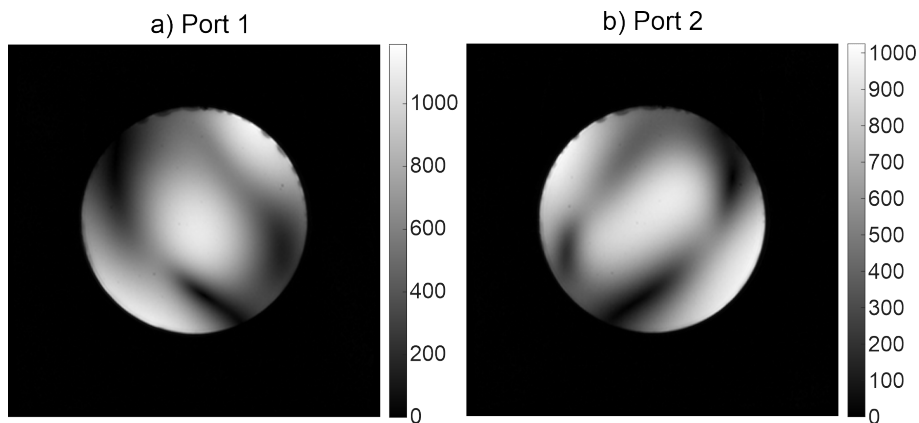
Figure 3.20 – Two gradient echo images (arbitrary units) of the spherical phantom obtained independently: (a) for Port 1; (b) for Port 2.

Eventually, images of the phantom have been acquired with the hybrid coupler interface using the same sequence (see Fig. 3.21(d-f)). They are compared to the one obtained with the commercial birdcage (see Fig. 3.21(a-c)). The measured images have been acquired with 212 V

as reference voltage for the birdcage coil and with 174 V as reference voltage for the opencage coil.
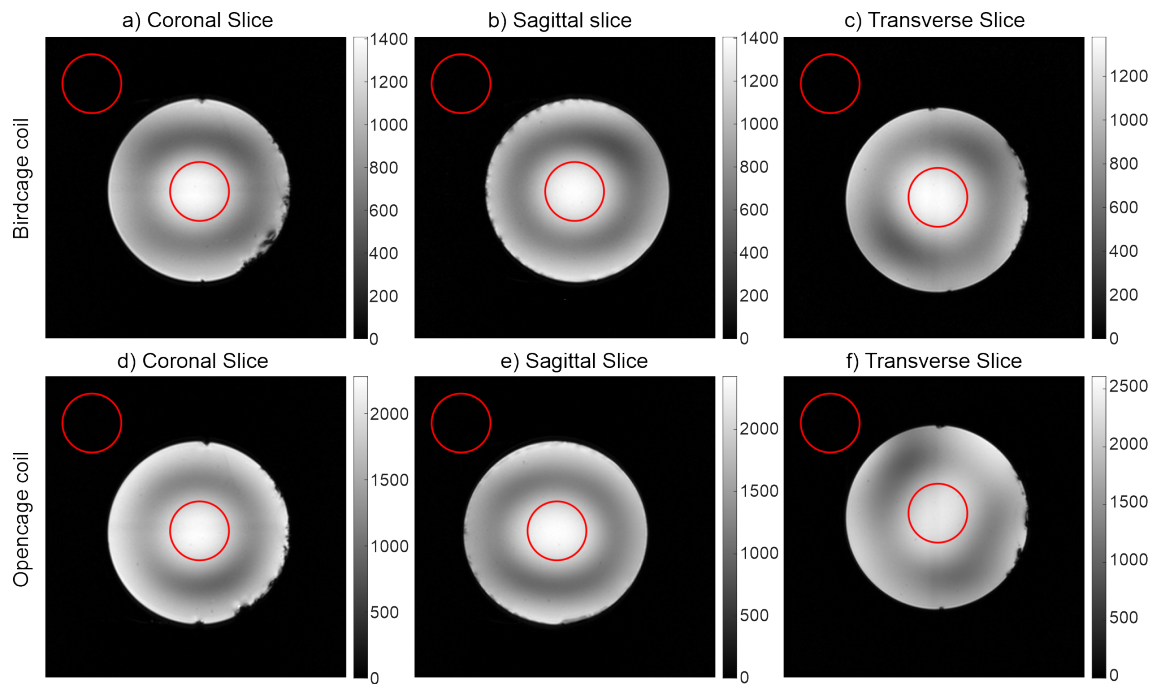
Figure 3.21 – (a-c) Images (a.u.) of the sphere phantom of the three central slices for the birdcage coil; (d-f) opencage coil. The red circles indicate the signal and noise ROI for calculations of average SNR.

As quantitative comparison of the obtained images [Fig. 3.21], the average SNR of the obtained images has been evaluated as the mean signal divided to the standard deviation of noise in the ROI. The average SNR for each image is shown in Tab. 3.3).

Table 3.3 – Average SNR of the opencage and birdcage coil in three slices.

Coil	Coronal slice	Sagittal slice	Transverse slice
Birdcage	240.4	229.3	198.1
Opencage	326.4	337.3	287.3

As it can be seen in the Tab. 3.3), the overall SNR of the images obtained with the opencage coil is approximately 43% better over that one acquired with the commercial birdcage coil. Such a huge increase in the SNR is reciprocal according to higher transmit efficiency, and can be explained by the slightly smaller size of the opencage coil compared to the conventional birdcage. Moreover, the use of two receive channels in opencage coil instead of receiving directly the CP mode could have positively affected the SNR as well.

3.2.7 In-vivo imaging

At last, three in-vivo images have been acquired for the birdcage and for the opencage coils. Here the proton density weighted gradient echo sequence has been used. The parameters of the used sequence are the following: TR/TE = 20000/3.06 ms, pixel in plane spacing of 2 mm, FOV of 256 mm by 256 mm, and FA of 3°. The measured images have been acquired with 255 V as reference voltage for the birdcage coil and with 203 V as reference voltage for the opencage coil. These images are shown in Fig. 3.22(a-c) for the birdcage coil, and in Fig. 3.22(d-f) for the opencage coil.

Eventually, we can conclude that opencage coil is also slightly better in terms of B_1 coverage compared to the birdcage coil. As it can be seen in the coronal slice [Fig. 3.22(a, d)] and the sagittal slice [Fig. 3.22(b, e)], opencage coil shows better coverage in the bottom part of the head. This can be explained by the slightly higher length of the built coil.
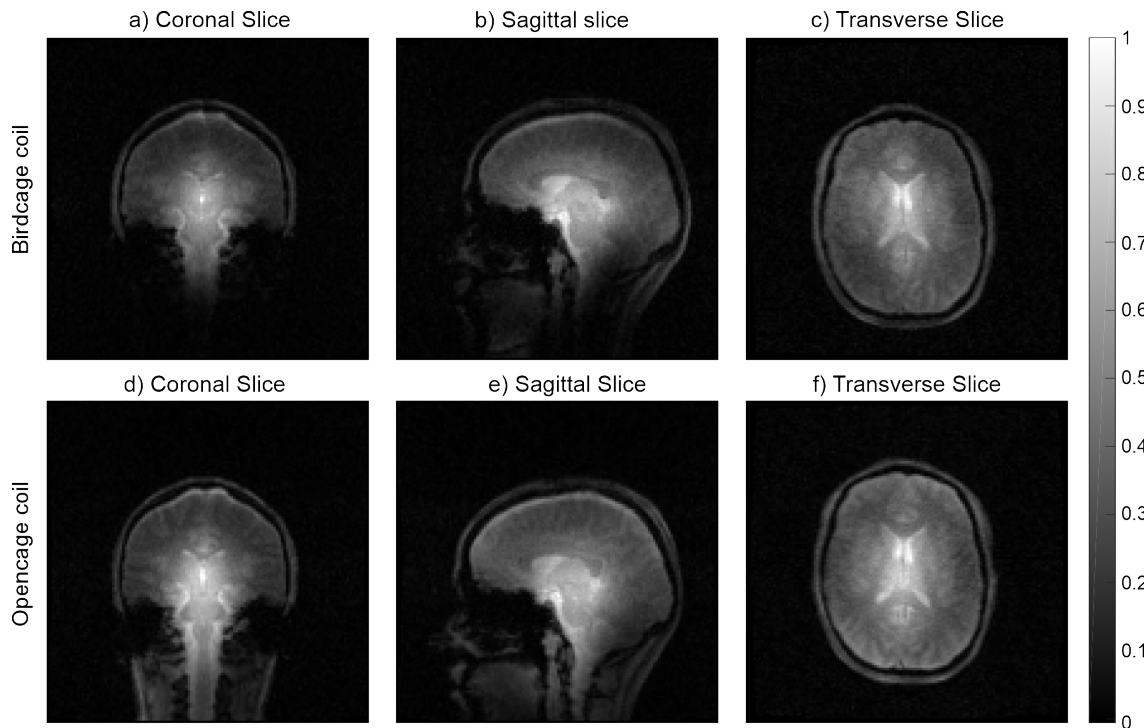
Figure 3.22 – (a-c) In-vivo images (a.u.) of the brain obtained in the three central slices for the birdcage coil; (d-f) opencage coil.

3.3 Conclusion

Eventually, in Chapter 3 we have proposed a new type of RF coil named opencage that facilitates the access to the region under study. In the first part of the chapter, a coil dedicated to imaging of small rodents working at 7 T has been presented. In the second part of the chapter, a larger coil working at 7T and optimized for imaging of human head has been developed. In both cases, the design of the proposed RF coil is based on Bloch impedance matching and the phase adjustment. The main parameters of the opencage coil have been determined analytically, tested numerically, and confirmed experimentally on bench and in MRI.

For the preclinical coil in-vitro and in-vivo images have been acquired. The opencage coil demonstrates substantially suitable signal homogeneity and sufficient FOV for MR imaging of small rodents at 7 T. The level of SNR obtained with the opencage coil is similar to one obtained with a conventional birdcage.

For the coil dedicated to head imaging, the prototype has been assembled and tested on a phantom in a clinical 7 T Siemens scanner. The opencage coil demonstrated a slightly worse homogeneity (14%) of B_1^+ field and higher (32%) transmit efficiency compared to a conventional birdcage coil. At the same time the SNR of the obtained images is 43% higher compared to the same images obtained with a birdcage coil.

The opencage head coil offers comfort for patients. In addition, the coil is especially suitable for motion correction at UHF Magnetic Resonance Imaging such as 7 T and some other applications. Moreover, as it was stated, the common setup in the 7T MRI is a combination of a birdcage coil for transmit and embedded phased array coil for receive. To that end, the next step is to develop a larger detunable opencage coil for transmit only and combine it with a receive phased array coil.

CHAPTER 4

Dual-band volume RF coils

Table of contents

Magnetic resonance of proton ^{1}H leads to anatomical images. Complementary information can be obtained by probing other nuclei [164] (X-nuclei). It exists a plurality of different biological applications such as tracking of injected cells into a body or detection and quantification of immune cell therapy for cancer using fluorine ^{19}F [46], [47]; studying tissue metabolism by phosphorus ^{31}P associated with many disorders and diseases [48]; elucidating the effects of sodium disequilibrium in multiple sclerosis pathology using sodium ^{23}Na imaging [7]; imaging breast cancer using hyperpolarized carbon ^{13}C [49], mapping of metabolism with deuterium ^{2}H [50].

Typically, all stated above applications require an elaborate RF coil working simultaneously at two Larmor frequencies corresponding to proton and another chosen X-nuclei. Actually, the Larmor frequency of proton is the largest one among other nuclei having half integer spin (except tritium ^{3}H). In terms of RF engineering, the coil should operate at two frequency bands, and moreover, these bands should be independently controllable. Several designs of volume coils have been earlier proposed in literature [165], [91], [92], [93], [94], [166], [167], [168]. However, a universal design of a probe compatible with any application depending on the chosen nuclei does not exist. Therefore, each application needs a specific design.

In this chapter, we present two designs of dual-band coils for UHF MRI and MRS. In the first section of the chapter, we describe a volume coil devoted to preclinical imaging of small animals working at the Larmor frequency of ^{19}F and ^{1}H . This coil is initially inspired by hybridized wire arrays investigated in [132] and [136], while here we expand this approach to the volume coil. In the second section, we reveal a dual-band opencage coil based on second order filter [92] designed for human head imaging by two nuclei (^{13}C and ^{1}H) at 7T.

4.1 Dual-band nested coil for ^{19}F$/^1$H preclinical imaging at 7 Tesla

In this first section we propose an original design of transmit/receive dual-band volume coil for fluorine ^{19}F and proton ^{1}H imaging. As it was mentioned previously, ^{19}F can be used as a component of several contrast agents [46] allowing accurate monitoring and tracking of injected cells into a body. The ^{1}H is used for anatomical imaging. It helps to localize the migration of injected fluorine that contains ^{19}F nucleus. One of the main difficulties in coil design is the proximity of the Larmor frequencies of proton (300.1 MHz) and fluorine (282.6 MHz). For instance, design of second order filter [92] is not feasible in this case.

One idea that can be interesting for the investigation, is the concept of hybridized resonators, which are flexible in terms of applications because their resonant frequencies can be adjusted over a large frequency range. Recently it has been shown that hybridized resonators can improve field homogeneity of B$_1^+$ and SNR for single-nuclei preclinical imaging at 7 T [129]. Later, it has been proposed to excite two different modes of two hybridized wire structures with

an electrically small loop antenna connected to a MRI scanner only with one feeding channel (^{1}H/^{19}F) [132]. A similar coil has been proposed later for 4.7 T preclinical imaging (^{1}H) and spectroscopy (^{31}P) [136].

As an improvement of these ideas stated above in this contribution, we propose to design a volume transmit/receive RF coil based on the combination of two geometrically and electrically independent structures that may be used simultaneously for ^{1}H/^{19}F imaging of small rodents at 7 Tesla. The proposed dual-band coil can be independently tuned at the two desired Larmor frequencies by adjusting the length of two sets of periodic telescopic wires located on cylindrical surfaces surrounding a scanned subject. While the impedance matching can be provided conventionally by trim capacitors.

4.1.1 Design of the proposed coil

The considered coil consists of two concentric structures. In each of them, the unit cells are distributed periodically forming a cylinder like in a birdcage coil (Fig. 4.1).
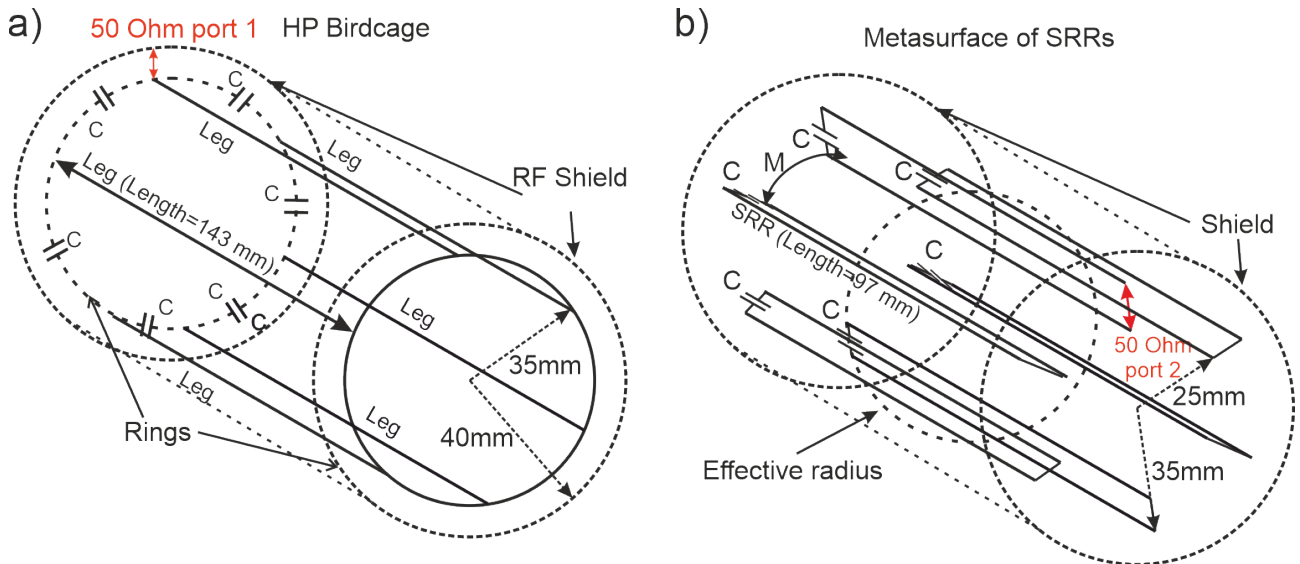
Figure 4.1 – **(a) Schematic of a HP birdcage coil, (b) schematic view of metasurface composed of coupled split-loop resonators SLRs.**

The first structure behaves as a left-handed transmission line (LHTL), which is suitable for UHF imaging. This structure is the high pass (HP) birdcage coil invented by Cecil Hayes in 1985 [80] and can easily be calculated as shown in [104]. The conventional birdcage is very convenient for single-nucleus imaging because its fundamental mode provides homogeneous magnetic field inside a whole sample. For the chosen HP birdcage coil, the fundamental or $k = 1$ mode is the highest one in the spectra. In this work, we propose to use the birdcage coil [Fig. 4.1(a)] for fluorine imaging. The used structure contains six legs that are separated by 60° and are 40 mm-distance from the center. Each leg consists of two sliding brass tubes of different diameters. The external diameter of the first one is 1.5 mm and 2 mm for the second one. On the one side, the conductors are interconnected by distributed planar capacitors formed between two stripes etched on PCB [169] and are short circuited to each other at the opposite end. The capacitors are etched on low-loss dielectric substrate Rogers 4003 ($\varepsilon_r = 3.38$ and $\delta = 0.0021$) with thickness 0.508 mm.

The second structure of the coil that is responsible for proton imaging at 300.1 MHz consists of an array of six split-loop resonators (SLRs) distributed along a circle of 30 mm radius. Sketch of the structure is shown in Fig. 4.1(b). The coupling between such SLRs has been studied previously in [170], [171]. The relative orientation between the SLRs changes the mutual inductance between them. It is positive when the SLRs are parallel and negative if coplanar [170]. Hence, this structure behaves differently depending on the relative positions of the SLRs. The behavior is LHTL-like when the SLRs are coplanar or RHTL-like when they are coaxial [170]. In our case the behavior of the SLRs is RHTL, therefore, the SLRs the fundamental mode that generates the homogenous magnetic field, which is located at the lowest frequency among plurality of modes in the spectra.

Finally, the dimensions of both structures are chosen in order to be compatible with full-body small animal imaging. The shape of the SLRs is rectangular with dimensions of 97 mm by 10 mm. As for the birdcage, the SLRs are telescopic. The geometry of the birdcage and the metasurface of SLRs are adjusted in numerical investigation to which the next section is devoted.

4.1.2   Numerical simulations of separated structures

At first, we numerically tested the two separated geometries composing the dual-band coil. The numerical simulations are performed using commercial software CST Microwave Suite 2018 (Frequency domain solver). In the conducted simulations, both structures are shielded by a cylindrical copper screen of 80-mm diameter. The 50-Ohm feeding of the birdcage is connected between one leg and the shield (Port 1). To excite the array of SLRs, we use another 50 Ohm port connected in a gap of one SLRs (Port 2).

Then, both structures have been adjusted to work at the desired Larmor frequencies of fluorine and proton at 7 Tesla (282.6/300.1 MHz) by adjusting the length of the telescopic wires and the overlapping of the etched capacitors. Eventually, the adjusted lengths equal to 143 mm for the birdcage and 97 mm for the SLRs (Fig. 4.1).

Then, the structures have been loaded by a cylindrical homogeneous phantom made of 60% 2-2-trifluoroethanol and 40% water ($\varepsilon_r = 39$ and $\sigma = 0.06$). Its radius and length are equal to 12.5 mm and 75 mm, respectively. Eventually, simulated S-parameters and magnetic field patterns are presented in Fig. 4.2. As it was expected, the last mode for the birdcage and the first mode of metasurface of SLRs provide homogeneous magnetic field polarized in the transverse plane (Fig. 4.3). In addition, as it can be seen in Fig. 4.3 the observed fields are orthogonal.

4.1.3   Investigation of the combined structure

Thereafter, both metasurfaces have been combined in one coil working simultaneously at the two frequencies. The combined setup is shown in Fig. 4.4. Here, the metasurface of SLR is the closest to the external surface of the phantom, meantime the radius of the birdcage equal to the outer radius of the metasurface of SLRs. Dimensions of the coil is limited by the RF shield that cannot exceed 90 mm due to the size of the MRI bore. Moreover, decreasing of the birdcage radius increases mutual coupling between two structures. As a result of this increase,
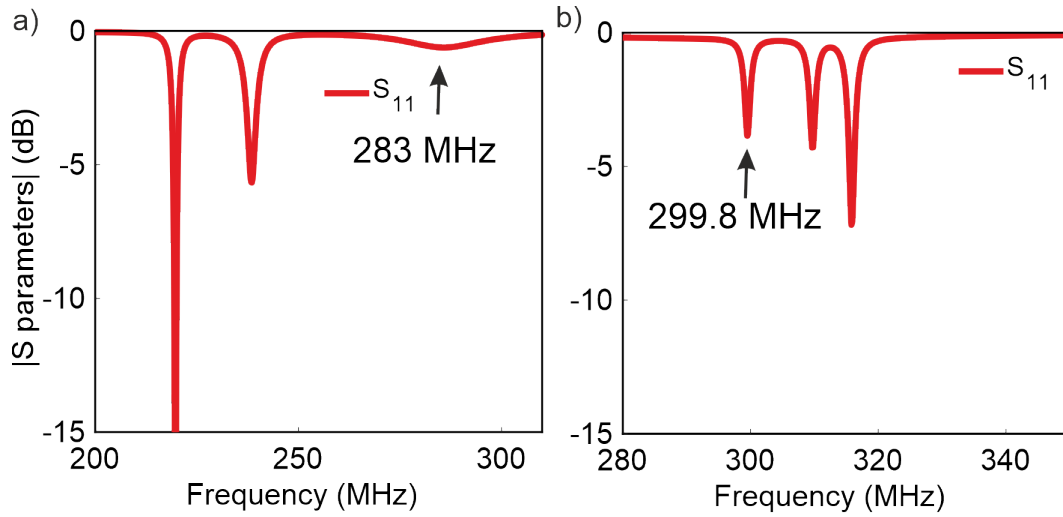
Figure 4.2 – $|S_{11}|$ **(reflection coefficient) of the simulated structures loaded by the cylindrical phantom: (a) HP birdcage; (b) the metasurface of SLRs.**
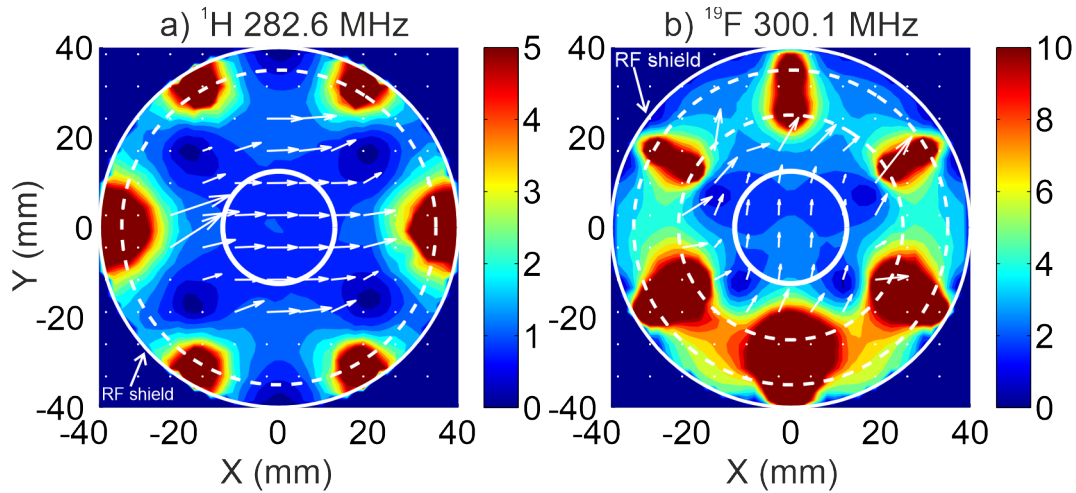
Figure 4.3 – **Amplitude of the magnetic field inside the coil in central transverse plane (Z = 0): (a) mode of the HP birdcage at 282.6 MHz; (b) mode of the metasurface of SLRs at 300.1 MHz.**

frequency tuning of the coil may be difficult to achieve. Therefore, radius of the birdcage is fixed to 40 mm. Finally, the setup including the RF shield and the phantom has not been changed compared to the uncombined structures. The dimensions of the combined coil coincide with the ones of the two independently optimized single-tuned structures (Fig. 4.1).

As for the independent structures, the combined one is investigated in full-wave simulations. First, an investigation of the S - parameters with respect to the length of the telescopic wires of the birdcage and the SLRs is shown in Fig. 4.5. Initial S - parameters of the coil (i.e. initial length of telescopic wires) are presented in Fig. 4.5(a). When the length of the metasurface of SRRs is modified, mainly S_{22} is affected [Fig. 4.5(b)]. Here, changing of S_{11} is negligible (0.1 MHz). Second when only the length of the birdcage is modified [Fig. 4.5(c)], mainly S_{11} is affected, while S_{22} shift is negligible (0.3 MHz). Both parts of the combined coil seem not to be sensitive to each other. The slight variation of the resonant frequencies may be compensated by changing the telescopic wires' length.

Eventually, the dual-tuned coil was adjusted for the two desired Larmor frequencies of ^{1}H
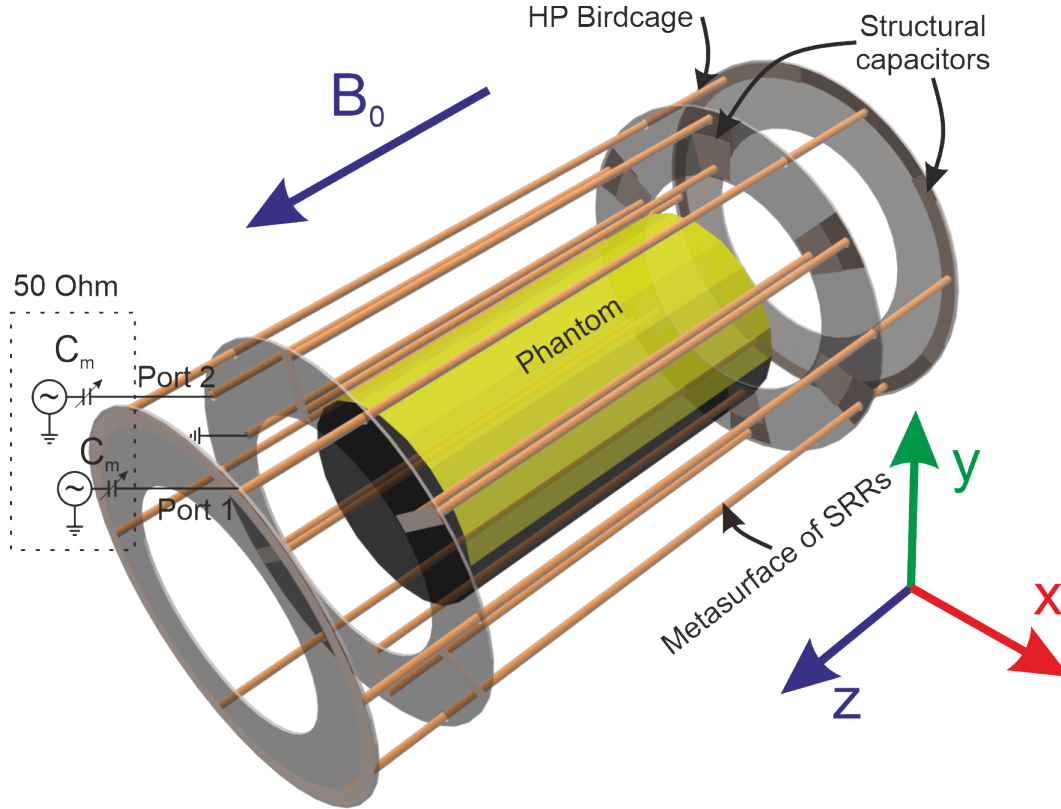
Figure 4.4 – **General view of the nested dual-tuned coil loaded by the phantom. Shield is hidden. Port 1 is in between the leg of the birdcage coil and the shield. Port 2 is in the gap of one SLR.**

and ^{19}F at 7T, i.e. 300.1 MHz and 282.6 MHz.
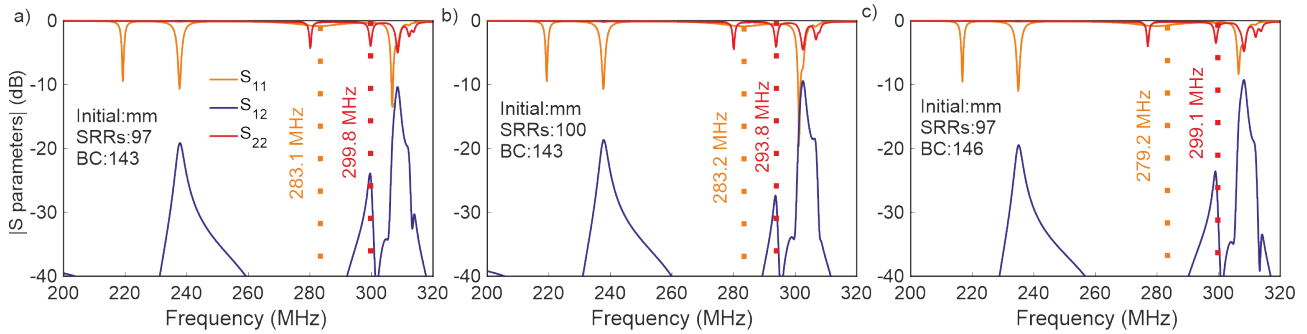
Figure 4.5 – **(a) S-parameters of the combined dual-tuned coil loaded by the phantom (initial S-parameters of the dual-tuned coil); (b) length of the metasurface of SLRs is changed; (c) length of the HP birdcage is changed.**

Finally, in order to analyze efficiency of the coil, we calculated B_1^+ (clockwise circularly polarized) magnetic field distribution and plotted it inside the ROI (phantom). In this case, the coil is matched by capacitors and tuned at desired frequencies by length adjustment. Ohmic losses (ESR) in these matching capacitors are deduced from the quality factor of commercially available capacitors which is typically equal to 1000 at the operating frequency.

As a result, the simulated reflection coefficients $|S_{11}|$ and $|S_{22}|$ are smaller than -10 dB. The level of transmission coefficient between the two ports ($|S_{12}|$ coefficient) equal to -15dB.

Finally, the calculated B_1^+ field patterns inside the phantom are presented in Fig. 4.6(a) for the birdcage and in Fig. 4.6(b) for SLRs. For fluorine (282.6 MHz) suitable spatial homogeneity of B_1^+ field inside the region of interest is observed (the HP birdcage). Indeed, the relative standard deviation (SD) of the field equals 2.1% for a mean value of 2.19 μT. At 300.1 MHz, the B_1^+ field is less homogenous compared to the one provided by the birdcage coil. Indeed the relative SD equals 13% for a mean value of 1.53 μT. This heterogeneity of the field can be explained by the interaction between the two structures and by the closeness of the phantom to the SLRs.
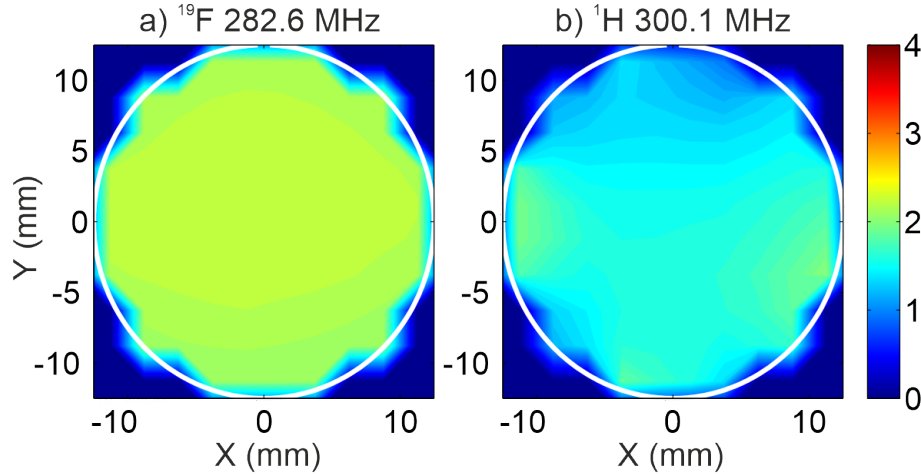
Figure 4.6 – Magnitude of B_1^+ at Z = 0 inside the ROI (phantom): (a) HP birdcage; (b) the metasurface of SRRs.

4.1.4 Experimental validation

In the end, the coil has been assembled, and then tested on-bench and in a MRI. The frame of the coil was 3d printed, and then used for attaching the telescopic wires at the proper positions. At first, we show the measured S-parameters on Fig. 4.7. All curves are shown for the coil loaded by the phantom (60% 2-2-trifluoroethanol and 40% water) containing both nuclei. The input impedance of the coil is matched simultaneously at both frequencies with reflection coefficients ($|S_{11,22}|$) below than -10 dB. The matching circuit is realized as shown in Fig. 4.4. In addition, transmission coefficient ($|S_{12}|$) between two structures is acceptable (around -10 dB).

After optimizing the input impedance, we put the coil inside the bore of a 7T Bruker PhrmaScan machine, and connected it to the scanner through BNC plug. Several imagining series with the phantom are performed (Fig. 4.8). For fluorine imaging, the spin echo sequence is employed (TR/TE = 3000/20.7547 ms, an anisotropic voxel of 0.2734 mm^2, slice spacing 2 mm, an FOV of 35 mm by 35 mm by 10 mm, the number of averages of 10, and the FA of 90°). For proton imaging, the same type of sequence is used, while parameters are different: TR/TE = 3000/18.2320 ms, an anisotropic voxel of 0.5469 mm^2, slice spacing 2 mm, an FOV of 35 mm by 35 mm by 10 mm, the number of averages of 10, and the FA of 90°.

For the birdcage part, which is responsible for fluorine, the obtained image demonstrated appropriate spatial homogeneity [Fig. 4.8(a)]. However, the proton image provides unsatisfactory
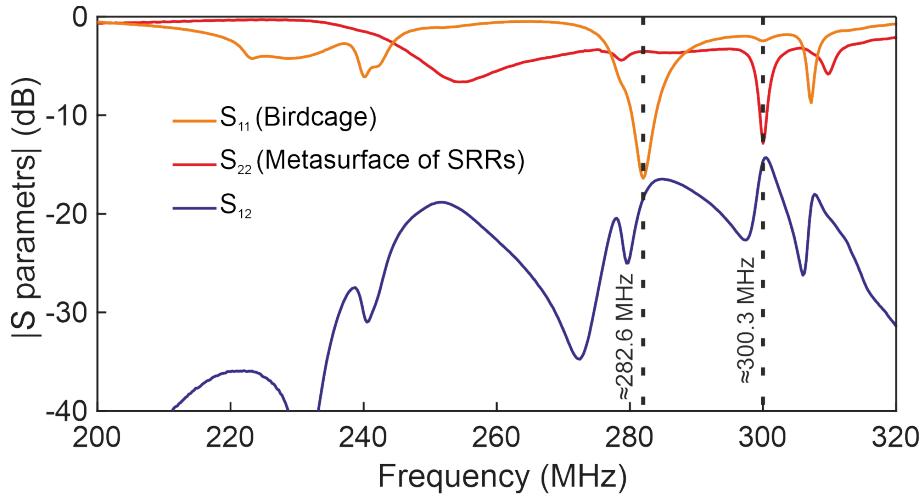
Figure 4.7 – S-parameters of the combined structure measured on bench.
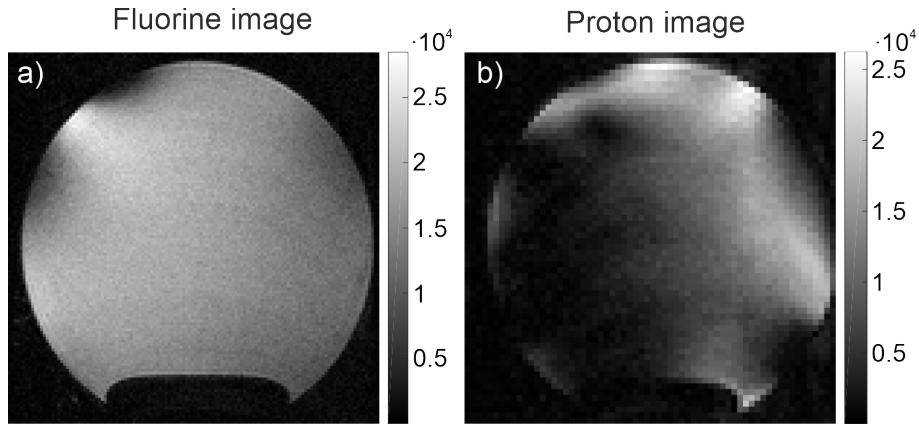
Figure 4.8 – S-parameters of the combined structure measured on bench.

performances [Fig. 4.8(b)]. Although, in the numerical study both structures are not much sensitive to each other, in the experiment, coupling between them seems to become dramatically high. Hence, frequency tuning of the metasurface of SRRs structure is sensitive to any manipulations with the birdcage coil, and the proper field distribution at the proton frequency is missed.

As a result, the concept of telescopic wires is found complicated to realize at such a high frequency as 300 MHz, which requires very stable contact between sliding conductors. Moreover, etched capacitors are not convenient to handle due to their inability to be changed in order to adjust the resonant frequency precisely once the structure was assembled. In contrast lumped capacitors can be more easily mounted.

4.2   Dual-band opencage coil

Here, we propose a new concept of a dual-band opencage coil based on the transfer matrix approach proposed in Chapter 2. In contrast to the previous section (^{19}F/^{1}H), we focus our attention on two nuclei with very different Larmor frequencies (^{13}C/^{1}H). In this case, we propose to design the unit cell as a band-stop (BS) or band-pass (BP) filter, which can be used for dual-band birdcages as described in [15].

Thus, the approach described in Chapter 2 is improved and adapted for dual frequency bands birdcage coils. In addition to the theory, we present a simulation of non-optimized and optimized dual-band opencage coil working simultaneously at 74.6 MHz and 297.2 MHz. These frequencies correspond to Larmor frequencies of carbon ^{13}C and proton ^{1}H at 7 T, respectively. However, the proposed approach is suitable for many pairs of nuclei having large frequency differences, for instance ^{23}Na/1H, ^{31}P/1H and others.

4.2.1 Theory of dual-band opencage coil

Generally, this method described in [92], is known as a second order filter or trap circuit [71]. This method consists in providing a new resonance in a resonance system by inserting another LC circuit into an initial circuit as shown in Fig. 4.9. Here, an additional lumped inductance could be either added in parallel to C_2 or in parallel to C_1. The new equivalent circuits presented in Fig. 4.9(a) and Fig. 4.9(b) correspond to a band-pass (BP) and a band-stop (BS) 2d order filter, respectively. This inserted lumped inductance is called trap inductance.

A coil composed of such unit cells retains the same general view as in Fig. 3.10 of Chapter 3.2 (8 rungs in the bottom and 2 in the top) but now 2 modes can be independently controllable in terms of phase shift. However, the model of a unit cell should be improved in order to fully
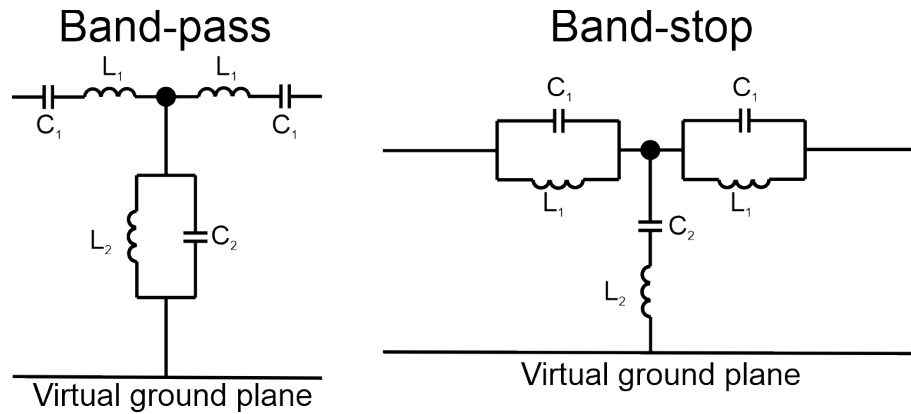
Figure 4.9 – Unit cell of BP and BS dual-band birdcages.

describe the geometry of a birdcage coil. Indeed, another inductance has to be added in series to the leg in the case of BS or to the end-ring in the case of BP. This inductance corresponds to the end-ring and the leg effective inductances. Eventually, the improved unit cell model is illustrated in the Fig. 4.10.

Here, the same transfer matrix (2.16) from Chapter 2 has been used. However, the expressions of impedance Z_i and admittance Y_i for the BP are changed to:

$$Z_i = \frac{1}{i\omega C_{r,i}} + i\omega L_{r,i},$$

$$Y_i = \frac{1}{Z_i'},$$

(4.1)

$$Z_i' = 2i\omega L_{i,l} + \frac{2i\omega L_{tr,i}}{1 - \omega^2 C_{l,i} L_{tr,i}}.$$

Band-pass   Band-stop
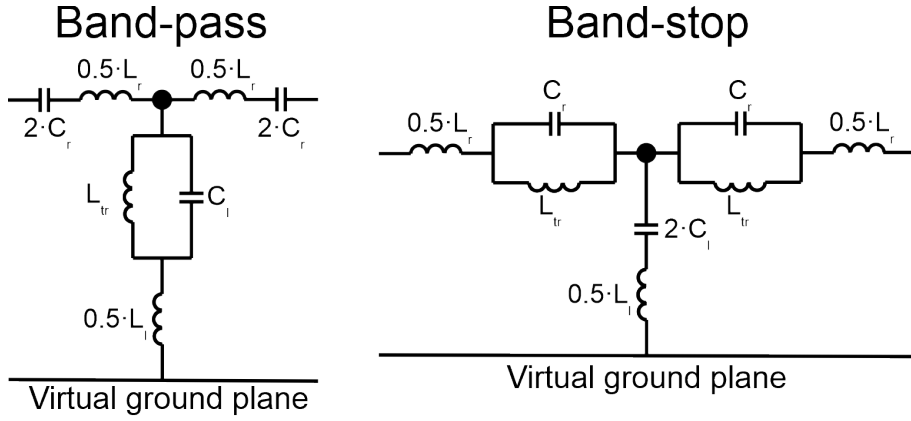
Figure 4.10 – Improved unit cell model of BP and BS dual-band birdcages that considers the effective inductance of the leg and ring.

where $L_{l,i}$, and $L_{r,i}$ are the effective inductance of the leg and the end-ring segment, respectively of the i-th unit cell (rung) and ω is the angular frequency. The inductance $L_{tr,i}$ is the trap lumped inductance of the leg. The capacitances $C_{r,i}$ and $C_{l,i}$ are ring and leg capacitances respectively. Finally, in the next section the phase shift and the Bloch impedance of the coil will be evaluated in the case of a head coil.

4.2.2   Head opencage coil for $^{13}\mathrm{C}/^{1}\mathrm{H}$ at 7 Tesla

As in the previous example of first order filter (Chapter 3), here, the geometry of the coil has been chosen to be compatible with head imaging (length of 240 mm, width of rings and legs of 10 mm, radius of 130 mm and radius of the shield of 155 mm). The same effective inductances of legs and end-rings have been calculated. Their values are reminded in Tab. 4.1.

Similarly, to the previous subchapter, the dispersion diagrams and impedance diagrams can be computed according to equations (2.19) and 2.22) respectively. Nevertheless, here we performed the calculations for the two types of dual-band birdcages composed of 4 and 16 rungs corresponding to 90° and 22.5° cells respectively. Eventually, the values of lumped legs and rings capacitances, lumped trap inductance has been adjusted in order to provide 22.5° of phase shift in case of 16 rungs and 90° in case of 4 rungs dual-band birdcage coils at both frequencies (Tab. 4.1). These frequencies are chosen for carbon $^{13}\mathrm{C}$ (74.7 MHz) and proton $^{1}\mathrm{H}$ (297.2 MHz) imaging at 7 T.

We can observe that the BS design requires ring capacitances that are very small and therefore the opencage would be sensitive to parasitic capacitance effects. Consequently, we chose the BP design. The obtained dispersion and impedance diagrams are presented in Fig. 4.11(a, b), in which we can observe two frequency spans. The advantage of such a design is the possibility to independently tune the high and low frequency slopes. Capacitance C_r modifies the low-frequency slope, while C_l changes the high-frequency one.

As it can be seen, the phases are adjusted for both types of unit cells (90° and 22.5°) at two frequencies (74.6 MHz and 297.2 MHz). While, at the same frequencies the impedances are dramatically different as shown in Fig. 4.11(b). Thereby, as in the previous case of the single frequency band opencage (Chapter 3), to adjust both impedances and phases it is necessary to

Table 4.1 – Parameters of the different BP and BS rungs (unit cell) types tuned to the desired frequencies.

Cell type	L_r (nH)	L_l (nH)	L_{tr} (nH)	C_r (pF)	C_l (pF)
Band-pass					
90° cells (as for 4 rungs)	149	132.6	150	6	3.47
22.5° cells (as for 16 rungs)	42.09	173.97	150	48	2.62
Band-stop					
90° cells (as for 4 rungs)	149	132.6	300	1	34
22.5° cells (as for 16 rungs)	42.09	173.97	800	1	7.5
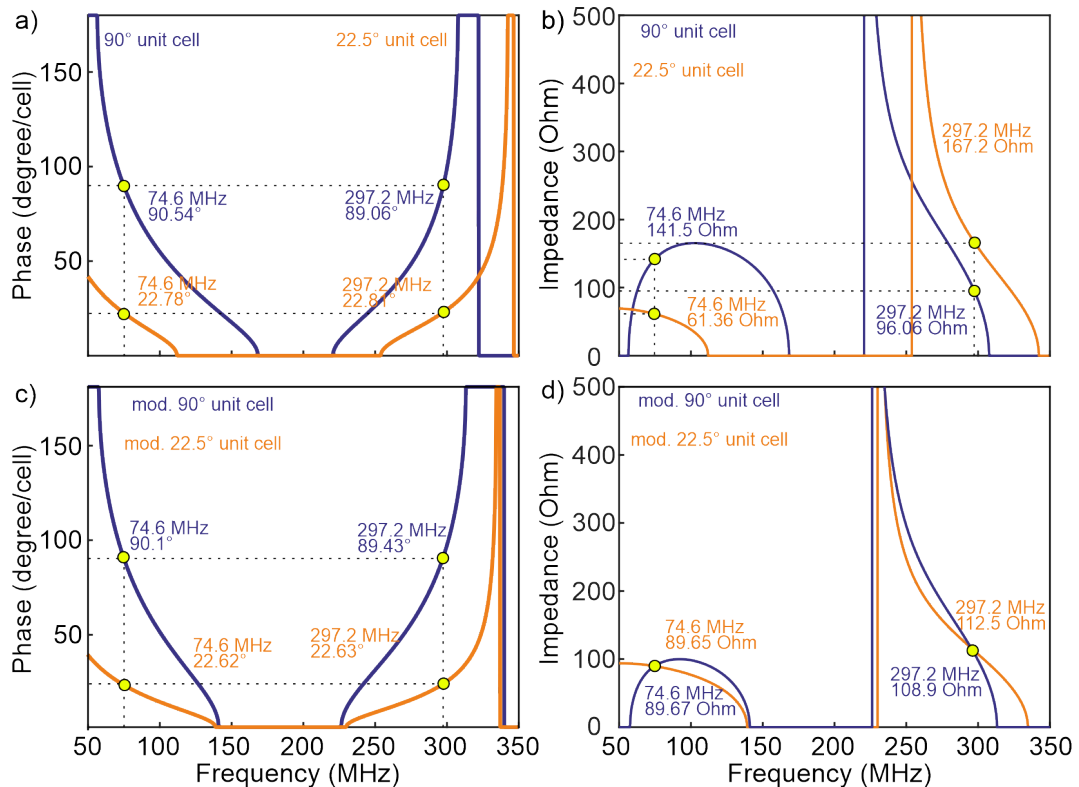
Figure 4.11 – (a, c) Dispersion diagram plotted for two types of BP unit cells corresponding to 16 and 4 rungs birdcages and modified 16 and 4 rungs birdcages. (b, d) Impedance diagram plotted for two types of BP unit cells corresponding to 16 and 4 rungs birdcages and modified 16 and 4 rungs birdcages.

thoroughly modify the parameters of each unit cell. However, in this case the problem becomes more complicated because of two frequency bands.

We need to optimize the capacitances (C_r and C_l), lumped trap inductance (L_{tr}) and leg effective inductance (L_l) to achieve the required phase and Bloch impedance expressed by equations (2.19) and (2.22). However, contrary to the single band opencage coil, explicit expressions for inductance and capacitance does not exist. Therefore, we solve the equations (2.19) and (2.22) using a numerical optimization algorithm.

To that end, we choose the gradient descent method, which is easy and convenient to handle. However, it has certain limitations. For example, the algorithm may converge toward non feasible values of inductance and capacitance. Therefore, to prevent this undesirable result, we use the constrained optimization algorithm where the upper and lower limits are set to each optimizing parameter.

Another issue arises when impedances of two cells branches are far from each other. This case requires dramatic changes in a unit cell, which are sometimes not possible to achieve. Consequently, contrary to the previous case of single frequency, wherein only 90° cells are modified in order to match with 22.5° cells, in this study, both cells are modified. The result of the optimization algorithm is shown in Tab. 4.2.

Table 4.2 – Optimized inductances and capacitances of different BP rungs (unit-cell) in order to match the impedances and the phase shifts at 74.6MHz and 297.2 MHz.

Cell type	L_r (nH)	L_l (nH)	L_{tr} (nH)	C_r (pF)	C_l (pF)
90° cells (as for 4 rungs)	149	79.4	99.7	8.55	4.96
22.5° cells (as for 16 rungs)	30.9	217.9	250	42.4	1.91

Eventually, the final Bloch impedance and phase diagram with respect to frequency are plotted in Fig. 4.11(b, d). Now, it can be clearly seen that at both frequencies the impedances and phases are matched. Modified values of inductances correspond to new widths of legs (w_l) and end-rings segments which are the following: width of leg and end-ring for 90° cells are 30.3 and 10 mm,respectively; 4 and 30 mm for the 22.5° unit cells.

As a conclusion of the section, the optimization has been performed, and the parameters of the coil have been computed. Hence the proposed concept can be studied numerically in full-wave simulations, which is shown in the next section.

4.2.3　Numerical investigation

The designed coil has been numerically tested with FEM-based software (CST Studio Suite). General view of the coil, excited in quadrature by two 90° distant 50-Ohm ports is shown in Fig. 4.12. The coil is shielded by the metal screen with a gap in front of 90° cell to coincide with the opening in the coil. The transverse width of that gap is 150 mm. Other geometrical parameters of the coil are shown in the caption of Fig. 4.12.
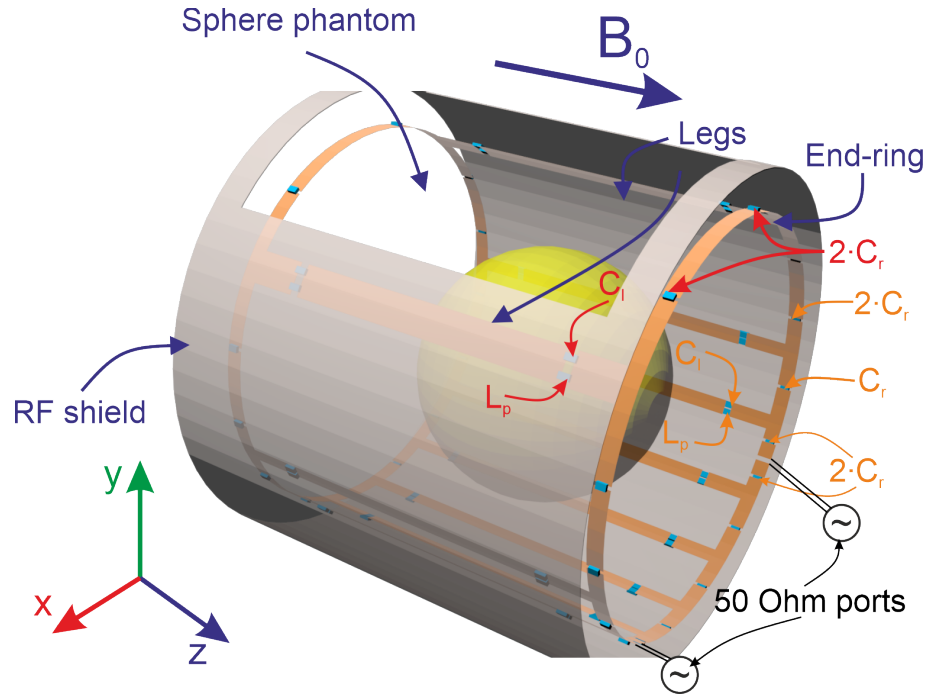
Figure 4.12 – General view of the simulated dual-band opencage coil loaded by a sphere phantom of 80 mm. The radius of the coil and shield is 130 mm and 150 mm. Their length is 240 mm and 300 mm. Width of the strips in the top and in the bottom are 20 and 4 mm respectively. End-ring width is 15 mm.

In the conducted investigations, the coil was loaded by a sphere phantom (ε_r=75, σ=1.8 S/m) with a radius of 80 mm. The phantom is placed in the center of the coil. Based on the value presented in the previous section, the parameters of the coil are adjusted manually to achieve a high isolation between the feeding ports at the operating frequencies. The final optimized parameters are shown in Tab. 4.3. Thus, the widths of the bottom and top legs became 4 mm and 20 mm, respectively. Both end-rings are now 10 mm wide. In addition, the capacitances are corrected to tune the coil slightly below the frequencies of interest, in order to compensate the impact of MRI scanner bore in future experiments.

Table 4.3 – Optimized in full-wave simulation parameters of different BP rungs (unit-cell) types. Here, the widths (w) correspond to the ring and legs inductances.

Cell type	w_r (mm)	w_l (mm)	L_{tr} (nH)	C_r (pF)	C_l (pF)
90° cells (as for 4 rungs)	15	20	90	10	3.4
22.5° cells (as for 16 rungs)	15	4	220	50	1.3

The final simulated S-parameters of the optimized coil are presented in Fig. 4.13(b). At the same time, this optimized coil has been compared to a non-optimized one, wherein only the phases are adjusted. For comparison purposes, the non-optimized case is presented in Fig. 4.13(a).
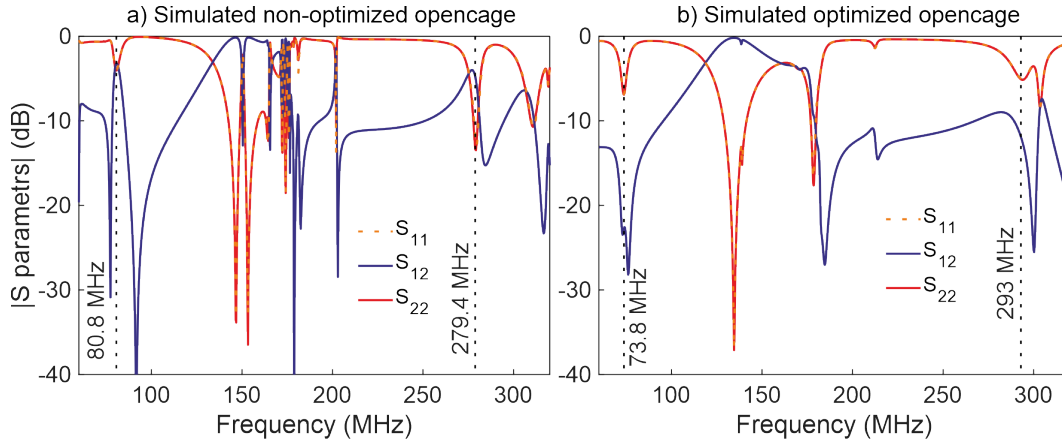
Figure 4.13 – **Simulated S-parameters of dual-band quadrature opencage coil: (a) non-optimized coil, (b) optimized coil.**

As it can be seen, an overall better isolation between the 2 port is obtained with the optimized coil. A good isotation (S_{12}) equal to -22 dB is reached for the carbon frequency. The isolation for the proton frequency is not as good (-12 dB). It is important to note that coils are not input impedance matched in the listed above cases.

Thereafter, the B_1^+ maps are shown in Fig. 4.14. These maps have been evaluated at frequencies of 73.8 [Fig. 4.14(a, c)] and 293 MHz [Fig. 4.14(b, d)]. Finally, the spatial field homogeneity is acceptable at both frequencies. In other words, the field pattern became like the ones provided by a birdcage coil.

4.3   Conclusion

To conclude the entire chapter, the two dual-band coils have been proposed and tested. In the first part of the chapter we have proposed the new design of a transmit/receive dual-tuned volume nested coil based on a joint structure of a birdcage and a closed SLRs metasurface [172]. The developed coil is devoted to ^{19}F/^{1}H imaging. We have shown the numerical study of the proposed geometry with Finite Element Method solver. The homogeneity of B_1^+ field at the two selected Larmor frequencies is suitable for preclinical imaging. After all, we have presented MRI tests performed with a phantom. However, unfortunately the proposed setup is not convenient to use. In other words, the quality of the acquired images is appropriate for fluorine but not for proton. The coil was unsuccessful because of the difficulties related to adjust simultaneously each structure responsible for each nucleus.

In contrast to the first section, in the second section, the dual band coil (opencage) based on second order filter has been proposed. Our approach is suitable for designing any kind of dual band opencage coil for many different applications, except when Larmor frequencies are close to each other for example ^{19}F/^{1}H. We have conducted the investigation for a coil working simultaneously at the two Larmor frequencies of ^{13}C and ^{1}H at 7 T. We have used a band-pass network wherein both frequency bands can be tuned independently by adjusting the capacitances in the rings or in the legs. In this case, leg capacitance (C_l) mainly tunes the high frequency band, while ring capacitance (C_r) mainly tunes the low frequency band. However, contrary to the first order filter, in the second order filter the proper values of capacitances and
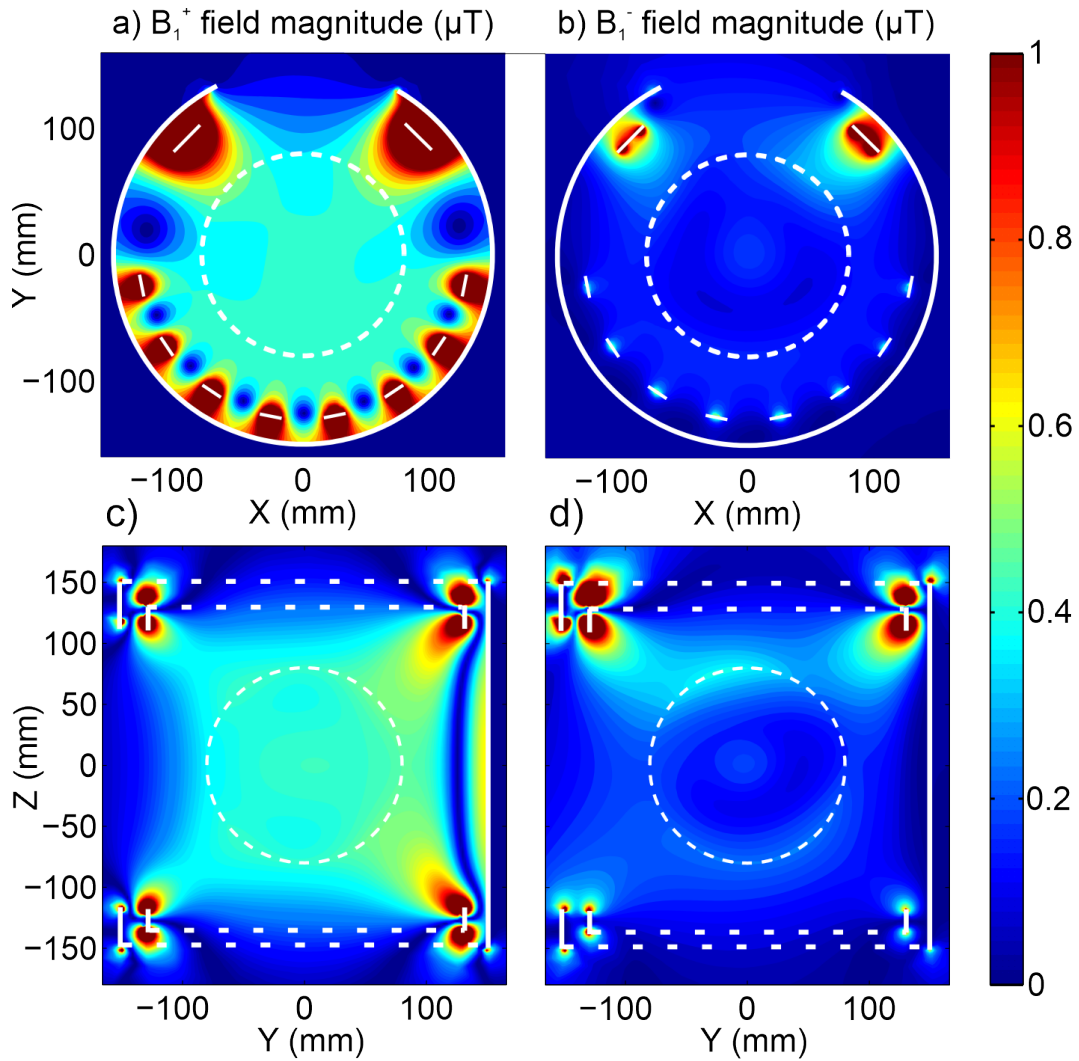
Figure 4.14 – B_1^+ **field distributions of the optimized dual-band opencage coil at 73.8 MHz and 293 MHz respectively: (a, c) the central transverse and sagittal slices; (b, d) the central transverse and sagittal slices.**

inductances cannot be explicitly computed. Hence, in order to optimize a unit cell, a constrain optimization method has been used. Eventually, we have verified the proposed approach in full-wave simulations, wherein the appropriate field homogeneity is observed. By lack of time, the coil for carbon and proton, was not tested experimentally.

CHAPTER 5

Phase conjugate inspired metacage coil for UHF MRI

Table of contents

In UHF field MRI, for instance at 7T, the working frequency for proton is approximately 300 MHz that corresponds to a wavelength in free space of 1 m. Inside a high index dielectric ($\varepsilon_r = 75$) such as a human brain, the wavelength becomes only 12 cm long. This wavelength decreasing leads to the deterioration of the B_1^+ field homogeneity [8], [9]. Thereby, a $\lambda/2$-wide focal spot of B_1^+ field appears at the center of the region of interest (ROI). The transmit efficiency is the highest inside the spot while rapidly decaying toward the periphery. This effect is observed with any kind of quadrature transmit coils for UHF brain imaging: TEM coils [28], [82], birdcage coils [9], [10]. This problem of B_1^+ inhomogeneity is also valid for transmit or transceiver phased array coils driven in CP mode [51].

The simplest method to overcome this fundamental limitation of UHF MRI implies the use of passive B_1^+ shimming techniques exploiting dielectric pads [16], [173] or passive resonators (HMA) [17], [137]. These devices can locally homogenies or more exactly enhance the B_1^+ field.

An outstanding solution that can mitigate this issue of weak B_1 coverage is provided by receive phased arrays [13], which become common in UHF MRI [9] and available commercially [174]. A receive phased array is usually made of several electrically small loop coils circumscribing a head. Indeed, while a single small loop coil provides a high SNR in small FOV by itself, being combined and decoupled they increase the FOV and provide a grater SNR compared to the conventional coil of the same size [10], [13]. As a result, phased arrays provide high SNR in the entire volume of the ROI even for UHF brain imaging [51], [175].

The B_1 field homogeneity can also be significantly improved with passive RF shimming [9], [108]. Such shimming implies driving the particular amplitudes and phases of transmit array elements [159], [176], [177]. Moreover, compared to conventional coils, use of transmit phased arrays lead to reduce the SAR. The cutting-edge technique in UHF field MRI, which can directly improve B_1 field homogeneity is active B_1 shimming or pT_x allowing to generate most homogeneous field distribution in transmit regime [15]. This method is one of the main advantages of using phased array coils in the transmission mode.

However, the realization of all these varieties of phased arrays coils requires care about decoupling (isolation) between the adjacent array's elements [160]; detuning of the transmit coil in the receive regime [10], decoupling of transmit and recieve channels in each individual T_x/R_x interface [13]. In addition, each element in the array needs a proper impedance matching circuit, cable traps or baluns, which, in the end, require numerous MRI compatible electronic components. All these factors bring certain engineering difficulties which, in the end, increase the price of the coils and decrease their reliability.

As an alternative and intermediate step between passive shimming and full active shimming, we propose a new coil based on phase conjugation (PC) [178] or time reversal (TR) techniques [144], [179], in order to deal with the problem of homogeneity in the UHF MRI. These two techniques are well known in optics and acoustics to focus waves at arbitrary positions. For example, it was implemented for: ultrasound biomedical imaging [180], focusing beyond the

diffraction limit in microwave frequency range [181], in optical domain [182]. From a mathematical point of view both techniques are similar. However the experiments are different [183]. Initially PC was proposed for quasi-monochromatic optical experiments. PC is based on nonlinear interaction of waves (3 or 4 wave mixing) [183]. Later, time reversal (TR) of ultrasonic waves was introduced using arrays of transducers and digital to analog and analog to digital converters. TR can be seen as a broadband extension of PC [184].

The aim of this chapter is to design a specific coil inspired by PC that is capable to focus transmit RF field B_1^+ in a region of the sample to be imaged. Up to now, we have always developed birdcage inspired coils wherein the angular phases of the currents on the legs correspond to the geometrical angles of the position of the legs with respect to the coil center. In such a case, as for birdcages [80], at the fundamental $k = 1$ mode, this phase distribution leads to homogeneous magnetic field [9] for low field MRI. However, this is not valid for UHF MRI, wherein the maximal B_1^+ field is achieved at the center [9]. In contrast to the conventional phase distribution, we propose here to determine specific phase distributions that can ensure the shifting of the B_1^+ focal spot toward any specific position of an image. We propose here to use the phase conjugation technique to compute this phase distribution. In other words, here, we propose a new kind of passive B_1^+ shimming technique.

This chapter consists of the two main parts. In the first section, we describe the principle of phase conjugation and its application for 7 T brain imaging. This section rises only the theoretical aspects. Further, in the next section, we consider the application of this approach to the preclinical volume coil for UHF imaging at 17.2 T of small rodents. We have called this coil metacage. In this section we provide the theoretical details and the experimental investigations.

5.1   Phase conjugated volume coil

5.1.1   Phase conjugation principle

Phase conjugation (PC) or time reversal (TR) mirrors are devices that reflect waves to the location, from which this wave is initially sent. Simplest understanding of PC/TR can be found in Fig. 5.1. In a first step, a source emits a diverging wave. Around the propagation medium, a set of transceivers probes the complex amplitude of the field in case of PC or the time dependence of the field in case of TR. In a second step, the recorded signal is flipped in time (or equivalently phase conjugated at one frequency) and remitted by the same transceivers. Due to the time reversal invariance of the propagation medium, the field backpropagates and finally focus on the initial source location. PC/TR is still valid in more complex configuration when the wave front is distorted by heterogeneities in the media [185].

5.1.2   Application to MRI

In order to make a link between phase conjugation principle and MRI application, we consider an array of N wires (dipoles-like) playing the role of transceivers, likewise in phased arrays. We have performed 2d simulations with a FEM solver (open source getDP software [186], [187]). This configuration is presented in Fig. 5.2.
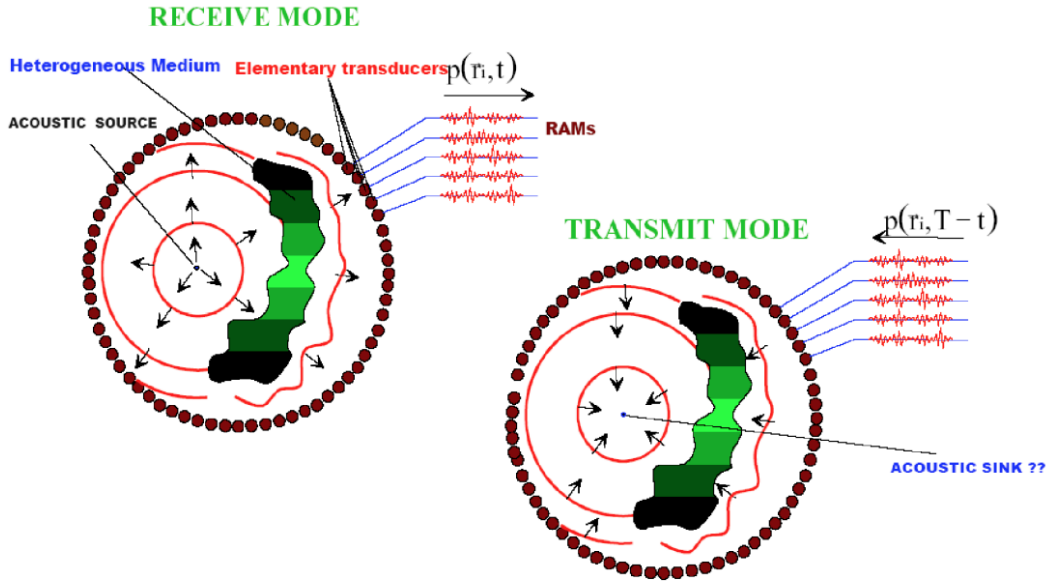
Figure 5.1 – Time reversal/phase conjugation principle [185].
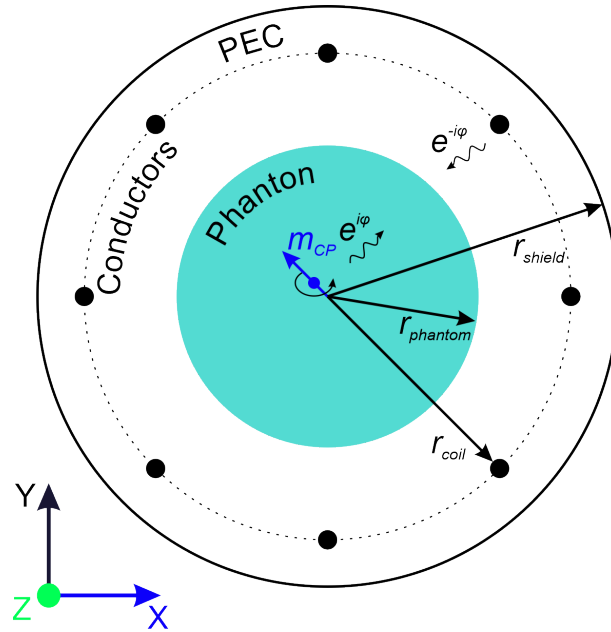
Figure 5.2 – Schematic view of 2d simulated setup consisting of the eight equidistantly distributed conductors.

In this simulation only the transverse plane is simulated. Each leg of the birdcage coil is modeled by a point-like conductor. The considered setup has similar geometrical parameters as the ones of a head birdcage coil working at the Larmor frequency of proton ^{1}H (≈ 300 MHz) at 7T. The conductors are arranged with a constant angle φ of 45° and distributed around the circumference with a radius r_{coil} of 130 mm. The whole setup is shielded by a PEC of radius r_{shield} of 155 mm. Moreover, the setup is loaded by a circular phantom of radius $r_{phantom}$ of 90 mm ($\varepsilon_r = 75$, $\sigma = 1$ S/m).

In the first step of a phase conjugation process, we consider a source placed in the center of a phantom. Here the source is a circularly polarized magnetic dipole within the simulation plane

to obtain after time reversal a circularly polarized magnetic field. The phase φ_i of the electric field amplitude is probed at each wire position. When the source is at the center, the phase shift between two consecutive conductors equals $2\pi/N$ (N=8) while it becomes more complex when the source is out of the center (see figure 5.4). In the second step of time reversal, the complex amplitudes of the currents are set to $e^{(-i\varphi_i)}$, i.e., phase conjugated (see figure 5.3). The resulting circularly polarized magnetic field distributions for the two initial source locations are shown in Fig. 5.3. When the source placed at the center of the setup, the PC is obviously equivalent to a conventional birdcage mode with a B_1^+ field pattern that shows a spot at the center [Fig. 5.4(a)].
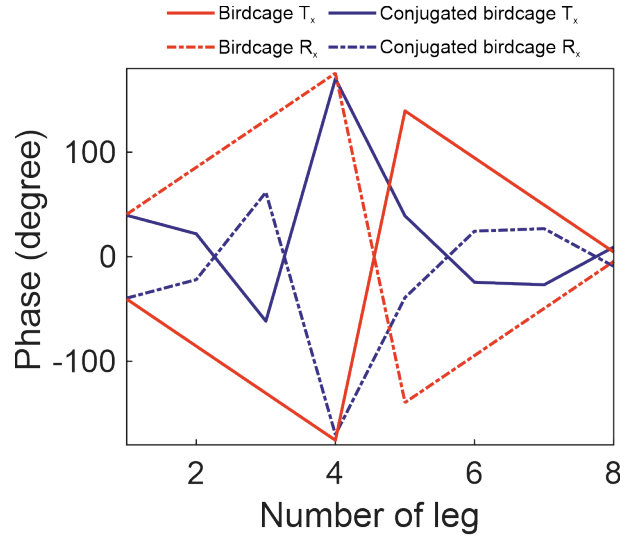
Figure 5.3 – **Desirable current phases as a function of the conductors' number. A specific current distribution when the source is placed 25 mm outside from the center is colored in purple. The conventional birdcage-like current distribution case is colored in red.**

Now, when we consider the more complicated case, wherein, the source is shifted 25 mm away from the center toward the periphery we observe a focusing of B_1^+ at the position of the initial source [Fig. 5.4(b)]. Consequently, by imposing a different current distribution in the transmission mode, the most sensitive region can be translated.

As it is mentioned earlier, the previous simulations have been performed with an array of elementary transmitters and receivers. However, in this work we are aimed to provide this unique phase distribution in a birdcage-like coil. We use the general approach presented in Chapter 2 to design a coil with the proper phase distribution. The equivalent circuit of the proposed conjugated birdcage coil shown in Fig. 5.5(a, b).

This circuit contains eight rungs [Fig. 5.5(b)]. In contrast to the previous chapters devoted to opencage coils, here, in order to obtain a mode with the specific phases $\varphi_1 \ldots \varphi_8$, one has to combine low pass and high pass unit cells in one coil [Fig. 5.5(c)].

As explained in Chapter 2, the provided theory evaluates the Bloch impedance and phases on nodes, i.e., between the cells, while phases $\varphi_1 \ldots \varphi_8$, should be imposed on the legs. To that purpose, we propose to use the simple rule expressed by formula (2.21). Based on this rule, the phase on one leg is the averaged contribution of two adjacent cells. For the Bloch impedance, the conventional way (formula 2.22) can be used, because matching is important in the connections (nods) of the cells (rungs). By substituting the phases from Fig. 5.3 and
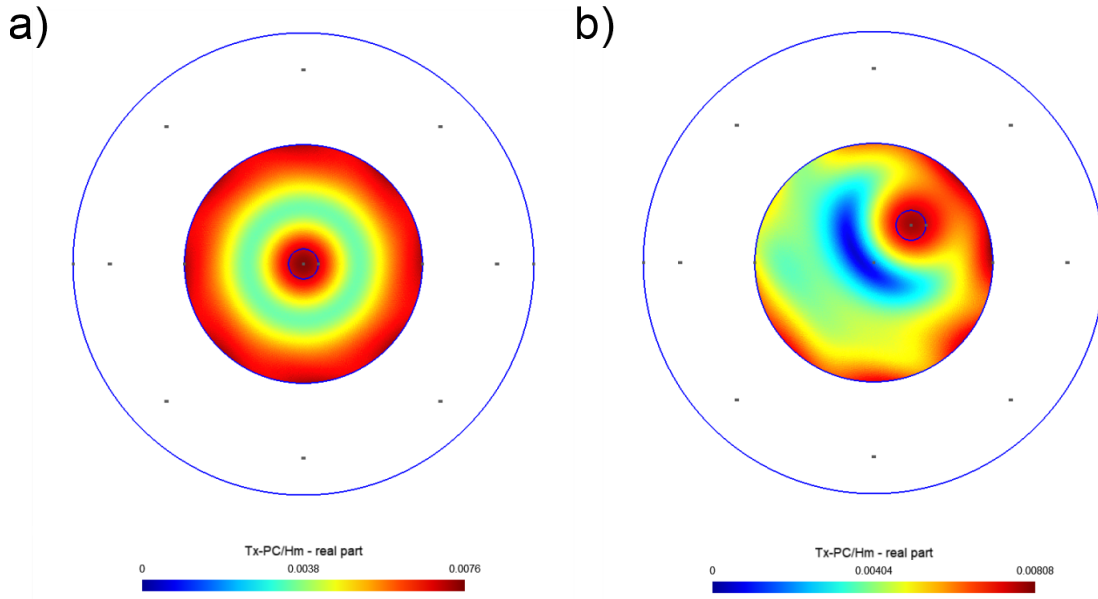
Figure 5.4 – **Amplitude of the magnetic field B_1^+ after the phase conjugation of the field generated by a circularly polarized magnetic dipole located inside the black circle that is: (a) at the coil center; (b) 25 mm away the coil center.**
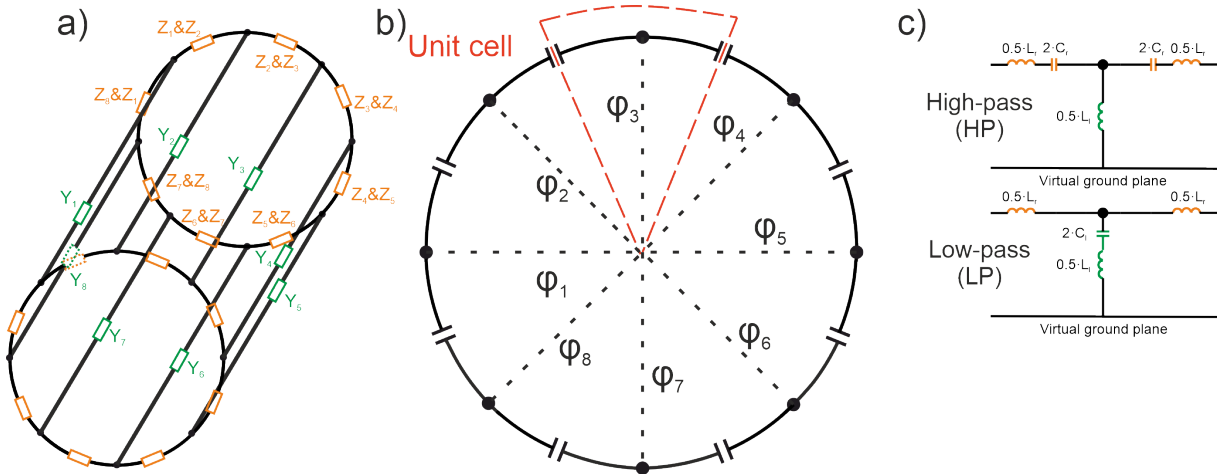
Figure 5.5 – **(a) Sketch of eight rungs conjugated coil. (b) Transverse view of the conjugated birdcage coil. (c) Equivalent circuits of high-pass and low-pass unit cells.**

fixing the Bloch impedance to 97.8 Ohm, one can compute the following inductances (widths) and capacitances listed below in Tab. 5.1.

It is confirmed that to provide the desired current distribution it is necessary to use both LP and HP in one setup. In practice it means that to achieve the desired values of impedance and phase, the width of the legs should be modified for HP cells (rungs 1-6), while for LP cells (rungs 7 and 8) width of end-rings should be modified. However, due to parasitic capacitances in a birdcage coil, values below 2 pF became unreachable [71]. Moreover, achievement of desired phases shift requires use of non-feasible values of inductance for some unit cells. Namely, the values of inductance are dramatically high for rung numbers 1,2,4 and 5. Therefore, the required inductances cannot be obtained just by changing the width of the legs. It may be provided by inserting additional lumped inductors. However, these inductors can dramatically complicate

Table 5.1 – Parameters of different HP or LP rungs (unit-cell) types tuned to the desired frequencies of 300 MHz. Impedances have been adjusted as well.

Conductors' number	L_1 (nH)	w_l (mm)	L_r (nH)	w_r (mm)	C (pF)	Type
1	325.72	NaN[1]	86.05	10	2.73	HP
2	335.37	NaN[1]	86.05	10	2.75	HP
3	263.76	0.9	86.05	10	2.62	HP
4	403.09	NaN[1]	86.05	10	2.82	HP
5	672.96	NaN[1]	86.05	10	2.99	HP
6	113.94	19.8	86.05	10	1.84	HP
7	146.59	10	219.45	NaN[1]	1	LP
8	146.59	10	89.35	9.8	1.12	LP

the setup. Eventually, the realization of such a coil is a complex task. Therefore, we consider a simpler in terms of focusing spot translation configuration for small animal imaging at 17.2 T. However, designing of a birdcage coil at such a high frequency also has challenges.

5.2 Conjugated birdcage coil for 17.2 Tesla preclinical imaging

In this part, we propose to apply the PC technique for proton ^{1}H imaging of small rodents at 17.2 T, where the working frequency is 730.2 MHz. At this frequency, the wavelength in free space is 41 cm, while it becomes about 5 mm in tissues. As in the previous case, here we consider the setup of eight conductors as it is shown in Fig. 5.2. These conductors arranged with the constant angle φ of 45° and distributed around the cylinder with radius r_{coil} of 30 mm (Fig. 5.2). The whole setup is shielded by PEC with radius r_{shield} of 40 mm. Moreover, the setup is loaded by a circular phantom with radius $r_{phantom}$ of 16.8 mm ($\varepsilon_r = 45.3$, $\sigma = 0.87$ S/m). As in the previous chapter, the design of the coil requires the same optimization procedure, which is expressed in the next section.

---

[1]Here NaN means that the needed width to obtain the desired inductance is unfeasibly small.

5.2.1 Theory of conjugated birdcage coil for 17.2 Tesla

However, according to the issues listed above (LP and HP cells in one network, not reachable inductances), we are not going to impose such a dramatic modification as previously. In this investigation we limit ourselves only by a 6 mm shift inside the phantom in order to use only HP cells. The B_1 field distribution for this displacement obtained in 2d simulations is presented in Fig. 5.6(b), while the conventional B_1 field distribution of a birdcage for the setup of the new size is shown in Fig. 5.6(a).
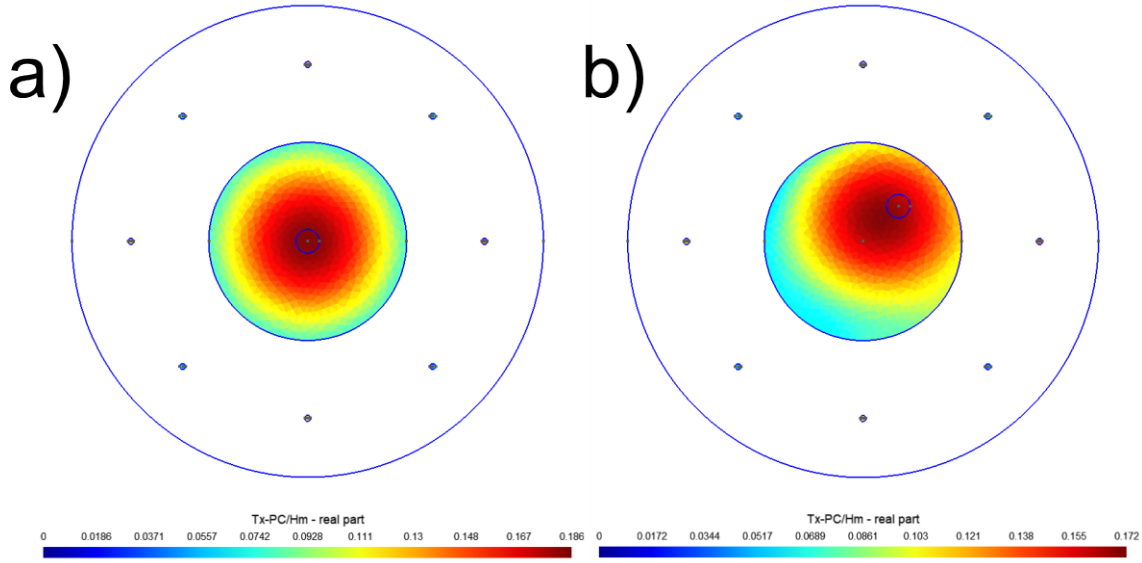
Figure 5.6 – (a) Magnetic field B_1^+ focused on the center, likewise to a conventional birdcage coil at UHF. (b) Magnetic field B_1^+ focused 6 mm away from the center of the setup.

In this case we obtain the unique current distribution presented in Fig. 5.7 (orange curve). For that current distribution, the combination of leg inductance and ring capacitances have been found according to the theory stated previously.

The evaluated capacitances and inductances, as well as the corresponding leg widths are presented in the Tab. 5.2. In order to compute these values, it is important to note, that the constant Bloch impedance is set to around 75 Ohm for each unit cell at the frequency of 730.2 MHz. Moreover, here we use only HP cell, therefore the L_r sets constant to 16.21 nH.

However, because the proposed theory approximates current on legs (half contribution of two neighboring rungs), we have performed additional investigations in circuit LC simulator. To that purpose, a network of eight-unit cells was composed with values from Tab. 5.2 and then simulated in CST Microwave Suite using circuit simulator. This simulation can show the actual phases in the legs of each unit cell. As it can be seen the obtained phases in circuit simulator are well matched with the desired ones seen in FEM simulations [Fig. 5.7 and Fig. 5.8(a)]. Moreover, the Bloch impedance of the unit cell is constant [Fig. 5.8(b)] for each unit cell as it is desired.

As a next step, the coil can be tested in full-wave simulations.

---

[2]Here the value of 100.4 nH requires very small value of width. Therefore, the maximal available width of 1 mm is set, thus it corresponds to the inductance in the brackets.
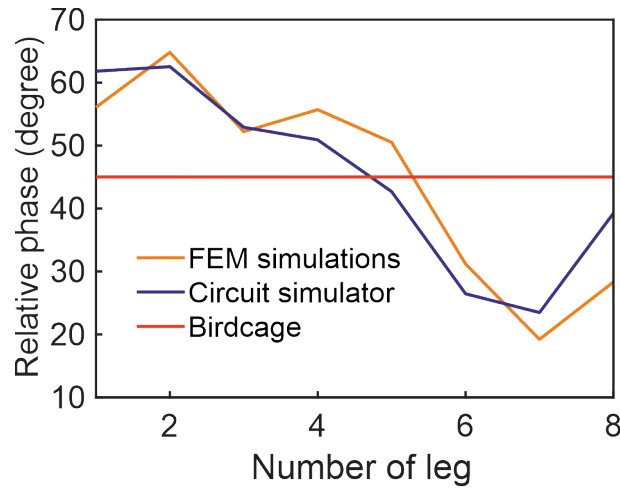
Figure 5.7 – **Desirable relative phases of current as a function of conductor number (rung). Phases obtained with FEM simulations (orange). Phases verified with circuit simulator (purple). Constant relative phase of the conventional birdcage coil (red).**

Table 5.2 – **Optimized parameters of different HP rungs (unit-cell) types tuned to the desired frequencies with the adjusted impedances.**

Conductors' number	Phase ($\varphi°$)	L_l (nH)	w_l (mm)	C_r (pF)
1	56.06	39.68	7.64	1.41
2	64.79	36.40	9.38	1.28
3	52.21	40.61	7.21	1.44
4	55.70	39.87	7.55	1.41
5	50.51	42.67	6.34	1.49
6	31.18	63.63	1.71	1.87
7	19.22	100.4 $(72.22)^2$	1	2.18
8	28.32	69.43	1.19	1.94

5.2.2   Numerical optimization

We have performed numerical full-wave simulations of the designed conjugated birdcage coil using CST Microwave Suite (Frequency domain solver). The length of the coil is set to 70 mm. To generate quadrature mode, the coil is excited by two 90° distant 50 Ohm ports. These ports are placed as shown in Fig. 5.9, i.e., between the end-ring segment and the shield. The coil is loaded by the cylindrical homogeneous phantom with relative permittivity (ε_r) and conductivity
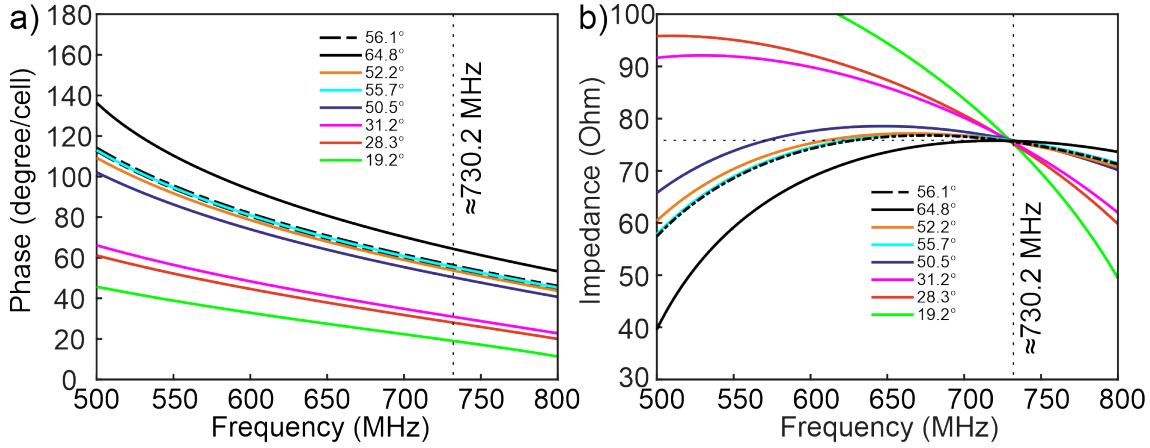
Figure 5.8 – **Calculated curves for the eighth LHTL cells involved in conjugated cage: (a) the dispersion diagram; (b) the Bloch impedance.**

(σ) of 45.3 and 0.87 S/m, respectively. The length of the phantom is 105 mm and its radius equals to 16.8 mm.
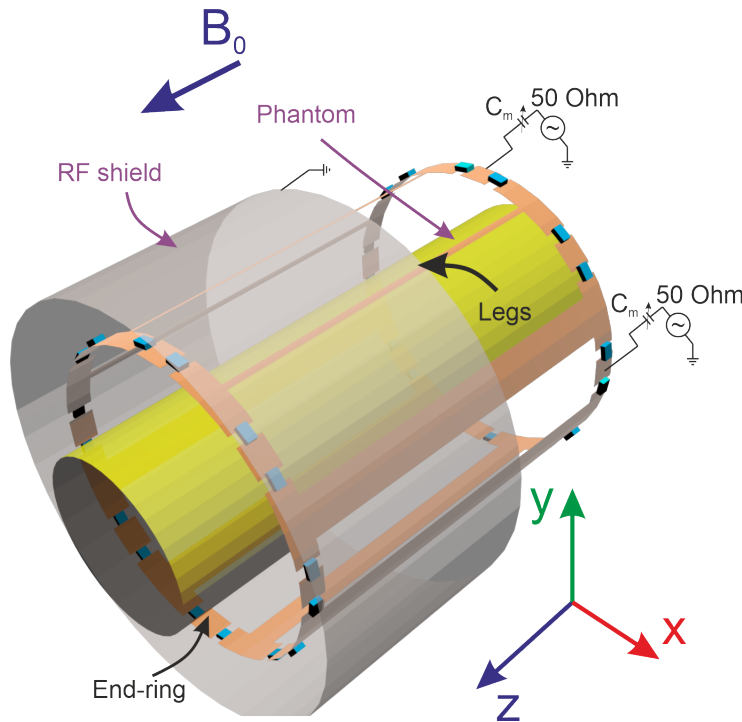
Figure 5.9 – **Geometry of the conjugated birdcage coil. The shield of the coil is partially hidden.**

The other geometrical parameters of the coil have not been changed compared to the 2d simulations. However, the capacitances are slightly corrected to tune the coil at the frequency of 730.2 MHz. Moreover, these capacitances are corrected to match the ones available in stock. The capacitances are listed in Tab. 5.3. In addition, all capacitances are twofold in the simulations and later in the experiment. In the simulations ESR of the capacitors has been estimated with quality factor of 1000. Typically, ESR equals to hundredths of Ohms.

At first, we have computed the S-parameters of the proposed coil (Fig. 5.10). Here the coil is tuned and matched at the desired frequency. For tuning and matching we have used the same network as in Chapter 3.2. Namely, the matching capacitor is connected in series to the feeding

Table 5.3 – Theoretically and numerically optimized capacitances (C_r) in pF.

Theory	2.82	2.56	2.88	2.82	2.98	3.74	4.36	3.88
Simulations	2.3	2	2.5	2	2.5	3	3.5	3.5

line, while the tuning capacitor replaces a ring capacitor. Here the appropriate matching is achieved with S_{11} and S_{22} around -20dB, while the isolation level S_{12} retains high (-20 dB).
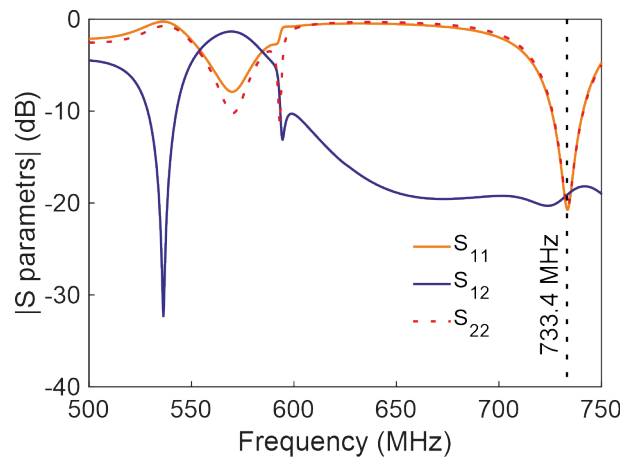
Figure 5.10 – Simulated S-parameters of the quadrature conjugated birdcage coil.

The B_1^+ map has been computed at the frequency of 733.4 MHz. This map is shown in Fig. 5.11(a). The B_1^+ map is compared to the map obtained with a conventional birdcage (The same structure has been used but with a constant phase shift between the rungs, see the previous section) [Fig. 5.11(b)]. As it can be seen in Fig. 5.11(a), the proposed coil behaves desirably, i.e. the focal spot is slightly shifted compared to the birdcage coil. To assess the offset value more evidently, we have plotted the same field but only inside the phantom for the conjugated coil [Fig. 5.11(c)] and for the birdcage coil [Fig. 5.11(d)].
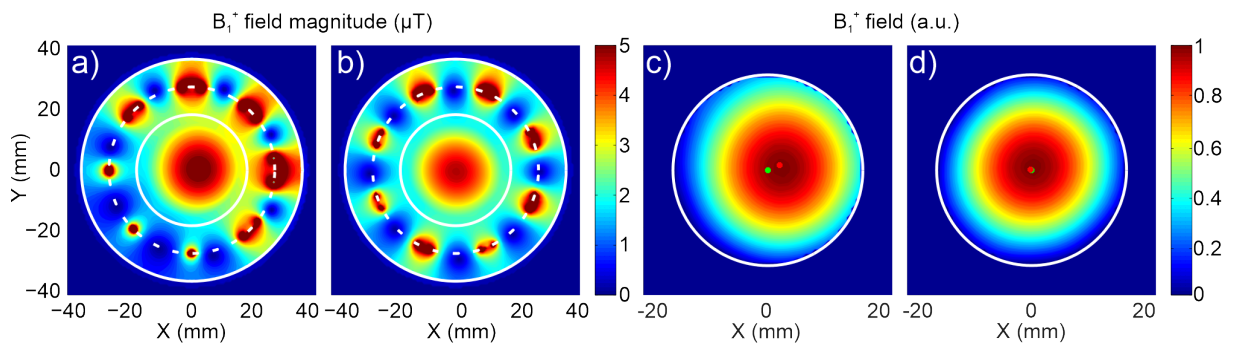
Figure 5.11 – B_1^+ maps of the simulated quadrature conjugated coil (a) and the conventional birdcage coil (b). The same maps but cropped outside the phantom, (c) for the conjugated birdcage coil, (d) for the conventional birdcage coil.

As it was mentioned earlier, the initial aim was to obtain a displacement of the focus of 6 mm from the center (36% of the radius). However, here only 2.2 mm has been obtained, which is

only 13% of the radius. This difference can be explained by several theoretical approximations. The currents are not directly controlled in the legs. Moreover, for the rung number 7, the inductance is significantly high, therefore, it is slightly lowered with the maximal feasible width of the legs. In addition, the values of capacitances are rounded to the ones available in stock. As a result, all these approximations seem to reduce the spot displacement. Nevertheless, the coil has been assembled and tested on a bench.

5.2.3 Experimental assessment

For the prototype assembling, we have used 3-d printed (PLA) hull of the coil wrapped by copper foil tape. The photograph of the prototype is shown in Fig. 5.12. In the prototype, the two coaxial cables are involved in feeding the coil. These cables are placed as it is shown in Fig. 5.9, i.e. 90° distant, and connected between the shield in end-ring segment. The commercial power splitter and T_x/R_x interface from Rapid Biomedical have been employed in order to feed the coil in the quadrature regime and connect it to the receive and transmit channels of our MRI scanner (Bruker Biospec 172/25).
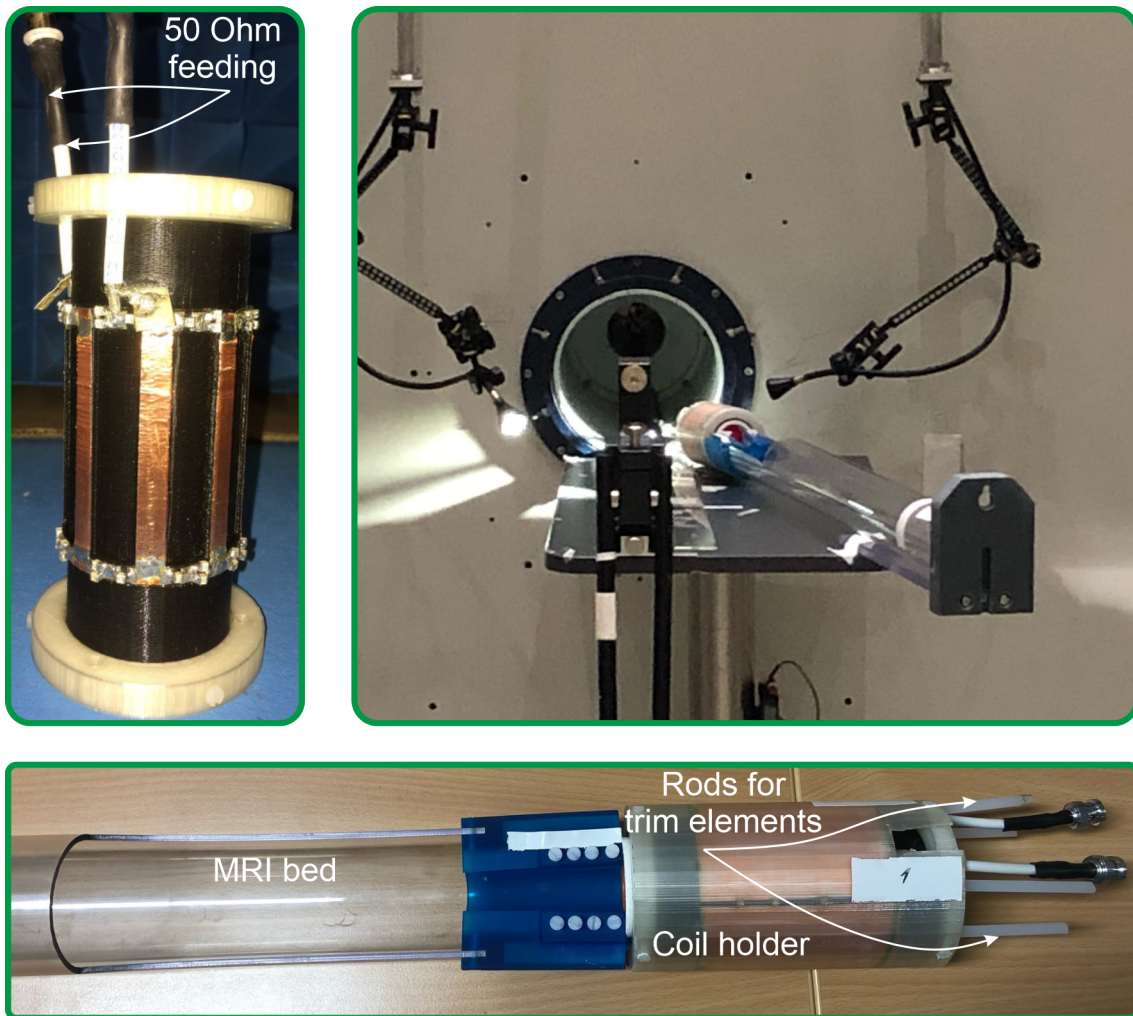
Figure 5.12 – Photographs of the assembled prototype.

The coil is completely shielded by a screen made of copper foil tape stuck to the internal surface of the external 3d printed coating of the holder. Three gaps have been made in the

shield, and capacitors of 80 pF are soldered in these gaps in order to prevent eddy currents [83].

Finally, two nonmagnetic capacitors are used for impedance matching. These capacitors are connected in series to the feeding line (Fig. 5.9). In addition, two fixed capacitors are replaced by tunable capacitors for frequency tuning as it was done for the opencage coil. Matching and tuning of the coil placed inside the MRI bore have been done in the presence of the homogeneous phantom. The measured S-parameters are shown in Fig. 5.13. As it can be seen, the coil is well matched (-30 dB), while isolation between port remains around -20 dB. These measured values are in good agreement with the simulated ones [Fig. 5.10].
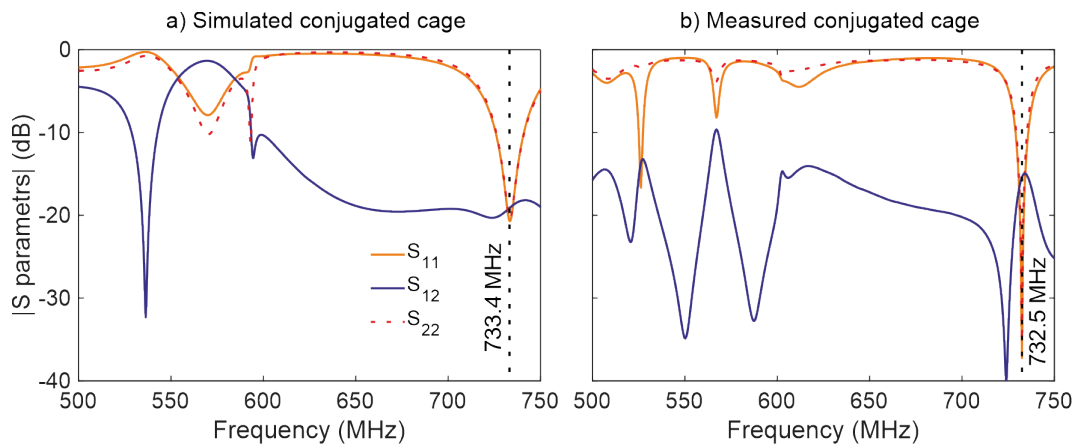
Figure 5.13 – Measured S-parameters of the quadrature conjugated birdcage coil.

5.2.4 Imaging with the conjugated birdcage

Finally, a few images of the phantom have been acquired using gradient echo sequence (GRE). The parameters of the used sequence are the following: TR/TE = 1500/3.842 ms, pixel in plane spacing of 0.2 mm, slice spacing 1 mm, a FOV of 45 mm by 45 mm by 40 mm, a FA of 30°. At first, we have performed acquisition using the linear polarization, when one port is plugged to the scanner, whereas second port is connected to the 50 ohm load and conjointly using commercial T_x/R_x interface. These acquired GRE images of the phantom are shown in Fig. 5.14(d-f). In addition, Fig. 5.14(a-c) shows the simulated B_1 maps of the phantom.

As it was mentioned in the beginning of the section, our aim was to obtain a displacement of 6 mm from the center. As in the prior section, in order to asses this displacement in the measured images as well as in the numerical simulations, we calculated the mass center of each image and compared them to the geometrical center of the phantom (Tab. 5.4). As it can be seen in table 4, we are able to provide a shift of only 6% of the phantom radius in the measurements instead of the 13% observed in the full-wave simulation. This difference can be explained by the tolerance of the capacitor values in the experiment, the impact of the matching and tuning circuit but most of all on the position of the phantom that cannot be precisely positioned at the center of the coil.

As a final test, we have put a rat under anesthesia inside the conjugated birdcage coil and acquired several images of its brain. These images are shown in Fig. 5.15. For in-vivo imaging we have used spin echo based sequence with the following parameters: TR/TE = 2500/13.2757
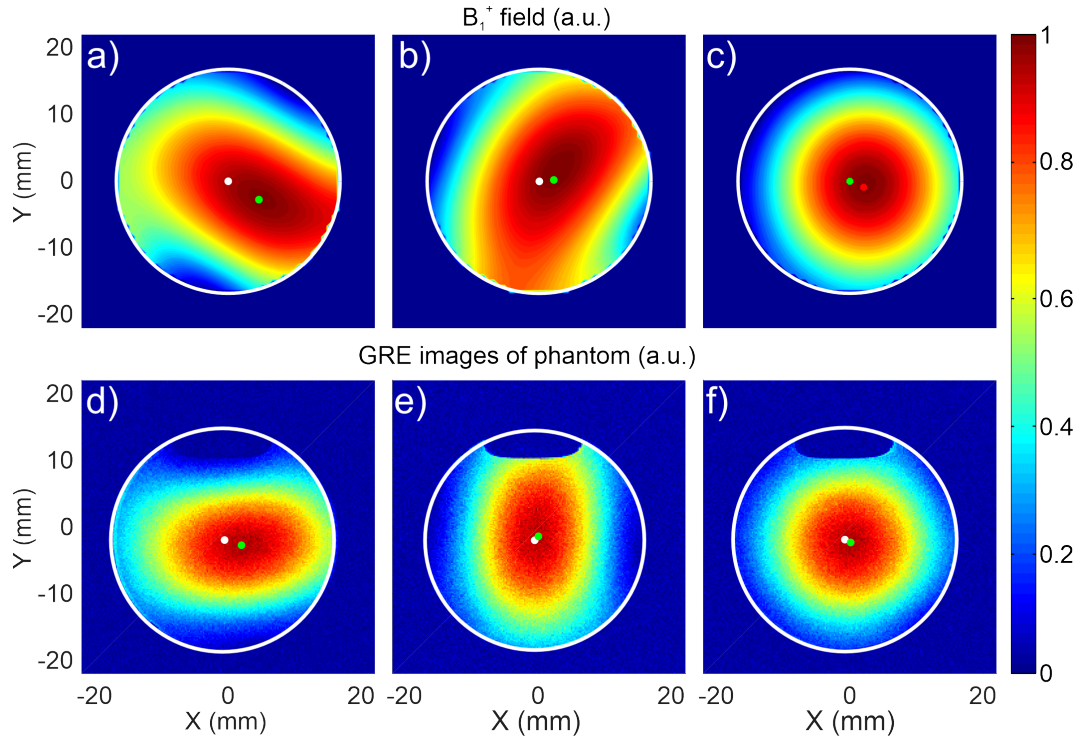
Figure 5.14 – The simulated B$_1$ maps of the conjugated birdcage coil: (a-c) normalized B$_1^+$ magnetic field obtained in simulations for port 1, port 2, and CP mode respectively; (d-f) normalized GRE images acquired with port 1, port 2 and CP mode respectively.

ms, pixel in plane spacing of 0.125 mm, slice thickness 0.5 mm, a FOV of 32 mm by 32 mm by 15 mm, a FA of 90° and 8 averages.

The obtained images demonstrate enough spatial homogeneity, therefore different parts of the head are distinguishable. However, the effect of focusing is not visible inside the head, because it is neglected by the inhomogeneous load such as an animal.

5.3 Conclusion

We have described an optimization method to build a "conjugated" birdcage coil that focuses a B$_1^+$ field spot appeared at UHF operations. This conjugated coil can be an efficient tool to

Table 5.4 – Displacements in mm of the focusing spot in the simulations and measurements with respect to the active port.

	Port 1	Port 2	CP mode
Simulations	6.2	2.5	2.2
Measurements	3.4	2.1	1
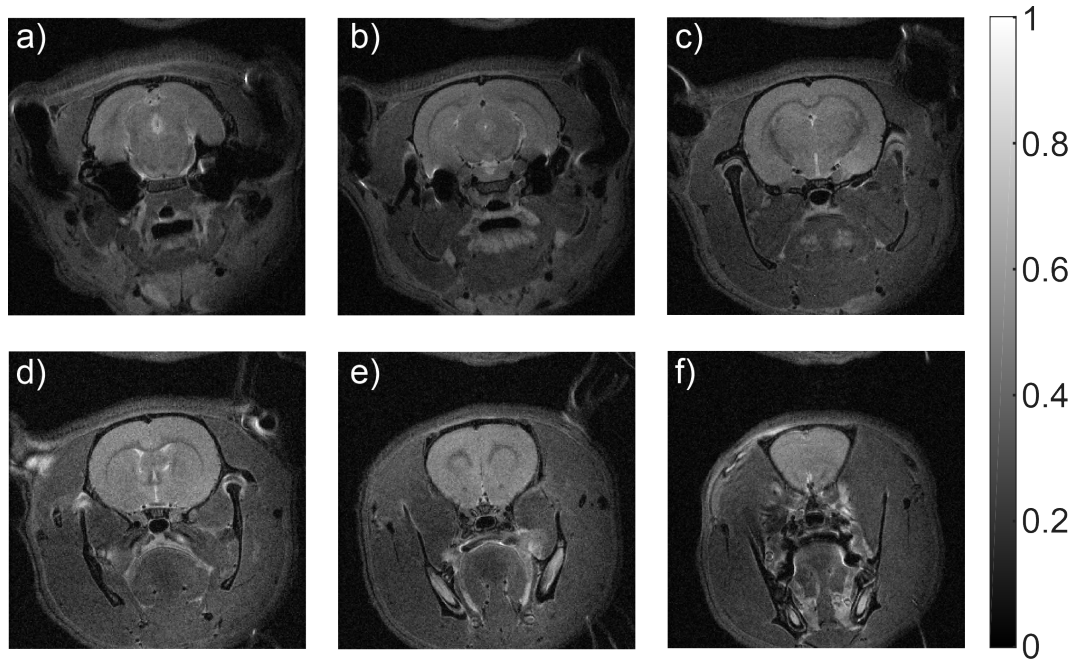
Figure 5.15 – **The in-vivo images of the rat brain in several transverse slices obtained using conjugated coil.**

perform passive B_1 shimming that can be especially actual for targeted spectroscopy, wherein the signal enhancement in a certain voxel can be important. Particularly, FEM simulations with elementary current sources have provided the phase shift of current to apply to each leg in order to focus B_1^+ on another location than the center as for a birdcage coil. From that distribution the inductances and capacitances have been computed and therefore the width of unit cell elements has been evaluated as well.

At first, this approach has been applied for a head coil at 7 T. Because of the difficulty to its realization, the concept has been then tested at 17.2 T for rodents imaging. The proposed coil for 17.2 T has been studied numerically and experimentally on bench and in MRI. The resulting images have shown a focal spot displacement of 2.2 mm in simulations and 1 mm in measurements. The proposed concept could be improved in order to become an efficient alternative to passive B_1 shimming at UHF MRI. As it is stated before, the focusing spot movement is hardly visible in in-vivo experiments. Thus, an initial optimization should be further done in the presence of a head phantom instead of a homogeneous circular phantom.

Conclusions and perspectives

In this manuscript we have proposed a general approach based on a metasurface approach to develop volume coils. This work has led to several RF coils aiming for different purposes.

In Chapter 1 we have first presented the emergence of MRI as a unique medical apparatus. The fundamental principles and abilities of MRI have been reviewed. Subsequently, the pros and cons of UHF MRI have been given. Then, we have defined the role and importance of some key parameters of RF coils, such as B_1 field, transmit efficiency, SAR and SNR. The several families of coils, such as surface coils, volume coils and phased arrays have been reviewed. The last section provided an overview of metamaterial-based coil in MRI.

Conventional volume coils such as birdcage or TEM remain ones of the best transmit coils for moderate and high field MRI, respectively. However, the latest developments on MRI show the breakthrough of ultra-high-field imaging. Because of the increase of Larmor frequency, new challenges arise to develop coils for such devices. Indeed, the coils cannot be considered anymore as quasi-static magnetic probe. To overcome this limitation, one efficient solution is to use array of coils. However, this solution is complex to implement. As a consequence, single or dual port coil are still very competitive solutions.

In this manuscript, we propose a general framework inspired by works on metasurface to develop volume coils for UHF MRI. To that end, in Chapter 2, we have introduced the general structure of such metasurface coil and proposed the theoretical tool for developing first order (LP and HP) metasurfaces. It has been shown that a unit cell of a birdcage coil is mainly characterized by two parameters, namely phase shift and Bloch impedance adjusted by equations (2.19) and (2.22) respectively. In addition, values of inductance and capacitance for HP cells can explicitly be calculated analytically using equations (2.23) and (2.24), respectively. The examples related to the particular RF coils, developed using the proposed transmission matrix approach have been presented in Chapters 3 to 5.

In Chapter 3, we have taken the benefit of the metamaterial formalism to build a birdcage-like coil that facilitates access to the region under study. This opening not only improves the comfort of patients but it is especially suitable for motion correction at UHF Magnetic Resonance Imaging such as 7T and some other applications.

This new type of RF coil has been named opencage. In the first part of the chapter, a coil dedicated to imaging of small rodents at 7T has been presented. In the second part of

the chapter, a larger coil working at 7 T and optimized for imaging of human head has been developed. The main parameters of the opencage coil have been determined analytically, tested numerically, and confirmed experimentally on the bench and in the MRI.

For the preclinical coil, phantom and in-vivo images have been acquired. The opencage coil demonstrates substantially suitable signal homogeneity and sufficient FOV and SNR. The average SNR obtained with the opencage coil is comparable to one obtained with a conventional birdcage, i.e., 1865 for the birdcage coil versus 1752 for the opencage coil. The relative standard deviation estimated for the opencage coil equals 8.8%, while for the birdcage coil this value equals 8.3%. These values have been estimated in the half of ROI where an animal is likely to be placed. When the ROI is enlarged to the whole coil volume, the standard deviation increases to 20.4% for the opencage coil while it remains almost constant (8.5%) for the birdcage coil. This increase in SD for the opencage coil can be explained by lower density of the legs at the top.

For the coil dedicated to head imaging, the prototype has been assembled and tested on phantom in a clinical 7 T Siemens scanner. The opencage coil demonstrated a slightly worse homogeneity (14%) of B_1^+ field and higher (32%) transmit efficiency compared to a conventional birdcage coil. At the same time, the overall SNR of the obtained images is 43% higher compared to same images obtained with a birdcage coil. We also have assessed the SAR to investigate safety aspect of the opencage coil. The local SAR_{10g} for the opencage is 0.5 W/kg, whereas for the birdcage coil it equals 0.52 W/kg.

In Chapter 4, we have proposed and tested two dual-band coils. These coils are based on 2 completely different principles. In the first part of the chapter we have proposed a new design for a transmit/receive dual-tuned nested volume coil based on the combination of a birdcage and a closed SLRs metasurface [24]. The developed coil is devoted for $^{19}F/^1H$ imaging of rodents at 7 T. We have studied numerically the proposed geometry with FEM solver. The homogeneity of B_1^+ field at the two selected Larmor frequencies is suitable for preclinical imaging. Then, we have presented MRI tests performed with the phantom. However, the quality of the acquired images is appropriate for fluorine but not for proton. Actually, the coil prototype was unsuccessful due to many difficulties related to the joint adjustment of the 2 structures.

The dual band opencage coil proposed in the second section is based on second order filter. We have conducted the investigation for a coil working simultaneously for ^{13}C and ^1H at 7 T. The design is based on a bandpass network wherein both frequency bands can be tuned independently by adjusting the capacitances in the rings or in the legs: leg capacitance (C_l) mainly tunes high frequency band, while ring capacitance (C_r) mainly tunes low frequency band. However, contrary to the first order filter, in the second order filter the proper values of capacitances and inductances cannot be explicitly computed. Hence, in order to design a unit cell, a constrain optimization method has been used. Eventually, we have verified the proposed approach in full-wave simulations, wherein the appropriate field homogeneity is observed.

Finally, in Chapter 5, we have described a method to build a "conjugated" UHF birdcage that focuses a B_1^+ field spot. Particularly, a FEM simulation with elementary current sources has provided the phase shifts of currents needed to apply to each leg in order to focus B_1^+ field on another location than the center as for a birdcage coil. From that distribution the inductances and capacitances have been computed and therefore the width of unit cell elements has been evaluated as well.

At first, this approach has been applied for a head coil at 7 T. However, because of the difficulty to its realization, the concept has been tested experimentally at 17.2 T for rodents imaging. The resulting images have shown a focal spot displacement of 2.2 mm in simulations and 1 mm in measurements. Thus, the proposed concept should be improved in order to become an efficient tool for passive B_1 shimming at UHF MRI. This conjugated coil can be especially useful for spectroscopy, wherein the signal enhancement in a limited volume can be important.

Perspectives. As it was already mentioned the opencage head coil offers comfort for patients compared to the conventional shielded birdcage coil. In addition, the coil is especially suitable for motion correction at UHF MRI such as 7 T and some other applications. However, the common setup in 7 T MRI is a combination of a birdcage coil for transmit and an embedded tight fit phased array coil for receive. To that end, the perspective of this work is to develop a larger detunable opencage coil only for transmit and combine it with a receive phased array coil.

By lack of time, the dual-band opencage coil for carbon and proton, was not tested experimentally, however expected to be built and tested on bench and in MRI condition. Ideally, this dual-band opencage coil has to be combined with a dual-band receive phased array coil as well.

Concerning phase conjugation, one can note that conjugated birdcage coil can be improved to provide a more dramatic focusing spot shift. Instead of using LP cells, one can consider use of BP unit cells having the same kind of behavior as LP unit cells at the high-frequency band. In addition, conjugated birdcage can be reconfigurable, namely by using varicap diodes that can vary capacitance in each unit cell depending on an applied voltage. Therefore, such parameters as impedance and phase can be controlled electrically without geometrical reconfiguration of the coil.

Journal papers and conference proceedings

Anton Nikulin, Julien de Rosny, Kylian Haliot, Benoit Larrat, Abdelwaheb Ourir, "Opencage radio frequency coil for magnetic resonance imaging," **Appl. Phys. Lett.** 114, 053503 (2019).

Anton Nikulin, Benoit Larrat, Julien de Rosny, Abdelwaheb Ourir, "Volume coil for MRI based on metasurface," **13th European Conference on Antennas and Propagation (EU-CAP 2019)** (2019).

Anton Nikulin, Julien de Rosny, Benoit Larrat, Kylian Haliot, Abdelwaheb Ourir, "Opencage Radiofrequency Coil Inspired by Metamaterials," **International Society of Magnetic Resonance in Medicine (ISMRM) 27th Annual Meeting & Exhibition** (2019).

Anton Nikulin, Abdelwaheb Ourir, Julien de Rosny, Stanislav Glybovski, Benoit Larrat, Frank Kober, Redha Abdeddaim, "Dual-tuned birdcage-like coil based on metasurfaces," **Annual International Conference Days on Diffraction (DD)**, 230-234 (2018).

Conference presentations

Anton Nikulin, Marc Dubois, Tania S.Vergara Gomez, Djamel Berrahou, Frank Kober, Alexandre Vignaud, Redha Abdeddaim, Julien de Rosny, and Abdelwaheb Ourir, "Experimental Realization of a Clinical Opencage Head Coil for Ultra-High Field MRI," **International Society of Magnetic Resonance in Medicine (ISMRM) 28th Annual Meeting & Exhibition** (2020).

Anton Nikulin, Marc Dubois, Tania Vergara Gomez, Djamel Berrahou, Alexandre Vignaud, Redha Abdeddaim, Julien de Rosny, Abdelwaheb Ourir, "Experimental Validation of the Concept of an Opencage Head Coil for Ultra-High Field MRI," **14th European Conference on Antennas and Propagation (EuCAP)** (2020).

Anton Nikulin, Benoit Larrat, Kylian Haliot, Abdelwaheb Ourir, Julien De Rosny, "Opencage: RF coil with an adjusted current distribution," **15th International Conference on Magnetic Resonance Microscopy (ICMRM)** (2019).

Anton Nikulin, Julien de Rosny, Benoit Larrat, Kylian Haliot, Redha Abdeddaim, Djamel Berrahou, Vignaud Alexandre, Abdelwaheb Ourir, "Opencage: a metasurface-inspired coil for MRI," **IV International Conference on Metamaterials and Nanophotonics (METANANO)** (2019).

Anton Nikulin, Julien de Rosny, Benoit Larrat, Kylian Haliot, Abdelwaheb Ourir, "Opencage Radiofrequency Coil Inspired by Metamaterials," **International Society of Magnetic Resonance in Medicine (ISMRM) 27th Annual Meeting & Exhibition** (2019).

Anton Nikulin, Abdelwaheb Ourir, Julien de Rosny, Stanislav Glybovski, Benoit Larrat, Frank Kober, Redha Abdeddaim, "Dual-tuned birdcage-like coil based on metasurfaces," **Annual International Conference Days on Diffraction (DD)** (2018).

Résumé Français

A.1   Introduction

L'imagerie par résonance magnétique (IRM) est un appareil non invasif utilisant un rayonnement non ionisant développé pour l'imagerie in vivo. L'IRM est fondée sur la résonance magnétique des noyaux (RMN) qui apparaît avec certains noyaux présentant un moment angulaire (spin) [1]. Grâce à la forte concentration de noyaux (^{1}H), la principale application des scanners IRM est de fournir des images anatomiques quantitatives des tissus basées sur la résonance des protons. Cependant, les scanners IRM sont également utiles à d'autres fins. Par exemple, associée à la spectroscopie par résonance magnétique (MRS), elle peut être utilisée pour étudier les processus métaboliques cellulaires [2], [3]. Profitant de la propriété paramagnétique des globules rouges désoxygénés, l'activité cérébrale peut être contrôlée (IRM fonctionnelle - IRMf) [4]. Cependant, pour certaines applications, le rapport signal / bruit (SNR) fourni par les scanners IRM cliniques actuels d'une intensité de champ de 1,5 Tesla et 3 Tesla n'est pas suffisant [5], [6]. Le SNR étant directement lié à l'intensité du champ, les scanners IRM à ultra haut champ (UHF) comme à 7 T sont prometteurs et deviennent des outils de plus en plus efficaces [7]. Ils ouvrent également la porte à de nouvelles applications telles que l'imagerie des noyaux X (exploitant d'autres noyaux que ^{1}H) [3].

Cependant, l'IRM UHF présente certains problèmes non résolus [8], [9]. L'un d'eux est la diminution de la longueur d'onde due à l'augmentation de la fréquence de Larmor. Par exemple, la longueur d'onde dans les tissus du proton à 7 T (298 MHz) est décimétrique . Par conséquent, les bobines RF ne peuvent plus être considérées comme des sondes magnétostatiques, mais plutôt comme des antennes radiofréquences. Cela rend le développement d'une telle antenne plus difficile.

Dans ce manuscrit, nous proposons une méthode basée sur l'analyse des métamatériaux pour développer des bobines de volume. Plus précisément, nous développons une nouvelle famille de métasurfaces pour construire des bobines de volume aux fonctionnalités innovantes. La métasurface est constituée d'un ensemble de résonateurs périodiques où les derniers résonateurs sont connectés au premier. L'approche en termes de métamatériaux permet d'ajuster précisément l'amplitude et la phase du champ qui se propage le long du métamatériau en forme d'échelle et

peut donc être utilisé pour façonner le champ magnétique presque comme on le souhaite. En fait, la bobine "cage à oiseaux" qui est l'une des bobines de volume les plus efficaces développées depuis les années 80 pour l'IRM appartient à cette famille de métasurface.

La première application, à laquelle nous appliquons cette approche, est liée au fait que pour l'imagerie de la tête à 7T, un réseau est utilisé en réception et une cage à oiseaux en transmission [10]. Malgré des performances satisfaisantes, la combinaison de la cage à oiseaux et du réseau en fait un casque volumineux. De ce fait, il réduit le confort des patients . De plus, cette combinaison ne peut pas être utilisée pour certaines applications, telles que la correction de mouvemen [11].

Dans ce but, nous proposons ici d'utiliser cette approche de métasurface pour développer une bobine en forme de cage à oiseaux dans laquelle la distance entre les éléments n'est pas constante. Nous avons appelé cette bobine "opencage" [12]. Cette bobine facilite l'accès à un patient ou à un échantillon à scanner grâce à l'élargissement de la distance entre certains éléments de la bobine. Deux prototypes ont été développés à 7 T. Le premier est dédié à l'imagerie préclinique des petits rongeurs et le second à l'imagerie clinique des têtes humaines. Parce que l'utilisation de noyaux autre que l'hydrogène devient de plus en plus courante, nous proposons une bobine ouverte à double fréquence.

La deuxième application est liée au manque d'homogénéité du champ B_1 en IRM UHF. Cela implique une réduction du SNR dans certaines régions où le champ B_1 est faible. Ce problème est particulièrement associé à l'imagerie cérébrale ou à l'imagerie du corps, car la longueur d'onde (λ) dans les tissus est inférieure à la taille du volume étudié. L'acquisition ou la transmission parallèle avec des réseaux de bobines est une solution pour résoudre ce problème. En fait, l'acquisition parallèle est déjà utilisée pour les scanners cliniques fonctionnant à 1,5 et 3 T [13], [14] ainsi que pour ceux à 7 T [10]. En ce qui concerne la transmission, la technique est appelée B_1 shimming [9], [15]. La combinaison de réseau d'émission et de réception offre des performances exceptionnelles, mais au prix d'une importante complexité.

Une solution plus simple est le shimming passif exploitant des éléments diélectriques non résonnants [16] ou des résonateurs hybridisés [17]. Ici, nous proposons une alternative inter-médiaire entre la transmission/réception parallèle et le shimming passif. Cette alternative est appelée bobine de cage à oiseaux conjuguée ou métacage. Il permet de focaliser le champ B_1 sur un autre emplacement que le centre de la bobine. Dans un premier temps, nous étudions ce concept pour l"imagerie cérébrale à 7 T, puis nous proposons un autre prototype fonctionnant à 17,2 T pour l'imagerie préclinique de petits animaux [25].

A.2   Chapitre 1: Techniques de pointe et nouvelles technologies d' imagerie par résonance magnétique à ultra-haut champ

Dans ce chapitre, nous décrivons les aspects les plus importants de l'imagerie par résonance magnétique (IRM). La RMN est basée sur la précession de Larmor de certains noyaux dans un fort champ magnétique statique B_0 [34]. Le moment angulaire (spin) précesse à une fréquence

(fréquence de Larmor) donnée par:

$$f = \gamma/2\pi B_0. \tag{A.1}$$

Où $\gamma/2\pi$ est le rapport gyromagnétique, B_0 est un champ magnétique statique.

Lorsqu'un matériau est placé dans un champ magnétique statique intense B_0 , à l' équilibre thermique, l'état d'énergie de la rotation le plus bas est plus peuplé que la plus élevée et l'aimantation M devient alignée avec B_0 (Fig. A.1).
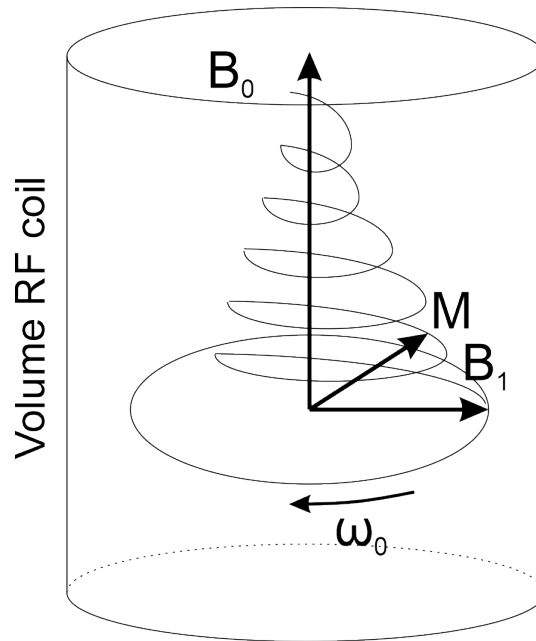
Figure A.1 – Principe du flip de magnétisation RMN.

Cependant, l' orientation de M peut être modifiée en appliquant un champ radiofréquence supplémentaire (B_1^+) oscillant à la fréquence de Larmor avec une polarisation circulaire qui est transversale au champ statique B_0. Le sens de rotation doit être identique à celui de la précession de Larmor [35]. Du fait de cette excitation stimulée de l'état de spin, l'aimantation M devient progressivement parallèle au champ B_1 . Par conséquent, l'angle de basculement maximal (FA) est de 90°.

Lorsque l'excitation du champ B_1^+ est interrompue, les spins nucléaires cessent progressivement de s'aligner, de sorte que l'aimantation M revient à son état initial. Au cours de ce processus, un écho, c'est-à-dire un champ RF, B_1 - est généré par les spins à la fréquence de Larmor [35].

Cet écho peut être collecté par la même bobine que celle d'émission ou une autre bobine dédiée à la réception [36]. La fréquence de travail de la bobine d'émission / réception est déterminée à partir de l'équation de Larmor, c.-à-d., à partir des noyaux étudiés.

Opérations UHF. Le principal avantage des scanners UHF, tels que les 7 T, est de fournir un SNR supérieur par rapport aux systèmes 1,5 T et 3 T [5], [7]. Un SNR plus élevé permet d'améliorer la qualité des images acquises et ainsi de détecter des maladies à un stade précoce. Un SNR plus élevé permet également de tirer de l'information quantitative de noyaux X, ce qui est difficilement le cas avec les IRM à 1,5 T [3].

En fait, l'augmentation fondamentale du SNR provient de l' aimantation de spin M. En effet ce dernier s'exprime par la formule [22]:

$$M = \rho_0 \frac{\gamma^2 \hbar^2}{4kT} B_0. \tag{A.2}$$

Où ρ_0 est la densité de spin du proton, γ est le rapport gyromagnétique ($\gamma/2\pi$), $\hbar$ est la constante de Planck réduite, k est la constante de Boltzmann, T est la température absolue (en Kelvin) et B_0 est le champ magnétique statique. On observe que l'aimantation M évolue linéairement avec l'intensité du champ B_0. Cependant, le SNR ne dépend pas linéairement du champ B_0.

En pratique, le SNR dépend de nombreux facteurs, par exemple la résolution spatiale (taille du voxel), le bruit thermique de l'échantillon, le bruit de l'électronique, le facteur de qualité de la bobine ainsi que le champ statique B_0.

Cependant, l' IRM UHF présente certains désavantages. L'un d'entre eux est la détérioration de l'homogénéité du champ B_1 en raison de la diminution de la longueur d' onde. Par exemple à 7 T, la longueur d'onde est aussi petite que $\lambda \approx 12$ cm dans les tissus [8]. En conséquence, une bobine conventionnelle ne peut pas générer un champ uniforme sur certains organes tels que la tête. Une zone sombre se produit lorsque le champ RF n'est pas suffisant pour inverser correctement l'aimantation (angle de basculement), ce qui entraîne une baisse du SNR. Une solution pour résoudre ce problème est l'utilisation de réseaux de bobines [13] où les amplitudes et les phases de chaque élément peuvent être réglées [9]. Cette technique de transmission parallèle (pT_x) [15], [53], [54] permet également de baisser le SAR [9]. Contrairement aux réseaux, les bobines conventionnelles sont généralement beaucoup plus proches des limites SAR en raison de la puissance plus élevée nécessaire pour obtenir un FA suffisant sur toute la zone à imager [22].

Néanmoins du fait de leur facilité d'usage, elles restent un élément indispensable même dans les IRM à haut champ. Ici nous proposons une approche globale pour réaliser des bobines volumiques à base de métamatériaux pour répondre à certaines problématiques des IRM UHF.

Projet M-CUBE (MetaMaterials for MRI). Ce travail a été réalisé dans le cadre du projet européen M-CUBE [59]. Ce projet réunit 8 universités et 2 partenaires industriels répartis dans le monde entier. Le projet vise à dépasser les limites de l'IRM clinique UHF. En rassemblant des experts en IRM et des physiciens travaillant dans le domaine de pointe des métamatériaux électrodynamiques, il est prévu de résoudre certaines restrictions fondamentales de l'IRM UHF dues aux bobines RF.

Dans cette partie nous réalisons un état des lieux d'une part des principales bobines utilisées en IRM et d'autre part des réseaux phasés. Nous terminons cette partie par une présentation des principales recherches sur les bobines à base de métamatériaux.

Bobine RF. Nous discutons ici de la classification des bobines RF utilisées pour l'IRM UHF. La conception et l'évaluation de bobines RF sont essentielles pour une imagerie IRM sûre et réussie. Pour rappel, des bobines RF sont nécessaires pour exciter les spins des noyaux (inverser leur aimantation) avec un champ B_1 (bobine d'émission) et un écho des noyaux de

sondage (bobine de réception). Ces deux opérations peuvent être effectuées par une seule bobine fonctionnant en mode émission/réception ou par deux bobines distinctes [36]. Généralement, les bobines RF peuvent être classées en deux groupes selon l'application: bobines de surface et bobines de volume, ou en deux groupes selon la fonctionnalité des bobines: bobines de réception ou d'émission.

Bobines de transmission. Contrairement aux bobines de réception (voir ci-dessous), les dimensions de la bobine d'émission sont généralement grandes. Malgré de nombreuses bobines de volume existantes pour l'IRM, telles que la bobine selle ou demi-selle [79], [71], la bobine de Helmholtz [165], la bobine de solénoïde [75], [188], nous nous concentrons ici uniquement sur les bobines, qui sont les plus usuelles en imagerie de la tête humaine UHF. La bobine de référence en transmission pour la plupart des scanners cliniques de 1,5 T et 3 T est une bobine cage à oiseaux intégrée au scanner [80]. Cette dernière est désacordable et associée à un réseau en réception [10], [174]. Une alternative à la cage à oiseaux à UHF est une bobine TEM de volume [81] particulièrement adaptée à l'imagerie de la tête à 7 T [28].

Récemment, des travaux sont menés sur les scanners UHF pour remplacer les bobines de transmission par des réseaux de bobines [51].

Les paramètres importants pour évaluer les performances des bobines de transmission sont:

- Efficacité de transmission ($\frac{B_1^+}{\sqrt{P}}$) liée à la puissance d'entrée [60];

- Homogénéité du champ magnétique B_1^+, qui peut être évaluée avec l'erreur quadratique moyenne normalisée (NRMSE) ou l'écart-type normalisé;

- Pour la bobine d'émission, le taux d'absorption spécifique (SAR) mesuré en W/kg, ou ce qui est plus pertinent - l' efficacité SAR, définie comme ($\frac{B_1^+}{\sqrt{SAR_{10g}}}$). Ainsi, la puissance d'entrée a une certaine limite liée à une limite SAR [61]. Cependant, la limite SAR ne dépend pas de l'intensité du champ, bien que la dissipation de puissance soit plus élevée dans le corps humain à une fréquence plus élevée [3]. De plus, l'inhomogénéité du champ électrique peut produire des points chauds locaux, qui ne sont pas souhaitables. Ce problème peut également être surmonté avec des réseaux phasés T_x en ajustant les amplitudes et les phases dans chaque élément [3].

Bobines en réception. Contrairement aux bobines d'émission, les bobines de réception idéales doivent être aussi petites que possible pour être au plus proche du volume scanné. La bobine R_x doit être sensible en fournissant un SNR élevé. Le SNR moyen de l'image peut être défini comme un signal moyen sur l'écart-type du bruit. La bobine la plus simple est une bobine à boucle unique [63], [189]. Cette bobine de surface est un outil utile en imagerie préclinique, quel que soit l'intensité de champ [64] et un outil clinique pour le poignet, les articulations des orteils et des doigts, la peau, l' imagerie des articulations temporo- mandibulaires [66]. Cette bobine boucle peut être utilisée comme bobine de réception uniquement ou comme bobine d'émission/réception. Les bobines de surface peuvent avoir différentes géométries, telles qu'en zigzag [190], en forme de papillon [191], ou croisée [192].

A.3   Chapitre 2: Bobine volumique à base de méta-matériaux

Ce chapitre révèle les principaux aspects théoriques de la conception de nouvelles bobines RF de volume pour l'IRM préclinique et clinique à ultra haut champ (UHF). Les bobines, proposées dans ce travail, sont inspirées des bobines de cage à oiseaux [80], [138]. Depuis leur introduction en 1985, les bobines de cage à oiseaux ont joué l'un des rôles clés dans l'imagerie IRM clinique et préclinique [71], [70]. Plusieurs approches théoriques pour décrire les bobines de cage à oiseaux sont déjà connues dans la littérature [104], [139], [140], [141], [142]. Toutes ces approches énoncées ci-dessus peuvent être utilisées pour ajuster la fréquence de fonctionnement d'une cage à oiseaux.

Dans cette étude, nous proposons d'appliquer la théorie des lignes de transmission pour décrire directement une bobine de cage à oiseaux [71]. En effet, une bobine de cage à oiseaux peut être considérée comme un réseau de périodique composé de cellules unitaires avec des éléments L et C. L'esquisse du réseau est représentée sur la figure A.2(a, b), et la cellule unitaire est représentée sur la figure A.2(c). Une seule cellule unitaire (ou barreau d'une échelle) peut être complètement décrite par une matrice de transmission ABCD [71]. Cette approche proposée est couramment utilisée dans la théorie des métamatériaux [12].

À partir de cette analyse, chaque cellule élémentaire d'une bobine de cage est complètement caractérisée par son impédance de Bloch ou d'impédance caractéristique et son déphasage. Ces valeurs peuvent être déduites des valeurs propres et vecteurs propres de la matrice de transmission T_i [12]. À partir des impédances et admittances introduites sur la figure A.2(b), il vient:

$$\delta\varphi_i = \cos^{-1}\left(1 + Z_i Y_i\right). \tag{A.3}$$

$$Z_b^i = \frac{1}{2}\sqrt{Z_i^2 + \frac{2Z_i}{Y_i}}. \tag{A.4}$$

Sur les figures A.2(d) et A.2(e) sont représentés le déphasage et l'impédance de Bloch pour des cages à oiseau composées de 4, 8 et 16 bras.

Cette approche fondée sur la matrice d'impédance permet de régler individuellement chaque cellule unitaire. Ce travail est la pierre angulaire de ce manuscrit pour concevoir des métacages, c'est-à-dire des bobines en forme de cage à oiseaux présentant une autre géométrie ou une autre distribution de champs.

A.4   Chapitre 3: Bobine RF d'ouverture

L'accès à la région d'intérêt (ROI) peut être souhaitable dans de nombreuses applications cliniques et précliniques. Par exemple, en imagerie cérébrale, elle améliore le confort des patients qui peuvent souffrir de claustrophobie. Il peut également faciliter la voie optique pour envoyer des stimuli visuels aux patients pendant le processus d'imagerie [145]. Pour l'imagerie multi-modale et interventionnelle, il peut faciliter l'accès à l'organe imagé avec une autre modalité telle qu'un laser [146], une sonde à ultrasons [55], un appareil RF ou de cryoablation [147],
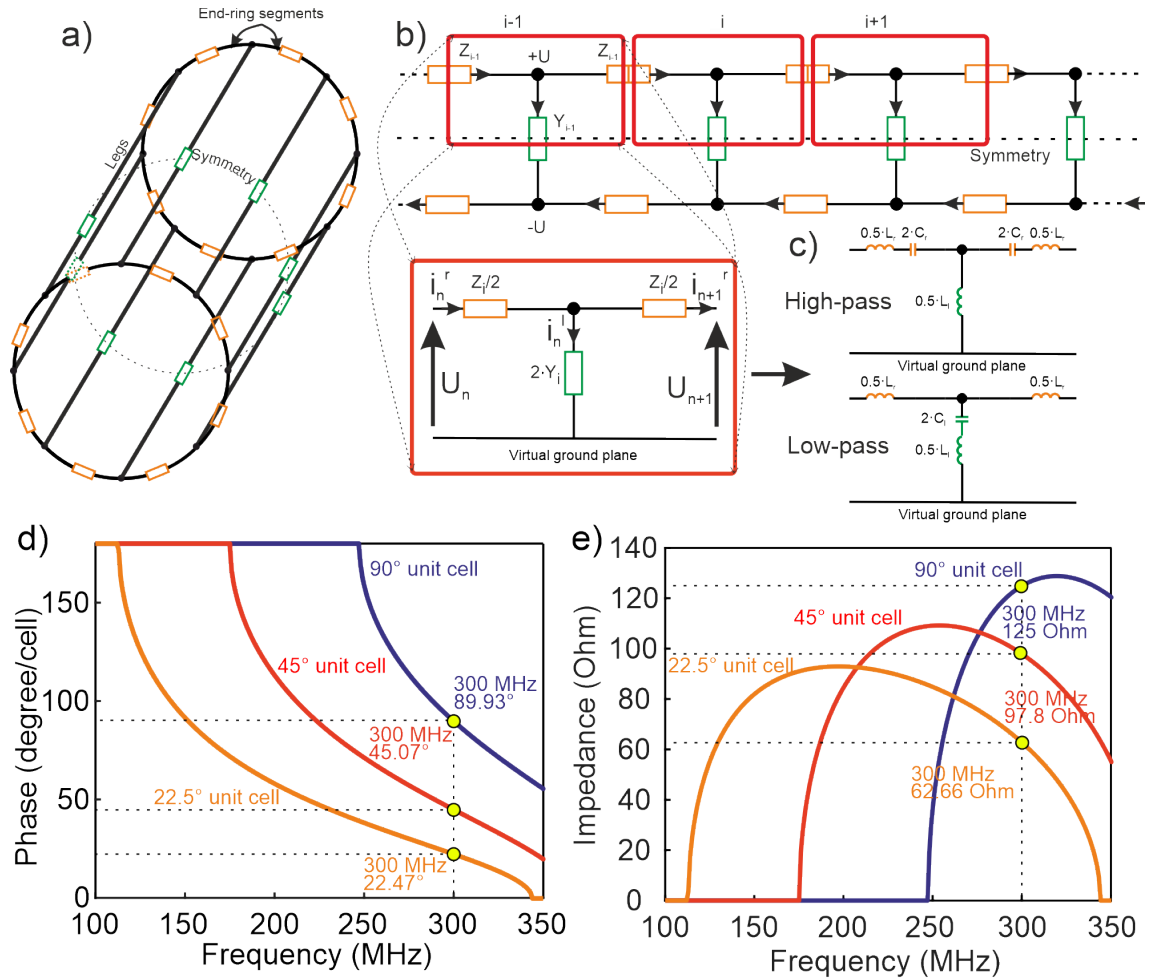
Figure A.2 – **(a) Esquisse d'une bobine de cage à oiseaux composée de huit barreaux. (b) Circuit équivalent simplifié d'un segment de bobine de cage à oiseaux. (c) Les cellules unitaires HP ou LP au moyen d'inductances et de capacités. (d) Diagramme de déphasage (dispersion) tracé pour trois types de cellules unitaires HP correspondant à des cages à oiseaux à 16, 8 et 4 échelons. (e) Diagramme d'impédance tracé pour trois types de cellules unitaires LH (HP) correspondants à des cages à oiseaux à 16, 8 et 4 échelons.**

une aiguille de biopsie [148]. En outre, il peut être utile dans une tâche spécifique telle qu'une correction de mouvement, où une caméra est placée à l'intérieur de l'alésage IRM [11].

De nombreux types de bobines RF ont été utilisés pour les applications indiquées ci-dessus. Cependant, les bobines conventionnelles présentent des inconvénients et, par conséquent, elles ne conviennent pas parfaitement aux applications souhaitées.

Dans ce but, nous proposons ici une bobine en forme de cage à oiseaux dans laquelle quelques bras sont retirés afin de faciliter l'accès à la région d'intérêt. La bobine proposée est appelée «opencage». La bobine d' ouverture nécessite la réalisation d'une structure apériodique avec une distribution de courant donnée sur les barreaux. Il existe une méthode brute fondée sur une approche électrocinétique globale plutôt que locale pour développer de telles structures. Cette solution a été utilisée très tôt pour développer des bobines de cage à oiseaux de formes elliptiques ou ovales [100], [101], [102]. Cependant, ici, nous utilisons une approche dans laquelle la bobine d'ouverture peut être considérée comme une métasurface ou une bobine à base de métamatériaux de ligne de transmission (TL).

A.4.1   Bobine d'ouverture pour l'imagerie préclinique à 7 Tesla

Ce sous-chapitre décrit la bobine d' ouverture développée pour l' imagerie préclinique de petits animaux à 7 T (300,1 MHz) . Alors qu'une bobine de cage à oiseaux conventionnelle pour l'imagerie préclinique UHF à 7 T contient généralement huit éléments (huit cellules à 45°), la bobine d'ouverture proposée est composée de deux types différents d'éléments (cellules), comme le montre la figure A.3(a) . Pour connecter ces cellules unitaires (cellules 45° et 90°), l'impédance Bloch ainsi que le déphasage ont été ajustés selon la théorie fournie dans le chapitre précédent.

Après l'optimisation analytique, la bobine opencage a été simulée en utilisant le CST Microwave Suite 2018 et plus particulièrement son solveur fondé sur les éléments finis. La conception de la bobine est illustrée sur la figure A.3(b). Les paramètres de la bobine tels que l'isolement entre les ports d'alimentation et la distribution du champ ont été vérifiés ont été validés. Ensuite, cette bobine a été fabriquée et testée dans une IRM.

Nous avons acquis plusieurs images in vitro [Fig. A.3(c, d)] . Pour évaluer les performances de cette bobine, nous avons également acquis des images avec une bobine cage à oiseaux conventionnelle de la même taille [Figs. A.3(e, f)]. Le SNR des images a été évalué comme étant le signal moyen dans un carré de 10 par 10 voxels au centre de l'image divisé par l'écart type du bruit. Le bruit est quant à lui évalué sur un carré de 10 par 10 voxels à l'extérieur du fantôme. Les SNR moyens des bobines "opencage" et cage à oiseau sont égaux à 1865 et 1752, respectivement. Par conséquent, on peut en conclure que les performances des 2 bobines sont semblables.

A.4.2   Bobine opencage en quadrature pour l'imagerie clinique du cerveau à 7 Tesla

Cette partie se concentre sur une bobine d'ouverture en quadrature pour l'imagerie clinique du cerveau à 7 Tesla. Dans ce cas, nous avons appliqué la même optimisation que celle proposée précédemment. Cependant, l'augmentation du volume de la bobine et l'exploitation du mode CP nécessitent de résoudre de nouveaux défis. Après avoir été optimisée analytiquement et numériquement, la bobine d'ouverture optimisée a été assemblée [Fig. A.4(a)]. Ensuite, une évaluation en dehors de l'IRM a été effectuée afin d'ajuster la bobine à la fréquence souhaitée.

Ensuite, les cartes de champ magnétique ont été acquises dans l'IRM clinique 7 T de neurospin. Les cartes B_1^+ affichées sur les figures A.4(b, c) été acquises avec 174 V comme tension d'excitation pour la bobine opencage. De manière à évaluer les performances de cette bobine, les résultats sont comparés à ceux obtenus avec une cage à oiseau commerciale. Les champs de la figure A.4(d, e) ont été obtenus avec une tension excitation de 214 V. Ainsi la bobine de cage à oiseaux a démontré une efficacité de transmission légèrement plus élevée. Normalisé par à la tension de référence, l'efficacité de transmission de la cage à oiseaux est égale à 0,034 μT/V au centre des cartes, tandis que pour la bobine opencage, elle est égale à 0,050 μT/V.

L'homogénéité du champ B_1^+ a été évaluée par l'intermédiaire de l' erreur quadratique moyenne normalisée (NRMSE). Le NRMSE est égal à 0,7096 pour la bobine opencage et 0,6267 pour la bobine cage à oiseaux dans la tranche sagittale centrale. Le NRMSE estimé pour le
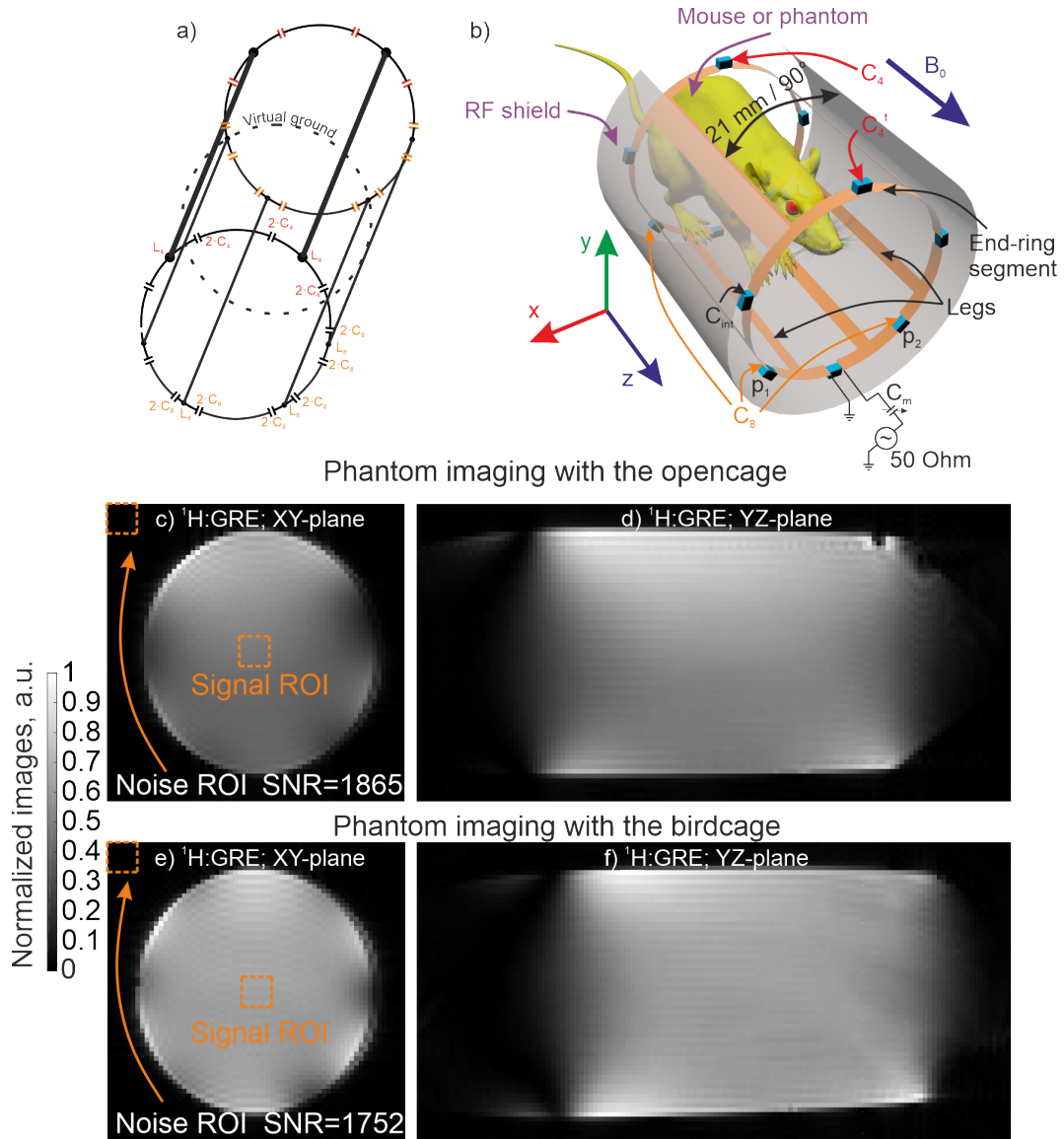
Figure A.3 – **(a) Vue générale de la bobine d'ouverture HP à six échelons pour l'imagerie préclinique à 7 T. (b) Conception finale de la bobine d'ouverture. Les images normalisées acquises avec la bobine d'ouverture: (c) image du fantôme dans le plan transversal central; (d) dans le plan sagittal central; images normalisées acquises avec la bobine de la cage à oiseaux: (e) image fantôme dans le plan transversal central; (f) dans le plan sagittal central.**

fantôme entier est de 0,6589 pour la bobine opencage et de 0,5665 pour la bobine cage à oiseaux. On peut conclure que la bobine cage à oiseaux présente homogénéité plus faible de 14%.

Pour terminer, le SNR moyen des images obtenues a été évalué comme un signal moyen divisé par l'écart type de bruit dans la région d'intérêt. Les résultats sont présentés sur le tableau Tab. A.1.

Comme on peut le voir, le SNR global des images obtenues avec la bobine opencage est environ 43% plus élevé que celui de la bobine commerciale de cage à oiseaux.
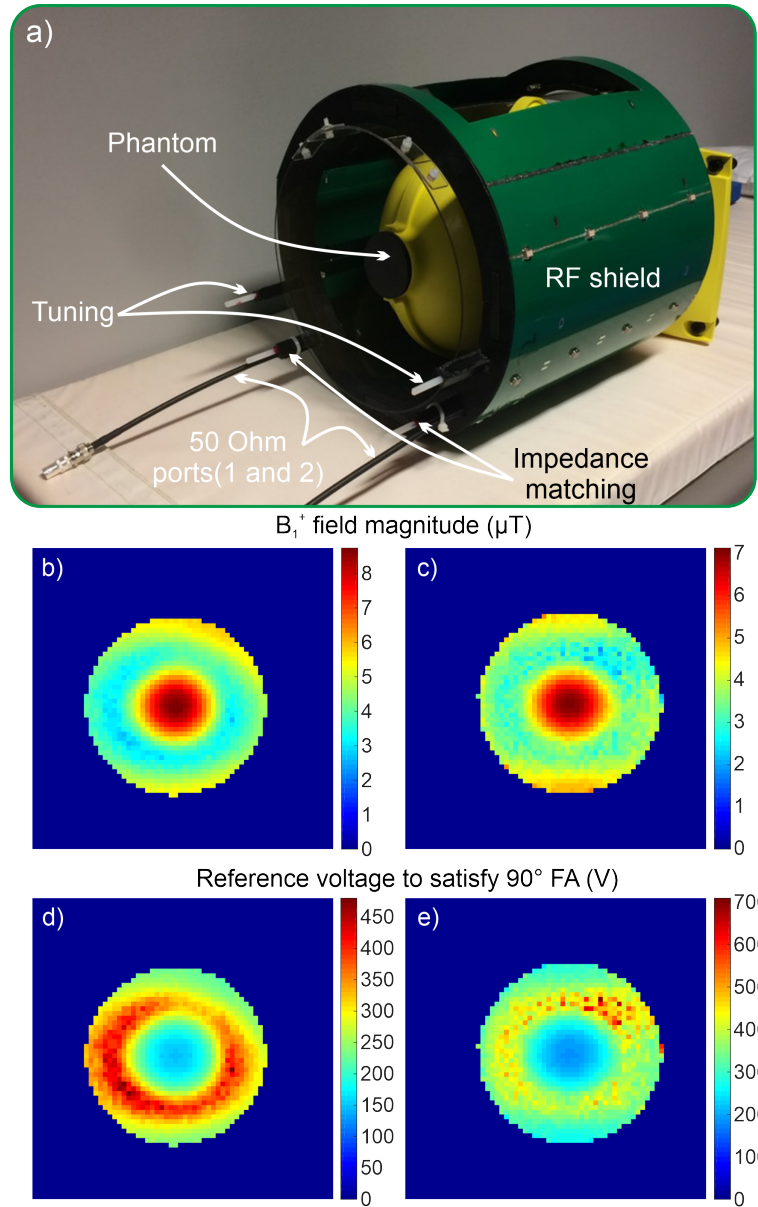
Figure A.4 – (a) Photographie d'une bobine d'ouverture. (b, c) Champ B_1^+ mesuré dans la tranche sagittale centrale pour la bobine de tête à ouverture et la bobine de cage à oiseaux; (d, e) Cartes de tension de référence mesurées dans la tranche sagittale centrale nécessaire pour satisfaire un angle de bascule de 90°.

A.5   Chapitre 4: Bobines de volume à double bande

Le proton ^{1}H permet un imagerie anatomique de grande qualité. Cette dernière peut être complétée grâce aux résonances d'autres noyaux X [164] qui conduisent à plusieurs applications biologiques différentes comme le suivi des cellules injectées avec par exemple la détection et la quantification de la thérapie cellulaire immunitaire contre le cancer en utilisant du fluor ^{19}F [46], [47]; l'étude du métabolisme tissulaire par le phosphore ^{31}P associés à de nombreux troubles et maladies [48]; la recherche des effets du déséquilibre du sodium dans la pathologie de la sclérose en plaque en utilisant l' imagerie au sodium ^{23}Na [7]; l'imagerie du cancer du sein à l'aide de carbone hyperpolarisé ^{13}C [49] ou encore la cartographie du métabolisme avec le deutérium ^{2}H [50].

Table A.1 – SNR moyen de la bobine d'ouverture et de cage à oiseaux en trois tranches.

Bobine	Tranche coronale	Coupe sagittale	Coupe transversale
Volière	240.4	229.3	198.1
Ouverture	326.4	337.3	287.3

A.5.1 Bobine de volume à double bande pour l'imagerie préclinique ^{19}F/^{1}H à 7T

Dans la première section, nous proposons une conception originale de bobine volumique à double bande imbriquée dédiée à l'imagerie du fluor ^{19}F et du proton ^{1}H. comme il a été mentionné précédemment, le ^{19}F peut être utilisé comme agents de contraste [46] permettant une surveillance et un suivi précis des cellules injectées dans un corps. Le ^{1}H est utilisé pour l'imagerie anatomique nécessaire à la localisation du ^{19}F injecté en raison de l'absence d'abondance naturelle de fluor. L'une des principales difficultés dans la conception des bobines est la proximité des fréquences de Larmor du proton (300,1 MHz) et du fluor (282,6 MHz) qui interdit l'usage d'un filtre de second ordre [92].

La bobine considérée se compose de deux structures concentriques. Dans chacune d'entre elles, les cellules unitaires sont distribuées périodiquement formant un cylindre [Fig. A.5(a)] . La première structure dédiée au fluor est une cage à cage à oiseaux passe-haut (HP) inventée par Cecil Hayes en 1985 [80].

La deuxième structure qui responsable de l'imagerie des protons à 300,1 MHz est constituée d'un réseau de six résonateurs à boucle ouverte (SLR pour split loop résonator) répartis sur un cercle de 30 mm de rayon. Le couplage entre ces SLR a été étudié précédemment dans [170], [171]. L'orientation entre les SLR modifie l'inductance mutuelle entre eux. Il est positif lorsque les SLR sont parallèles et négatifs s'ils sont coplanaires [170]. En conséquence, le comportement de cellules est de type main gauche lorsque les SLR sont coplanaires ou de type main droite lorsqu'ils sont coaxiaux [170]. Dans notre cas, le comportement des SLR est main droite. Par conséquent, le mode fondamental qui génère un champ magnétique homogène est situé à la fréquence la plus basse parmi la pluralité de modes. Le champ magnétique correspondant à chaque structure est présenté sur la figure A.5(b, c).

A.5.2 Bobine d'ouverture bibande

Ici, nous proposons de développer une bobine "opencage" bibande. Contrairement à la section précédente, nous concentrons notre attention sur deux noyaux avec des fréquences de Larmor très différentes (^{13}C/^{1}H) à 7 T . Dans ce cas, nous proposons de concevoir la cellule unitaire comme un filtre coupe-bande (BS) ou passe-bande (BP), qui est utilisée pour les cages à oiseaux à double bande comme décrit dans [92].

La bobine conçue a été testée numériquement avec un code d'éléments finis (CST Studio
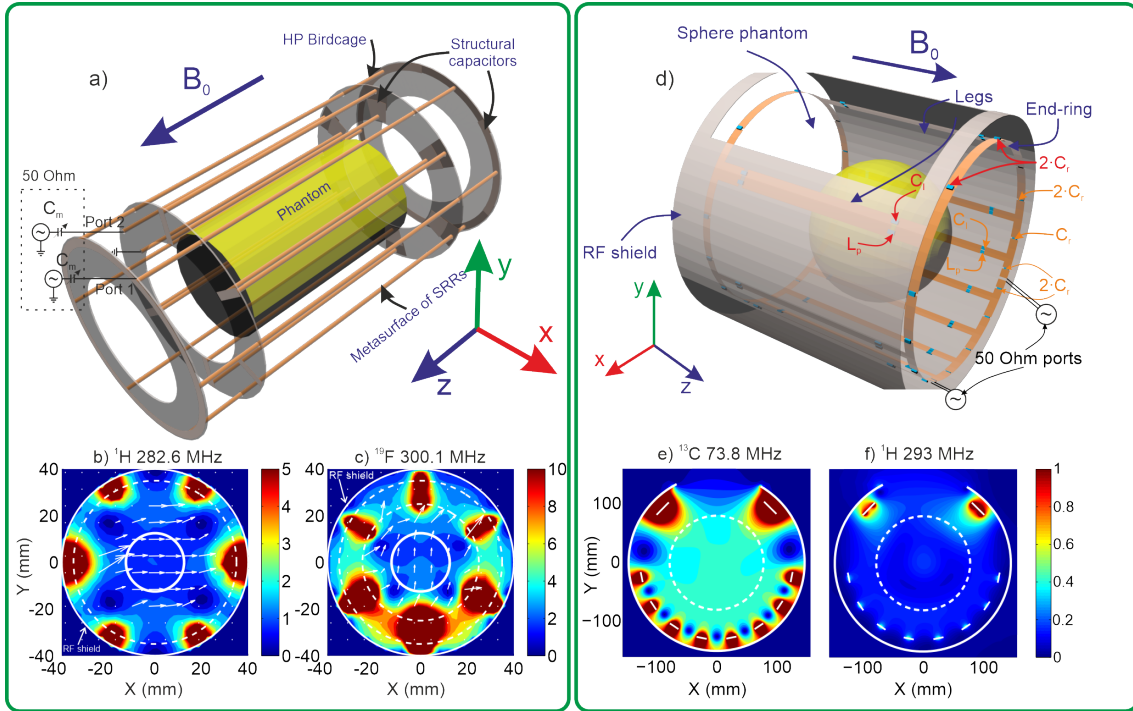
Figure A.5 – **(a) Vue générale de la bobine à double accord chargée par le fantôme ; amplitude du champ magnétique à l'intérieur de la bobine dans le plan transversal central (Z = 0) obtenu par simulation: (b) mode de la cage à oiseaux HP à 282,6 MHz; (c) mode de la métasurface deSLR à 300,1 MHz ; (d) Vue générale de la bobine d'ouverture bibande simulée chargée par un fantôme sphérique; (e, f) distributions de champ B_1^+ dans les tranches transversales centrales de la bobine d'ouverture bibande optimisée à 73,8 MHz et 293 MHz respectivement.**

Suite). La figure A.5(d) présente une vue générale de la bobine, excitée en quadrature par deux ports 50 ohms distants de 90°. Un blindage avec une ouverture recouvre la bobine.

La bobine a été ajustée pour fonctionner aux deux fréquences pour ^{13}C et ^{1}H. Les cartes de champ magnétique B_1^+ ont été calculées pour les deux bobines [Fig A.5(e, f)]. On observe que l'homogénéité du champ est acceptable aux deux fréquences.

A.6   Chapitre 4: Bobine de métacage inspirée du conjugué de phase pour l'IRM UHF

Le but de ce chapitre est de concevoir une bobine spécifique inspirée de la conjugaison de phase ([144], [178], [179]) capable de focaliser le champ B_1^+ dans une région de l'échantillon à imager autre que le centre comme c'est le cas pour les cages à oiseaux [80]. A bas champ, une cage à oiseaux génère un champ magnétique est homogène [9], mais ce dernier devient très hétérogène à 7 T [9]. Contrairement à la distribution de phase conventionnelle, nous proposons ici d'imposer des distributions de phase spécifiques qui peuvent assurer le décalage du point focal B_1^+ vers n'importe quelle position. En d'autres termes, nous proposons ici un nouveau type de technique de shimming passif B_1^+.

Dans la première étape d'un processus de conjugaison de phase, nous considérons une source placée dans un fantôme. Ici, la source est un dipôle magnétique polarisé circulairement dans

le plan de simulation pour obtenir après inversion temporelle un champ magnétique polarisé circulairement. La phase de l'amplitude du champ électrique est sondée à chaque position du bras de la metacage. Lorsque la source est au centre, le déphasage entre deux conducteurs consécutifs est égal à $2\pi/N$ (N = 8) tandis qu'il devient plus complexe lorsque la source est hors du centre (voir figure 3). Dans la deuxième étape de l'inversion du temps, les amplitudes complexes des courants sont réglées sur , c'est- à -dire conjuguées en phase (voir figure 6). Les distributions de champ magnétique polarisées circulairement qui en résultent pour les deux emplacements de source initiaux sont représentées sur la figure 6 . Lorsque la source est placée au centre de l'installation, la conjugaison de phase est évidemment équivalente à la cage à oiseaux un champ B_1^+ concentré au centre [Fig. A.6(a)].

Maintenant, si la source est déplacée de 25 mm du centre, on observe bien que les courants conjugués en phase engendrent un champ qui focalise bien le champ à la position de la source initiale [Fig. A.6(b)].

L'application d'un déplacement aussi important nécessite de combiner des cellules passe-bas et passe-haut. Pour simplifier la réalisation d'une telle bobine, nous nous limitons uniquement à un décalage de 6 mm à l'intérieur du fantôme pour un scanner petit animal fonctionnant à 17.2 T afin de n'utiliser que des cellules HP. La distribution de champ B_1 pour ce déplacement obtenu dans les simulations 2d est présentée sur la figure A.6(d), tandis que la distribution de champ B_1 qui serait obtenue avec une cage à oiseau est représentée sur la figure A.6(c).
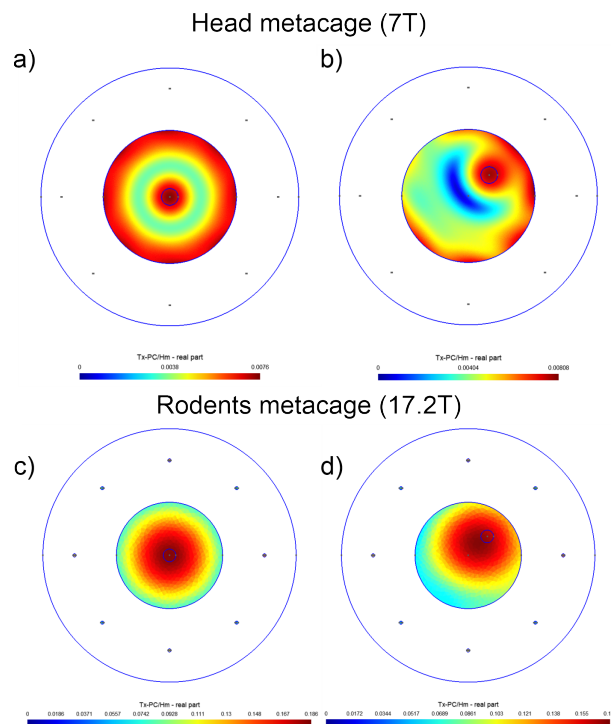

Figure A.6 – **(a, c) Champs B_1^+ engendrés par des cages à oiseau fonctionnant à 7 T et 17.2 T, respectivement, pour l'imagerie du proton. (b, d) Champs B_1^+ engendrés par des bobines opencage fonctionnant à 7 T et 17.2 T, respectivement, pour l'imagerie du proton.**

Après avoir effectué une optimisation analytique et numérique, la bobine a été assemblée et testée.

References

[1] P C Lauterbur. Image formation by induced local interactions: Examples employing nuclear magnetic resonance. *Nature*, 242(5394):190–191, 1973.

[2] B. Ross and T. Michaelis. Clinical applications of magnetic resonance spectroscopy., dec 1994.

[3] Mark E Ladd, Peter Bachert, Martin Meyerspeer, Ewald Moser, Armin M Nagel, David G Norris, Sebastian Schmitter, Oliver Speck, Sina Straub, and Moritz Zaiss. Pros and cons of ultra-high-field MRI/MRS for human application. 109:1–50, dec 2018.

[4] Gary H. Glover. Overview of functional magnetic resonance imaging, apr 2011.

[5] Rolf Pohmann, Oliver Speck, and Klaus Scheffler. Signal-to-noise ratio and MR tissue parameters in human brain imaging at 3, 7, and 9.4 tesla using current receive coil arrays. *Magnetic Resonance in Medicine*, 75(2):801–809, feb 2016.

[6] Anja G Van Der Kolk, Jeroen Hendrikse, Jaco J M Zwanenburg, Fredy Visser, and Peter R Luijten. Clinical applications of 7 T MRI in the brain, may 2013.

[7] Konstantin Huhn, Tobias Engelhorn, Ralf A Linker, and Armin M Nagel. Potential of sodium MRI as a biomarker for neurodegeneration and neuroinflammation in multiple sclerosis, feb 2019.

[8] J.T. Vaughan, M. Garwood, C.M. Collins, W. Liu, L. DelaBarre, G. Adriany, P. Andersen, H. Merkle, R. Goebel, M.B. Smith, and K. Ugurbil. 7T vs. 4T: RF power, homogeneity, and signal-to-noise comparison in head images. *Magnetic Resonance in Medicine*, 46(1):24–30, jul 2001.

[9] Andrew G. Webb and Christopher M. Collins. Parallel transmit and receive technology in high-field magnetic resonance neuroimaging. *International Journal of Imaging Systems and Technology*, 20(1):2–13, feb 2010.

[10] G C Wiggins, C J Wiggins, A Potthast, V Alagappan, O Kraff, A Reykowski, and L L Wald. A 32 Channel Receive-only Head Coil And Detunable Transmit Birdcage Coil For 7 Tesla Brain Imaging. Technical report, 2006.

[11] Robert Frost, Paul Wighton, F. Işık Karahanoğlu, Richard L. Robertson, P. Ellen Grant, Bruce Fischl, M. Dylan Tisdall, and André van der Kouwe. Markerless high-

frequency prospective motion correction for neuroanatomical MRI. *Magnetic Resonance in Medicine*, 82(1):126–144, jul 2019.

[12] Christophe Caloz and Tatsuo. Itoh. *Electromagnetic metamaterials : transmission line theory and microwave applications : the engineering approach.* John Wiley & Sons, 2006.

[13] P. B. Roemer, W. A. Edelstein, C. E. Hayes, S. P. Souza, and O. M. Mueller. The NMR phased array. *Magnetic Resonance in Medicine*, 16(2):192–225, nov 1990.

[14] Graham C Wiggins, C Triantafyllou, A Potthast, A Reykowski, M Nittka, and L L Wald. 32-Channel 3 tesla receive-only phased-array head coil with soccer-ball element geometry. *Magnetic Resonance in Medicine*, 56(1):216–223, jul 2006.

[15] Francesco Padormo, Arian Beqiri, Joseph V Hajnal, and Shaihan J Malik. Parallel transmission for ultrahigh-field imaging. *NMR in Biomedicine*, 29(9):1145–1161, sep 2016.

[16] Qing X. Yang, Weihua Mao, Jinghua Wang, Michael B. Smith, Hao Lei, Xiaoliang Zhang, Kamil Ugurbil, and Wei Chen. Manipulation of image intensity distribution at 7.0 T: Passive RF shimming and focusing with dielectric materials. *Journal of Magnetic Resonance Imaging*, 24(1):197–202, jul 2006.

[17] Marc Dubois, Lisa Leroi, Zo Raolison, Redha Abdeddaim, Tryfon Antonakakis, Julien De Rosny, Alexandre Vignaud, Pierre Sabouroux, Elodie Georget, Benoit Larrat, Gérard Tayeb, Nicolas Bonod, Alexis Amadon, Franck Mauconduit, Cyril Poupon, Denis Le Bihan, and Stefan Enoch. Kerker Effect in Ultrahigh-Field Magnetic Resonance Imaging. *Physical Review X*, 8(3):31083, sep 2018.

[18] I I Rabi, J R Zacharias, S Millman, and P Kusch. A new method of measuring nuclear magnetic moment [5], feb 1938.

[19] F Bloch, W W Hansen, and Martin Packard. Nuclear induction [5], feb 1946.

[20] E M Purcell, H C Torrey, and R V Pound. Resonance absorption by nuclear magnetic moments in a solid [7], jan 1946.

[21] P Mansfield. Multi-planar image formation using NMR spin echoes. *Journal of Physics C: Solid State Physics*, 10(3), 1977.

[22] Ewald Moser, Freddy Stahlberg, Mark E. Ladd, and Siegfried Trattnig. 7-T MR-from research to clinical applications? *NMR in Biomedicine*, 25(5):695–716, may 2012.

[23] J Sijbers, P Scheunders, N Bonnet, D Van Dyck, and E Raman. Quantification and improvement of the signal-to-noise ratio in a magnetic resonance image acquisition procedure. *Magnetic Resonance Imaging*, 14(10):1157–1163, jan 1996.

[24] Ewald Moser and Siegfried Trattnig. 3.0 Tesla MR systems, jul 2003.

[25] Siegfried Trattnig, Wolfgang Bogner, Stephan Gruber, Pavol Szomolanyi, Vladimir Juras, Simon Robinson, Štefan Zbýň, and Stefan Haneder. Clinical applications at ultrahigh field (7 T). Where does it make the difference? *NMR in Biomedicine*, 29(9):1316–1334, sep 2016.

[26] H. Bomsdorf, T. Helzel, D. Kunz, P. Röschmann, O. Tschendel, and J. Wieland. Spectroscopy and imaging with a 4 tesla whole-body mr system. *NMR in Biomedicine*, 1(3):151–158, jun 1988.

[27] P.-M. L. Robitaille, A. M. Abduljalil, A. Kangarlu, X. Zhang, Y. Yu, R. Burgess, S. Bair, P. Noa, L. Yang, Hui Zhu, B. Palmer, Z. Jiang, D. M. Chakeres, and D. Spigos. Human magnetic resonance imaging at 8 T. *NMR in Biomedicine*, 11(6):263–265, oct 1998.

[28] Nikolai I. Avdievich, Hoby P. Hetherington, Andrey M. Kuznetsov, and Jullie W. Pan. 7T head volume coils: Improvements for rostral brain imaging. *Journal of Magnetic Resonance Imaging*, 29(2):461–465, feb 2009.

[29] Thomas Vaughan, Lance DelaBarre, Carl Snyder, Jinfeng Tian, Can Akgun, Devashish Shrivastava, Wanzahn Liu, Chris Olson, Gregor Adriany, John Strupp, Peter Andersen, Anand Gopinath, Pierre-Francois van de Moortele, Michael Garwood, and Kamil Ugurbil. 9.4T human MRI: Preliminary results. *Magnetic Resonance in Medicine*, 56(6):1274–1282, dec 2006.

[30] Alireza Sadeghi-Tarakameh, Lance DelaBarre, Russell L. Lagore, Angel Torrado-Carvajal, Xiaoping Wu, Andrea Grant, Gregor Adriany, Gregory J. Metzger, Pierre-Francois Van de Moortele, Kamil Ugurbil, Ergin Atalar, and Yigitcan Eryaman. In vivo human head MRI at 10.5T: A radiofrequency safety study and preliminary imaging results. *Magnetic Resonance in Medicine*, 84(1):484–496, jul 2020.

[31] CEA. 11.7 teslas: The World-Record Magnetic Field Generated by a Human MRI Magnet. 2019.

[32] Chunqi Qian, Ihssan S. Masad, Jens T. Rosenberg, Malathy Elumalai, William W. Brey, Samuel C. Grant, and Peter L. Gor'Kov. A volume birdcage coil with an adjustable sliding tuner ring for neuroimaging in high field vertical magnets: Ex and in vivo applications at 21.1 T. *Journal of Magnetic Resonance*, 221:110–116, aug 2012.

[33] Ewald Moser, Elmar Laistler, Franz Schmitt, and Georg Kontaxis. Ultra-High Field NMR and MRI—The Role of Magnet Technology to Increase Sensitivity and Specificity. *Frontiers in Physics*, 5(AUG):33, aug 2017.

[34] Robert W. Brown, Yu Chung N. Cheng, E. Mark Haacke, Michael R. Thompson, and Ramesh Venkatesan. *Magnetic Resonance Imaging: Physical Principles and Sequence Design: Second Edition*, volume 9780471720. Wiley Blackwell, Chichester, UK, jun 2014.

[35] Manushka V. Vaidya, Christopher M. Collins, Daniel K. Sodickson, Ryan Brown, Graham C. Wiggins, and Riccardo Lattanzi. Dependence of B1- and B1+ field patterns of surface coils on the electrical properties of the sample and the MR operating frequency. *Concepts in Magnetic Resonance Part B: Magnetic Resonance Engineering*, 46(1):25–40, feb 2016.

[36] Enzo A. Barberi, Joseph S. Gati, Brian K. Rutt, and Ravi S. Menon. A transmit-only/receive-only (TORO) RF system for high-field MRI/MRS applications. *Magnetic Resonance in Medicine*, 43(2):284–289, feb 2000.

[37] Cynthia B. Paschal and H. Douglas Morris. K-Space in the Clinic, feb 2004.

[38] 3 MAGNETOM Flash · 2/2013 · www.siemens.com/magnetom-world. Technical report.

[39] Gerard E. Boyle, Mary Ahern, Jennie Cooke, Niall P. Sheehy, and James F. Meaney. An interactive taxonomy of MR imaging sequences. *Radiographics*, 26(6), nov 2006.

[40] G M Bydder and R E Steiner. NMR imaging of the brain. *Neuroradiology*, 23(5):231–240, sep 1982.

[41] Michael Markl and Jochen Leupold. Gradient echo imaging, jun 2012.

[42] Kay Nehrke. On the steady-state properties of actual flip angle imaging (AFI). *Magnetic Resonance in Medicine*, 61(1):84–92, jan 2009.

[43] Alexis Amadon, Martijn Anton Cloos, Nicolas Boulant, Marie-France Hang, Christopher John Wiggins, and Hans-Peter Fautz. Validation of a very fast B1-mapping sequence for parallel transmission on a human brain at 7T. *MRM*, 60(9):84, 2008.

[44] Matt A. Bernstein, Kevin F. King, and Xiaohong Joe Zhou. *Handbook of MRI Pulse Sequences.* Elsevier Inc., sep 2004.

[45] J P Cousins. Clinical MR spectroscopy: Fundamentals, current applications, and future potential, 1995.

[46] Mangala Srinivas, Arend Heerschap, Eric T Ahrens, Carl G Figdor, and I Jolanda M de Vries. 19F MRI for quantitative in vivo cell tracking, jul 2010.

[47] Fanny Chapelin, Christian M Capitini, and Eric T Ahrens. Fluorine-19 MRI for detection and quantification of immune cell therapy for cancer, oct 2018.

[48] Yuchi Liu, Yuning Gu, and Xin Yu. Assessing tissue metabolism by phosphorous-31 Magnetic resonance spectroscopy and imaging: A methodology review, dec 2017.

[49] Ferdia A. Gallagher, Ramona Woitek, Mary A. McLean, Andrew B. Gill, Raquel Manzano Garcia, Elena Provenzano, Frank Riemer, Joshua Kaggie, Anita Chhabra, Stephan Ursprung, James T. Grist, Charlie J. Daniels, Fulvio Zaccagna, Marie-Christine Laurent, Matthew Locke, Sarah Hilborne, Amy Frary, Turid Torheim, Chris Boursnell, Amy Schiller, Ilse Patterson, Rhys Slough, Bruno Carmo, Justine Kane, Heather Biggs, Emma Harrison, Surrin S. Deen, Andrew Patterson, Titus Lanz, Zoya Kingsbury, Mark Ross, Bristi Basu, Richard Baird, David J. Lomas, Evis Sala, James Wason, Oscar M. Rueda, Suet-Feung Chin, Ian B. Wilkinson, Martin J. Graves, Jean E. Abraham, Fiona J. Gilbert, Carlos Caldas, and Kevin M. Brindle. Imaging breast cancer using hyperpolarized carbon-13 MRI. *Proceedings of the National Academy of Sciences*, 117(4):201913841, jan 2020.

[50] Henk M De Feyter, Kevin L Behar, Zachary A Corbin, Robert K Fulbright, Peter B Brown, Scott McIntyre, Terence W Nixon, Douglas L Rothman, and Robin A De Graaf. Deuterium metabolic imaging (DMI) for MRI-based 3D mapping of metabolism in vivo. *Science Advances*, 4(8):eaat7314, aug 2018.

[51] Jérémie Clément, Rolf Gruetter, and Özlem Ipek. A combined 32-channel receive-loops/8-channel transmit-dipoles coil array for whole-brain MR imaging at 7T. *Magnetic Resonance in Medicine*, page mrm.27808, may 2019.

[52] Jesús Ruiz-Cabello, Brad P. Barnett, Paul A. Bottomley, and Jeff W.M. Bulte. Fluorine (19F) MRS and MRI in biomedicine. 24(2):114–129, feb 2011.

[53] Ulrich Katscher and Peter Börnert. Parallel RF transmission in MRI, may 2006.

[54] U Katscher. Basic and Tailored RF Shimming in a Multi-transmit Whole Body MR System. Technical Report 7, 2008.

[55] Daniel Speicher, T Bartscherer, F J Becker, J W Jenne, K Mrosk, C Degel, M Günther, and S Tretbar. MRI compatible ultrasound transducers for simultaneous acquisition of coregistered ultrasound to MRI data. In *Physics Procedia*, volume 70, pages 1002–1006. Elsevier, 2015.

[56] Klaas P. Pruessmann, Markus Weiger, Markus B. Scheidegger, and Peter Boesiger. SENSE: Sensitivity encoding for fast MRI. *Magnetic Resonance in Medicine*, 42(5):952–962, 1999.

[57] Mark A. Griswold, Peter M. Jakob, Robin M. Heidemann, Mathias Nittka, Vladimir Jellus, Jianmin Wang, Berthold Kiefer, and Axel Haase. Generalized Autocalibrating Partially Parallel Acquisitions (GRAPPA). *Magnetic Resonance in Medicine*, 47(6):1202–1210, 2002.

[58] Boy, 6, Dies Of Skull Injury During M.R.I. - The New York Times.

[59] M-Cube – MetaMaterials antenna for ultra-high field Mri.

[60] Irena Zivkovic, Catalina Arteaga de Castro, and Andrew Webb. Design and characterization of an eight-element passively fed meander-dipole array with improved specific absorption rate efficiency for 7 T body imaging. *NMR in Biomedicine*, 32(8):e4106, aug 2019.

[61] IEC 60601-2-33:2010 | IEC Webstore.

[62] Axel Haase, Florian Odoj, Markus Von Kienlin, Jan Warnking, Florian Fidler, Alexander Weisser, Mathias Nittka, Eberhard Rommel, Titus Lanz, Bernhard Kalusche, and Mark Griswold. NMR probeheads for in vivo applications. *Concepts in Magnetic Resonance*, 12(6):361–388, jan 2000.

[63] O. C. Morse and J. R. Singer. Blood velocity measurements in intact subjects. *Science*, 170(3956):440–441, oct 1970.

[64] F. David Doty, George Entzminger, Jatin Kulkarni, Kranti Pamarthy, and John P. Staab. Radio frequency coil technology for small-animal MRI. *NMR in Biomedicine*, 20(3):304–325, may 2007.

[65] Michael G. Crowley, Jeffrey L. Evelhoch, and Joseph J.H. Ackerman. The surface-coil NMR receiver in the presence of homogeneous B1 excitation. *Journal of Magnetic Resonance (1969)*, 64(1):20–31, aug 1985.

[66] Loop Coils - Siemens Healthineers Global.

[67] MRI RF Coils | Bruker.

[68] Giulio Giovannetti, Alessandra Flori, Daniele De Marchi, Giuseppe Matarazzo, Francesca Frijia, Silvia Burchielli, Domenico Montanaro, Giovanni Donato Aquaro, and Luca Menichetti. Simulation, design, and test of an elliptical surface coil for magnetic resonance imaging and spectroscopy. *Concepts in Magnetic Resonance Part B: Magnetic Resonance Engineering*, 47B(4):e21361, oct 2017.

[69] Mirjam Visscher, Guillaume Lajoinie, Emilie Blazejewski, Gert Veldhuis, and Michel Versluis. Imported from https://physicsworld.com/a/ct-dose-calculations-can-be-both-quick-and-accurate/. *Physics in Medicine & Biology*, 64(3):034001, apr 2019.

[70] J. Thomas Vaughan and John R. Griffiths. *RF coils for MRI*. Wiley, 2012.

[71] Joël Mispelter, Mihaela Lupu, and André Briguet. *NMR Probeheads for Biophysical and Biomedical Experiments.* IMPERIAL COLLEGE PRESS, jul 2015.

[72] John David Jackson and John Wiley. Classical Electrodynamics Third Edition. Technical report, 1998.

[73] Cecil E. Hayes and Leon Axel. Noise performance of surface coils for magnetic resonance imaging at 1.5 T. *Medical Physics*, 12(5):604–607, sep 1985.

[74] Frederick W. Grover. *Inductance Calculations: Working Formulas and Tables.* Dover publications, 1971.

[75] Raju Subramanian and Andrew G Webb. Design of Solenoidal Microcoils for High-Resolution 13C NMR Spectroscopy. *Analytical Chemistry*, 70(13):2454–2458, jul 1998.

[76] Marine A C Moussu, Luisa Ciobanu, Sergej Kurdjumov, Elizaveta Nenasheva, Boucif Djemai, Marc Dubois, Andrew G Webb, Stefan Enoch, Pavel Belov, Redha Abdeddaim, and Stanislav Glybovski. Systematic Analysis of the Improvements in Magnetic Resonance Microscopy with Ferroelectric Composite Ceramics. *Advanced Materials*, 31(30):1900912, jul 2019.

[77] Joël Mispelter and Mihaela Lupu. Homogeneous resonators for magnetic resonance: A review, apr 2008.

[78] Lizann Bolinger, Manfred G. Prammer, and John S. Leigh. A multiple-frequency coil with a highly uniform B1 field. *Journal of Magnetic Resonance (1969)*, 81(1):162–166, jan 1989.

[79] J. W. Carlson. Currents and fields of thin conductors in rf saddle coils. *Magnetic Resonance in Medicine*, 3(5):778–790, oct 1986.

[80] Cecil E Hayes, William A Edelstein, John F Schenck, Otward M Mueller, and Matthew Eash. An efficient, highly homogeneous radiofrequency coil for whole-body NMR imaging at 1.5 T. *Journal of Magnetic Resonance (1969)*, 63(3):622–628, 1985.

[81] J. Thomas Vaughan, Hoby P. Hetherington, Joe O. Otu, Jullie W. Pan, and Gerald M. Pohost. High frequency volume coils for clinical NMR imaging and spectroscopy. *Magnetic Resonance in Medicine*, 32(2):206–218, aug 1994.

[82] G. Bogdanov and R. Ludwig. Coupled microstrip line transverse electromagnetic resonator model for high-field magnetic resonance imaging. *Magnetic Resonance in Medicine*, 47(3):579–593, mar 2002.

[83] Marcello Alecci and Peter Jezzard. Characterization and reduction of gradient-induced eddy currents in the RF shield of a TEM resonator. *Magnetic Resonance in Medicine*, 48(2):404–407, aug 2002.

[84] Xiaoliang Zhang, Kamil Ugurbil, and Wei Chen. A microstrip transmission line volume coil for human head MR imaging at 4 T. *Journal of Magnetic Resonance*, 161(2):242–251, apr 2003.

[85] H M Borsboom, T Claasen-Vujcic, H J G Gaykema, and T Mehlkopf. Low-frequency quadrature mode birdcage resonator. *Magnetic Resonance Materials in Physics, Biology, and Medicine*, 5(1):33–37, 1997.

[86] M Lupu, J L Dimicoli, A Volk, and J Mispelter. An efficient design for birdcage probes dedicated to small-animal imaging experiments. *Magnetic Resonance Materials in Physics, Biology and Medicine*, 17(3-6):363–371, dec 2004.

[87] D W J Klomp, M Van Der Graaf, M A A P Willemsen, Y M Van Der Meulen, A P M Kentgens, A Heerschap, · M Van Der Graaf, and · A Heerschap. Transmit /receive headcoil for optimal 1 H MR spectroscopy of the brain in paediatric patients at 3 T. *MAGMA*, 17:1–4, 2004.

[88] GE Healthcare Systems | GE Healthcare.

[89] G. H. Glover, C. E. Hayes, N. J. Pelc, W. A. Edelstein, O. M. Mueller, H. R. Hart, C. J. Hardy, M. O'Donnell, and W. D. Barber. Comparison of linear and circular polarization for magnetic resonance imaging. *Journal of Magnetic Resonance (1969)*, 64(2):255–270, sep 1985.

[90] C. N. Chen, D. I. Hoult, and V. J. Sank. Quadrature detection coils-A further improvement in sensitivity. *Journal of Magnetic Resonance (1969)*, 54(2):324–327, sep 1983.

[91] Joseph Murphy-Boesch, Ravi Srinivasan, Lucas Carvajal, and Truman R. Brown. Two Configurations of the Four-Ring Birdcage Coil for 1H Imaging and 1H-Decoupled 31P Spectroscopy of the Human Head. *Journal of Magnetic Resonance, Series B*, 103(2):103–114, feb 1994.

[92] Alan R. Rath. Design and performance of a double-tuned bird-cage coil. *Journal of Magnetic Resonance (1969)*, 86(3):488–495, feb 1990.

[93] Jeffrey R. Fitzsimmons, Barbara L. Beck, and H. Ralph Brooker. Double resonant quadrature birdcage. *Magnetic Resonance in Medicine*, 30(1):107–114, jul 1993.

[94] Smain Amari, Aziz Müfit Ulu??, Jens Bornemann, Peter C. M. Van Zijl, and Peter B. Barker. Multiple tuning of birdcage resonators. *Magnetic Resonance in Medicine*, 37(2):243–251, feb 1997.

[95] J.T. Vaughan, G. Adriany, C.J. Snyder, J. Tian, T. Thiel, L. Bolinger, H. Liu, L. DelaBarre, and K. Ugurbil. Efficient high-frequency body coil for high-field MRI. *Magnetic Resonance in Medicine*, 52(4):851–859, oct 2004.

[96] Yong Pang, Zhentian Xie, Duan Xu, Douglas A. Kelley, Sarah J. Nelson, Daniel B. Vigneron, and Xiaoliang Zhang. A dual-tuned quadrature volume coil with mixed $\lambda/2$ and $\lambda/4$ microstrip resonators for multinuclear MRSI at 7 T. *Magnetic Resonance Imaging*, 30(2):290–298, feb 2012.

[97] D Ballon, M C Graham, S Miodownik, and J A Koutcher. A 64 MHz half-birdcage resonator for clinical imaging. *Journal of Magnetic Resonance (1969)*, 90(1):131–140, oct 1990.

[98] Alex M J Hudson, Walter Köckenberger, and Richard W Bowtell. Open access birdcage coils for microscopic imaging of plants at 11.7T. *Magma: Magnetic Resonance Materials in Physics, Biology, and Medicine*, 10(2):69–74, jun 2000.

[99] A S Peshkovsky, R P Kennan, M E Fabry, and Nikolai I Avdievich. Open half-volume quadrature transverse electromagnetic coil for high-field magnetic resonance imaging. *Magnetic Resonance in Medicine*, 53(4):937–943, apr 2005.

[100] Shizhe Li, Christopher M. Collins, Bernard J. Dardzinski, Chih-Liang Chin, and Michael B. Smith. A method to create an optimum current distribution and homogeneous B1 field for elliptical birdcage coils. *Magnetic Resonance in Medicine*, 37(4):600–608, apr 1997.

[101] Mark C. Leifer. Theory of the quadrature elliptic birdcage coil. *Magnetic Resonance in Medicine*, 38(5):726–732, nov 1997.

[102] Nicola De Zanche, Atiyah Yahya, Fred. E. Vermeulen, and Peter S. Allen. Analytical approach to noncircular section birdcage coil design: Verification with a Cassinian oval coil. *Magnetic Resonance in Medicine*, 53(1):201–211, jan 2005.

[103] Nicola De Zanche, Navjeet Chhina, Kevin Teh, Chris Randell, Klaas P. Pruessmann, and Jim M. Wild. Asymmetric quadrature split birdcage coil for hyperpolarized 3He lung MRI at 1.5T. *Magnetic Resonance in Medicine*, 60(2):431–438, aug 2008.

[104] Chih-Liang Chin, Christopher M. Collins, Shizhe Li, Bernard J. Dardzinski, and Michael B. Smith. BirdcageBuilder: Design of specified-geometry birdcage coils with desired current pattern and resonant frequency. *Concepts in Magnetic Resonance*, 15(2):156–163, jun 2002.

[105] Steven M. Wright, Richard L. Magin, and James R. Kelton. Arrays of mutually coupled receiver coils: Theory and application. *Magnetic Resonance in Medicine*, 17(1):252–268, jan 1991.

[106] Gang Chen, Bei Zhang, Martijn A. Cloos, Daniel K. Sodickson, and Graham C. Wiggins. A highly decoupled transmit–receive array design with triangular elements at 7T. *Magnetic Resonance in Medicine*, 80(5):2267–2274, nov 2018.

[107] James S Hyde, A Jesmanowicz, W Froncisz, J Bruce Kneeland, Thomas M Grist, and Nicholas F Campagna. Parallel image acquisition from noninteracting local coils. *Journal of Magnetic Resonance (1969)*, 70(3):512–517, dec 1986.

[108] Nikolai I Avdievich. Transceiver-Phased Arrays for Human Brain Studies at 7 T. *Applied Magnetic Resonance*, 41(2-4):483–506, dec 2011.

[109] Nikolai I. Avdievich, Jullie W. Pan, and Hoby P. Hetherington. Resonant inductive decoupling (RID) for transceiver arrays to compensate for both reactive and resistive components of the mutual impedance. *NMR in Biomedicine*, 26(11):1547–1554, nov 2013.

[110] Jovan Jevtic. Ladder Networks for Capacitive Decoupling in Phased-Array Coils *. Technical report, 2001.

[111] Ray F. Lee, Randy O. Giaquinto, and Christopher J. Hardy. Coupling and decoupling theory and its application to the MRI phased array. *Magnetic Resonance in Medicine*, 48(1):203–213, jul 2002.

[112] Graham C. Wiggins, Jonathan R. Polimeni, Andreas Potthast, Melanie Schmitt, Vijay Alagappan, and Lawrence L. Wald. 96-Channel receive-only head coil for 3 Tesla: Design optimization and evaluation. *Magnetic Resonance in Medicine*, 62(3):754–762, sep 2009.

[113] Gregor Adriany, Pierre Francois Van De Moortele, Florian Wiesinger, Steen Moeller, John P. Strupp, Peter Andersen, Carl Snyder, Xiaoliang Zhang, Wei Chen, Klaas P. Pruessmann, Peter Boesiger, Tommy Vaughan, and Kamil Uğurbil. Transmit and receive transmission line arrays for 7 tesla parallel imaging. *Magnetic Resonance in Medicine*, 53(2):434–445, feb 2005.

[114] A. J.E. Raaijmakers, O. Ipek, D. W.J. Klomp, C. Possanzini, P. R. Harvey, J. J.W. Lagendijk, and C. A.T. Van Den Berg. Design of a radiative surface coil array element at 7 T: The single-side adapted dipole antenna. *Magnetic Resonance in Medicine*, 66(5):1488–1497, nov 2011.

[115] Gregor Adriany, Edward J. Auerbach, Carl J. Snyder, Ark Gözübüyük, Steen Moeller, Johannes Ritter, Pierre François Van De Moortele, Tommy Vaughan, and Kâmil Uğurbil. A 32-channel lattice transmission line array for parallel transmit and receive MRI at 7 tesla. *Magnetic Resonance in Medicine*, 63(6):1478–1485, jun 2010.

[116] Bing Wu, Chunsheng Wang, Douglas A.C. Kelley, Duan Xu, Daniel B. Vigneron, Sarah J. Nelson, and Xiaoliang Zhang. Shielded microstrip array for 7T human MR imaging. *IEEE Transactions on Medical Imaging*, 29(1):179–184, jan 2010.

[117] Gang Chen, Martijn Cloos, Daniel Sodickson, and Graham Wiggins. A 7T 8 channel transmit-receive dipole array for head imaging: dipole element and coil evaluation. Technical report, 2013.

[118] Nikolai I. Avdievich, Ioannis Angelos Giapitzakis, Jonas Bause, Gunamony Shajan, Klaus Scheffler, and Anke Henning. Double-row 18-loop transceive–32-loop receive tight-fit array provides for whole-brain coverage, high transmit performance, and SNR improvement near the brain center at 9.4T. *Magnetic Resonance in Medicine*, 81(5):3392–3405, may 2019.

[119] Shubharthi Sengupta, Alard Roebroeck, Valentin G. Kemper, Benedikt A. Poser, Jan Zimmermann, Rainer Goebel, and Gregor Adriany. A Specialized Multi-Transmit Head Coil for High Resolution fMRI of the Human Visual Cortex at 7T. *PLOS ONE*, 11(12):e0165418, dec 2016.

[120] Viktor G Veselago. THE ELECTRODYNAMICS OF SUBSTANCES WITH SIMULTANEOUSLY NEGATIVE VALUES OF ϵ AND μ. *Soviet Physics Uspekhi*, 10(4):509–514, apr 1968.

[121] J B Pendry. Negative refraction makes a perfect lens. *Physical Review Letters*, 85(18):3966–3969, oct 2000.

[122] R. A. Shelby, D. R. Smith, and S. Schultz. Experimental verification of a negative index of refraction. *Science*, 292(5514):77–79, apr 2001.

[123] Manuel J. Freire, Ricardo Marques, and Lukas Jelinek. Experimental demonstration of a $\mu=$ -1 metamaterial lens for magnetic resonance imaging. *Applied Physics Letters*, 93(23):231108, dec 2008.

[124] Manuel J. Freire, Lukas Jelinek, Ricardo Marques, and Mikhail Lapine. On the applications of $\mu_r = - 1$ metamaterial lenses for magnetic resonance imaging. *Journal of Magnetic Resonance*, 203(1):81–90, mar 2010.

[125] M D Schnall, C Barlow, V Harihara Subramanian, and J S Leigh. Wireless implanted magnetic resonance probes for in vivo NMR. *Journal of Magnetic Resonance (1969)*, 68(1):161–167, jun 1986.

[126] P. A. Belov, R. Marqués, S. I. Maslovski, I. S. Nefedov, M. Silveirinha, C. R. Simovski, and S. A. Tretyakov. Strong spatial dispersion in wire media in the very large wavelength limit. *Physical Review B - Condensed Matter and Materials Physics*, 67(11):1131031–1131034, mar 2003.

[127] Xavier Radu, Didier Garray, and Christophe Craeye. Toward a wire medium endoscope for MRI imaging. *Metamaterials*, 3(2):90–99, oct 2009.

[128] Stanislav B Glybovski, Sergei A Tretyakov, Pavel A Belov, Yuri S Kivshar, and Constantin R Simovski. Metasurfaces: From microwaves to visible, may 2016.

[129] C. Jouvaud, R. Abdeddaim, B. Larrat, and J. De Rosny. Volume coil based on hybridized resonators for magnetic resonance imaging. *Applied Physics Letters*, 108(2):023503, jan 2016.

[130] Alexey P. Slobozhanyuk, Alexander N. Poddubny, Alexander J. E. Raaijmakers, Cornelis A. T. van den Berg, Alexander V. Kozachenko, Irina A. Dubrovina, Irina V. Melchakova, Yuri S. Kivshar, and Pavel A. Belov. Enhancement of Magnetic Resonance Imaging with Metasurfaces. *Advanced Materials*, 28(9):1832–1838, mar 2016.

[131] Alena V. Shchelokova, Cornelis A.T. van den Berg, Dmitry A. Dobrykh, Stanislav B. Glybovski, Mikhail A. Zubkov, Ekaterina A. Brui, Dmitry S. Dmitriev, Alexander V. Kozachenko, Alexander Y. Efimtcev, Andrey V. Sokolov, Vladimir A. Fokin, Irina V. Melchakova, and Pavel A. Belov. Volumetric wireless coil based on periodically coupled split-loop resonators for clinical wrist imaging. *Magnetic Resonance in Medicine*, 80(4):1726–1737, oct 2018.

[132] Anna Hurshkainen, Anton Nikulin, Elodie Georget, Benoit Larrat, Djamel Berrahou, Ana Luisa Neves, Pierre Sabouroux, Stefan Enoch, Irina Melchakova, Pavel Belov, Stanislav Glybovski, and Redha Abdeddaim. A Novel Metamaterial-Inspired RF-coil for Preclinical Dual-Nuclei MRI. *Scientific Reports*, 8(1):1–13, dec 2018.

[133] Anna A Hurshkainen, Tatyana A Derzhavskaya, Stanislav B Glybovski, Ingmar J Voogt, Irina V Melchakova, Cornelis A T Van Den Berg, and Alexander J E Raaijmakers. Element decoupling of 7 T dipole body arrays by EBG metasurface structures: Experimental verification. *Journal of Magnetic Resonance*, 269:87–96, aug 2016.

[134] Anna Hurshkainen, Ksenia Lezhennikova, Constantin Simovski, and Stanislav Glybovski. An artificial magnetic shield for a volume coil for 7T MRI. In *Proceedings of the 2019 21st International Conference on Electromagnetics in Advanced Applications, ICEAA 2019*, pages 899–901. Institute of Electrical and Electronics Engineers Inc., sep 2019.

[135] Jan Taro Svejda, Andreas Rennings, and Daniel Erni. A metamaterial based dual-resonant coil element for combined sodium/hydrogen MRI at 7 Tesla. *tm - Technisches Messen*, 84(1), nov 2016.

[136] Anna Hurshkainen, Marc Dubois, Anton Nikulin, Christophe Vilmen, David Bendahan, Stefan Enoch, Stanislav Glybovski, and Redha Abdeddaim. Radiofrequency Coil for Dual-nuclei MR Muscle Energetics Investigation Based on Two Capacitively Coupled

Periodic Wire Arrays. *IEEE Antennas and Wireless Propagation Letters*, page 1, feb 2020.

[137] Marc Dubois, Lisa Leroi, Alexandre Vignaud, Stefan Enoch, and Redha Abdeddaim. Enhancement of transmit and receive efficiencies with hybridized meta-atom in 7t head coil array. In *Proceedings of the 2019 21st International Conference on Electromagnetics in Advanced Applications, ICEAA 2019*, page 942. Institute of Electrical and Electronics Engineers Inc., sep 2019.

[138] Cecil E. Hayes. The development of the birdcage resonator: a historical perspective. *NMR in Biomedicine*, 22(9):908–918, nov 2009.

[139] R. J. Pascone, B. J. Garcia, T. M. Fitzgerald, T. Vullo, R. Zipagan, and P. T. Cahill. Generalized electrical analysis of low-pass and high-pass birdcage resonators. *Magnetic Resonance Imaging*, 9(3):395–408, jan 1991.

[140] Michael D. Harpen. Equivalent circuit for birdcage resonators, feb 1993.

[141] Mark C. Leifer. Resonant Modes of the Birdcage Coil. *Journal of Magnetic Resonance*, 124(1):51–60, jan 1997.

[142] Giulio Giovannetti, Luigi Landini, Maria Filomena Santarelli, and Vincenzo Positano. A fast and accurate simulator for the design of birdcage coils in MRI. *Magma: Magnetic Resonance Materials in Physics, Biology, and Medicine*, 15(1-3):36–44, nov 2002.

[143] Romeo Pascone, Thomas Vullo, John Farrelly, and Patrick T. Cahill. Explicit treatment of mutual inductance in eight-column birdcage resonators. *Magnetic Resonance Imaging*, 10(3):401–410, 1992.

[144] Mathias Fink. Time Reversed Acoustics. *Physics Today*, 50(3):34–40, mar 1997.

[145] Ruey Song Huang and Martin I. Sereno. Visual stimulus presentation using fiber optics in the MRI scanner. *Journal of Neuroscience Methods*, 169(1):76–83, mar 2008.

[146] Usama Salem, Vinodh A Kumar, John E Madewell, Donald F Schomer, Dhiego Chaves de Almeida Bastos, Pascal O Zinn, Jeffrey S Weinberg, Ganesh Rao, Sujit S Prabhu, and Rivka R Colen. Neurosurgical applications of MRI guided laser interstitial thermal therapy (LITT). *Cancer Imaging*, 19(1):65, dec 2019.

[147] Eugene G. Kholmovski, Nicolas Coulombe, Joshua Silvernagel, Nathan Angel, Dennis Parker, Rob MacLeod, Nassir Marrouche, and Ravi Ranjan. Real-Time MRI-Guided Cardiac Cryo-Ablation: A Feasibility Study. *Journal of Cardiovascular Electrophysiology*, 27(5):602–608, may 2016.

[148] Meng Li, Berk Gonenc, Kiyoung Kim, Weijian Shang, and Iulian Iordachita. Development of an MRI-compatible needle driver for in-bore prostate biopsy. In *Proceedings of the 17th International Conference on Advanced Robotics, ICAR 2015*, pages 130–136. Institute of Electrical and Electronics Engineers Inc., oct 2015.

[149] A Nikulin, J De Rosny, K Haliot, B Larrat, and A Ourir. Opencage radio frequency coil for magnetic resonance imaging. *Applied Physics Letters*, 114(5), feb 2019.

[150] R Lazar, F Schmitt, W Renz, B Stoeckel, G Wiggins, and L Wald. Integrated RF Birdcage Head Coil* for 7T MRI. In *Proc. Intl. Soc. Mag. Reson. Med. 15*, 2007.

[151] Ulrich Katscher, Dong-Hyun Kim, and Jin Keun Seo. Recent progress and future challenges in MR electric properties tomography. *Computational and mathematical methods in medicine*, 2013:546562, 2013.

[152] S Gabriel, R W Lau, and C Gabriel. The dielectric properties of biological tissues: {II}. Measurements in the frequency range 10 Hz to 20 {GHz}. *Physics in Medicine and Biology*, 41(11):2251–2269, nov 1996.

[153] Pierre-François Van de Moortele, Can Akgun, Gregor Adriany, Steen Moeller, Johannes Ritter, Christopher M. Collins, Michael B. Smith, J. Thomas Vaughan, and Kāmil Uğurbil. B1 destructive interferences and spatial phase patterns at 7 T with a head transceiver array coil. *Magnetic Resonance in Medicine*, 54(6):1503–1518, dec 2005.

[154] Florian Wiesinger, Peter Boesiger, and Klaas P. Pruessmann. Electrodynamics and ultimate SNR in parallel MR imaging. *Magnetic Resonance in Medicine*, 52(2):376–390, aug 2004.

[155] Nikolai I. Avdievich, Georgiy Solomakha, Loreen Ruhm, Klaus Scheffler, and Anke Henning. Evaluation of short folded dipole antennas as receive elements of ultra-high-field human head array. *Magnetic Resonance in Medicine*, 82(2):811–824, aug 2019.

[156] Ulrich Katscher, Peter Börnert, Christoph Leussler, and Johan S. Van den Brink. Transmit SENSE. *Magnetic Resonance in Medicine*, 49(1):144–150, jan 2003.

[157] Yudong Zhu. Parallel Excitation with an Array of Transmit Coils. *Magnetic Resonance in Medicine*, 51(4):775–784, apr 2004.

[158] Peter Ullmann, Sven Junge, Markus Wick, Frank Seifert, Wolfgang Ruhm, and Jürgen Hennig. Experimental analysis of parallel excitation using dedicated coil setups and simultaneous RF transmission on multiple channels. *Magnetic Resonance in Medicine*, 54(4):994–1001, oct 2005.

[159] Weihua Mao, Michael B. Smith, and Christopher M. Collins. Exploring the limits of RF shimming for high-field MRI of the human head. *Magnetic Resonance in Medicine*, 56(4):918–922, oct 2006.

[160] N. I. Avdievich, A. Pfrommer, I. A. Giapitzakis, and A. Henning. Analytical modeling provides new insight into complex mutual coupling between surface loops at ultrahigh fields. *NMR in Biomedicine*, 30(10):e3759, oct 2017.

[161] Xin Li and Joseph V. Rispoli. Toward 7T breast MRI clinical study: safety assessment using simulation of heterogeneous breast models in RF exposure. *Magnetic Resonance in Medicine*, 81(2):1307–1321, feb 2019.

[162] GitHub - https://github.com/rispoli-lab/Bilateral-Breast-Fusion-.

[163] Joseph V Rispoli, Steven M Wright, Craig R Malloy, and Mary P McDougall. Automated modification and fusion of voxel models to construct body phantoms with heterogeneous breast tissue: Application to MRI simulations. *Journal of Biomedical Graphics and Computing*, 7(1):1, feb 2017.

[164] Ruomin Hu, Dennis Kleimaier, Matthias Malzacher, Michaela A.U. Hoesl, Nadia K. Paschke, and Lothar R. Schad. X-nuclei imaging: Current state, technical challenges, and future directions, feb 2020.

[165] K. Derby, J. Tropp, and C. Hawryszko. Design and evaluation of a novel dual-tuned resonator for spectroscopic imaging. *Journal of Magnetic Resonance (1969)*, 86(3):645–651, feb 1990.

[166] Gamaliel Isaac, Mitchell D. Schnall, Robert E. Lenkinski, and Katherine Vogele. A design for a double-tuned birdcage coil for use in an integrated MRI/MRS examination. *Journal of Magnetic Resonance (1969)*, 89(1):41–50, aug 1990.

[167] Boguslaw Tomanek, Vyacheslav Volotovskyy, Marco L.H. Gruwel, Eilean McKenzie, and Scott B. King. Double-frequency birdcage volume coils for 4.7T and 7T. *Concepts in Magnetic Resonance Part B: Magnetic Resonance Engineering*, 26B(1):16–22, aug 2005.

[168] Gunthard Lykowsky, Flavio Carinci, Markus Düring, Daniel Weber, Peter M Jakob, and Daniel Haddad. Optimization and comparison of two practical dual-tuned birdcage configurations for quantitative assessment of articular cartilage with sodium magnetic resonance imaging. *Quantitative imaging in medicine and surgery*, 5(6):799–805, 2015.

[169] S. B. Glybovski, A. V. Shchelokova, A. V. Kozachenko, A. P. Slobozhanyuk, I. V. Melchakova, P. A. Belov, A. V. Sokolov, A. Yu Efimtsev, and V. A. Fokin. Capacitively-loaded metasurfaces and their application in magnetic resonance imaging. In *2015 IEEE Radio and Antenna Days of the Indian Ocean, RADIO 2015*. Institute of Electrical and Electronics Engineers Inc., nov 2015.

[170] L. (Laszlo) Solymar and E. (Ekaterina) Shamonina. *Waves in metamaterials*. Oxford University Press, 2009.

[171] Elodie Georget, Michel Luong, Alexandre Vignaud, Eric Giacomini, Edouard Chazel, Guillaume Ferrand, Alexis Amadon, Franck Mauconduit, Stefan Enoch, Gérard Tayeb, Nicolas Bonod, Cyril Poupon, and Redha Abdeddaim. Stacked magnetic resonators for MRI RF coils decoupling. *Journal of Magnetic Resonance*, 275:11–18, feb 2017.

[172] Anton Nikulin, Abdelwaheb Ourir, Julien De Rosny, Stanislav Glybovski, Benoit Larrat, Frank Kober, and Redha Abdeddaim. Dual-tuned birdcage-like coil based on metasurfaces. In *Proceedings of the International Conference Days on Diffraction, DD 2018*, pages 230–234. Institute of Electrical and Electronics Engineers Inc., nov 2018.

[173] Jeroen van Gemert, Wyger Brink, Andrew Webb, and Rob Remis. High-permittivity pad design tool for 7T neuroimaging and 3T body imaging. *Magnetic Resonance in Medicine*, 81(5):3370–3378, may 2019.

[174] Nova. 1Tx 32Rx Head Coil 7T Clinic1 from Nova Medical - Siemens Healthineers USA.

[175] Gaham C. Wiggins, A. Potthast, C. Triantafyllou, C. J. Wiggins, and L. L. Wald. Eight-channel phased array coil and detunable TEM volume coil for 7 T brain imaging. *Magnetic Resonance in Medicine*, 54(1):235–240, jul 2005.

[176] David I. Hoult. Sensitivity and Power Deposition in a High-Field Imaging Experiment. *Journal of Magnetic Resonance Imaging*, 12(1):46–67, jul 2000.

[177] Lin Tang, Yik Kiong Hue, and Tamer S Ibrahim. Studies of RF shimming techniques with minimization of RF power deposition and their associated temperature changes. *Con-*

cepts in Magnetic Resonance Part B: Magnetic Resonance Engineering, 39 B(1):11–25, feb 2011.

[178] Boris Ya. Zel'dovich, Nikolai F Pilipetsky, and Vladimir V Shkunov. *Principles of Phase Conjugation*, volume 42 of *Springer Series in Optical Sciences*. Springer Berlin Heidelberg, Berlin, Heidelberg, 1985.

[179] M. Fink, C. Prada, F. Wu, and D. Cassereau. Self focusing in inhomogeneous media with 'time reversal' acoustic mirrors. In *Ultrasonics Symposium Proceedings*, volume 2, pages 681–686. Publ by IEEE, 1989.

[180] Mickael Tanter and Mathias Fink. Ultrafast imaging in biomedical ultrasound. *IEEE Transactions on Ultrasonics, Ferroelectrics, and Frequency Control*, 61(1):102–119, 2014.

[181] Geoffrey Lerosey, Julien De Rosny, Arnaud Tourin, and Mathias Fink. Focusing beyond the diffraction limit with far-field time reversal. *Science*, 315(5815):1120–1122, feb 2007.

[182] Guang S. He. Optical phase conjugation: Principles, techniques, and applications. 26(3):131–191, may 2002.

[183] Arnaud Derode, Arnaud Tourin, and Mathias Fink. Time reversal versus phase conjugation in a multiple scattering environment. In *Ultrasonics*, volume 40, pages 275–280, may 2002.

[184] Mathias Fink. Phase conjugation and time reversal in acoustics. In *AIP Conference Proceedings*, volume 524, pages 33–44. AIP Publishing, feb 2003.

[185] Mathias Fink. Related content Time-Reversal Acoustics. *J. Phys.: Conf. Ser*, 118:12001, 2008.

[186] P. Dular, C. Geuzaine, F. Henrotte, and W. Legros. A general environment for the treatment of discrete problems and its application to the finite element method. *IEEE Transactions on Magnetics*, 34(5):3395–3398, 1998.

[187] P. Dular, C. Geuzaine, A. Genon, and W. Legros. An evolutive software environment for teaching the finite element method in electromagnetism. *IEEE Transactions on Magnetics*, 35(3 PART 1):1682–1685, 1999.

[188] F. David Doty, Jatin Kulkarni, Christopher Turner, George Entzminger, and Anthony Bielecki. Using a cross-coil to reduce RF heating by an order of magnitude in triple-resonance multinuclear MAS at high fields. *Journal of Magnetic Resonance*, 182(2):239–253, oct 2006.

[189] Leon Axel. Surface coil magnetic resonance imaging. *Journal of Computer Assisted Tomography*, 8(3):381–384, jun 1984.

[190] Tsutomu Nakada, Ingrid L. Kwee, Toshiyuki Miyazaki, Norio Iriguchi, and Takeshi Maki. 31P NMR spectroscopy of the stomach by zig–zag coil. *Magnetic Resonance in Medicine*, 5(5):449–455, nov 1987.

[191] M Alfonsetti, V Clementi, S Iotti, G Placidi, R Lodi, B Barbiroli, A Sotgiu, and M Alecci. Versatile coil design and positioning of transverse-field RF surface coils for clinical 1.5-

T MRI applications. *Magnetic Resonance Materials in Physics, Biology and Medicine*, 18(2):69–75, may 2005.

[192] Timothy L. Nagel, Jacob A. Stolk, Donald W. Alderman, Robin Schoenborn, and Martin P. Schweizer. The crossover surface coil: an efficient in vivo nmr detector. *Magnetic Resonance in Medicine*, 13(2):271–278, feb 1990.

RÉSUMÉ

Le travail présenté dans ce manuscrit vise à créer un nouveau type de bobine volumique dédié à l'imagerie par résonance magnétique ultra haut champ ($B_0 \geq 7$ T) dérivé de la cage à oiseaux bien connue. Son design s'inspire des travaux sur les métamatériaux. Sur la base d'une analyse en termes de lignes de transmission, le champ de la radiofréquence B_1 et la géométrie de la bobine peuvent être façonnés de manière presque arbitraire. Dans un premier temps, nous proposons une bobine qui facilite l'accès à son volume intérieur. Cette bobine "ouverte" améliore non seulement le confort des patients lors d'examens IRM, en particulier pour les patients souffrant de claustrophobie, mais elle peut également être utile pour certaines applications spécifiques de l'IRM telles que la correction de mouvements. Un prototype dédié au petit animal et un autre prototype dévolu à l'imagerie de la tête ont été construits et testés sur un IRM 7 T. Ensuite, nous proposons d'appliquer cette approche à base de métamatériaux pour développer des bobines volumiques à double bande qui peuvent être sensibles simultanément à deux noyaux. Enfin, nous introduisons une nouvelle méthode de façonnage du champ B1 fondée sur la technique de conjugaison de phase. Nous étudions théoriquement cette méthode pour développer une bobine pour l'imagerie à 7 T de la tête et développons un prototype pour l'imagerie des rongeurs dans un scanner 17,2 T.

MOTS CLÉS

IRM très haut champ, Cage à oiseaux, Bobine tête, Optimisation des courants, Métamatériaux

ABSTRACT

This manuscript aims to create new kinds of volume radiofrequency coils for UHF MRI ($B_0 \geq 7$ T) derived from the well-known birdcage coil. Their designs are inspired from metamaterials. Based on transmission line analysis, the radiofrequency B_1 field and coil's geometry can be shaped almost as will in order to obtain coils with unique features. At first, we propose a volume coil that eases access to its inner volume. This "opencage" coil does not only improve the comfort during MRI examinations, especially for patients suffering from claustrophobia but it can also be useful for some specific applications of MRI such as motion correction. A small-animal and a head-size prototypes working at 7 T have been built and tested. Then we propose to apply this metamaterial approach to develop dual-band birdcages that are sensitive simultaneously to two nuclei. Finally, we introduce a new method of passive B_1 shimming based on phase conjugation technique. We theoretically investigate this method for developing a head coil for 7 T imaging, whereas later we build a prototype for imaging of rodents in a 17.2 T scanner.

KEYWORDS

UHF MRI, Birdcage coil, Head coil, Optimization of currents, Metamaterials